Synthesis, Characterization and Amphiphilicity-Driven Self-Assembly of Quantum Dots with Mixed Polymer Brush Layers

By

Yunyong Guo

B.Sc., Nankai University, China, 2000

M.Sc., Nankai University,China, 2003

A Dissertation Submitted in Partial Fulfillment of the

Requirements for the Degree of

DOCTOR OF PHILOSOPHY

in the Department of Chemistry

University of Victoria

Synthesis, Characterization and Amphiphilicity-Driven Self-Assembly of Quantum Dots with Mixed Polymer Brush Layers

By

Yunyong Guo

B.Sc., Nankai University, China, 2000

M.Sc., Nankai University,China, 2003

Supervisory Committee

Dr. Matthew Moffitt, Supervisor
(Department of Chemistry)

Dr. David Harrington, Departmental Member
(Department of Chemistry)

Dr. Lisa Rosenberg, Departmental Member
(Department of Chemistry)

Dr. David Sinton, Outside Member
(Department of Mechanical Engineering)

Supervisory Committee

Dr. Matthew Moffitt, Supervisor
(Department of Chemistry)

Dr. David Harrington, Departmental Member
(Department of Chemistry)

Dr. Lisa Rosenberg, Departmental Member
(Department of Chemistry)

Dr. David Sinton, Outside Member
(Department of Mechanical Engineering)

Abstract

The synthesis, characterization and self-assembly behavior of semiconductor quantum dots (QDs) with mixed polystyrene (PS) / poly (methyl methacrylate) (PMMA) polymer brush layers (PS/PMMA-CdS) are described. The environmentally-responsive PS/PMMA-CdS nanoparticles are investigated in various solvents with different polarities. Static and dynamic light scattering results suggest conformational changes in the mixed brush structure in response to different solvent polarities. UV-vis and photoluminescence spectra show that QD sizes and optical properties are independent of the solvent medium due to protection by the block copolymer. Long-term stability of QD size distributions in the studied solvents is demonstrated for period of up to six months. 2D ^{1}H NOESY experiments indicate that PS and PMMA coronal chains are statistically distributed around the QDs within the mixed brush layer. PS/PMMA-CdS nanoparticles

are also shown to self-assemble at the polymer/polymer interface of a phase-separating blend of the corresponding homopolymers, forming an encapsulating shell surrounding PMMA islands in a PS matrix. The segregated QDs regulate phase separation during spin-coating and dramatically stabilize the spin-coated blend morphologies during subsequent annealing. Free-standing arrays of QD/polymer rings are developed by selective solvent washing and removal of homopolymers from the spin-coated films. After converting the PMMA coronal chains to poly (methacrylic acid) (PMAA) via a hydrolysis reaction, the resulting amphiphilic PS/PMAA-CdS nanoparticles are found to show rich and tunable self-assembly behavior in mixtures of organic solvents and water. The block copolymer-like self-assembly behavior of PS/PMAA-CdS suggests phase separation of randomly-distributed PS and PMAA chains within the mixed brush structure, leading to anisotropic interactions between nanoparticles mediated by energetic contributions from interfacial tension and chain stretching. As a result, PS/PMAA-CdS forms a wide range of interesting colloidal superstructures, including spherical supermicelles, worms, and vesicles, all with well-defined internal organization of QDs. Based on annealing experiments at a relative low water content above *cwc*, a mechanism of the formation of worm-like and continent aggregates is proposed. Thermodynamic and kinetic aspects of formation of the various QD/polymer colloids are also described.

Table of Contents

Supervisory Committee ..... **ii**

Abstract ..... **iii**

Table of Contents ..... **v**

List of Tables ..... **x**

List of Schemes and Figures ..... **x**

List of Abbreviation ..... **xix**

Acknowlegement ..... **xx**

CHAPTER 1

GENERAL INTRODUCTION **1**

1.1 Background and Motivation 2

1.2 Polymer and Block Copolymers 9

1.2.1 Polymers 9

1.2.2 Molecular Weight Distribution 10

1.2.3 Sequential Anionic Polymerization 13

1.3 Micellization of Block Copolymers 16

1.3.1 Formation of Block Copolymer Micelles 16

1.3.2 Thermodynamics of Block Copolymer Micellization 18

1.4 Semiconductor Nanoparticles (Quantum Dots) 24

1.5 Characterization and Methods and Instrumentation 27

1.5.1 Static and Dynamic Light Scattering (SLS and DLS) 27

1.5.2 Atomic Force Microscopy (AFM) 28

1.5.3 Laser Scanning Confocal Flourescence Microscopy (LSCFM) 29

1.5.4 Transmission Electron Microscopy (TEM) 31

1.6 Content of the Thesis 32

1.7 References 35

CHAPTER 2
SEMICONDUCTOR QUANTUM DOTS WITH ENVIRONMENTALLY RESPONSIVE MIXED POLYSTYRENE/POLY(METHYL METHACRYLATE) BRUSH LAYERS..... 42

2.1. Introduction..... 43
2.2. Experimental..... 47
2.2.1. Synthesis of Polystyrene-*b*-Poly (*tert*-Butyl Acrylate)-*b*-Poly(Methyl Methacrylate) (PS-*b*-P*t*BA-*b*-PMMA) Triblock Copolymer..... 47
2.2.2. Selective Hydrolysis of PS-*b*-P*t*BA-*b*-PMMA..... 48
2.2.3. Preparation of Polystyrene-*b*-Poly(Cadmium Acrylate)-*b*-Poly(Methyl methacrylate) (PS-*b*-PACd-*b*-PMMA) Micelles..... 49
2.2.4. Preparation of Mixed Polymer Brush-Stabilized QDs (PS/PMMA-CdS)..... 49
2.2.5. Dispersion of PS/PMMA-CdS in PS or PMMA Homopolymers..... 50
2.2.6. Gel Permeation Chromatography (GPC)..... 50
2.2.7. ^{1}H NMR Analysis..... 51
2.2.8. UV-Vis Absorption and Photoluminescence Measurements..... 51
2.2.9. Static and Dynamic Light Scattering Measurements..... 51
2.2.10. Laser Scanning Confocal Fluorescence Microscopy (LSCFM)..... 54
2.2.11. Transmission Electron Microscopy..... 54
2.3. Results and Discussion..... 55
2.3.1. Characterization of PS-*b*-P*t*BA-*b*-PMMA and Hydrolyzed PS-*b*-PAA-*b*-PMMA Triblock Copolymers..... 55
2.3.2. Copolymer Micellization and Formation of Mixed Polymer Brush-Stabilized QDs (PS/PMMA-CdS)..... 61
2.3.3. Optical Properties and Stability of PS/PMMA-CdS in Various Solvents..... 66
2.3.4. Nuclear Overhauser Effect (NOESY) Investigation of PS/PMMA-CdS..... 70

2.3.5. Static and Dynamic Light Scattering: Solvent-Responsive Brush Conformations in PS/PMMA-CdS Colloids 72
2.3.6. Dispersion of PS/PMMA-CdS in PS and PMMA Homopolymers 84
2.4 Conclusions 89
2.5 References 94

CHAPTER 3
"SMART" SELF-ASSEMBLED QUANTUM DOTS REGULATE AND STABILIZE STRUCTURE IN PHASE-SEPARATED POLYMER BLENDS 95

3.1. Introduction 96
3.2. Experimental 98
3.2.1. Preparation of Spin-Coated Blend Films 98
3.2.2. Atomic Force Microscopy (AFM) 99
3.2.3. Laser Scanning Confocal Fluorescence Microscopy (LSCFM) 100
3.2.4. Transmission Electron Microscopy (TEM) 100
3.2.5. Photoluminescence Measurements 100
3.2.6. Analysis of AFM Surface Features 101
3.3. Results and Discussion **101**
3.4. Conclusions **120**
3.5. References **121**

CHAPTER 4
AMPHIPHLIC-DRIVEN SELF-ASSEMBLY OF POLYMER-COATED QUANTUM DOTS INTO MORPHOLOGICALLY-TUNABLE AGGREGATES 125

4.1. Introduction **126**
4.2. Experimental **129**
4.2.1. Synthesis of Polystyrene-*b*-Poly (Acrylic Acid)-*b*-Poly(Methyl Methacrylate) (PS-*b*-PAA-*b*-PMMA) Triblock Copolymer 129

4.2.2. Preparation of Polystyrene-*b*-Poly(Cadmium Acrylate)-*b*-Poly(Methyl Methacrylate) (PS-*b*-PACd-*b*-PMMA) Micelles 130
4.2.3. Preparation of Cd^{2+}-crosslinked and Diamide Crosslinked of PS/PMMA-CdS 130
4.2.4. Hydrolysis of PMMA blocks in PS/PMMA-CdS (Cd^{2+}-Crosslinked) and PS/PMMA-CdS (Diamide-Crosslinked) 132
4.2.5. Self-assembly of PS/PMAA-CdS in Mixtures of Polar Organic Solvents and Water (Immediate Quenching Method) 132
4.2.6. Self-assembly of PS/PMAA-CdS in Mixtures of THF and Water (Annealing Method) 133
4.2.7. Gel Permeation Chromatography (GPC) 134
4.2.8. ^{1}H NMR 134
4.2.9. UV-vis Absorption and Photoluminescence Measurements 134
4.2.10. Transmission Electron Microscopy (TEM). 135
4.2.11. Powder X-ray Diffraction (XRD) 136
4.2.12. Dynamic Light Scatteing (DLS) 136
4.2.13. Atomic Force Microscopy (AFM) 137
4.2.14. Laser Scanning Confocal Fluorescence Microscopy (LSCFM) 137
4.2.15. Zeta Potential Measurement. 138

4.3. Results and Discussion 138
4.3.1. Hydrolysis of PS/PMMA-CdS to PS/PMAA-CdS (Cd^{2+}-crosslinked) 138
4.3.2. Hydrolysis of PS/PMMA-CdS to PS/PMAA-CdS 144
4.3.3. Characterization of PS/PMAA-CdS Amphiphilic Nanoparticles 149
4.3.3.1. UV-vis Absorption Spectroscopy 149
4.3.3.2. Transmission Electron Microscopy (TEM) 150
4.3.3.3. High Resolution TEM (HRTEM) and Powder X-ray Diffraction (XRD) 151
4.3.3.4. Photoluminescence (PL) 154
4.3.3.5. Dynamic Light Scattering (DLS) 155

4.3.4. Self-assembly of PS/PMAA-CdS Nanoparticles into QD/Polymer Aggregates of Various Morphologies 156
4.3.4.1. Spherical Supermicelles (c_o = 0.5 wt% DMF/Water and THF/Water, Immediate Quenching Method). 156
4.3.4.2. Worm-like Supermicelles (c_o = 1.0 wt%, THF/water, Immediate Quenching Method). 165
4.3.4.3. Self-assembly of PS/PMAA-CdS into Large Internally-Structured Aggregates (Continents) Via Annealing Method. 177
4.3.4.4. Proposed Formation for Worms and Continents 181
4.3.4.5. QD/polymer Vesicles (c_o = 1.0 wt% THF/Water, Immediate Quenching Method) Via Salt or Acid Addition 188
4.3.4.6. pH-Dependent Surface Charge and Hydrodynamic Diameter of PS/PMAA-CdS Vesicles 198
4.3.4.7. Photoluminescence of QD/Polymer Spherical Supermicelles and Vesicles 201
4.4. Conclusions 202
4.5. References 204

CHAPTER 5
CONTRIBUTION TO ORIGINAL KNOWLEDGE AND SUGGESTS FOR FUTUURE WORK 207

List of Tables

Table 2.1. Characteristics of PS-b-PtBA-b-PMMA Triblock Copolymer Synthesized by Sequential Anionic Polymerization 59

Table 2.2. Summary of PS/PMMA–CdS Structure in Various Solvents Determined from Static and Dynamic Light Scattering Data 74

Table 4.1. Characteristics of PS-b-PAA-b-PMMA Triblock Copolymer Synthesized by Sequential Anionic Polymerization 130

List of Schemes and Figures

CHAPTER 1 1

Scheme 1.1. (a) PS-CdS nanoparticle, (b) PS/PMMA-CdS nanoparticle 4

Scheme 1.2. α-methylstyrene initiated with sec-BuLi. 14

Scheme 1.3. Propagating step of styrene reacting with **1** 15

Scheme 1.4. Propagating step of tert-butylacrylate reacting with 2 16

Scheme 1.5. Propagating step of methyl methacrylate reacting with 3 16

Figure 1.1. Types of copolymers formed from A and B repeat units 10

Figure 1.2. Molecular weight distribution of a theoretical polymer sample highlighting the position of different types of average molecular weights. 10

Figure 1.3. Schematic of micellization of a diblock copolymer in selective solvent 16

Figure 1.4. Schematic diagram of star-like (a) and crew-cut (b) micelles 18

Figure 1.5. Morphologies of PS-*b*-PAA aggregates in aqueous solution with different amounts of NaCl added to DMF solutions prior to water addition. From A to I, the concentration of NaCl increased from 0 to 21 mM. 20

Figure 1.6. UV-vis absorption spectra of CdS nanoparticles of different mean particle sizes 25

Figure 1.7. Illustration of atomic force microscopy (AFM) 28

Figure 1.8. Schematic representation of laser scanning confocal fluorescence microscopy (LSCFM). 30

Figure 1.9. Schematic illustration of transmission electron microscope (TEM) 31

Chapter 2 42

Scheme 2.1. Formation of PS/PMMA-CdS via self-assembly of PS-*b*-PAA-*b*-PMMA triblock copolymers, followed by templated QD growth in the copolymer micelle cores. 47

Scheme 2.2. Mixed-brush conformations of environmentally-responsive PS/PMMA-CdS nanoparticles in different solvents based on DLS data 83

Figure 2.1. Gel permeation chromatograms (refractive index detector response) of aliquots removed from reaction solution after polymerization of each block during sequential anionic polymerization of PS-*b*-P*t*BA-*b*-PMMA. 56

Figure 2.2. ^{1}H NMR spectrum and peak assignments of PS-*b*-PtBA-*b*-PMMA triblock copolymer in chloroform-D, before selective hydrolysis of the PtBA block. 58

Figure 2.3. ^{1}H NMR spectrum and peak assignments of PS-*b*-PAA-*b*-PMMA triblock copolymer in chloroform-D, after selective hydrolysis of the PtBA block. 60

Figure 2.4. Photos of (a) PS/PMMA-CdS and (b) PS-CdS dispersions in acetone, chloroform, toluene, and THF. 63

Figure 2.5. (a) Transmission electron micrograph (TEM) of PS/PMMA-CdS cast from a dilute (2 mg/mL) benzene dispersion onto a carbon-coated TEM grid. (b) CdS QD size distribution determined from several TEM images such as those shown in (a) taken in different regions of the grid. 65

Figure 2.6. (a) UV-vis absorption spectra and (b) photoluminescence (PL) spectra of PS/PMMA-CdS dispersions in various solvents. For PL spectra, λ_{ex} = 400 nm. 67

Figure 2.7. Investigation of long-term stability of QD size distributions for PS/PMMA-CdS dispersions in various solvents. UV-vis spectra of PS/PMMA-CdS in (a) acetone, (b) THF, (c) chloroform, and (d) toluene after 1 day (solid lines) and 180 days (dashed lines) storage under ambient conditions. 69

Figure 2.8. 2D 1H NMR NOESY spectra of (a) PS/PMMA-CdS and (b) PS-b-PAA-b-PMMA in THF-D8. Circles in (a) indicate cross-peaks between PS and

PMMA blocks in the PS/PMMA-CdS spectrum which are not present in the reference spectrum (b) of PS-*b*-PAA-*b*-PMMA single chains 71

Figure 2.9. Representative Zimm plots of static light scattering (SLS) data for PS/PMMA-CdS in (a) acetone, (b) THF, (c) chloroform, and (d) toluene. The measured scattering angles were from 5° to 155° in 15° increments, and concentrations were between 0.1 to 1.0 mg/mL 75

Figure 2.10. Dynamic light scattering (DLS) results for PS/PMMA-CdS. (a) Representative plots of $\overline{\Gamma}$ vs. q^2 for PS/PMMA-CdS dispersions in different solvents of approximately equal concentration (~0.2 mg/mL). (b) Plots of D_T vs. concentration for PS/PMMA-CdS in acetone, THF, chloroform, and toluene 79

Figure 2.11. Hydrodynamic size distributions from CONTIN analysis of dynamic light scattering (DLS) data for PS/PMMA-CdS in various solvents: (a) acetone, (b) THF, (c) chloroform, and (d) toluene. Results are from representative autocorrelation functions obtained at a 90°-scattering angle and approximately equal concentrations (~0.1 mg/mL). 80

Figure 2.12. PS/PMMA-CdS dispersed in blend films with (a, c) PS and (b, d) PMMA homopolymer by spin-coating from toluene solutions. (a, b) Laser scanning confocal fluorescence microscopy (LSCFM) images of blend films, showing spatially-uniform PL from QDs dispersed in both homopolymers. (c, d) TEM images of microtomed sections of blend films 85

Figure 2.13. Photoluminescence emission spectra (λ_{ex} = 400 nm) of PS/PMMA-CdS dispersed in toluene (black line), a blend film of 30/70 (w/w) PS/PMMA-CdS / PS (blue line) and a blend film of 30/70 (w/w) PS/PMMA-CdS / PMMA (red line)..... 86

Figure 2.14. Laser scanning confocal fluorescence microscopy (LSCFM) images of blend films of PS/PMMA-CdS with (a) PS and (b) PMMA homopolymers, prepared by drop-casting and slow solvent evaporation over 7 days. Unlike spin-coated films of the same composition (Figure 2.12), micron-scale phase separation is observed between the photoluminescent PS/PMMA-CdS nanoparticle phase and the non-photoluminescent homopolymer phases,

suggesting kinetic trapping of uniform PS/PMMA-CdS dispersion in the spin-coated blend films 88

Chapter 3 95

Scheme 3.1. Structure of PS/PMMA-CdS Mixed Brush-Stabilized QDs 102

Figure 3.1. Atomic force microscopy (AFM) images of neat PS:PMMA (30:70) blend films for various periods of annealing at 150 ºC following spin-coating. In a-d), films were imaged with no selective solvent washing; in e-h), films were washed with cyclohexane to remove the PS phase. a,e) 0 h annealing; b,f) 4 h annealing; c,g) 8 h annealing; d,h) 24 h annealing. All scale bars represent 2 μm. Part i) shows a schematic (not to scale) of the PS and PMMA phase distributions following spin-coating (i) and for different stages of phase coarsening (ii, iii), as described in text 104

Figure 3.2. Atomic force microscopy (AFM) images of PS:PMMA (30:70) blend films with 10% PS/PMMA-CdS QDs following spin-coating: a) film without solvent washing; b) film washed with cyclohexane to remove the PS phase only; c) film washed with acetic acid to remove the PMMA phase only; d) film washed with cyclohexane then acetic acid to remove both the PS and PMMA phases; remaining rings of PS/PMMA-CdS indicate interfacial self-assembly of QDs during spin-coating. All scale bars represent 2 μm; the dimensions of inset to d) are 5 μm x 5 μm. Part e) shows a schematic (not to scale) of phase distributions in the spin-coated film with relative heights of the PS, PMMA and PS/PMMA-CdS phases. 106

Figure 3.3. Atomic force microscopy (AFM) images of PS:PMMA (30:70) blend films with 10% added PS/PMMA-CdS QDs for various periods of annealing at 150 ºC following spin-coating: a) 4 h annealing; b) 8 h annealing; c) 12 h annealing; d) 24 h annealing. Inset to d) shows film washed with cyclohexane then acetic acid to reveal the distribution of PS/PMMA-CdS QDs. All scale bars represent 2 μm; the dimensions of inset to d) are 5 μm x 5 μm. e) Plots of the surface correlation length, Λ_m, vs. annealing time for different

PS/PMMA-CdS QD contents. Λ_m determined from fast Fourier transforms (FFT) of AFM images, as described in the text 110

Figure 3.4. Transmission electron microscopy (TEM) images of parallel sections of PS:PMMA (30:70) blend films with a,d) 0%, b,e) 10% and c,f) 20% added PS/PMMA-CdS QD*s* 112

Figure 3.5. PMMA domain size distributions from transmission electron microscopy (TEM) images of parallel sections of PS:PMMA (30:70) blend films with different amounts of PS/PMMA-CdS: a) 0% b) 10% and c) 20%.. 114

Figure 3.6. Laser scanning confocal fluorescence microscopy (LSCFM) images of PS:PMMA (30:70) blend films with a) 10% and b) 20% added PS/PMMA-CdS QDs. c) Normalized photoluminescence (PL) spectra of blend films in a) (red line) and b) (blue line); PL spectrum of PS/PMMA-CdS QDs dispersed in toluene (dashed line) is shown for comparison. 116

Figure 3.7. Three-dimensional (3D) atomic force microscopy (AFM) images of PS:PMMA (30:70) blend films with 20% added PS/PMMA-CdS QDs: a) film obtained by spin-coating and 8 h annealing at 150 ºC, with no solvent washing; b) film obtained by spin-coating and 8 h annealing at 150 ºC, followed by solvent washing with cyclohexane then acetic acid to remove the PS and PMMA phases, respectively. Nearly identical blend morphologies were obtained by spin-coating and solvent development without annealing 119

Chapter 4 125

Figure 4.1. Morphologies of PS-*b*-PAA aggregates in aqueous solution with different amounts of added NaCl to DMF solutions prior to water addition. From a to d, the concentration of NaCl increased from 2.1 to 16.0 mM 127

Figure 4.2. Schematic showing various synthetic steps for the formation of PS/PMMA-CdS (Cd^{2+}-crosslinked). 140

Figure 4.3. Schematic of hydrolysis PS/PMMA-CdS (Cd^{2+}-crosslinked) to PS/PMAA-CdS (Cd^{2+}-crosslinked) nanoparticle 141

Figure 4.4. (a) ^{1}H NMR peak assignments of PS-b-PAA-b-PMMA triblock copolymer, and ^{1}H NMR spectra of (b) PS/PMMA-CdS (Cd^{2+} -crosslinked), (c) PS/PMAA-CdS (Cd^{2+}-crosslinked) in DMSO-d. 142

Figure 4.5. GPC (refractive index detector response) of (a) PS-*b*-PtBA-*b*-PAA starting copolymer (single chains), (b) PS/PMMA-CdS (Cd^{2+}-crosslinked) (before hydrolysis reaction), and (c) PS/PMAA-CdS (Cd^{2+}-crosslinked)(after hydrolysis reaction).All GPC chromatograms were run with THF as the eluting solvent. 143

Figure 4.6. Schematic showing various synthetic steps for the formation of PS/PMMA-CdS (diamide-crosslinked). 145

Figure 4.7. Schematic hydrolysis of PS/PMMA-CdS (diamide-crosslinked) to PS/PMAA-CdS (diamide-crosslinked) nanoparticle 146

Figure 4.8. (a) ^{1}H NMR peak assignments of PS-*b*-PAA-*b*-PMMA triblock copolymer, and ^{1}H NMR spectra of (b) PS/PMMA-CdS (diamide-crosslinked), (c) PS/PMAA-CdS (diamide-crosslinked) in DMSO-d. 147

Figure 4.9. GPC (refractive index detector response) of (a) PS-*b*-PtBA-*b*-PAA starting copolymer (single chains), (b) PS/PMMA-CdS (diamide-crosslinked) (before hydrolysis reaction), and (c) PS/PMAA-CdS (diamide-crosslinked)(after hydrolysis reaction).All GPC chromatograms were run with THF as the eluting solvent. 148

Figure 4.10. UV-vis absorption spectra of PS/PMMA-CdS (blue line) and PS/PMAA-CdS (red line) in DMF. 150

Figure 4.11. (a)Transmission electron micrograph (TEM) of PS/PMAA-CdS cast from a dilute (2 mg/mL) THF solution. (b) CdS QD size distribution determined from several TEM images such as that shown in (a) QDs measured in the analysis with a total of 100. 152

Figure 4.12. (a) High resolution transmission electron micrograph (HRTEM) of a single CdS QD for PS/PMAA-CdS cast from a dilute (2 mg/mL) THF solution. (b) X-ray powder diffraction pattern from PS/PMAA-CdS. The red lines correspond to peak positions for cubic CdS 153

Figure 4.13. Photoluminescence spectra of PS/PMMA-CdS (blue line) and PS/PMAA-CdS (red line) in DMF, λ_{ex} = 400 nm. 155

Figure 4.14. The plot of effective $2r_h$ vs concentration for PS/PMAA-CdS in DMF. 157

Figure 4.15. Schematic showing steps for self-assembly of PS/PMAA-CdS in DMF/water and THF/water (immediate quenching method). 160

Figure 4.16. TEM images of QD/polymer aggregates (spherical supermicelles) of PS/PMAA-CdS obtained from initial polymer concentration c_o = 0.5 wt% in DMF (a) and THF (b). The scale bar in the inset of (a) is 100 nm. Aggregate size distributions based on measurement of 100 particles for (a) and (b) are shown in (c) and (d), respectively. 161

Figure 4.17. TEM images of QD/polymer aggregates (spherical supermicelles) obtained from initial polymer concentration c_o = 0.5 wt% in THF: (a) TEM image of PS/PMAA-CdS cross-section film; (b) dark-field TEM image. (c) Proposed self-assembly process for QD/polymer spherical supermicelles in mixtures of water and polar organic solvents. (d) QDs size distributions based on measurement of 100 particles for (a) and other TEM images 164

Figure 4.18. TEM images of QD/polymer aggregates (worm-like supermicelles) of PS/PMAA-CdS obtained from initial polymer concentration c_o = 1 wt% in THF: (a) low and (b)high-magnification TEM images; (c) TEM image of cross-section film; (d) dark-field TEM image 168

Figure 4.19. TEM images of QD/polymer aggregates (worm-like supermicelles) of PS/PMAA-CdS obtained from initial polymer concentration c_o = 1 wt% in THF: (a) low -magnification TEM images and (b) dark field TEM image; (c) TEM image of cross-section film; (d) dark-field TEM image. (c) and (d) are size distributions of width of worm and spacing between QD regions measured from 100 particles or regions in several TEM images. 169

Figure 4.20. Dark field TEM images of QD/polymer aggregates (worms) for different angles of rotation of the TEM sample holder (dashed lines indicate axis of rotation) : (a) 0^o; (b) 30^o; (c) 50^o. The right-hand side shows a schematic

of the 2D projections of the proposed supermicelle structures at corresponding angles of rotation. 171

Figure 4.21. (a) Dark-field TEM image of QD/polymer aggregate (worm) (b) Energy-dispersive X-ray spectra corresponding to regions 1,2 and 3 indicated by red spots in (a)..... 172

Figure 4.22. (a) Dark-field TEM image of QD/polymer aggregates (worms). (b) EDX profiles corresponding to red line indicated in (a)..... 173

Figure 4.23. (a) AFM images of QD/polymer aggregate (worm) cast on glass from aqueous solution. (b) Surface feature topology profile for white line in (a). and 3D obtained from (a); (c) Height and (d) FWHM width distributions determined from 100 measured aggregates in several AFM images..... 175

Figure 4.24. Laser scanning confocal fluorescence microscopy (LSCFM) images of QD/polymer aggregates (worms). λ_{ex} = 488 nm, $\lambda_{em} \geq$ 515 nm 176

Figure 4.25. TEM images of QD/polymer aggregates from self-assembly of PS/PMAA-CdS in THF/water mixtures (c_o = 1.0 wt%) at different water contents. Colloids were annealed at the indicated water contents for two weeks (annealing method) before final quenching and dialysis. 178

Figure 4.26. (a) High-magnification TEM image of QD/polymer aggregates (continents) from self-assembly of PS/PMAA-CdS in THF/water (c_o = 1.0 wt%, 50 wt% water, annealing method) (b) cross section TEM image of continent. (c) Statistical analysis of diameter of CdS QDs within continent aggregates obtained from measuring 100 particles..... 180

Figure 4.27. High magnification TEM images of various QD/polymer aggregates from self-assembly of PS/PMAA-CdS in THF/water (c_o = 1.0 wt%, 11wt % water, annealing method). 182

Figure 4.28. Proposed mechanism for the formation and growth of QD/polymer worms and continent aggregates..... 186

Figure 4.29. TEM images of QD/polymer vesicles formed via self-assembly of PS/PMAA-CdS in THF/water with small quantity of added NaCl (c_o = 1.0 wt%, R_{NaCl} = 3.0 immediate quenching method). 189

Figure 4.30. Cross-section TEM images of QD/polymer vesicles formed via self-assembly of PS/PMAA-CdS in THF/water with small quantity of added NaCl (c_o = 1.0 wt%, R_{NaCl} = 3.0 immediate quenching method).. 191
Figure 4.31. Proposed self-assembly process for QD/polymer vesicles in THF/water. 193
Figure 4.32. (a),(b) TEM images of QD/polymer vesicles formed via self-assembly of PS/PMAA-CdS in THF/water with small quantity of added NaCl (c_0 =1.0 wt%, R_{NaCl} = 3.0, immediate quenching method) (c) and (d) Vesicle diameter and PS wall thickness size distribution determined from measurement of 100 particles in several TEM images. 194
Figure 4.33. (a) AFM images of QD/polymer vesicle cast on glass from aqueous solution. (b) Surface feature topology profile for white line in (a).; (c) Height and (d) FWHM width distributions determined from 100 measured aggregates in several AFM images 196
Figure 4.34. (a) Dark field TEM image of QD/polymer vesicles formed by adding NaCl (b) Energy-dispersive X-ray spectra corresponding to regions 1, 2,3, 4,5 and 6 indicated by red spots in (a). 197
Figure 4.35. (a) and (b)TEM images of QD/polymer vesicles formed via self-assembly of PS/PMAA-CdS in THF/water with small quantity of added HCl (c_o = 1.0 wt%, R_{HCl} = 0.8 immediate quenching method). (c) and (d) Vesicle diameter and PS wall thickness size distribution determined from measurement of 100 particles in several TEM images.. 199
Figure 4.36 (a) Plot of zeta potential vs pH value of QD/polymer vesicle by adding HCl. (b) Plot of hydrodynamic diameter of QD/polymer vesicle by adding HCl . (c) Schematic diagram of vesicle with increasing pH value. 200
Figure 4.37. Photoluminescence spectra of PS/PMAA-CdS dispersed in THF (red line), QD/polymer spherical supermicelle (dark green line), and QD/polymer vesicle (formed with R_{HCl} = 0.8) (dark blue line), all spectra run at excition wavelength λ_{ex} = 400 nm using a 420 nm long-pass filter 201

List of Abbreviations

AFM	atomic force microscopy
cmc	critical micelle concentration
cwc	critical water concentration
DLS	dynamic light scattering
DMF	Dimethylformamide
EDC	*N*-ethyl-*N*'-(3-dimethylaminopropyl)carbodiimide methiodide
EDX	energy-dipserive X-ray spectroscopy
FFT	fast Fourier transforms
LSCFM	laser scanning confocal fluorescence microscopy
PAA	poly (acrylic acid)
PL	photoluminescence
PMAA	poly (methyl acrylic acid)
PMMA	poly (methyl methacrylate)
PS	polystyrene
P*t*BA	poly (tert-butylacrylate)
QDs	quantum dots
SLS	static light scattering
TEM	transmission electron microscopy
THF	Tetrahydrofuran
XRD	X-ray diffraction

Acknowledgements

I would like to express my immense gratitude to my supervisor, Dr. Matthew Moffitt, for his instruction and guidance during the past five years. I express deep appreciation to my committee members for their advice about my research work.

I would also like to thank my past and present group members for their suggestions and help. In addition, big thanks to all of Dr. van Veggal group's members for their fruitful discussion and kindly sharing AFM and other instruments.

I truly obtain wonderful experience with all the Chemistry Faculty and staff and fellow graduate students at Victoria.

It would be hard to express enough thanks to my dear family, my parents and my brother, for their consistent encouragement. To my wife, Man, her eternal love and unconditional support truly help me whenever I need. To my son, Bryan, his joyfulness always inspires me.

CHAPTER 1

General Introduction

1.1. Background and Motivation

Semiconductor nanoparticles, or quantum dots (QDs), have been the focus of intense research interest in recent years because of their immense potential role as fluorescent biological labels and as key elements in device applications ranging from diagnostics to catalysts to optical computing.[1-6] The current interest in QDs stems from their generally high quantum yields, high photo-stabilities, and their size-tunable optical and electronic properties arising from quantum confinement and surface effects. Nevertheless, in order to apply QDs as building blocks for various device structures, it remains a critical challenge to control their organization on multiple length scales leading to functional films and colloids with structural hierarchy. As well, incorporating QDs into polymer matrices offers the advantage of combining the interesting properties of nanoparticles with desirable optical and mechanical properties of specific polymers. En route to both of these goals, it has been established that the organic stabilizing layer surrounding colloidal QDs plays an important role in both their self-assembly characteristics and compatibility in polymer media.[7-13]

Two general approaches have been explored for the controlled organization of QDs and metal nanoparticles in films and colloids: self-assembly (bottom-up) and lithography (top-down). Lithographic strategies for patterning nanoparticles on surfaces have included soft lithography,[14-23] photolithography,[24-31] and electron lithography.[32-36] However, lithographic methods are not the most economical approaches in terms of time, labor or energy input, and do not allow for organization of nanoparticles within colloidal structures. Therefore, increasing focus has turned to a variety of self-assembly strategies, which offer fast and efficient routes to complex nanoparticle assemblies.[37-49]

Several strategies for the dispersion and self-assembly of QDs and metal nanoparticles within polymer-based films and colloids target the manipulation of nanoparticles with a polymeric brush layer coating the inorganic nanoparticles.[50-56] This hybrid building block approach provides an opportunity to build up nanocomposites with structural hierarchy; the appropriate polymer brush layer can disperse nanoparticles in the corresponding homopolymer[51] or give rise to self-assembly of nanoparticles via steric repulsions among the polymer brushes, leading to 2D ordered arrays.[55,56]

Moffitt and co-workers have extensively explored the self-assembly of CdS QDs coated with polystyrene-*b*-poly (acrylic acid) (PS-*b*-PAA) diblock copolymers which contribute a PAA layer at the QD surface and an external polystyrene (PS) brush layer.[57-63] They have shown that such hybrid particles, termed PS-CdS (Scheme 1.1a), can be self-assembled into mesoscale wires, rings and cables at the air-water interface,[60,61] or mesoscale spheres in aqueous media,[62,63] by blending with amphiphilic block copolymers which regulate their self-assembly. They have also shown that phase separation between PS-CdS and poly (methyl methacrylate) (PMMA) homopolymer within spin-coated polymer blend films on glass substrates results in various hierarchical QD/polymer patterns at the micron scale.[59] Although these various PS-CdS assemblies are reproducible and tunable via kinetic control, superstructures of PS-CdS are severely limited in their order and structural complexity. The essential limitation of PS-CdS,[57-63] and of other QD/polymer and polymer/metal nanoparticle hybrid building blocks,[50-56] is the homogeneous and isotropic nature of their external polymer brush layers, which give rise to either uniform dispersion in favorable environments, or macroscopic phase

separation in unfavorable environments, with no inherent tendency to self-assemble into complex equilibrium structures.

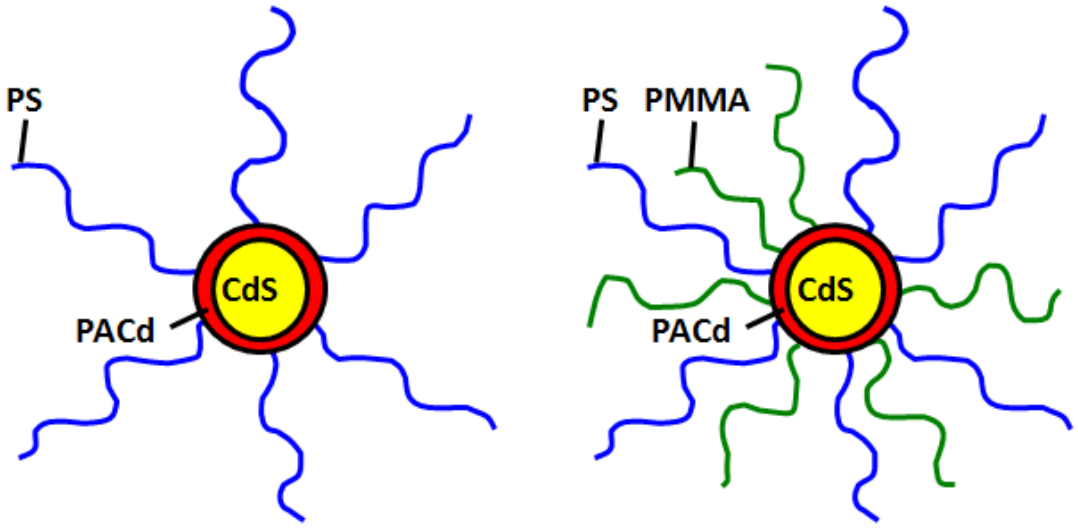

a b

Scheme 1.1 (a) PS-CdS nanoparticle, (b) PS/PMMA-CdS nanoparticle

In recent years, it has been recognized that, in order to increase the complexity and control of superstructures obtained by inorganic nanoparticle self-assembly, more complex hybrid building blocks are required; therefore, increasing attention has turned to designing inorganic nanoparticles with anisotropic interactions, via control of the nanoparticle surface functionality. Computer simulations by Glotz and coworkers[64-67] have demonstrated that self-assembly of such nanoparticles should lead to a wide range of complex structures, comparable to anisotropic molecules such as amphiphilic surfactants or block copolymers. Experimentally, various types of inorganic nanoparticles exhibiting anisotropic interactions have been recently produced, have been shown to undergo interesting self-assembly behavior in a range of environments.[68-74]

One route to anisotropically-interacting building blocks is the production of nanoparticles consisting of two phase-separated inorganic species.[68-71] Along these lines, "nanoacorns" with distinct PdS_x and CoPd faces,[68] bifunctional heterodimers of CdS QDs and FePt nanoparticles,[69] and Janus (bifacial) nanoparticles with gold and iron oxide moieties,[70] have been produced. Surfactant-like activity for such biphasic nanoparticles has also been demonstrated via self-assembly at a hexane/water interface.[70] As well, CdSe nanorods and tetrapods with gold tips have been synthesized; the nanorods self-assembled into chains when a dithiol was added, via selective linking of gold tips.[71]

Another strategy for anisotropic nanoparticles that has been explored involves the production of colloidal nanostructures with hybrid metal/polymer surfaces.[72-74] Mirkin and coworkers have produced mesoscale rods consisting of distinct gold and polypyrrole blocks, which self-assembled into microscale bundles, tubes, and sheets, via strong interactions between chemically-identical moieties of adjacent rods.[72] Subsequently, Kumacheva and coworkers produced gold nanorods with polystyrene brushes selectively grafted to both ends ("pom-poms"); in various mixtures of polar organic solvents and water, self-assembly into rings, chains, and spheres was observed via amphiphilic interactions.[74] As well, hydrophobic gold nanoparticles grafted to an average of two hydrophilic polymer chains were found to exhibit amphiphilic self-assembly behavior in aqueous solutions.[74]

Of particular relevance to this thesis are recent examples of inorganic nanoparticles stabilized by mixed polymer brush layers consisting of two types of chemically-dissimilar polymer chains.[75-83] In some cases, anisotropic interactions between nanoparticles have been induced via a Janus brush structure, with dissimilar

polymer chains grafted to opposite faces of the nanoparticle.[75-79] For example, gold nanoparticles coated with an amphiphilic Janus polymer brush were found to self-assemble into spherical supermicelles,[75] and polymer-stabilized Janus magnetic nanoparticles exhibited reversible clustering in water via anisotropic interactions. In other examples, nanoparticles with dissimilar polymer chains grafted in a random or alternating fashion exhibited anisotropic interactions via local phase separation within the mixed brush prior to self-assembly;[80-82] for example, amphiphilic gold nanoparticles with mixed brushes consisting of alternating polystyrene (PS)/poly (ethylene oxide) (PEO) chains underwent amphiphilic self-assembly in water to form colloidal rods with PS cores, PEO coronae and gold nanoparticles localized at the interface.[82]

Block copolymer self-assembly has also been found to be a viable strategy for forming anisotropically-interacting colloids, although thus far the resulting building blocks have been purely polymeric micelles, without inorganic nanoparticle cores.[84-91] Muller and coworkers produced spherical Janus micelles via microphase separation of a triblock copolymer in the solid state. The resulting micelles consisted of crosslinked poly butadiene (PB) cores, with polystyrene (PS) and poly(methyl methacrylate) (PMMA) coronal hemispheres.[84,85] The PMMA blocks were subsequently hydrolyzed to produce amphiphilic Janus micelles, which self-assembled into spherical supermicelles in water.[85] Using a similar approach, but a different triblock copolymer composition for self-assembly, Janus cylindrical micelles were subsequently prepared by the Muller group.[88] Liu *et al*.[87,90] and others[89] have applied self-assembly of triblock copolymers in solution to yield micelles with "patchy" or microphase-separated coronal structures, in contrast to the Janus distribution of coronal chains obtained via self-assembly in the solid state.

Despite the recent success in the self-assembly of anisotropically-functionalized gold and magnetic nanoparticles, and gold nanorods, polymer-coated semiconductor QDs exhibiting amphiphilic self-assembly behavior had not been demonstrated prior to this work. This thesis describes the synthesis, characterization and self-assembly of cadmium sulfide (CdS) QDs coated with mixed brush layers consisting of polystyrene (PS) and either poly (methyl methacrylate) (PMMA) or poly (methacylic acid) (PMAA) chains. Our strategy for producing these hybrid nanoparticles is an extension of previous work in the Moffitt group, in which CdS QDs were synthesized in the polyacrylic acid (PAA) cores of PS-*b*-PAA reverse micelles, to produce PS-coated QDs with homogeneous and isotropic surface functionality (PS-CdS, Scheme 1.1a). In the present case, we employ a triblock copolymer, PS-*b*-PAA-*b*-PMMA, to form reverse micelles via self-assembly of the core-forming PAA blocks, followed by templated CdS QD formation. The result is CdS QDs with a mixed polymer brush layer consisting of equal numbers of PS and PMMA chains (designated PS/PMMA-CdS, Scheme 1.1b).

Following the synthesis of PS/PMMA-CdS hybrid nanoparticles, we describe their rigorous characterization in various organic solvents via fluorescence, UV-vis, NOESY ^{1}H-NMR, static and dynamic light scattering (SLS, DLS), and transmission electron microscopy (TEM). We show evidence that PS/PMMA-CdS nanoparticles maintain colloidal stability in organic solvents with a wide range of polarities, via conformational rearrangement of the mixed brush layer in response to the external solvent environment. These environmentally-responsive nanoparticles are then shown to undergo self-assembly in PS/PMMA homopolymer blend films, localizing at the polymer-polymer interface, due to their mixed polymer layer; this interfacial localization

is found to have a regulating and stabilizing effect on the resulting blend structure. For the final stage of the research, the PMMA chains are hydrolyzed to PMAA, producing the amphiphilic nanoparticles PS/PMAA-CdS. The PS/PMAA-CdS nanoparticles are found to show rich and tunable self-assembly behavior in mixtures of polar organic solvents and water, forming spherical supermicelles, worm-like supermicelles, and vesicles, all with well-defined internal organization of QDs, depending on experimentally-tunable conditions. The block copolymer-like self-assembly behavior of PS/PMAA-CdS suggests phase separation of statistically-distributed PS and PMAA chains within the mixed brush structure, leading to anisotropic interactions between nanoparticles mediated by energetic contributions from interfacial tension and chain stretching.

The remainder of this introductory chapter is designed to provide the basic background required for readers to understand the principles of this thesis, and is divided as follows: Section 1.2 introduces polymers and block copolymers, along with providing a description of anionic polymerization and the characterization of block copolymers. Section 1.3 describes the micellization of block copolymers in selective solvents, in general, and then specifically the thermodynamics of micellization in aqueous solutions. Section 1.4 concerns the general principles of semiconductor nanoparticles (quantum dots) and quantum confinement. Section 1.5 introduces some of basic tools which are employed to characterize the colloidal structures and the organization of nanoparticles, including static and dynamic light scattering (SLS and DLS), atomic force microscopy (AFM), transmission electron microscopy (TEM) and laser scanning confocal fluorescence microscopy (LSCFM). Finally, section 1.6 outlines the remaining content in the thesis.

1.2. Polymers and Block Copolymers

1.2.1 Polymers. A *polymer* is a large natural or synthetic molecule made from smaller molecules (termed *monomers*) connected by covalent links.[92] Depending on the connectivity of monomers, polymers can be linear, branched, or form interconnected networks. When monomers connect together within a polymer, they are called *repeat units*, and the number of repeat units in a polymer chain is known as the *degree of polymerization*.[92]

When there is only one species of monomer in the polymer, it is called a *homopolymer*. If there is more than one type of monomers, this kind of polymer is termed a *copolymer*. The categories of copolymers vary depending on the arrangement of monomers: there are *random copolymers*, *block copolymers*, *alternating copolymers*, or *graft copolymers* (Figure 1.1). Random copolymers, also called *statistical copolymers*, have two different repeat units (A and B) distributed randomly along the polymer chain. Block copolymers consist of sequences (or blocks) of A units covalently attached to blocks of B units; if there are only two blocks in the chain, it is termed a *diblock copolymer* ,whereas a *triblock copolymer* consists of three blocks, with blocks arranged either ABA, BAB, or ABC (if three chemically distinct monomers are involved). Alternating copolymers, as the name implies, consist of A and B repeat units arranged in an alternating fashion along the polymer chain. Graft copolymers are made up of blocks of A repeat units attached to a backbone of B repeat units or vice-versa.

AAABBBAABAAABBBBAAABBBBBAABBBBA Random Copolymer

ABABABABABABABABABABABABABABA Alternating Copolymer

AAAAAAAAAAAAABBBBBBBBBBBBBBBB Block Copolymer

BBBBBBBBBBBBBBBBBBBBBBBBBBBBB Graft Copolymer
A
A
A
A

Figure 1.1. Types of copolymers formed from A and B repeat units

1.2.2. Molecular Weight Distributions. Unlike small organic molecules, synthetic polymers do not possess a single ,well-defined molecular weight; instead, a sample of many polymer chains will possess a distribution of molecular weights arising from the statistical nature of any polymerization reaction.[92,93] A typical molecular weight distribution for a synthetic polymer is shown in Figure 1.2. [94]

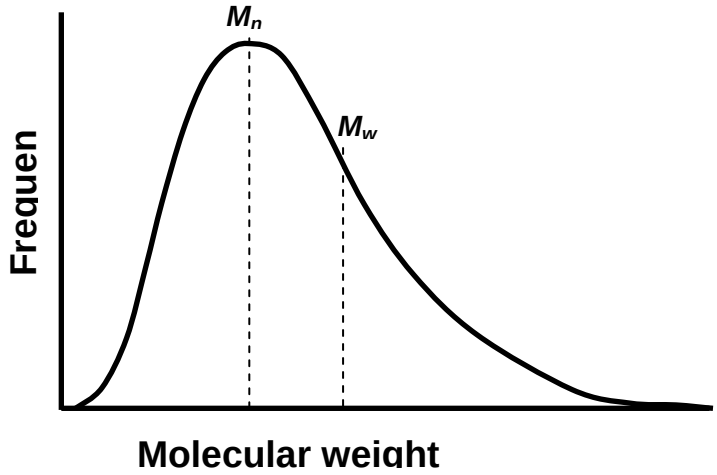

Figure 1.2. Molecular weight distribution of a theoretical polymer sample highlighting the position of different types of average molecular weights.[94]

As indicated by the figure, more than one type of average molecular weight can be defined for a given distribution. The number average molecular weight (M_n) is defined by Equation 1.1:

$$M_n = \frac{\sum_i N_i M_i}{\sum_i N_i} \qquad (\mathbf{1.1})$$

where N_i is the number of molecules of species i with molecular weight M_i and the sum is over all species within the distribution. The average M_n is determined by techniques which measure the colligative properties of polymer solutions, including osmotic pressure, since these methods are sensitive to the number of polymer chains in solution.

M_w, the weight-average molecule weight, is another average value which is used to define the molecule weight of a polymer sample. M_w is measured using analytical methods that are sensitive to the size of molecules in solution, the most important example for polymers being static light scattering. As a result, larger molecules in the distribution contribute more strongly to M_w than to M_n. M_w is defined by Equation 1.2:

$$M_w = \frac{\sum_i W_i M_i}{\sum_i W_i} \qquad (\mathbf{1.2})$$

where W_i is the total mass of species with molecular weight M_i. The polydispersity index (*P.I.*) characterizes the width of a molecular weight distribution , and is defined according to Equation 1.3:

$$P.I. = \frac{M_w}{M_n} \qquad (\mathbf{1.3})$$

When *P.I.* is unity, the sample is *monodisperse*, meaning that all chains have the same molecular weight. Normal synthetic polymer samples have *P.I.* > 1 with varying polydispersities depending on the method of polymerization. Some polymerization techniques, such as anionic polymerization, allow very low polydispersities (between 1.01 and 1.10), to be obtained. On the other hand, the theoretical value obtained from step-growth polymerization methods, such as condensation reactions, is ~2.0 indicating relatively broad size distributions of chains. [92]

In this thesis, the number-average degree of polymerization (N) per chain is generally employed to describe the length of polymer chains or individual blocks within a block copolymer, and is defined:

$$N = \frac{M_n}{M_0} \qquad (\mathbf{1.4})$$

Where M_0 is the molecular weight of single repeat unit.

1.2.3. Sequential Anionic Polymerization. Anionic polymerization is an *addition polymerization* technique (meaning no small molecules are evolved in the polymerization reaction), which is often employed to synthesize block copolymers with well-defined and relatively narrow molecular weight distributions.[92] In the anionic polymerization mechanism, each polymer chain maintains an active center (a carbanion) until the reaction is "killed" by adding an impurity such as water or alcohol to terminate the polymerization. Anionic polymerization includes three steps: initiation, propagation, and termination.[95] In the initiation step, vinyl-substituted monomers, such as styrene, *tert*-

butylacrylate, etc; are activated by an electropositive initiator, producing an anionic reactive center. Following the initiation step, other monomers react with the "living polymer" in a consecutive manner, resulting in chain growth until all of the monomer in the reaction system is consumed. Unlike free radical polymerization, there is no inherent termination step, such that the length of chains can be continuously increased by adding more monomer into the reaction container. The composition and the degree of polymerization is easy to control via the sequential addition of different monomers to the living chains, producing block copolymers with any desired composition and narrow molecular weight distributions. Finally, the termination of the living reaction is induced by adding methanol or any other small molecule with a labile proton.

Since the work of this thesis is built on a triblock copolymer of the type polystyrene-*b*-poly (*tert*-butylacrylate)-*b*-poly (methyl methacrylate) (PS-*b*-P*t*BA-*b*-PMMA) as the starting material, its anionic polymerization process is of particular relevance to this thesis and worth being described in more detail here. The presence of impurities such as water or oxygen are extremely detrimental to anionic polymerization as they will terminate living polymer chains within the reaction mixture, resulting in a broadening of the molecular weight distribution. Therefore, each synthesis step described below is performed using rigorous Schlenk line techniques, under an environment of ultra-pure nitrogen.

The anionic polymerization of the PS-*b*-P*t*BA-*b*-PMMA copolymer is carried out in tetrahydrofuran (THF) as the reaction solvent, in the presence of α-methylstyrene and LiCl, both of which serve as capping species for the living chains.[96-98] The reaction is initiated by adding *sec*-butyllithium (*sec*-BuLi) into a solution of α-methylstyrene and

LiCl in THF at room temperature until a persistent red colour is observed; at the beginning stage, the added initiator eliminates any residual impurity (e.g. H_2O) from the mixture, and then yields the living carbanion species **1**, by reacting with α-methylstyrene, showing a deep red colour (Scheme 1.2).

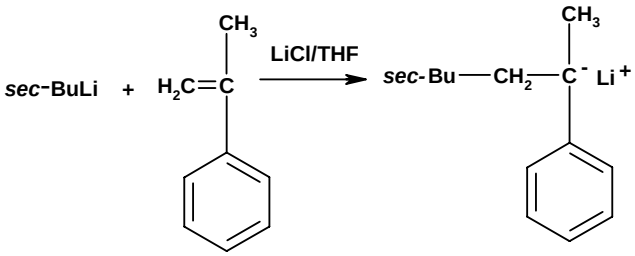

1

Scheme1.2. α-methylstyrene initiated with *sec*-BuLi

Following initiation, the system is cooled down to -78^{o}C, and the styrene monomers are added into the mixture dropwise to form the first block, PS. The immediate polymerization of styrene is obviated by a rapid colour change from dark red to deep orange-yellow. As the polymerization proceeds, the active centre is continually regenerated at the chain ends, until all of the styrene monomer is consumed. At that time, the colour of the solution changes back to a deep red color as the remaining α-methylstyrene recaps the ends of the living chains, producing **2** (Scheme 1.3).

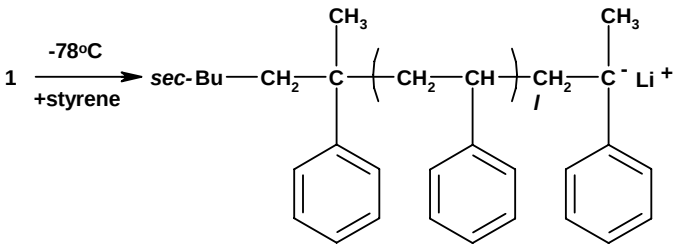

2

Scheme 1.3. Propagating step of styrene reacting with **1**.

The polymerization of the second block (P*t*BA) is carried out by adding the second monomer to the mixture, *tert*-butylacrylate. The sudden disappearance of the deep red colour indicates polymerization of the monomer via production of species (**3**). The presence of the α-methylstyrene end cap helps to sterically regulate the polymerization of the highly reactive *tert*-butylacrylate monomer. As well, LiCl serves to stabilize the living polymer chains and prevent undesirable side reactions with the ester group on the monomer (Scheme 1.4).[96-98]

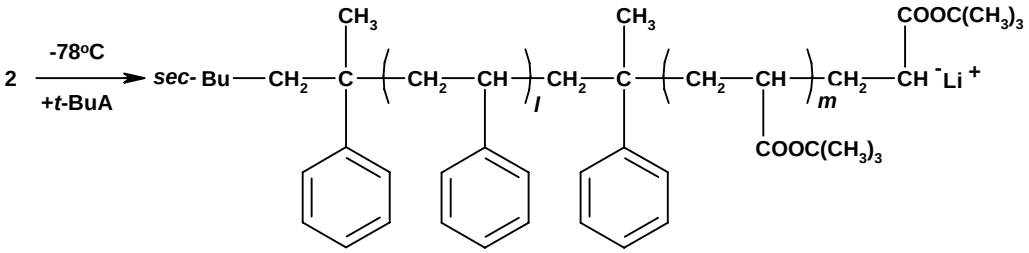

3

Scheme 1.4. Propagating step of *tert*-butylacrylate reacting with **2**.

Finally, the third block (PMMA) is introduced to the polymer chain by adding methyl methacrylate monomer to the system, as shown in scheme 1.5.

As scheme 1.4 indicates, the living end will persist after all methyl methacrylate monomers have been polymerized, resulting in the "living" triblock species **4**. The triblock copolymer PS-*b*-PtBA-*b*-PMMA was recovered by terminating the reactive with a small amount of methanol and precipitating into methanol. More experimental details about the synthesis and characterization of the specific PS-*b*-PtBA-*b*-PMMA triblock copolymer used in this thesis will be presented in Chapter 2.

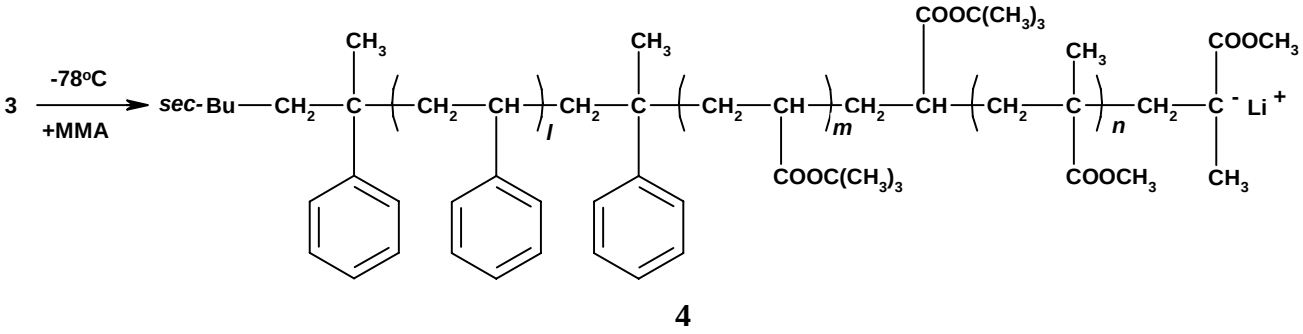

4

Scheme 1.5. Propagating step of methyl methacrylate reacting with **3**.

1.3 Micellization of Block Copolymers

1.3.1 Formation of Block Copolymer Micelles. Most of the interest in block copolymers is due to their self-assembly in solution and in the solid state, as a result of their unique molecular architecture, involving covalent connectivity between chemically incompatible and distinct blocks.[99-103] When a block copolymer is dissolved in a solvent that is a good solvent for one block and a poor solvent for the other block (termed a selective solvent), a number of single chains will aggregate to yield micelles, analogous

to micelles of low-molecular weight surfactants.[99-103] Micellization is spontaneous above a concentration of chains known as the *critical micelle concentration* (cmc).[99-103] The resulting micelles consist of a compact core of multiple insoluble blocks, along with a corona of highly swollen soluble blocks surrounding the micelle cores, as shown in Figure 1.3:[99-103] Block copolymer micelles are often spherical with a relatively narrow size distribution, although other non-spherical morphologies are possible as discussed later.

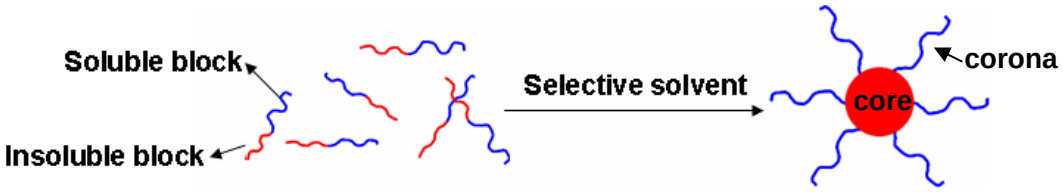

Figure 1.3. Schematic of micellization of a diblock copolymer in selective solvent

When the insoluble blocks have glass transition temperature (T_g) higher than the experimental temperature, their low mobility within the core will restrict exchange of single chains between the micelles and solvent, providing kinetic stability against micelle dissociation.[104] In these cases, micelles are referred to as being "frozen" on experimental time scales.[104] In many cases, micelles are formed by gradually adding a selective solvent to a solution of unmicellized single chains in a non-selective solvent. If the selective solvent is water, then micelle formation is found above a *critical water content* (known as the cwc), which depends on the initial concentration of polymer in solution. At water contents just above the cwc, the micelle cores will be highly swollen with the non-selective solvent, providing chain mobility such that micelles and single chains exist in

dynamic equilibrium. However, as water is continuously added to the solution, the degree of mobility of the core-forming blocks decreases, as the non-selective solvent is leached from the core, eventually resulting in kinetically-frozen micelles above a certain water content. [104-106]

According to the relative lengths of the corona and core-forming block, block copolymer micelles are categorized into two types: 1) star-like micelles and 2) crew-cut micelles. For star-like micelles, the core-forming block is significantly shorter than the corona-forming block. Therefore, the cores of star-like micelles are relatively small, compared to a large expanded corona (Figure 1.4.a). In contrast, the relatively short coronal chains in crew-cut micelles result in a thinner corona surrounding a large core (Figure 1.4.b). [104]

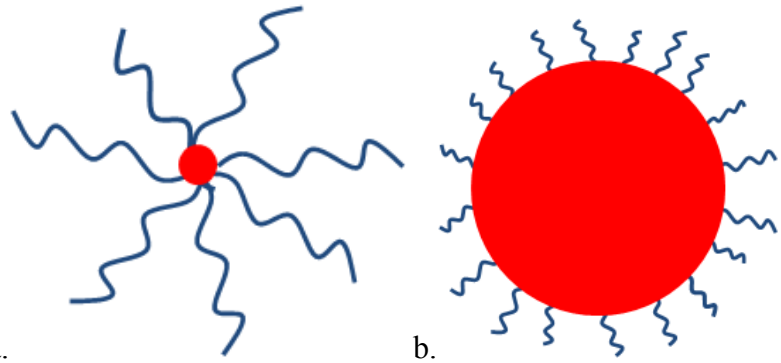

Figure 1.4. Schematic diagram of star-like (a) and crew-cut (b) micelles.

1.3.2. Thermodynamics of Block Copolymer Micellization. The thermodynamic tendency of a physical or chemical process is related to the change in the

Gibbs free energy, ΔG, which is calculated from entropic and enthalpic contributions.[107] For any process, including block copolymer micellization, the change in the Gibbs free energy, ΔG, can be calculated as:

$$\Delta G = \Delta H - T\Delta S \quad \textbf{(1.5)}$$

Where ΔH is the enthalpy change, T is the absolute temperature, and ΔS is the entropy change. The micellization of block copolymers in organic solvents is well known to be an enthalpically-driven process.[104] Above the cmc, negative ΔG for micellization results from negative ΔH and ΔS contributions.[99-102] The decrease in entropy, which limits micelle growth, arises due to a combination of localization of block junctions at the core/corona interface, as well as stretching of core and coronal blocks (loss of conformational entropy) upon packing of chains within the micelle. The decrease in enthalpy, which provides the driving force for micellization, results from the exothermic interchange energy, due to replacement of unfavorable polymer/solvent with favorable polymer/polymer interactions for the insoluble core-forming block.[99-102]

In contrast to organic solvents, the micellization of block copolymers in aqueous media is entropically driven.[99-102] Generally speaking, although self-assembly of block copolymer molecules reduces their entropy by forming micelles in an aqueous environment, the micellization of molecules is driven by an increase in the entropy of the water (hydrophobic effect). Above the *cmc*, due to hydrophobic interactions which change the water structure in the vicinity of the hydrophobic polymer chains, the entropic penalty of block copolymer self-assembly is less than the entropic penalty of the caging water molecules surrounding unmicellized chains.[99-102]

Eisenberg and co-workers[108] have also carried out an experimental study of the thermodynamics of micellization in polar organic/water solutions. The study shows that, at low water content, the negative enthalpy change is the predominant contributor for the micellization of amphiphilic block copolymers, since the favorable interactions between hydrophobic core-forming blocks will replace the unfavorable interactions between the hydrophobic blocks and the solvent. At high water contents, hydrogen bonding between water molecules plays an important role in micellization, such that the positive entropy change, the entropy becomes the main effect during the micellization (hydrophobic effect). Between the low and high water content, both enthalpy and entropy are driving forces for the micellization. This study is of relevance to Chapter 4 of this thesis, which concerns the self-assembly of amphiphilic nanoparticles in mixtures of polar organic solvents and water.

Along with spherical micelles, a wide range of interesting non-spherical morphologies have been observed via self-assembly of amphiphilic block copolymers possessing long hydrophobic blocks and short hydrophilic block in aqueous media (crew-cut micelles).[104-106,109-117] These block copolymer colloids, and the experimental and thermodynamic factors which govern their morphological tunability, provide the inspiration for our strategy for colloidal QD self-assembly explored in Chapter 4, and so will be discussed briefly here. These block copolymer systems generally consist of a long polystyrene (PS) block covalently connected to a short polyacrylic acid (PAA), polyethylene oxide (PEO), or other water-soluble block. The copolymer is first dissolved in a non-selective polar organic solvent, and then water is added to the polymer solution to induce micellization; the remaining organic solvent can be removed from the system

by dialysis. [109-116,118] In the course of crew-cut micelle formation, three thermodynamic factors will contribute to the specific morphologies and sizes of micelles formed from the amphiphilic block copolymers: (1) the interfacial tension at the core-corona interface (enthalpic factor), (2) chain stretching in the core (entropic factor) and (3) and chain stretching in the corona (entropic factor). Experimentally, a large number of variables will influence these thermodynamic factors and therefore allow the morphologies to be tuned, including the block copolymer composition, the initial polymer concentration, the choice of non-selective solvent, the pH, the presence of added salt, etc. Based on theoretical and experimental considerations, variables that increase the interfacial tension will lead to an increase in aggregation number and micelle size, at the entropic cost of increased chain stretching.[104-106,109-117] The wide range of interesting non-spherical morphologies observed in block copolymer crew-cut micelle systems can be explained by the entropic penalty of chain stretching in the core, which dominates over the effect of chain stretching of the shorter coronal blocks.[119-122] When chain stretching at the concave surface of a sphere becomes unfavorable, the system lowers the overall stretching by lowering the interfacial curvature, giving rise to morphological changes from spheres to cylinders, and eventually to bilayers and vesicles. Figure 1.5 shows the range of morphologies possible from a single PS-*b*-PAA block copolymer, simply by varying the salt concentration and screening repulsive interactions between coronal blocks. With adding increasing salt into the initial organic solution, the morphology of the diblock copolymer micelles changes from spheres to cylinders, to vesicles, and finally to large compound aggregates.[115]

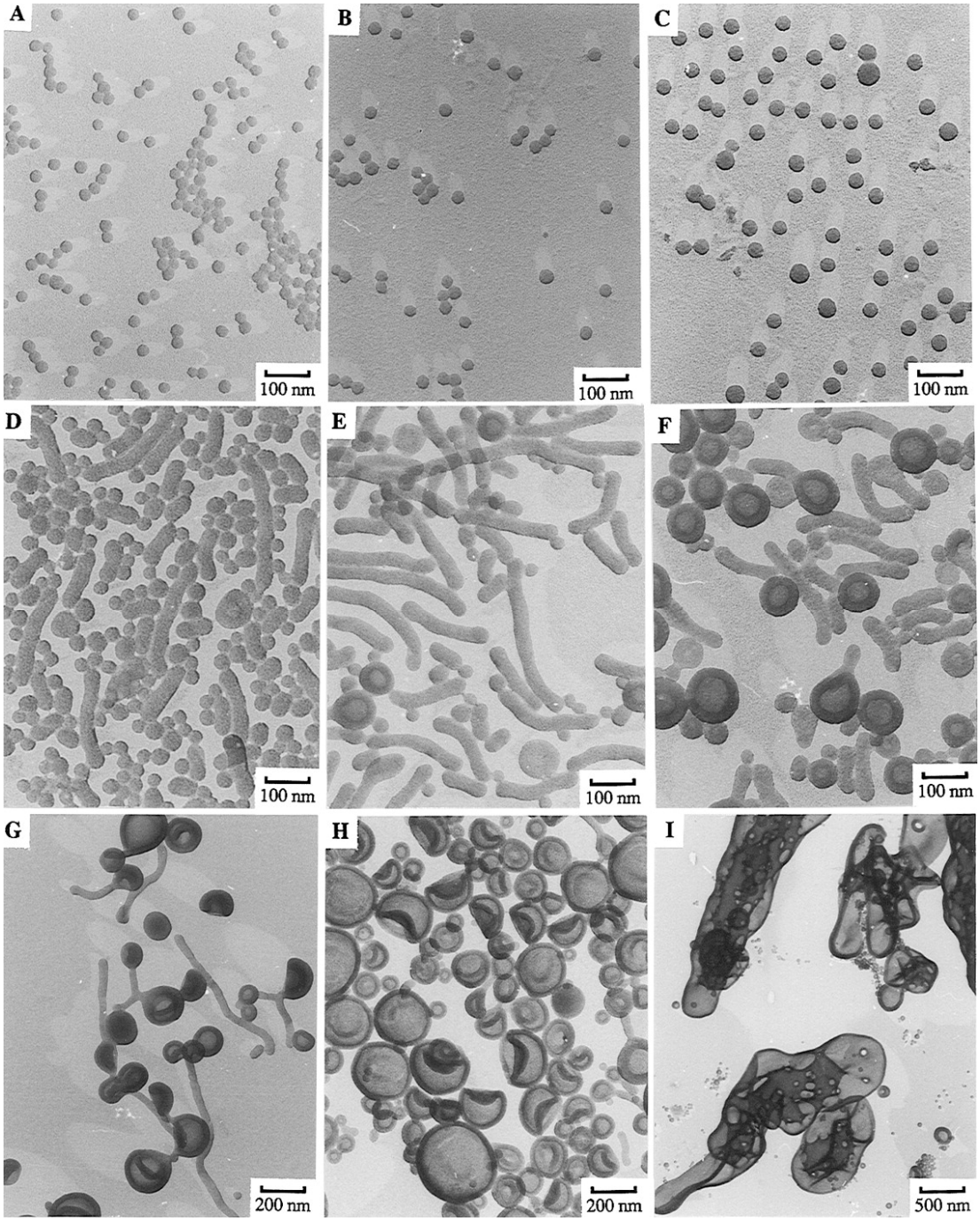

Figure 1.5. Morphologies of PS-*b*-PAA aggregates in aqueous solution with different amounts of NaCl added to DMF solutions prior to water addition. From A to I, the concentration of NaCl increased from 0 to 21 mM.[115](Reprinted with permission from Lifeng Zhang and Adi Eisenberg, *Macromolecules,* **1996,** *29*, 8805-8815. Copyright 2009 American Chemical Society.)

1.4 Semiconductor Nanoparticles (Quantum Dots). Recently, an increasing amount of research has been focused on the synthesis and characterization of inorganic nanoparticles, since metallic or semiconductor nanoparticles exhibit extraordinary properties due to their small size relative to bulk crystals. The size of nanoparticles lies in a range between bulk solids and single molecules, approximately 1-10 nm.[1] Two main factors contribute to the size-dependent properties of nanoparticles: 1) an increase in the surface-to-volume ratio compared to bulk materials and 2) changes in the electronic structure arising from quantum confinement effects.[1,2] One example of the first effect is observed from the different melting points between bulk and nanocrystalline cadmium sulfide (CdS): CdS nanocrystals have a melting points of ~400^0C, while CdS in the bulk has melting point of 1600^0C.[1] The higher surface area of the nanocrystals compared to the bulk form contributes to this dramatic change of melting point. Along with such effects of large surface areas, quantum dots (QDs) possess interesting optical and electronic properties arising from their nanometer sizes, which is induced by the quantum confinement effect. To understand the optical properties of CdS nanoparticles, a basic discussion of the quantum confinement effect is of importance and will now be presented.

When excited by light of sufficient energy, an electron in a bulk semiconductor can jump from the valence band to the conduction band, leading to a hole of positive charge in the valence band. The resulting electron-hole pair is called an exciton; in a bulk semiconductor, the excitation energy (which is the energy of the first excited state) is equal to the bandgap energy of the bulk material. The energy of the exciton increases significantly and the band structure becomes increasingly localized, as the size of the

exciton decreases below the size of the Bohr exciton radius. [1] Brus[2] has applied the particle-in-a-box model, with the particle being the exciton and the box being the spherical nanoparticle, to explain this situation, in which the exciton is confined by an infinitely high potential at the nanoparticle surface. The energy states of the system are given by the quantum mechanical solution. As a result, the first exciton energy in this spherical box can be calculated by the Equation 1.6:

$$E^* \cong E_g + \frac{\hbar^2 \pi^2}{2R^2}\left[\frac{1}{m_c} + \frac{1}{m_h}\right] - \frac{1.8e^2}{\varepsilon R} + \ldots \qquad (\mathbf{1.6})$$

Where E^* is the energy of the exciton, E_g is the bandgap energy of the bulk semiconductor, $\hbar$ is the reduced Planck's constant, R is the radius of the particle, m_e and m_h are the mass of electrons and holes in the lattices, e is the charge of an electron and ε is the permittivity. The positive confinement energy term (second term on the right hand side of the equation) is inversely proportional to the square of the radius of the particle, therefore, the exciton energy increases dramatically with decreasing particle in agreement with experiment. Compared with this confinement term, the R-dependence of the negative-energy third term, arising from Columbic attraction between electrons and holes, is relatively weak (~1/R), such that E^* increases with decreasing R overall. This quantum confinement effect is easily observed from the absorption spectra of semiconductor nanoparticles of various average sizes.

Colloidal cadmium sulfide (CdS) QDs are widely-studied materials due to their range of potential applications.[1,2,123,124] CdS QD sizes are easily characterized using conventional UV-vis absorption spectroscopy (Figure 1.6).[1] When the size of CdS nanoparticles is larger than 5.8 nm, the electronic and optical properties are similar to

bulk CdS, since the exciton diameter of the bulk CdS is 5.8 nm, corresponding to absorption starting at wavelengths below ~515 nm. For nanoparticle sizes smaller than the exciton, the absorption threshold shifts to shorter wavelengths as predicted by Equation 1.6, as shown by the spectra in Figure 1.6.

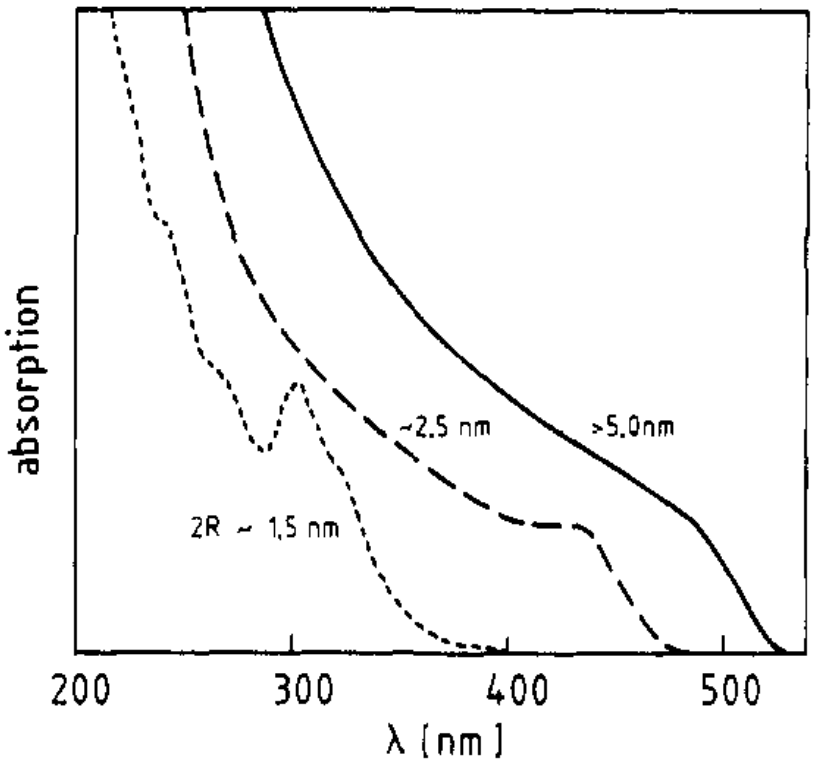

Figure 1.6. UV-vis absorption spectra of CdS nanoparticles of different mean particle sizes.[1]

1.5 Characterization Methods and Instrumentation

To characterize the structure of polymer-coated QDs and their assemblies in various media and on different length scales, we employed a range of experimental techniques, including dynamic and static light scattering (DLS and SLS), atomic force microscopy (AFM), transmission electron microscopy (TEM) and laser scanning confocal fluorescence microscopy (LSCFM). For imaging hierarchical QD organization in polymer environments, the three microscopy techniques listed above are complementary, in part because of different length scales probed by the different instruments, ranging from nanometer to micrometer. A brief introduction to each of these techniques is given in this section.

1.5.1. Static and Dynamic Light Scattering (SLS and DLS).

The primary tool used to determine the molecular weight, size and structure of polymer chains and colloidal particles in solution is light scattering, which measures either the time-average intensity (static light scattering) or the time-dependent intensity fluctuations (dynamic light scattering) of light scattered elastically from particles dispersed in solution.

Static light scattering (SLS) experiments involve measurements of the time-average scattered light intensity from solutions of polymers or micelles at various concentrations (c), and scattering angles (θ). Analysis of the data allows the weight-average molecular weight, M_w, the radius of gyration, R_g , and the second virial coefficient, A_2, for the particles in solution to be determined. The data is treated according to the Zimm equation :[92,125]

$$\frac{Kc}{R_\theta} = \frac{1}{M_w P(\theta)} + 2A_2 c \qquad (\mathbf{1.7})$$

where R_θ is termed the Rayleigh ratio and is calculated from $R_\theta = i_\theta r^2 / I_0$, where I_0 is the intensity of incident light, i_θ is the scattered light intensity per unit volume at angle θ, and distance r from the sample to observer;[92] $P(\theta)$ is an angle-dependent function called the form factor, which describes attenuation in the scattering light intensity due to interparticle interference, and is dependent on particle size (i.e. r_g) and shape. K is a composite of optical and fundamental constants for the system, including the differential refractive index, dn/dc .[92] For polymer chains in solution, r_g describes the average distance between the centre of gravity of the particles and the chain ends. A_2 is a thermodynamic quantity describing the extent of attractive or repulsive interactions between chains (or micelles) in solution, and depends on the solvent quality for the polymer/solvent system at a given temperature.

In dynamic light scattering (DLS) experiments, time dependent fluctuations in the scattered light intensity are analyzed to determine the diffusion coefficient, D_0, of the polymer chains or micelles in solution. The Stokes-Einstein equation is then applied to determine the hydrodynamic radius, r_h, of the particles:

$$D_0 = k_B T / 6\pi\eta r_h \qquad (\mathbf{1.8})$$

Where k_B is the Boltzmann constant, T is the temperature and η is the viscosity of the solvent. Combining particle sizes from SLS and DLS, the r_g/r_h [11] ratio can supply information about the shape of the particle in solution. A ratio of $r_g/r_h = 0.775$ indicates

hard spheres, $r_g/r_h \approx 1.1$,is consistent with star-like structures, and $r_g/r_h = 1.5$ is the theoretical value for a flexible, linear chains.[11,126]

1.5.2. Atomic Force Microscopy (AFM). Atomic force microscopy (AFM) is a scanning probe microscopy technique used to image the surface topology of non-conductive samples with very high resolution. There are two types of scanning modes named contact and non-contact modes, depending on whether or not probe tip makes physical contact with the surface of the sample.[127] A schematic of an AFM instrument is shown in Figure 1.7.

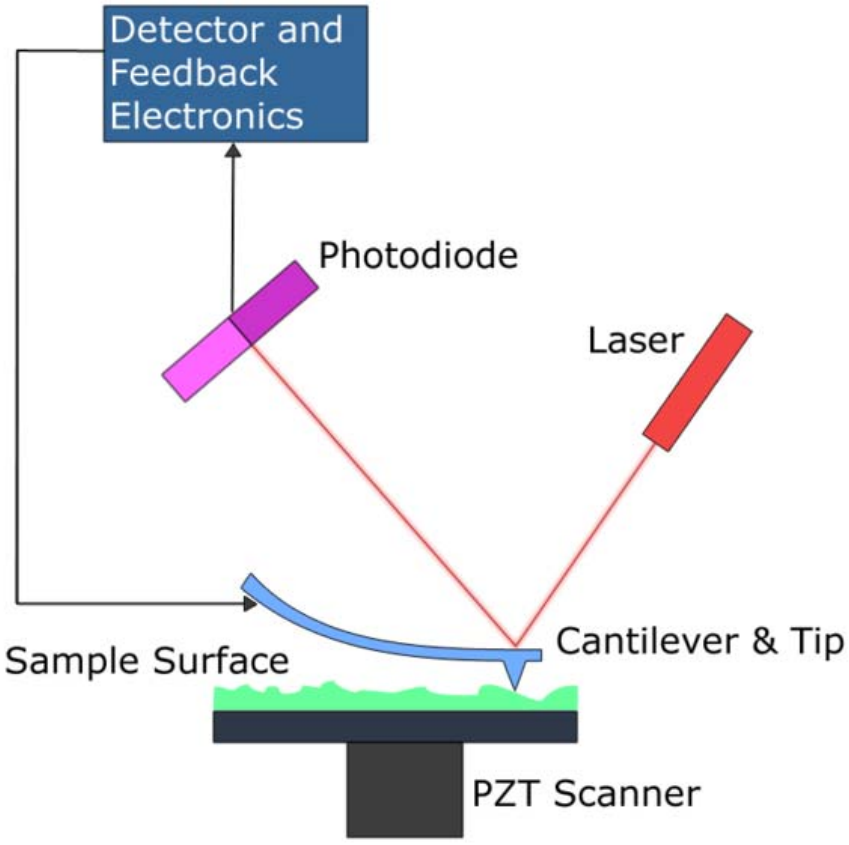

Figure 1.7. Illustration of atomic force microscopy (AFM).[128]

All of the AFM for this thesis was carried out in contact mode. The probe tip scans across the sample surface in close contact with the surface. A piezoelectric element deflects the tip to maintain a constant repulsive force on the tip, according to the varying topographic features of the sample surface. A light beam from a small laser focused on the tip is bounced off the cantilever and reflected to a four-section photodetector, which is correlated to the height of the surface at a given *x*,*y* position. The resulting topographic images of surface features contain both lateral and height information, with lateral resolution of about 10 nm and a vertical resolution of 1-2 nm for the AFM instrument used in this thesis.

1.5.3. Laser Scanning Confocal Fluorescence Microscopy (LSCFM). Laser scanning confocal fluorescence microscopy (LSCFM) is a fluorescence imaging technique in which light emission from organic dyes or QDs within a sample provide contrast between fluorescent and non-fluorescent regions for imaging on the micron scale. A schematic diagram of an LSCFM microscope is shown in Figure 1.8.

For LSCFM imaging, the excitation light at various wavelengths is provided by a laser. The excitation beam passes through a beam-expanding lens and reflects off a dichroic mirror to the sample. The emitted light produced from the QDs or any organic dyes in the sample is focused back via the objective lens and the dichroic mirror, then through the focusing lens and pinhole aperture to the photomultiplier detector. An image is compiled using computer software by scanning the sample through *x* and *y* directions.[129]

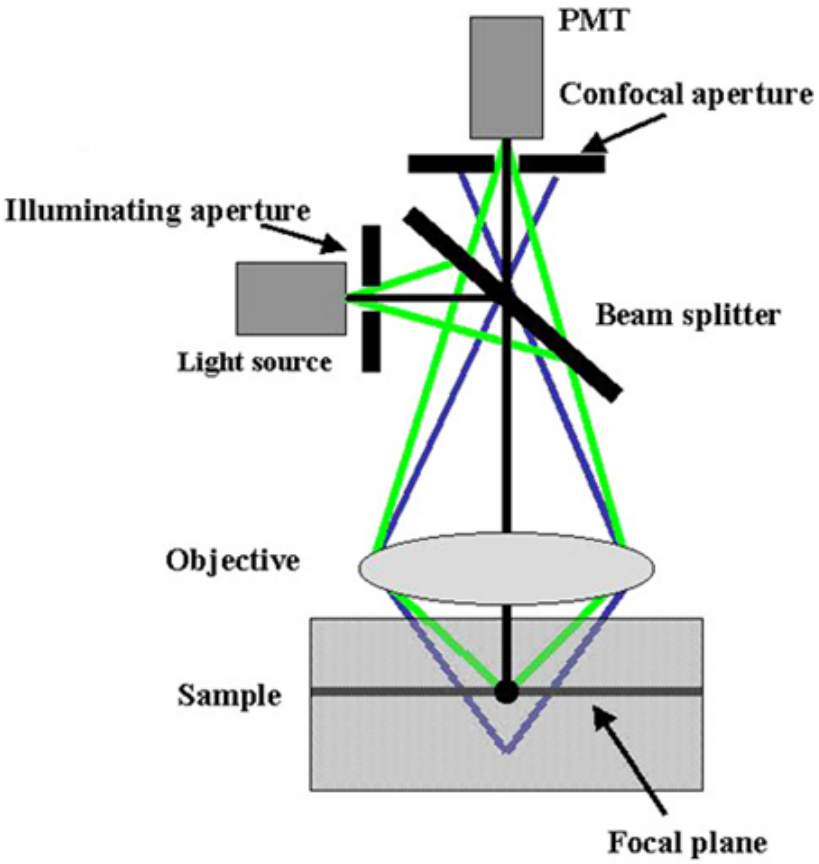

Figure 1.8. Schematic representation of laser scanning confocal fluorescence microscopy (LSCFM)[129]

The most important difference between LSCFM and ordinary epifluorescence microscopy is the occurrence of an adjustable pinhole in front of the photomultiplier detector, which only permits light from a thin focal plane to reach the detector. Therefore, "optical sections" at various depths of the sample can be collected by changing the focus in a stepwise manner (a *z*-scan) then edited into a three-dimensional image. The thickness of the optical sections decreases with the pinhole size, allowing *z*-resolution down to 0.5 μm. [129]

1.5.4. Transmission Electron Microscopy (TEM). Based on the work of de Broglie, an accelerated electron beam is determined to have an effective wavelength ~10^5 times shorter than visible light, allowing electrons to be used for imaging nanoparticles. A basic schematic illustrating a TEM instrument is shown in Figure 1.9.

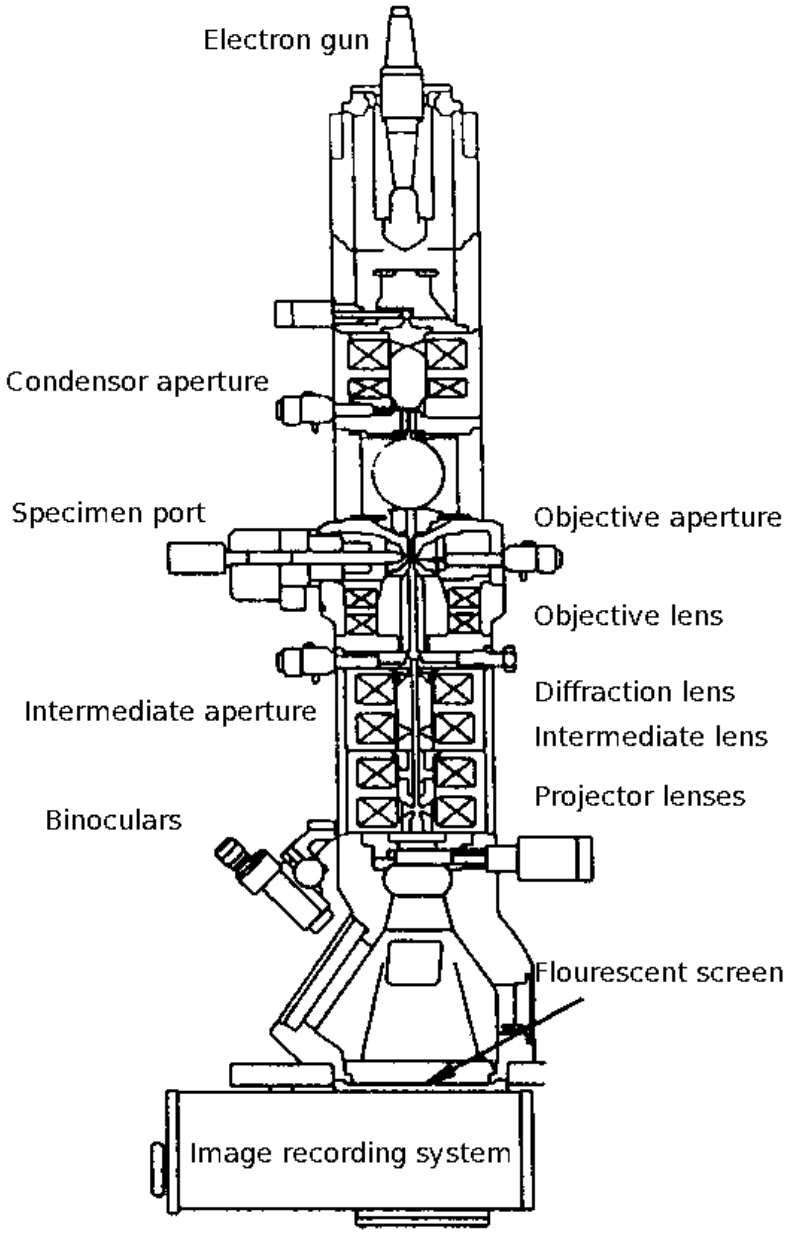

Figure 1.9. Schematic illustration of transmission electron microscope (TEM).[130]

The electron gun in the TEM accelerates a stream of electrons which is focused to a narrow, coherent beam by passing through a series of condenser lenses. [131] This narrow beam hits the specimen and the electrons are scattered at different angles depending on the electron density of the material they strike in the sample, they are either a) undeflected, b) deflected without loss of any energy (elastically scattered), or c) deflected with considerable loss of energy (inelastically scattered). According to their scattering angle, the electrons may or may not pass through the objective aperture. The relative brightness of the image is determined by the number of unscattered electrons which pass through the light atoms, such as carbon, and reach the fluorescent screen.

1.6 Content of the Thesis

The main body of this thesis is divided into three parts: 1) the synthesis and characterization of PS/PMMA-CdS, 2) the self-assembly and structure-stabilizing effects of PS/PMMA-CdS within films of PS/PMMA homopolymer blends and 3) the synthesis and self-assembly of amphiphilic nanoparticles PS/PMAA-CdS in mixtures of organic solvents and water to form colloidal QD/polymer aggregates with multiple morphologies. The content of the remaining chapters is as follows:

Chapter 2 describes the synthesis and characterization of QDs with mixed polystyrene/poly (methyl methacrylate) (PS/PMMA) polymer brush layers via the anionic polymerization and micellization of the triblock block copolymer polystyrene-*b*-poly-(acrylic acid)-*b*-poly (methyl methacrylate) (PS-*b*-PAA-*b*-PMMA), followed by growth of cadmium sulfide (CdS) QDs in the ionic cores. The structure and stability of

these hybrid nanoparticles (PS/PMMA-CdS) are characterized in solvents of various polarities. Static and dynamic light scattering are employed to observe conformational changes in the mixed brush structure in response to the solvent environment, which allows the nanoparticles to maintain colloidal stability in solvents of wide-ranging polarities. UV-vis and photoluminescence spectra demonstrate that QD size and optical properties are independent of the solvent medium due to protection by the block copolymer. 2D ^{1}H NOESY experiments indicate that PS and PMMA chains are statistically distributed around the QDs within mixed brush layer. Finally, it is also shown that the mixed brush QDs can be dispersed in both PS and PMMA homopolymers within spin-coated films due to their environmentally-responsive mixed brush layers.

Chapter 3 investigates the self-assembly of PS/PMMA-CdS nanoparticles within spin-cast blend films of PS and PMMA homopolymers. Due to their mixed brush structure, PS/PMMA-CdS nanoparticles are found to self-assemble at the polymer/polymer interface of the phase-separating blend, forming an encapsulating shell surrounding PMMA islands in a PS matrix. The segregated QDs thus regulate phase separation during spin-coating and dramatically stabilize the spin-coated blend morphologies during subsequent annealing, compared to neat PS:PMMA blends which undergo rapid phase inversion and coarsening. PS/PMMA-CdS QDs are shown to retain their photoluminescence following interfacial self-assembly and subsequent annealing. Free-standing arrays of QD/polymer rings formed via directed self-assembly can be developed by selective solvent washing and removal of homopolymers from the spin-coated films. This chapter demonstrates the principle that colloidal inorganic elements

such as QDs, along with possessing interesting optical properties, can also play a key role in the self-organization and stability of polymer blend-based devices.

Chapter 4 of the thesis explores the self-assembly of amphiphilic mixed-brush CdS QDs in DMF/water and THF/water mixtures, following hydrolysis of the hydrophobic PMMA of PS/PMMA-CdS to poly (methacrylic acid) (PMAA) to form PS/PMAA-CdS nanoparticles. We show that under varying conditions of self-assembly (polymer concentration, water content, salt/acid addition), PS/PMAA-CdS undergoes self-assembly into a wide range of interesting colloidal superstructures, including spherical supermicelles, worms, and vesicles, all with well-defined internal organization of QDs. Based on annealing experiments at different water contents, a mechanism of the formation of worm-like assemblies is proposed. Thermodynamic and kinetic aspects of the formation of the various colloidal superstructures are also discussed.

Finally, Chapter 5 of this thesis summarizes the important contributions of this work, and proposes some key topics for future study.

1.7. References

(1) Henglein, A. *Chem.Rev.* **1989**, *89*, 1861.

(2) Brus, L. *J.Phys.Chem.* **1986**, *90*, 2555.

(3) Chan, W.; Nie, S. *Science* **1998**, *281*, 2016-2018.

(4) Klein, D.; Roth, R.; Lim, A.; Alivisatos, A.; McEuen, P. *Nature (London)* **1997**, *389*, 699-701.

(5) Murray, C.; Kagan, C.; Bawendi, M. *Annu. Rev. Mater. Sci.* **2000**, *30*, 545-610.

(6) Steigerwald, M.; Brus, L. *Acc. Chem. Res.* **1990**, *23*, 183-188.

(7) Duxin, N.; Liu, F.; Vali, H.; Eisenberg, A. *J. Am. Chem. Soc.* **2005**, *127*, 10063-10069.

(8) Gupta, S.; Zhang, Q.; Emrick, T.; Balazs, A.; Russell, T. *Nature Mater.* **2006**, *5*, 229-233.

(9) Kim, B.; Taton, T. *Langmuir* **2007**, *23*, 2198-2202.

(10) Li, D.; Sheng, X.; Zhao, B. *J. Am. Chem. Soc.* **2005**, *127*, 6248-6256.

(11) Moffitt, M.; Eisenberg, A. *Macromolecules* **1997**, *30*, 4363-4373.

(12) Moffitt, M.; Vali, H.; Eisenberg, A. *Chem. Mater.* **1998**, *10*, 1021-1028.

(13) Shan, J.; Nuopponen, M.; Jiang, H.; Viitala, T.; Kauppinen, E.; Kontturi, K.; Tenhu, H. *Macromolecules* **2005**, *38*, 2918-2926.

(14) Xia, Y.; Whitesides, G. *Angew. Chem. Int. Ed.* **1998**, *37*, 551-575.

(15) Zhao, X.; Xia, Y.; Whitesides, G. *J. Mater. Chem.* **1997**, *7*, 1069-1074.

(16) Mirkin, C.; Rogers, J. *MRS Bulletin* **2001**, *26*, 506-508.

(17) Babayan, Y.; Barton, J.; Greyson, E.; Odom, T. *Adv. Mater.* **2004**, *16*, 1341.

(18) Innocenzi, P.; Kidchob, T.; Falcaro, P.; Takahashi, M. *Chem. Mater.* **2008**, *20*, 607-614.

(19) Jiang, C.; Markutsya, S.; Shulha, H.; Tsukruk, V. *Adv. Mater.* **2005**, *17*, 1669.

(20) McAlpine, M.; Friedman, R.; Lieber, D. *Nano Lett* **2003**, *3*, 443-445.

(21) McLellan, J.; Geissler, M.; Xia, Y. *J. Am. Chem. Soc.* **2004**, *126*, 10830-10831.

(22) Zhang, H.; Wang, C.; Li, M.; Zhang, J.; Lu, G.; Yang, B. *Adv. Mater.* **2005**, *17*, 853.

(23) Andersson, A.; Glasmastar, K.; Hanarp, P.; Seantier, B.; Sutherland, D. *Nanotechnol.* **2007**, *18*. 5691

(24) Akamatsu, K.; Samitsu, S.; Tsuruoka, T.; Hasegawa, J.; Nawafune, H. *Small* **2006**, *2*, 1130-1133.

(25) Falconnet, D.; Koenig, A.; Assi, T.; Textor, M. *Advanced Functional Materials* **2004**, *14*, 749-756.

(26) Gorelikov, I.; Kumacheva, E. *Chem. Mater.* **2004**, *16*, 4122-4127.

(27) Hua, F.; Shi, J.; Lvov, Y.; Cui, T. *Nano Lett* **2002**, *2*, 1219-1222.

(28) Lu, C.; Wei, F.; Wu, N.; Huang, L.; Zhao, X.; Jiao, X.; Luo, C.; Cao, W. *Langmuir* **2004**, *20*, 974-977.

(29) Porter, L.; Choi, H.; Schmeltzer, J.; Ribbe, A.; Elliott, L.; Buriak, J. *Nano Lett* **2002**, *2*, 1369-1372.

(30) Xia, D.; Brueck, S. *Nano Lett* **2004**, *4*, 1295-1299.

(31) Xu, H.; Hong, R.; Lu, T.; Uzun, O.; Rotello, V. *J. Am. Chem. Soc.* **2006**, *128*, 3162-3163.

(32) Bedson, T.; Nellist, P.; Palmer, R.; Wilcoxon, J. *Microelectron. Eng.* **2000**, *53*, 187-190.

(33) Bedson, T.; Palmer, R.; Jenkins, T.; Hayton, D.; Wilcoxon, J. *Appl. Phys. Lett.* **2001**, *78*, 1921-1923.

(34) Bedson, T.; Palmer, R.; Wilcoxon, J. *Appl. Phys. Lett.* **2001**, *78*, 2061-2063.

(35) Griffith, S.; Mondol, M.; Kong, D.; Jacobson, J. *Journal Of Vacuum Science & Technology B* **2002**, *20*, 2768-2772.

(36) Tzeng, S.; Lin, K.; Hu, J.; Chen, L.; Gwo, S. *Adv Mater* **2006**, *18*, 1147.

(37) Jiang, Y.; Shen, Y.; Wu, P. *J. Colloid Interface Sci.* **2008**, *319*, 398-405.

(38) Nguyen, T.; Mrabet, D.; Do, T. *J. Phys. Chem. C* **2008**, *112*, 15226-15235.

(39) Ruan, W.; Wang, C.; Ji, N.; Lu, Z.; Zhou, T.; Zhao, B.; Lombardi, J. *Langmuir* **2008**, *24*, 8417-8420.

(40) Werts, M.; Lambert, M.; Bourgoin, J.; Brust, M. *Nano Lett* **2002**, *2*, 43-47.

(41) Jakobsen, U.; Simonsen, A. C.; Vogel, S. *J. Am. Chem. Soc.* **2008**, *130*, 10462.

(42) Lim, I. I. S.; Ouyang, J.; Luo, J.; Wang, L. Y.; Zhou, S. Q.; Zhong, C. J. *Chem.* Mater. **2005**, 17, 6528-6531.

(43) Si, S.; Mandal, T. K. *Langmuir* **2007**, *23*, 190-195.

(44) Diao, P.; Guo, M.; Hou, Q. C.; Xiang, M.; Zhang, Q. *J. Phys. Chem. B* **2006**, *110*, 20386-20391.

(45) Norsten, T. B.; Frankamp, B. L.; Rotello, V. M. *Nano Letters* **2002**, *2*, 1345-1348.

(46) Saponjic, Z. V.; Csencsits, R.; Rajh, T.; Dimitrijevic, N. M. *Chem. Mater.* **2003**, *15*, 4521-4526.

(47) Kumara, M. T.; Tripp, B. C.; Muralidharan, S. *Chem. Mater.* **2007**, *19*, 2056-2064.

(48) Wang, H. T.; Wang, Z. B.; Huang, L. M.; Mitra, A.; Yan, Y. S. *Langmuir* **2001**, *17*, 2572-2574.

(49) Rana, R. K.; Zhang, L. Z.; Yu, J. C.; Mastai, Y.; Gedanken, A. *Langmuir* **2003**, *19*, 5904-5911.

(50) Carrot, G.; Scholz, S.; Plummer, C.; Hilborn, J.; Hedrick, J. *Chem. Mater.* **1999**, *11*, 3571-3577.

(51) Corbierre, M.; Cameron, N.; Sutton, M.; Mochrie, S.; Lurio, L.; Ruhm, A.; Lennox, R. *J. Am. Chem. Soc.* **2001**, *123*, 10411-10412.

(52) Potapova, I.; Mruk, R.; Prehl, S.; Zentel, R.; Basche, T.; Mews, A. *J. Am. Chem. Soc.* **2003**, *125*, 320-321.

(53) Skaff, H.; Emrick, T. *Chem. Commun* **2003**, 52-53.

(54) Tadd, E.; Zeno, A.; Zubris, M.; Dan, N.; Tannenbaum, R. *Macromolecules* **2003**, *36*, 6497-6502.

(55) Moller, M.; Kunstle, H.; Kunz, M. *Synth. Met.* **1991**, *41*, 1159-1162.

(56) Spatz, J.; Herzog, T.; Mossmer, S.; Ziemann, P.; Moller, M. *Adv. Mater.* **1999**, *11*, 149-153.

(57) Wang, C.; Moffitt, M. *Langmuir* **2004**, *20*, 11784-11796.

(58) Wang, C.; Moffitt, M. *Langmuir* **2005**, *21*, 2465-2473.

(59) Wang, C.; Moffitt, M. *Chem. Mater.* **2005**, *17*, 3871-3878.

(60) Cheyne, R.; Moffitt, M. *Langmuir* **2005**, *21*, 10297-10300.

(61) Cheyne, R.; Moffitt, M. *Macromolecules* **2007**, *40*, 2046-2057.

(62) Yusuf, H.; Kim, W.; Lee, D.; Aloshyna, M.; Brolo, A.; Moffitt, M. *Langmuir* **2007**, *23*, 5251-5254.

(63) Yusuf, H.; Kim, W.; Lee, D.; Guo, Y.; Moffitt, M. *Langmuir* **2007**, *23*, 868-878.

(64) Glotzer, S.; Solomon, M. *Nature Mater* **2007**, *6*, 557-562.

(65) Zhang, Z.; Glotzer, S. *Nano Lett* **2004**, *4*, 1407-1413.

(66) Zhang, Z.; Horsch, M.; Lamm, M.; Glotzer, S. *Nano Lett* **2003**, *3*, 1341-1346.

(67) Zhang, Z.; Keys, A.; Chen, T.; Glotzer, S. *Langmuir* **2005**, *21*, 11547-11551.

(68) Teranishi, T.; Inoue, Y.; Nakaya, M.; Oumi, Y.; Sano, T. *J. Am. Chem. Soc.* **2004**, *126*, 9914-9915.

(69) Gu, H.; Zheng, R.; Zhang, X.; Xu, B. *J. Am. Chem. Soc.* **2004**, *126*, 5664-5665.

(70) Glaser, N.; Adams, D.; Boker, A.; Krausch, G. *Langmuir* **2006**, *22*, 5227-5229.

(71) Mokari, T.; Rothenberg, E.; Popov, I.; Costi, R.; Banin, U. *Science* **2004**, *304*, 1787-1790.

(72) Park, S.; Lim, J.; Chung, S.; Mirkin, C. *Science* **2004**, *303*, 348-351.

(73) Jang, K.; Lee, H.; Yang, H.; An, E.; Kim, T.; Choi, S.; Kim, J. *Soft Matter* **2008**, *4*, 349-356.

(74) Nie, Z.; Fava, D.; Kumacheva, E.; Zou, S.; Walker, G.; Rubinstein, M. *Nature Mater* **2007**, *6*, 609-614.

(75) Nie, L.; Liu, S.; Shen, W.; Chen, D.; Jiang, M. *Angew. Chem. Int. Ed.* **2007**, *46*, 6321-6324.

(76) Lattuada, M.; Hatton, T. *J. Am. Chem. Soc.* **2007**, *129*, 12878-12889.

(77) Isojima, T.; Lattuada, M.; Vander Sande, J.; Hatton, T. *Acs Nano* **2008**, *2*, 1799-1806.

(78) van Herrikhuyzen, J.; Portale, G.; Gielen, J.; Christianen, P.; Sommerdijk, N.; Meskers, S.; Schenning, A. *Chem. Comm.* **2008**, 697-699.

(79) Wang, B.; Li, B.; Zhao, B.; Li, C. *J. Am. Chem. Soc.* **2008**, *130*, 11594.

(80) Genson, K.; Holzmueller, J.; Jiang, C.; Xu, J.; Gibson, J.; Zubarev, E.; Tsukruk, V. *Langmuir* **2006**, *22*, 7011-7015.

(81) Kim, B.; Bang, J.; Hawker, C.; Chiu, J.; Pine, D.; Jang, S.; Yang, S.; Kramer, E. *Langmuir* **2007**, *23*, 12693-12703.

(82) Zubarev, E.; Xu, J.; Sayyad, A.; Gibson, J. *J. Am. Chem. Soc.* **2006**, *128*, 15098-15099.

(83) Zubarev, E.; Xu, J.; Sayyad, A.; Gibson, J. *J. Am. Chem. Soc.* **2006**, *128*, 4958-4959.

(84) Erhardt, R.; Boker, A.; Zettl, H.; Kaya, H.; Pyckhout-Hintzen, W.; Krausch, G.; Abetz, V.; Mueller, A. *Macromolecules* **2001**, *34*, 1069-1075.

(85) Erhardt, R.; Zhang, M.; Boker, A.; Zettl, H.; Abetz, C.; Frederik, P.; Krausch, G.; Abetz, V.; Muller, A. *J. Am. Chem. Soc.* **2003**, *125*, 3260-3267.

(86) Xu, H.; Erhardt, R.; Abetz, V.; Muller, A.; Goedel, W. *Langmuir* **2001**, *17*, 6787-6793.

(87) Hoppenbrouwers, E.; Li, Z.; Liu, G. *Macromolecules* **2003**, *36*, 876-881.

(88) Liu, Y.; Abetz, V.; Muller, A. *Macromolecules* **2003**, *36*, 7894-7898.

(89) Schmalz, H.; Schmelz, J.; Drechsler, M.; Yuan, J.; Walther, A.; Schweimer, K.; Mihut, A. *Macromolecules* **2008**, *41*, 3235-3242.

(90) Zheng, R.; Liu, G.; Yan, X. *J. Am. Chem. Soc.* **2005**, *127*, 15358-15359.

(91) Cheng, L.; Zhang, G.; Zhu, L.; Chen, D.; Jiang, M. *Angew. Chem. Int. Ed.* **2008**, *47*, 10171-10174.

(92) Cowie, J. M. G. *Polymer: Chemistry & Physics of Modern Materials, 2nd ed.* New York, 1991.

(93) Sperling, L. H. *Introdution to Physical Polymer Science;* ; John Wiley & Sons,Inc.: New York, 1992.

(94) Charles E. Carraher, J. *Seymour/Carraher's Polymer Chemistry, 5th ed.;*; Marcel Dekker: : New York, 2000.

(95) Szwarc, M. *Caranions, Living Polymes and Electron Transfer Process;*, 1968.

(96) Zhong, X.; Varshiney, S.; Eisenberg, A. *Macromolecules* **1992**, *25*, 7160-7167.

(97) Gao, Z.; Zhong, X. F.; Eisenberg, A. *Macromolecules* **1994**, *27*, 7160.

(98) Hautekeer, J.; Varshney, S.; Fayt, R.; Jacobs, C.; Jerome, R.; *Macromolecules* **1990**, *23*, 3893-3898.

(99) Hadjichristidi, N.; Pispas, S.; Floudas, G. *Block Copolymers*; John Wiley & Sons, Inc: : New Jersey, 2003.

(100) Hamley, I. W. *The Physics of Block Copolymers*; Oxford University Press: , 1998.

(101) Paschalis Alexandridies; Lindman., B. *Amphiphilic Block Copolymers ELSEVIER* : : New York, 2000.

(102) Stephen E.Webber; Munk, P.; and Zdenek Tuzar *Solvents and Self-Organization of Polymers* Kluwer Academic Publishers, 1996.

(103) Tuzar, Z.; Kratochvil, P. *In Surface and Colloid Science; Matijevic, E., Ed.;* ; Plenum Press: New York, 1993; Vol. 15.

(104) Moffitt, M.; Khougaz, K.; Eisenberg, A. *Acc. Chem. Res.* **1996**, *29*, 95-102.

(105) Zhang, L.; Eisenberg, A. *Macromolecules* **1999**, *32*, 2239-2249.

(106) Yu, Y.; Zhang, L.; Eisenberg, A. *Macromolecules* **1998**, *31*, 1144-1154.

(107) Lewis, G. N.; Randall, M. *Thermodynamics*; McGraw-Hill: New York, 1923.

(108) Shen, H.; Zhang, L.; Eisenberg, A. *Journal of Physical Chemistry B* **1997**, *101*, 4697-4708.

(109) Yu, G.; Eisenberg, A. *Macromolecules* **1998**, *31*, 5546-5549.

(110) Yu, K.; Bartels, C.; Eisenberg, A. *Macromolecules* **1998**, *31*, 9399-9402.

(111) Yu, K.; Eisenberg, A. *Macromolecules* **1998**, *31*, 3509-3518.

(112) Yu, K.; Zhang, L.; Eisenberg, A. *Langmuir* **1996**, *12*, 5980-5984.

(113) Yu, Y.; Zhang, L.; Eisenberg, A. *Langmuir* **1997**, *13*, 2578-2581.

(114) Zhang, L.; Eisenberg, A. *Science* **1995**, *268*, 1728-1731.

(115) Zhang, L.; Eisenberg, A. *Macromolecules* **1996**, *29*, 8805-8815.

(116) Zhang, L.; Eisenberg, A. *J. Am. Chem. Soc.* **1996**, *118*, 3168.

(117) Zhang, L.; Yu, K.; Eisenberg, A. *Science* **1996**, *272*, 1777-1779.

(118) Yu, Y.; Eisenberg, A. *J. Am. Chem. Soc.* **1997**, *119*, 8383-8384.

(119) T.P.Lodge; Joona Bang; Z, L. A. H.; Y, T. **2005**, *128*, 1-12.

(120) Safran, S. A.; Pincus, P.; Andelman, D. *Science* **1990**, *248*, 354.

(121) Bergstrom, M.; Eriksson, J. C. *Langmuir* **1998**, *14*, 288.

(122) Shen, H. W.; Eisenberg, A. *J. Phys. Chem. B* **1999**, *103*, 9473.

(123) Brus, L. *J. Chem. Phys.* **1983**, *79*, 5566-5571.

(124) Brus, L. *J. Chem. Phys.* **1984**, *80*, 4403-4409.

(125) Halperin, A. *Macromolecules* **1987**, *20*, 2943.

(126) Forster, S.; Zisenis, M.; Wenz, E.; Antonietti, M. *J. Chem. Phys.* **1996**, *104*, 9956-9970.

(127) Marek, T. *Explorer^{TM} Instrument Operation Manual;Thermomicroscopes Corporation* CA, 2001.

(128) http://en.wikipedia.org/wiki/Atomic_force_microscope.Updated 25 May 2009. Access 19 June 2009

(129) http://www.lci.kent.edu/Lavrentovich/FCPMweb_site/fcm.html Updated 24 May 2009. Access 19 June 2009.

(130) http://en.wikipedia.org/wiki/Transmission_electron_microscope. Updated 17 June 2009. Access 19 June 2009.

(131) Agar, A. W.; Alderson, R. H.; Chescoe, D. *Priciples and Practice of Electron Microscope Operation*; American Elsevier Publishing Company, Inc : New York, 1974.

CHAPTER 2

Semiconductor Quantum Dots with Environmentally Responsive Mixed Polystyrene/Poly (methyl methacrylate) Brush Layers

---

2.1. Introduction

Colloidal metal and semiconductor nanoparticles have received widespread due to their immense potential for applications ranging from biological labeling and diagnostics, to photonics and all-optical computing. In recent years, it has been recognized that the utilization of nanoparticles as building blocks within various devices will require their controlled assembly into one-, two-, and three-dimensional superstructures organized on multiple functional length scales. As well, the incorporation of colloidal nanoparticles into polymer environments offers the added advantage of combining the properties of nanoparticles with the mechanical, optical, and electronic properties of specific polymers. Hybrid building blocks consisting of an inorganic nanoparticle core and an external stabilizing polymer brush layer provide a range of interesting routes toward dispersion or controlled self-assembly of nanoparticles within polymers. A wide range of strategies have been employed to generate polymer brush-stabilized nanoparticles, including polymerizations from the surface of colloidal nanoparticles,[1-6] specific binding or ligand exchange with functionalized polymers,[7-14] and growth or encapsulation of nanoparticles within block copolymer micelles.[15-28]

In the above examples, the polymer brushes surrounding the nanoparticles consist of a single type of polymer chain which responds uniformly to an external stimulus such as changes in temperature or the surrounding solvent. A key challenge in the self-assembly of such “dumb” particles into interesting superstructures is their inherent lack of anisotropic interparticle interactions, resulting in a thermodynamic tendency to be either uniformly dispersed in the surrounding medium, or to undergo macroscopic phase separation. In our group, we extensively studied cadmium sulfide

(CdS) quantum dots (QDs) encapsulated within diblock copolymer micelles which contribute an external homogenous polystyrene (PS) brush layer;[20, 29] such particles (termed PS-CdS) can be "tricked" into forming mesoscale spheres in aqueous media,[30, 31] or mesoscale wires and cables at the air-water interface,[32, 33] by blending with amphiphilic block copolymers which regulate their self-assembly. We have also shown that phase separation between PS-CdS and PMMA homopolymer within spin-coated polymer blend films gives rise to various hierarchical QD/polymer patterns at the micron scale, including networks of wires and arrays of spatially correlated islands.[34] Although reproducible, these various superstructures form under non-equilibrium conditions, currently limiting the complexity of nanoparticle self-assembly within polymers.

For many applications, the quest for reversible thermodynamic self-assembly of nanoparticles into a variety of complex 3D superstructures has created a need for more sophisticated hybrid building blocks.[35-38] Very recently, several examples of colloidal nanoparticles coated with mixed brushes of two different types of homopolymers have appeared in the literature.[39-44] Such hybrid particles can be regarded as "smart" particles, since external stimuli such as solvent or temperature changes result in conformational reorganization of the mixed brush, which can dramatically change the surface properties of the polymer layer. Li *et al*. carried out ATRP from Y-initiator-modified silica nanoparticles to produce mixed poly(*tert*-butyl acrylate)/polystyrene (PtBA/PS) brushes.[39] Subsequent hydrolysis resulted in amphiphilic nanoparticles with a mixed poly(acrylic acid)/polystyrene (PAA/PS) layer which were soluble in both chloroform (a good solvent for PS chains) and water (a good solvent for PAA chains). Shan *et al*. used a "grafting-to" approach to produce mixed brush amphiphilic gold nanoparticles by

reducing $HAuCl_4 \cdot xH_2O$ in the presence of a mixture of dithioester-terminated poly(N-isopropylacrylamide) (PNIPAM) and PS chains.[40, 41] When these particles were cast at the air-water interface from a spreading solvent, the mixed brushes reorganized with PNIPAM chains spreading on the water surface and PS chains collapsing into globules.[41] Using a similar "grafting-to" approach, Chiu *et al*. synthesized gold nanoparticles coated with mixed brushes of poly(2 vinyl pyridine) (PVP) and PS chains, which were found to localize at the interface of PS and PVP domains when blended with a PS-*b*-PVP block copolymer.[42] Zubarev and co-workers used a surface polymerization strategy to form amphiphilic gold nanoparticles with V-shaped ligands consisting of either polybutadiene-poly(ethylene oxide) (PB-PEO) or polystyrene-poly(ethylene oxide) (PS-PEO) arms.[43] Interestingly, they showed that the mixed brush PS-PEO nanoparticles underwent a comformational rearrangement during water addition to THF solutions, forming nanoparticle amphiphiles with linear symmetry that self-assembled into 1D wormlike superstructures.[44]

A different route to nanoparticles with mixed polymer brushes involves the self-assembly of triblock copolymers with an insoluble core-forming center block and two different soluble end blocks.[45-48] Erdhardt *et al*. employed bulk microphase separation of a polystyrene-*block*-polybutadiene-*block*-poly(methyl methacrylate) (PS-*b*-PB-*b*-PMMA) triblock copolymer with a relatively short center block to generate a morphology of PB nanospheres distributed at the interface of a PS/PMMA lamellar structure.[45] Chemical crosslinking of the PB spheres resulted in "Janus" PS/PMMA mixed brush micelles which could be dispersed in various organic solvents[45] and underwent self-assembly into surface aggregates at the air-water interface.[46] Subsequent hydrolysis of the PMMA

chains resulted in amphiphilic spheres which formed supermicelles in aqueous media.[47] Liu and co-workers have formed amphiphilic micelles with mixed coronal chains via self-assembly of a poly(butyl methacrylate)-*block*-poly(2-cinnamoyloxyethyl methacrylate)-*block*-poly(*tert*-butyl acrylate) (PBMA-*b*-PCEMA-*b*-P*t*BA) triblock copolymer, followed by crosslinking of the PCEMA cores and hydrolysis of PtBA coronal chains.[48] These examples demonstrate that triblock copolymer self-assembly is an interesting route toward environmentally-responsive nanoparticles with a mixed brush external layer. However, in the triblock copolymer systems explored to date, the mixed-brush nanoparticles possess cores comprised solely of crosslinked polymers without interesting optical properties.

The present work utilizes self-assembly of a triblock copolymer to synthesize the first example of semiconductor QDs possessing environmentally responsive mixed polymer brush layers (Scheme 2.1.). First, the micellization of a polystyrene-*block*-poly(acrylic acid)-*block*-poly(methyl methacrylate) (PS-*b*-PAA-*b*-PMMA) triblock copolymer in organic solvent is induced by cadmium acetate addition and ionization of the relatively short PAA blocks; self-assembly forms poly(cadmium acrylate) (PACd) ionic cores surrounded by mixed coronae of PS and PMMA chains. Next, the micelle cores are reacted with hydrogen sulfide (H_2S), resulting in growth of CdS QDs with a mixed polymer brush layer (PS/PMMA-CdS). We show that these particles can be dispersed in solvents of wide-ranging polarities while maintaining both colloidal stability and stability of QD optical properties. Structural characterization of PS/PMMA-CdS particles by 2D ^{1}H NOESY NMR and static and dynamic light scattering indicates conformational changes in the mixed brush in response to different solvent environments.

We also show that PS/PMMA-CdS QDs can be uniformly dispersed in both PS and PMMA homopolymers via spin-coating. These semiconductor QDs coated with mixed polymer brushes represent an important step toward a new type of "smart" self-assembling element for nanostructured QD/polymermaterials and devices.

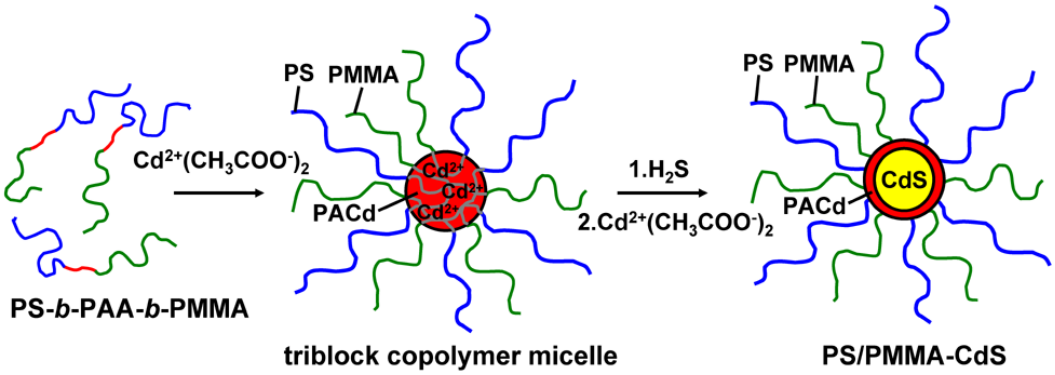

Scheme 2.1. Formation of PS/PMMA-CdS via self-assembly of PS-*b*-PAA-*b*-PMMA triblock copolymers, followed by templated QD growth in the copolymer micelle cores.

2.2. Experimental

2.2.1. Synthesis of Polystyrene-*b*-Poly (*tert*-Butyl Acrylate)-*b*-Poly(Methyl Methacrylate) (PS-*b*-P*t*BA-*b*-PMMA) Triblock Copolymer. The triblock copolymer used as a precursor material in the present study was synthesized using anionic polymerization techniques described elsewhere in the literature.[49, 50] All monomers were stirred over calcium hydride for 24 h, distilled under vacuum, and stored under nitrogen at -20 ^{o}C. Immediately prior to the polymerization reaction, styrene, *tert*-butylacrylate

and methyl methacrylate monomers (Aldrich) were further purified by the addition of fluorenyllithium to styrene, and triethylaluminum to *tert*-butylacrylate and methyl methacrylate, followed by vacuum distillation into flame-dried cylinders. The tetrahydrofuran (THF) reaction solvent was freshly distilled following reflux over sodium/benzophenone. Solvents, monomers, and initiator were transferred using rigorous Schlenk-line techniques under ultrahigh purity (UHP) nitrogen atmosphere and vacuum.

Several drops of α-methylstyrene (Aldrich) were added to the reaction flask containing LiCl (10 mol LiCl : 1 mol *sec*-butyllithium) dissolved in THF. The *sec*-butyllithium initiator (1.3M in hexanes, Aldrich) was then added drop-wise until a dark red color persisted, followed by the addition of the desired quantity of initiator. The reaction flask was cooled to -78 ^{o}C using a dry ice/acetone bath, followed by the sequential addition of styrene, *tert*-butylacrylate, and methyl methacrylate monomers, allowing 30 min for the polymerization of each block. Aliquots of the reaction mixture were withdrawn following polymerization of each of the first two blocks (PS and P*t*BA) for analysis by gel permeation chromatography (GPC). Finally, the polymerization reaction was terminated by the addition of degassed methanol.

2.2.2. Selective Hydrolysis of PS-*b*-P*t*BA-*b*-PMMA. The P*t*BA block of PS-*b*-P*t*BA-*b*-PMMA was selectively hydrolyzed to form polystyrene-*b*-poly(acrylic acid)-*b*-poly (methyl methacrylate) (PS-*b*-PAA-*b*-PMMA) by reflux in toluene with *p*-toluenesulfonic acid (5 mol% relative to the *tert*-butylacrylate content) for 5 hours. ^{1}H

NMR was used to confirm that the P*t*BA block was completely hydrolyzed without significant hydrolysis of the PMMA block.

2.2.3. Preparation of Polystyrene-*b*-Poly(Cadmium Acrylate)-*b*-Poly(Methyl methacrylate) (PS-*b*-PACd-*b*-PMMA) Micelles. The methodology used for preparing PS-*b*-PAA-*b*-PMMA triblock copolymer-stabilized QDs was similar to that described previously for forming PS-*b*-PAA diblock copolymer-stabilized QDs.[17,20] The triblock copolymer was dissolved in benzene/methanol (90:10 v/v) at a concentration of ca. 2 wt%. The formation of reverse micelles via self-assembly of insoluble PACd cores was induced by the addition of excess 0.25 M cadmium acetate dihydrate (Aldrich) in methanol (1.5 mol cadmium acetate dihydrate:1 mol acrylic acid repeat units) followed by stirring of the solution for 4 h. The onset of a bluish tinge to the solution with cadmium acetate addition suggested an increase in light scattering caused by the formation of micelles. The material was recovered by freeze-drying and then dried in a vacuum oven at 70°C for 24 h. Excess cadmium acetate was removed by washing the freeze-dried powder repeatedly with methanol followed by drying under vacuum at 70°C for 24 h.

2.24. Preparation of Mixed Polymer Brush-Stabilized QDs (PS/PMMA-CdS). The white powder consisting of freeze-dried PS-*b*-PACd-*b*-PMMA micelles (PACd cores and mixed PS/PMMA coronae) was exposed to an atmosphere of 100% humidity for a period of 1 week. The powder was then exposed to wet H_2S for 9 h, resulting in CdS QD

formation in the PACd cores, then stored under active vacuum for 12 h to remove excess H_2S. To stabilize the resulting micelle-encapsulated QDs, the yellow powder was dispersed in THF (2 wt %) and excess cadmium acetate dihydrate in methanol (2 mol cadmium acetate dihydrate : 1 mol acrylic acid repeat units) was added to re-neutralize the acrylic acid blocks. After overnight stirring, the sample was recovered by precipitation into methanol, then washed repeatedly with methanol and dried for 24 h in a vacuum oven at 70 ^{o}C. This final product was designated PS/PMMA-CdS.

2.2.5. Dispersion of PS/PMMA-CdS in PS or PMMA Homopolymers. Films were prepared by solution blending PS/PMMA-CdS QDs with either PS homopolymer (prepared in our lab by anionic polymerization: M_n = 130 000 g mol^{-1}, M_w/M_n = 1.01) or PMMA homopolymer (Aldrich, M_w = 120 000 g mol^{-1}). All blend components were first dissolved separately in toluene to 6 wt% polymer and allowed to stir overnight. Two different blends were then prepared by mixing component solutions in appropriate ratios: 1) PS/PMMA-CdS / PS and 2) PS/PMMA-CdS / PMMA, each with PS/PMMA-CdS : homopolymer ratios of 30 : 70 (w/w). The solutions were stirred for 2 h then left overnight to equilibrate. Blend films were prepared by spin-coating blend solutions onto clean glass microscope coverslips at a spinning rate of 3000 rpm. All films were dried overnight under vacuum at 70 °C before analysis.

2.2.6. Gel Permeation Chromatography (GPC). GPC measurements were performed using a Viscotek Model 302 liquid chromatography system equipped with

refractive index (RI), low-angle light scattering (LALS, θ = 7°), right-angle light scattering (RALS, θ = 90°), and UV detectors. THF was used as the eluent at a flow rate of 1 mL/min, and the column temperature was set at 35 °C. All polymer solutions were filtered through membrane filters with a nominal pore size of 0.45 μm before injection into the GPC column. The data were collected and analyzed on a Dell Dimension 2300 computer with appropriate GPC software from Viscotek. Two ViscoGEL HR High-Resolution Columns (styrene-divinyl benzene columns) in series were used: G3000 HR 60 k and GMHHR-M Mixed Bed 4 M columns. The molecule weight distribution for the PS block of the triblock copolymer was determined from GPC data using an algorithm from Viscotek, which relies on LALS detection from a 670 nm diode laser source.

2.2.7. ^{1}H NMR Analysis. ^{1}H NMR spectra of triblock copolymers and micelles were recorded using a Bruker AC 300 MHz spectrometer. 2D 1H Nuclear Overhauser Effect Spectroscopy (NOESY) experiments were made at 300 K on a Bruker Avance 500 MHz spectrometer. For the 2D NOESY spectra, 256 experiments of 2000 data points were recorded, consisting of 8 scans per increment, using standard Bruker software. The clearest contour plots were obtained using a mixing time of 300 ms.

2.2.8. UV-Vis Absorption and Photoluminescence Measurements. Absorption spectra were recorded on a Cary 50-scan UV-vis spectrophotometer. Static photoluminescence (PL) measurements were recorded on an Edinburgh Instruments FLS 920 instrument equipped with a Xe 450W arc lamp and a red-sensitive PMT (R928-P). Typical PL measurements involved λ_{ex} = 400 nm excitation and collection of emitted

light with a long-pass 450 nm emission filter in place. For PL measurements of QDs in solution, the PS/PMMA-CdS sample was dispersed in various solvents (spectroscopic grade acetone, chloroform, THF and toluene) at concentrations such that the measured absorbance at 400 nm was less than 0.1. For PL measurements of polymer blend films on glass, front-face excitation of the films was used, with an angle of ca. 45° between the detector and the film normal. All spectra were collected at 1 nm spectral resolution and the appropriate background was subtracted.

2.2.9. Static and Dynamic Light Scattering Measurements. Static light scattering (SLS) and dynamic light scattering (DLS) experiments were carried out on a Brookhaven Instruments photon correlation spectrometer equipped with a BI-200SM goniometer, a BI-9000AT digital autocorrelator, and a Melles Griot He-Ne Laser (632.8 nm) with a maximum power output of 75 mW. To ensure the accuracy for both SLS and DLS measurements, great care was taken to eliminate dust from the samples. Spectroscopic grade acetone, chloroform, THF and toluene were filtered through two membrane filters with 0.20 μm nominal pore size connected in series. Stock solutions (ca. 5 mg/mL) of PS/PMMA-CdS colloids in various solvents were prepared the night before SLS or DLS measurements to ensure equilibration, then filtered through two membrane filters with 0.45 μm nominal pore size connected in series to remove dust. All scintillation vials were thoroughly cleaned with filtered solvent before stock solutions of the PS/PMMA-CdS colloids were transferred into the vials. Successive dilutions of the colloids were carried out by adding known quantities of the filtered solvents.

SLS measurements of PS/PMMA-CdS in various solvents were carried out in a concentration range from 0.2 - 1 mg/mL. For each concentration, angles of detection from 15° to 155° were measured with 15° increments between angles. Ten repeat measurements of scattered light intensity were taken at each angle and concentration to obtain Zimm plots based on the fundamental Zimm equation 2.1 for light scattering from polymer solutions:

$$\frac{Kc}{\Delta R_\theta} = \frac{1}{M_w P(\theta)} + 2A_2 c \qquad \textbf{(2.1)}$$

where ΔR_θ is the excess Rayleigh scattering ratio, $P(\theta)$ is the particle scattering factor, M_w is the apparent weight-average molecular weight of the sample, A_2 is the second virial coefficient, c is the polymer concentration and K is a composite of optical and fundamental constants. For each solvent, reported values of M_w and root-mean-square z-average radii of gyration, r_g, were determined from the average results of three separate Zimm plots obtained from different stock solutions; average errors on M_w and r_g values were 7%. All SLS measurements were conducted at 23° C.

The differential refractive index values, dn/dc, for PS/PMMA-CdS dispersed in acetone, chloroform, THF and toluene were required for Zimm plot analysis of static light scattering results. These were determined using a BI-DNDC Differential Refractometer which was calibrated using a known standard of potassium chloride (KCl) in water. Stock solutions of PS/PMMA-CdS of ca. 10 mg/mL were diluted to obtain 5

concentrations from 1 to 5 mg/mL for *dn*/*dc* determination. Three repeat measurements of *dn*/*dc* were obtained for PS/PMMA-CdS in each solvent.

DLS measurements of PS/PMMA-CdS in each solvent were conducted at five different angles, 35°, 50°, 70°, 90°, and 120°, and at various concentrations in the range of 0.02-1 mg mL^{-1}. For each angle and concentration, three repeat measurements of the autocorrelation function were obtained. Average errors on hydrodynamic radii, r_h, determined for each solvent from DLS at multiple angles and several concentrations were 4%. All DLS measurements were conducted at 23 °C.

2.2.10. Laser Scanning Confocal Fluorescence Microscopy (LSCFM). Laser scanning confocal fluorescence microscopy measurements of polymer blend films containing PS/PMMA-CdS were done on a Zeiss LSM 410 equipped with an Ar/Kr laser. A Zeiss Plane-Aprochromat 63x oil immersion objective was used. All films were excited at ~488 nm, using a band-pass 485 ± 20 nm line selection filter and a FT 510 dichroic beam splitter. A long-pass 515 emission filter was used such that only light above 515 nm reached the PMT. A pinhole diameter of 0.984 Airy Units was used for all measurements, resulting in an optical section thickness of 0.62 μm fwhm.

2.2.11. Transmission Electron Microscopy. TEM was performed on a Hitachi H-700 electron microscope, operating at an electron accelerating voltage of 75 kV. Solution-cast samples were prepared by depositing a drop of 2 mg/mL PS/PMMA-CdS solution in benzene on a copper grid (300 mesh) coated with an amorphous carbon film and immediately blotting excess solution; the grids were then dried at room temperature

for 2 hours before imaging. For TEM of polymer blends of PS/PMMA-CdS dispersed in PS or PMMA homopolymer, the films were first were first embedded in an Epon resin, and then ~50 nm-thick sections were produced with a diamond knife on Reichert UltraCut E ultra-microtone. The thin sections were placed on carbon/formvar-coated 300 mesh copper grids for imaging.

2.3. Results and Discussion

2.3.1. Characterization of PS-*b*-P*t*BA-*b*-PMMA and Hydrolyzed PS-*b*-PAA-*b*-PMMA Triblock Copolymers. During anionic polymerization of the triblock copolymer, progressive growth of living chains after the addition of each monomer component was followed by GPC (Figuure 2.1). Following styrene polymerization, GPC revealed a single narrow peak with number-average molecular weight M_n = 30 800 g mol^{-1}, from which the number-average degree of polymerization of the PS block was determined (N_{PS} = 296). Subsequent polymerization of *tert*-butyl acrylate amd methyl methacrylate resulted in the single GPC peak progressively shifting to lower elution volumes, indicating growth of the living chain to form a P*t*BA middle block and PMMA end block. GPC of the PS-*b*-P*t*BA-*b*-PMMA triblock copolymer after termination of the living chains revealed a very narrow polydispersity with M_w/M_n = 1.05.

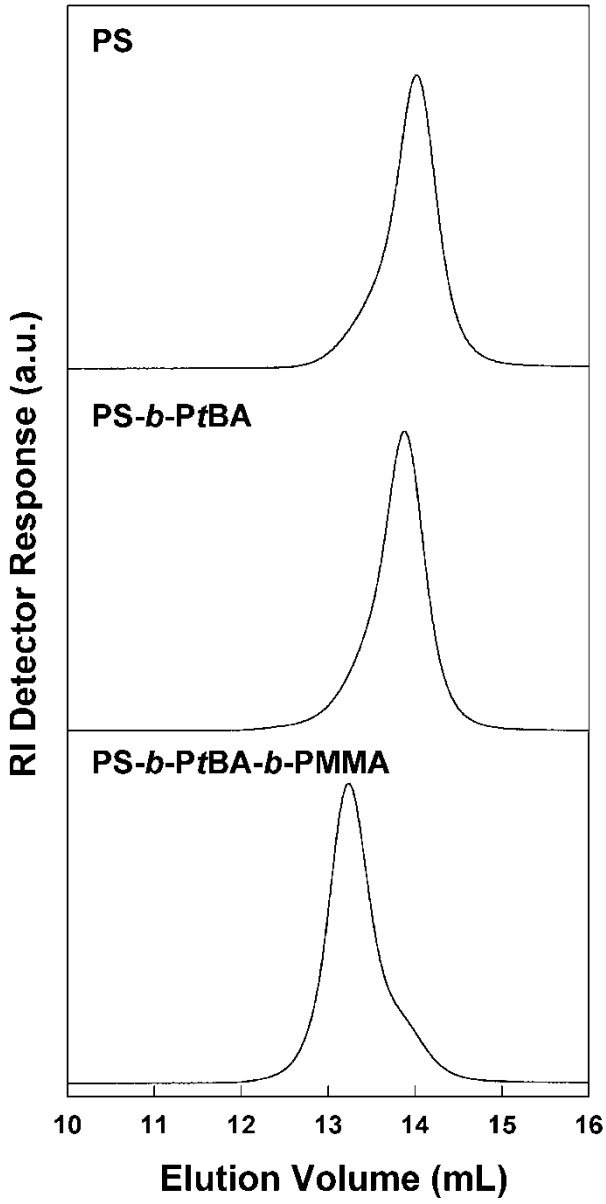

Figure 2.1. Gel permeation chromatograms (refractive index detector response) of aliquots removed from reaction solution after polymerization of each block during sequential anionic polymerization of PS-*b*-P*t*BA-*b*-PMMA.

The ^{1}H NMR spectrum of the synthesized copolymer confirmed incorporation of PS, P*t*BA and PMMA blocks and allowed the relative block lengths to be determined via integrated intensities of characteristic resonances. The spectrum and key proton peak assignments are shown in Figure 2.2. Most important for composition determination were resonances at δ = 7.07 ppm and δ = 6.57 ppm (5 phenyl ring protons from each styrene repeat unit), δ = 3.59 ppm (3 methyl ester protons from each methyl methacrylate repeat unit), and δ = 1.42 ppm (an overlap of 2 methylene protons from each styrene repeat unit and 9 *tert*-butyl ester protons from each *tert*-butyl acrylate repeat unit).[51] Based on the relative integrated intensities of these resonances, the mole fractions of PS, P*t*BA, and PMMA repeat units in the copolymer could be determined: x_{PS} = 0.52, x_{PtBA} = 0.07, x_{PMMA} = 0.41. From these mole fraction values, and the number-average degree of polymerization of the PS block determined by GPC (N_{PS} = 296), the number-average degrees of polymerization of the PtBA and PMMA blocks were assigned: N_{PtBA} = 41 and N_{PMMA} = 236. The characterized triblock copolymer before selective hydrolysis was therefore designated PS(296)-*b*-P*t*BA(41)-*b*-PMMA(236), with numbers in brackets representing the number-average degrees of polymerization of the respective blocks. The ^{1}H NMR spectrum of the copolymer following the hydrolysis reaction confirmed that the central P*t*BA block had been selectively hydrolyzed to PAA, without significant hydrolysis of the PMMA block. The spectrum and key proton peak assignments following hydrolysis are shown in Figure 2.3. Compared to the spectrum obtained before hydrolysis, the intensity of the δ = 1.42 ppm resonance has decreased considerably: after hydrolysis, the integrated intensity ratio of the δ = 1.42 ppm peak to the phenyl ring

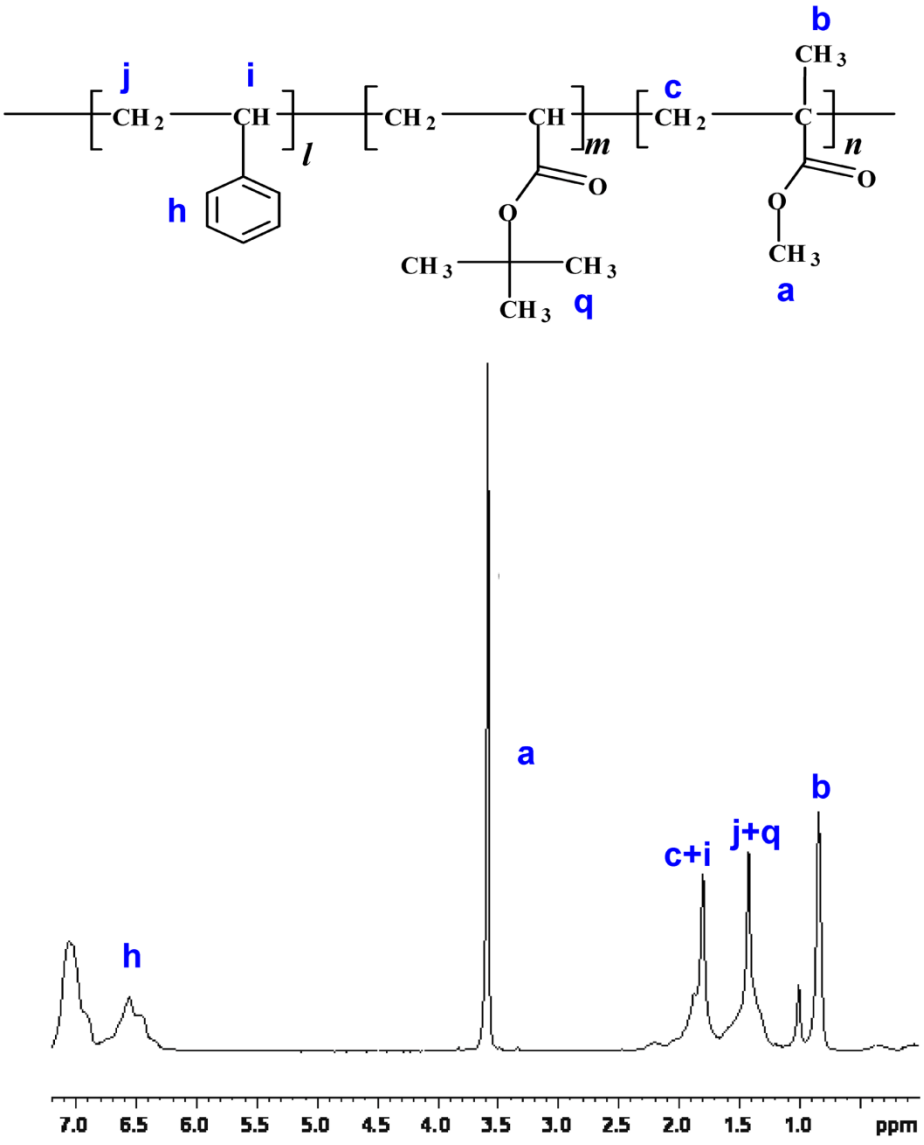

Figure 2.2. ^{1}H NMR spectrum and peak assignments of PS-*b*-P*t*BA-*b*-PMMA triblock copolymer in chloroform-D, before selective hydrolysis of the P*t*BA block.

protons (δ = 7.07 ppm and δ = 6.57 ppm) was determined to be 0.40, which is the predicted ratio of methylene to phenyl ring protons on styrene (2/5), confirming that the overlapping *tert*-butyl ester resonance at δ = 1.42 ppm has completely disappeared. As well, the integrated ratio of the phenyl ring protons (δ = 7.07 ppm and δ = 6.57 ppm) to the PMMA methyl ester protons (δ = 3.59 ppm) was found to be identical before and after hydrolysis, indicating that only the P*t*BA block and not the PMMA block was hydrolyzed in the reaction. Table 2.1 lists composition data for the hydrolyzed PS(296)-*b*-PAA(41)-*b*-PMMA(236) triblock copolymer from the combination of GPC and NMR analysis.

Table 2.1. Characteristics of PS-*b*-PtBA-*b*-PMMA Triblock Copolymer Synthesized by Sequential Anionic Polymerization

M_n,g/mol	M_w/M_n	N_{PS}	N_{PtBA}	N_{PMMA}
59700	1.05	296	41	236

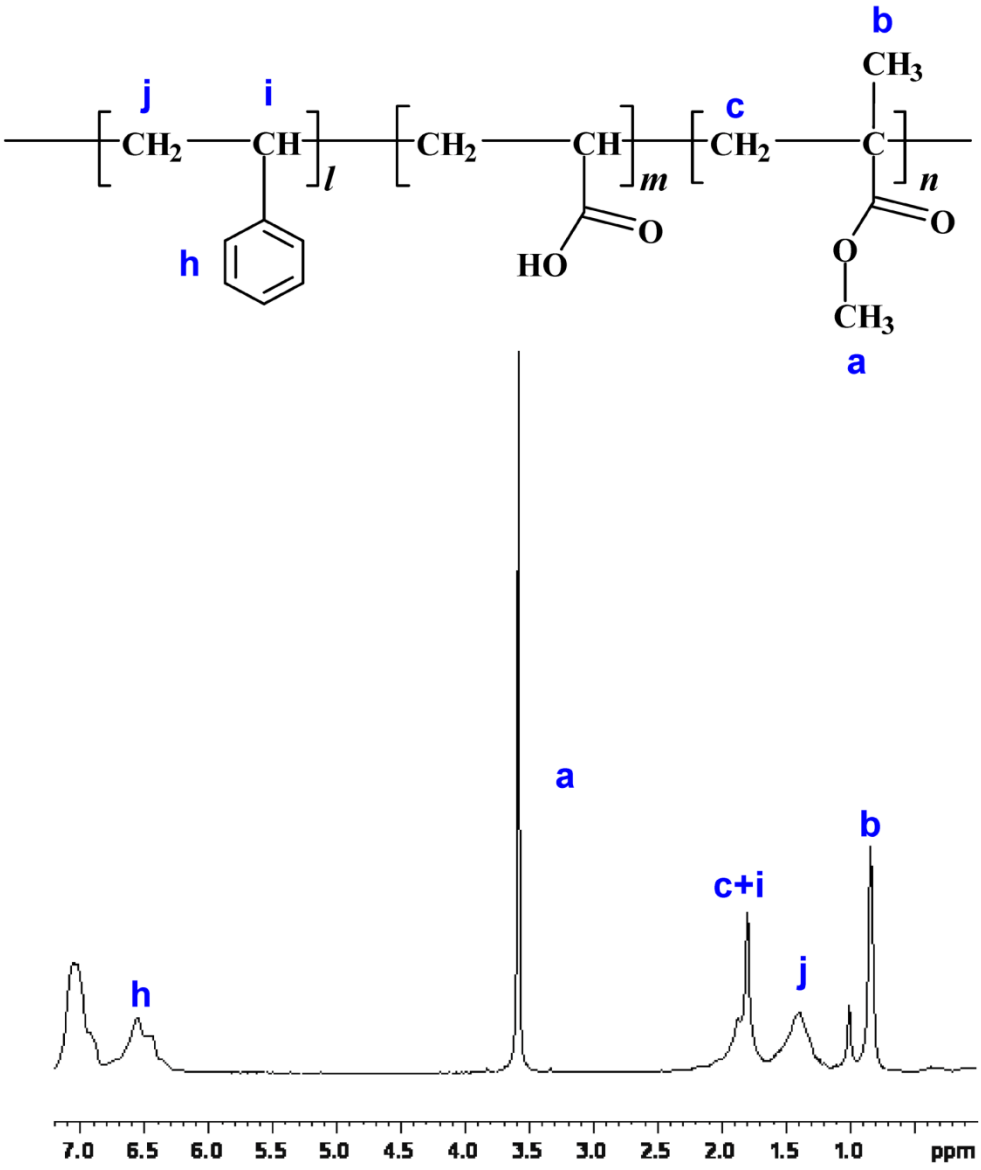

Figure 2.3. ^{1}H NMR spectrum and peak assignments of PS-*b*-PAA-*b*-PMMA triblock copolymer in chloroform-D, after selective hydrolysis of the P*t*BA block.

2.3.2. Copolymer Micellization and Formation of Mixed Polymer Brush-Stabilized QDs (PS/PMMA-CdS). The addition of a stoichiometric excess of cadmium acetate (1.5 mol cadmium acetate dihydrate:1 mol acrylic acid repeat units) to PS(296)-*b*-PAA(41)-*b*-PMMA(236) in benzene/methanol resulted in neutralization of PAA, forming a negatively-charged middle block which underwent immediate self-assembly in the organic media. The appearance of a blue tinge upon addition of cadmium acetate indicated fast formation of micelles with an insoluble poly (cadmium acrylate) (PACd) core; the micellization of the triblock copolymer was confirmed by GPC following freeze-drying, washing, and re-suspension of the micelles in THF (not shown). The soluble PS and PMMA end blocks form a mixed corona of PS and PMMA chains upon copolymer micellization (Scheme 2.1), as confirmed by later analysis. Due to the relatively long soluble PS and PMMA end blocks compared to the short middle insoluble PACd block, the resulting micelles are best described as starlike.

Exposure of freeze-dried PS-*b*-PACd-*b*-PMMA micelles to H_2S resulted in a recovered yellow powder consisting of CdS QDs encapsulated in the cores of micelles with mixed PS/PMMA coronae (Scheme 2.1). Subsequent re-neutralization of the PAA blocks (which had been protonated during H_2S exposure) was carried out in order to stabilize the micelles, forming a high-T_g and ionically crosslinked PACd layer surrounding the QDs. We will show that these micelle-encapsulated QDs can be regarded as chemically-fixed colloidal brushes, which undergo changes in conformation, but not changes in grafting density, in different solvents. The resulting QD sample coated with a mixed polymer brush of PS and PMMA chains is designated PS/PMMA-CdS.

The yellow solid PS/PMMA-CdS could be easily dispersed in organic solvents of various polarities to yield clear colloidal dispersions. Figure 2.4a shows photographs of the resulting dispersions in acetone, chloroform, toluene and THF, all at a concentration of ~5 mg/mL. The clarity of the dispersions indicates good dispersion of PS/PMMA-CdS in all four solvents, including acetone, the most polar of the four solvents, which is a good solvent for PMMA but a poor solvent for PS. For comparison, Figure 2.4b shows dispersions in the same solvents of a sample of CdS QDs coated by a homogenous PS brush layer (PS-CdS)[30] with PS chain length of N_{PS} = 300 (similar to N_{PS} = 296 for PS/PMMA-CdS). The PS-CdS particles are clearly well dispersed in chloroform, toluene and THF, although could not be dispersed in acetone even after 12 h sonication. The dispersion of PS/PMMA-CdS in acetone is thus attributed to the presence of PMMA chains within a mixed brush layer surrounding the QDs. This suggests a conformational rearrangement to maintain colloidal stability of PS/PMMA-CdS in solvents both "good" and "poor" for PS. The electron-dense QDs were visualized by transmission electron microscopy (TEM) following deposition of dilute solutions of PS/PMMA-CdS onto carbon-coated TEM grids. Figure 2.5a shows a typical TEM image of deposited PS/PMMA-CdS, indicating a distribution of QD sizes (dark spots) formed in the cores of triblock copolymer micelles. Although the vast majority of QDs appear as individual nanoparticles on the TEM grids, larger clusters of QDs are also occasionally observed. These clusters may represent micelle clusters that form upon solvent evaporation, or else larger micelle cores containing multiple dots. Figure 2.5b and c are high-magnification TEM images demonstrating the typical QD with the big (red arrow) and small (blue arrow) size, respectively. Size distribution analysis (Figure 2.5d) was carried out based

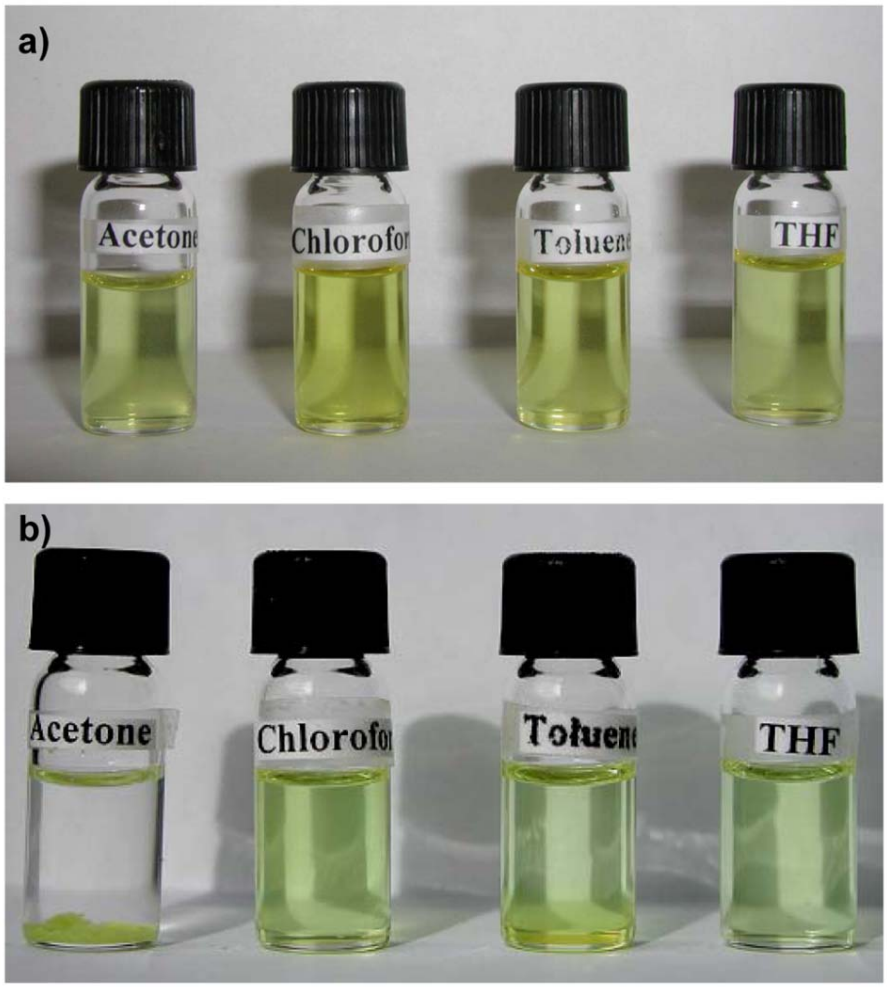

Figure 2.4. Photos of (a) PS/PMMA-CdS and (b) PS-CdS dispersions in acetone, chloroform, toluene, and THF.

on measurement of ~300 QDs in several regions of the TEM grids, giving an average particle size and standard deviation of $2r_{CdS} = 4.9 \pm 1.8$ nm. The resulting QD diameter distribution is clearly bimodal, with a larger particle population centered at $2r_{CdS} \sim 7$ nm and a smaller particle population centered at $2r_{CdS} \sim 4$ nm. There are two possible explanations for a bimodal distribution of QDs formed in the cores of the triblock copolymer micelles: 1) the distribution of micelle aggregation numbers is itself bimodal or 2) some micelles contain multiple very small CdS QDs due to incomplete reaction of Cd^{2+} ions in their cores, resulting in the smaller population, whereas cores in which all Cd^{2+} ions are converted into a single QD represent a significantly larger and separated QD population. CONTIN analysis of dynamic light scattering results (discussed later) show that PS/PMMA-CdS dispersed in various solvents possess a single distribution of hydrodynamic radii, which lends support to the second of the above possibilities.

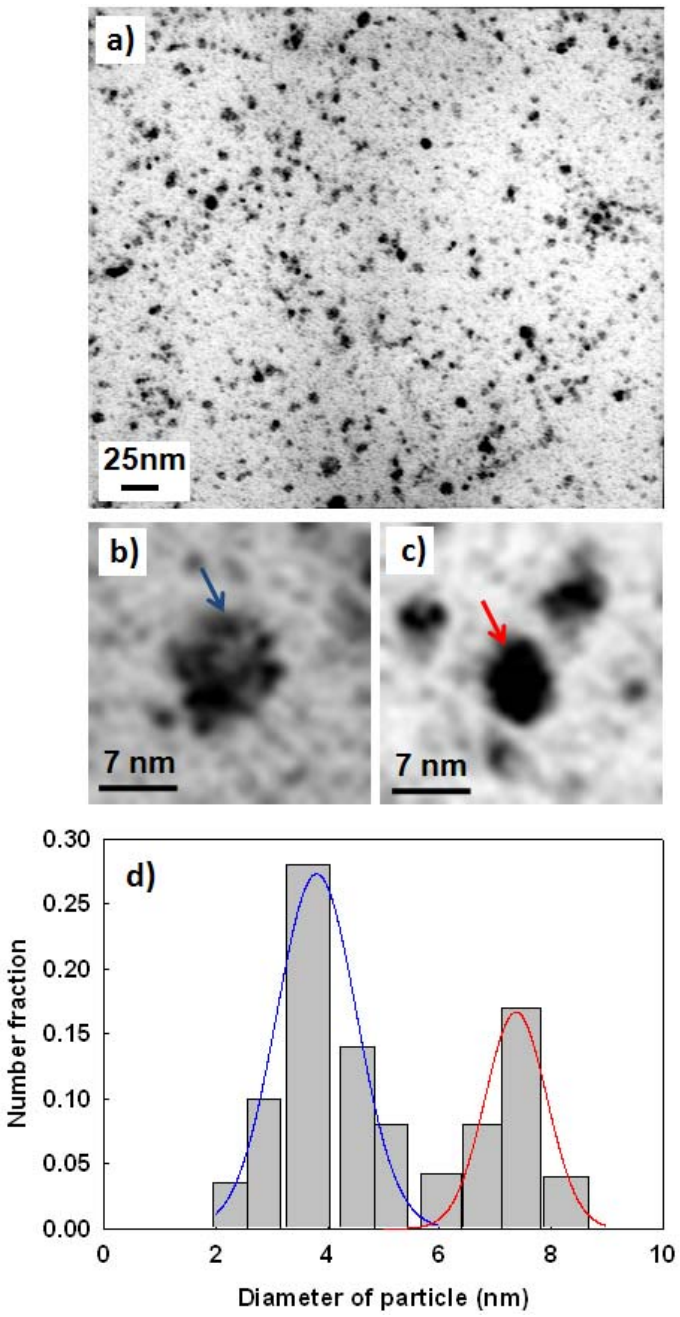

Figure 2.5. (a) Transmission electron micrograph (TEM) of PS/PMMA-CdS cast from a dilute (2 mg/mL) benzene dispersion onto a carbon-coated TEM grid. (b) and (c) are high- magnification TEM images showing a typical multiple-QD core contributing to the smaller-particle population (blue arrow) and a typical single-QD core contributing to the larger-particle population (red arrow).(d) CdS QD size distribution determined from several TEM images such as those shown in (a) taken in different regions of the grid.

2.3.3. Optical Properties and Stability of PS/PMMA-CdS in Various Solvents.

The optical properties of PS/PMMA-CdS were determined in various solvents (acetone, THF, chloroform, toluene, in order of decreasing dielectric constant). Figure 2.6a shows normalized absorbance spectra of PS/PMMA-CdS dispersed in each of the four solvents. The spectra in each case are attributed to absorption of CdS QDs encapsulated in the cores of the triblock copolymer micelles. The spectra can be regarded as fingerprints of the QD size distribution via the quantum confinement effect. In each spectra, two exciton shoulders are observed at ~385 nm and ~470 nm, corresponding to populations of smaller and larger quantum dots, respectively, and consistent with the bimodal size distribution determined from TEM results. From the absorption threshold of the toluene solution, λ_{thresh} = 512 nm, a QD diameter of $2r_{CdS}$ = 7.3 nm is determined from the following empirical formula (obtained by fitting data published previously by Henglein): $2r_{CdS} = 1 / (0.1338 - 0.0002345\lambda_{thresh})$.[17, 52] This size is consistent with the larger QD population ($2r_{CdS}$ ~ 7 nm) determined from TEM, which is reasonable considering the higher wavelength region of the absorption spectrum corresponds to larger particles within the distribution. When the normalized spectra of PS/PMMA-CdS in different solvents are compared, they are found to overlap almost exactly (Figure 2.6a), indicating that the QD sizes are stable during dispersal of PS/PMMA-CdS in media of very different polarity. Normalized photoluminescence spectra of PS/PMMA-CdS in the different solvents (Figure 2.6b) are also similar, each showing a broad peak at ~610 nm attributed to emission from QD trap states.

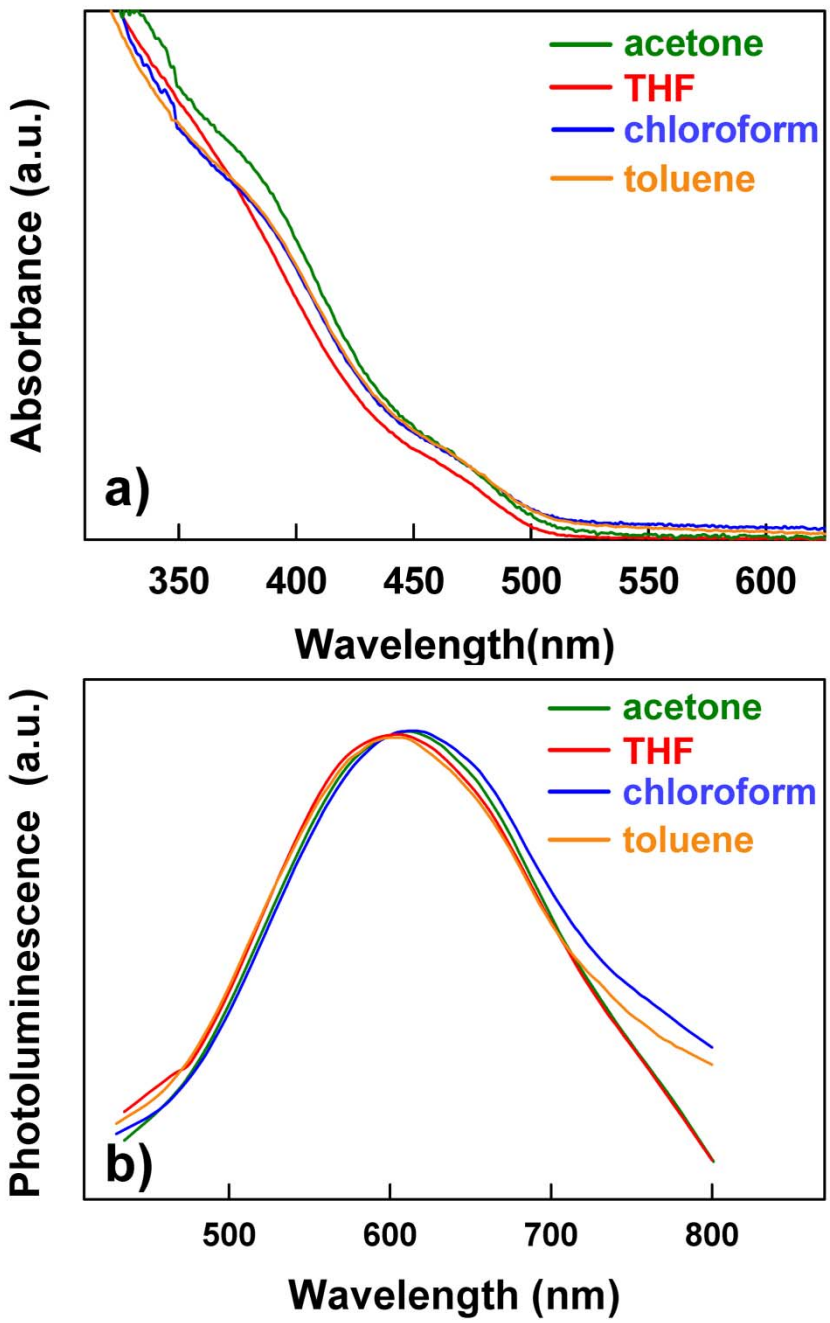

Figure 2.6. (a) UV-vis absorption spectra and (b) photoluminescence (PL) spectra of PS/PMMA-CdS dispersions in various solvents. For PL spectra, λ_{ex} = 400 nm.

Dispersions of PS/PMMA-CdS in all investigated solvents showed good long-term colloidal stability when stored in the dark under ambient conditions, and remained clear without evidence of precipitation for periods of over 6 months. UV-vis absorption spectra also revealed long-term stability of QD size distributions in acetone, chloroform and toluene (Figure 2.7), as evidenced by exact overlap of absorption spectra obtained on Day 1 and Day 180 following PS/PMMA-CdS dispersion. This indicates that the QDs are protected from agglomeration and Ostwald ripening in solvents of varying polarities ranging from acetone (dielectric constant, $\varepsilon = 21$) to toluene ($\varepsilon = 2.4$) within the cores of the triblock copolymer micelles. THF was the only solvent in which a noticeable change in the absorption spectrum was observed after 180 days; although the absorption threshold and exciton shoulder at 470 nm did not shift, the exciton shoulder at 385 nm disappeared over the aging period. A possible explanation is that the smaller QD population decreased due to Ostwald ripening in THF, while the maximum particle size, determined by the average number of cadmium ions in each of the original micelles, remained constant. It is not clear why THF, with an intermediate dielectric constant ($\varepsilon = 7.5$), allowed for such QD ripening while the other solvents did not, although it is postulated that a combination of good solubility of both coronal blocks, along with partial swelling of the core, could explain the results.

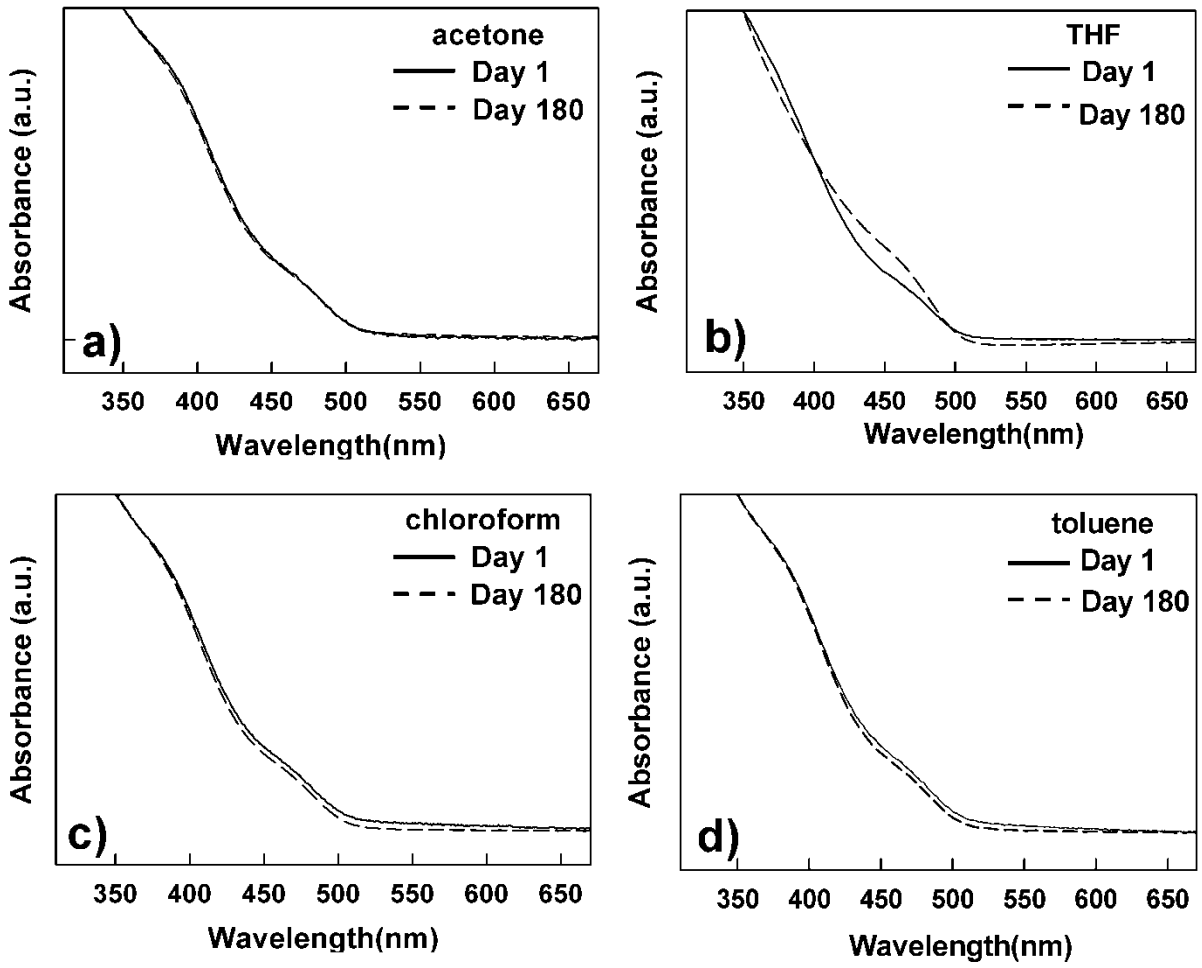

Figure 2.7. Investigation of long-term stability of QD size distributions for PS/PMMA-CdS dispersions in various solvents. UV-vis spectra of PS/PMMA-CdS in (a) acetone, (b) THF, (c) chloroform, and (d) toluene after 1 day (solid lines) and 180 days (dashed lines) storage under ambient conditions.

2.3.4. Nuclear Overhauser Effect (NOESY) Investigation of PS/PMMA-CdS.

An important question regarding the colloidal structure of PS/PMMA-CdS particles is the distribution of PS and PMMA chains in the mixed polymer brush layer. Erhardt *et al*. previously studied crosslinked micelles formed by self-assembly of PS-*b*-PB-*b*-PMMA triblock copolymers in the solid state, which were found to possess an asymmetric "Janus" PS/PMMA brush structure due to segregation of incompatible PS and PMMA blocks.[45, 47] An important difference in the formation of PS/PMMA-CdS in the present study is that self-assembly of the PS-*b*-PAA-*b*-PMMA triblock copolymers occurred in the presence of a good solvent for both PS and PMMA, such that the dissimilar end blocks are not expected to be strongly segregated within the micelle corona; therefore, a random distribution of PS and PMMA chains around the QD cores is thought to be the most likely arrangement of the brush. 2D ^{1}H NOESY experiments probe through-space dipolar interactions of proximal protons (< 0.5 nm), and was therefore employed to determine whether PS and PMMA chains were mixed or compartmentalized within PS/PMMA-CdS.[53-55]

2D ^{1}H NMR NOESY spectra of PS/PMMA-CdS and the reference triblock copolymer PS(296)-*b*-PAA(41)-*b*-PMMA(236) in THF-D8 are shown in Figure 2.8. THF was chosen as the solvent since DLS experiments show that the reference triblock copolymer exists as single chains in this solvent due to the relative solubility of all three blocks, whereas PS/PMMA-CdS exists as kinetically-frozen micelles. Both spectra display several off-diagonal cross-peaks, indicating proximal protons with cross-relaxation effects. In the PS/PMMA-CdS spectrum (top), distinct symmetric cross-peaks

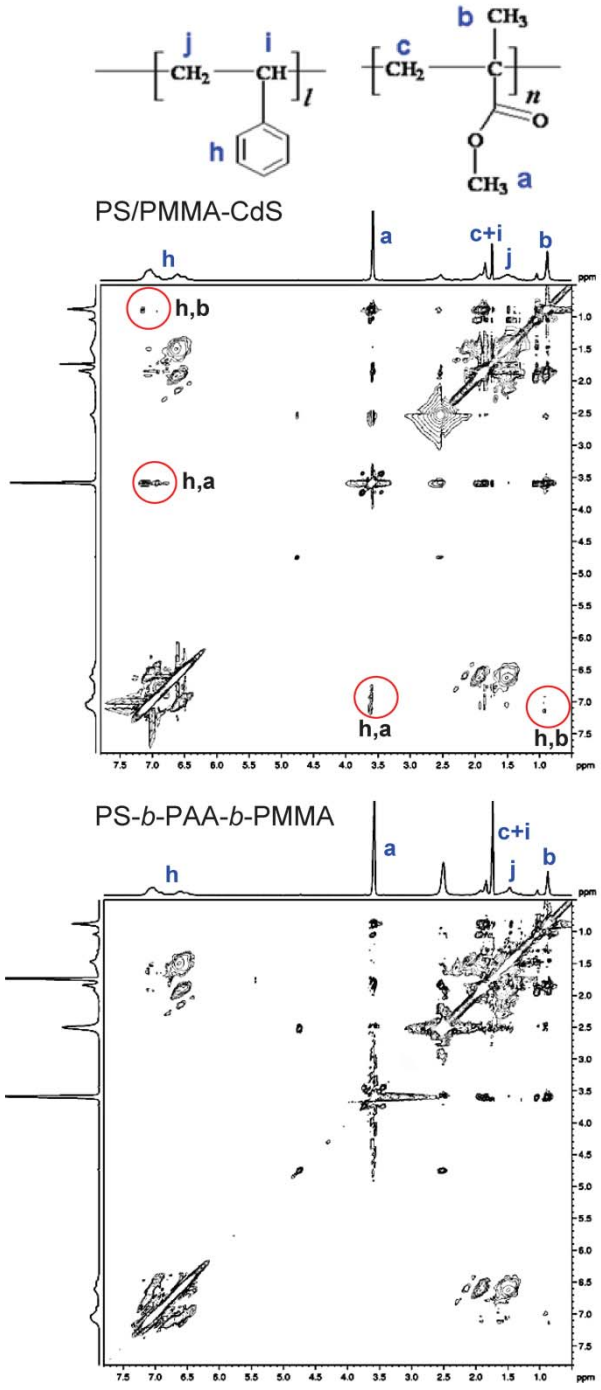

Figure 2.8. 2D 1H NMR NOESY spectra of (a) PS/PMMA-CdS and (b) PS-*b*-PAA-*b*-PMMA in THF-D8. Circles in (a) indicate cross-peaks between PS and PMMA blocks in the PS/PMMA-CdS spectrum which are not present in the reference spectrum (b) of PS-*b*-PAA-*b*-PMMA single chains.

between protons of the PS and PMMA blocks are observed (red circles), specifically between phenyl ring protons on PS and methyl protons on PMMA (h,b) and between phenyl ring protons on PS and ester methyl protons on PMMA (h,a); this indicates proximal mixing of PS and PMMA segments within the brush layer. These cross-peaks are not observed in the NOESY spectrum of the reference sample (bottom), confirming that mixing between PS and PMMA blocks is a result of micelle formation and does not occur within individually-solubilized chains. Significant mixing between PS and PMMA segments would not be expected if the coronal chains were compartmentalized in the manner of Janus or "patchy"[48] micelles. Thus NOESY experiments appear to confirm the proposed random distribution of PS and PMMA chains within PS/PMMA-CdS.

2.3.5. Static and Dynamic Light Scattering: Solvent-Responsive Brush Conformations in PS/PMMA-CdS Colloids. Zimm plot analysis of SLS data allowed the apparent weight-average molecular weight, M_w, and the root-mean-square *z*-average radius of gyration, r_g, of the PS/PMMA-CdS particles in various solvents to be determined. Representative Zimm plots in each of the four solvents investigated are provided in Figuure 2.9. Based on GPC in THF, a small fraction of unmicellized single chains (<10 wt%) is present in the PS/PMMA-CdS sample along with the micelle-encapsulated QDs; measured M_w values therefore contain a small contribution from these unmicellized chains. SLS analysis of M_w required measurement of differential refractive index values, dn/dc, for PS/PMMA-CdS in each of the solvents studied since this parameter is a component of the constant K within the Zimm equation (Eq. 2.1). From three repeat measurements, differential refractive index values were as follows: dn/dc =

0.094 ± 0.003 (acetone); dn/dc = 0.064 ± 0.002 (chloroform); dn/dc = 0.071 ± 0.003 (THF); dn/dc = 0.045 ± 0.002 (toluene). Using these values together with Zimm plot results, M_w values for PS/PMMA-CdS in acetone, THF, chloroform, and toluene were determined, as listed in Table 2.2. To calculate aggregation numbers, Z (Table 2), M_w values were divided by the molecular weight of a single unimer (unimer $M_{w,u}$ = 62,600 g/mol) consisting of the sum of: 1) one PS(296)-*b*-PAA(41)-*b*-PMMA(236) chain, 2) one CdS unit per carboxylate group, and 3) one Cd^{2+} ion for every two carboxylate groups. Importantly, the resulting aggregation numbers were found to be nearly identical within experimental error in all four solvents, Z ~ 200. This confirmed that PS/PMMA-CdS micelles are fixed by ionic crosslinking in the PACd layer, with no dynamic equilibrium between micelles and single chains in various solvents. Despite large differences in the surrounding solvent environment, therefore, the stabilizing chains are locked into the mixed polymer brush, similar to the situation of colloidal brushes with polymer chains covalently grafted to a particle surface.

The PS/PMMA-CdS aggregation number (Z ~ 200) allowed the chain surface density within the mixed brush layer to be estimated. Each triblock copolymer unimer in the aggregate will contribute one PS and one PMMA block, giving a total of ~400 chains within the brush; the middle block of each copolymer will contribute to the PACd layer surrounding the encapsulated QD. The PS/PMMA polymer brush is therefore grafted to a hybrid core consisting of a central QD and a surface layer of collapsed PACd chains; we estimate a total core diameter of $2r_c$ = 12.6 nm based on QDs of 7.3 nm (from UV-vis) each surrounded by 200 PACd chains in the melt state. From this core size and the total number of chains, the estimated brush density is ~1.3 nm^2 / chain.

Radii of gyration, r_g, of PS/PMMA-CdS particles determined from Zimm plot analysis were found to be significantly different in the various solvents, despite nearly identical aggregation numbers. These changes in r_g with constant Z provide direct evidence of conformational changes in the brush layer in response to different solvent environments. Table 2 lists r_g values for PS/PMMA-CdS in the various solvents, which range from r_g = 24 nm to r_g = 41 nm and increase in the order of r_g (acetone) < r_g (chloroform) < r_g (THF) < r_g (toluene).

Table 2.2. Summary of PS/PMMA–CdS Structure in Various Solvents Determined from Static and Dynamic Light Scattering Data

Solvent	M_w **x** 10^{-7} ***g/mol***	***Z***	r_g***, nm***	D_0 **x** 10^{-7}***,*** nm^2s^{-1}	r_h***, nm***	t_b***, nm***	***extension, %***	r_g/r_h
acetone	1.22	195	24	3.30	21	15	25 (PMMA)	1.1
THF	1.20	190	30	1.84	26	20	27 (PS)	1.2
chloroform	1.21	193	29	1.50	27	21	28 (PS)	1.1
toluene	1.31	209	41	1.26	31	25	34 (PS)	1.3

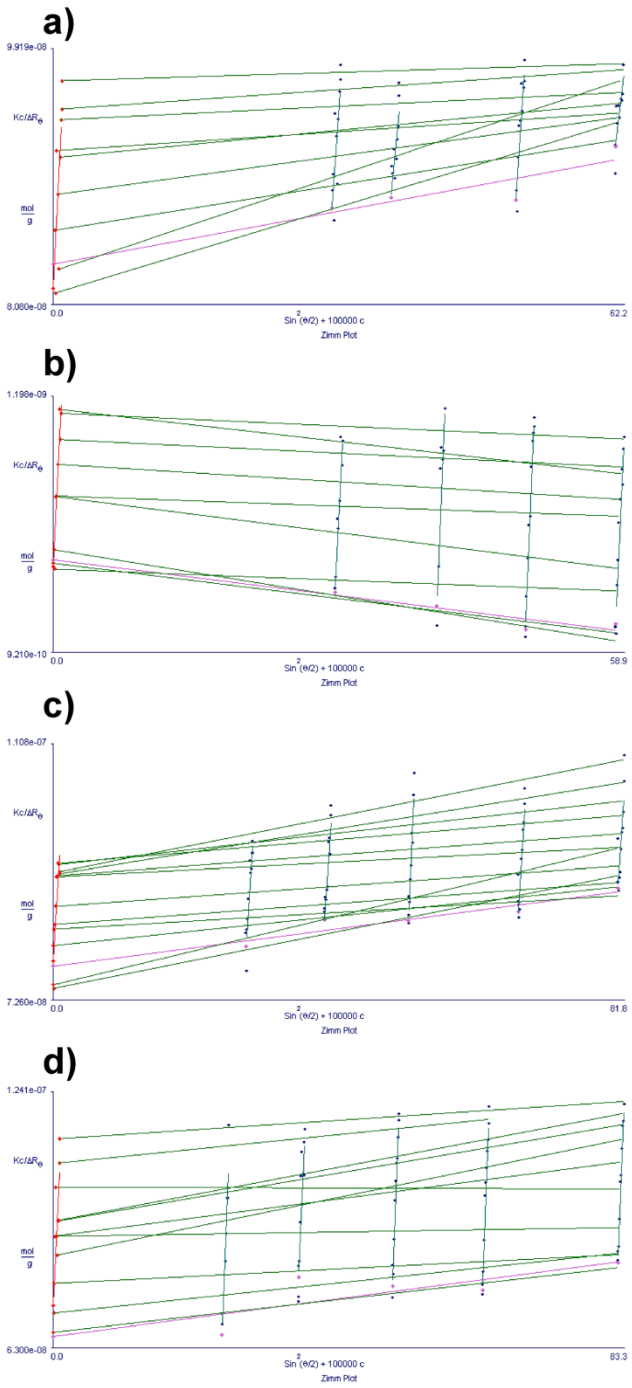

Figure 2.9. Representative Zimm plots of static light scattering (SLS) data for PS/PMMA-CdS in (a) acetone, (b) THF, (c) chloroform, and (d) toluene. The measured scattering angles were from 5° to 155° in 15° increments, and concentrations were between 0.1 to 1.0 mg/mL.

PS/PMMA-CdS hydrodynamic radii, r_h, were determined from a series of multi-angle and multi-concentration dynamic light scattering (DLS) experiments in each solvent. For each DLS measurement, the normalized time correlation function of the electric field was analyzed using a cumulant expansion for pointlike, isotropic particles with a distribution of particle sizes:

$$\left|g(\tau)\right| = \exp[-\overline{\Gamma}\tau + (\mu_2 / 2!)\tau^2 + ...] \quad \textbf{(2.2)}$$

where $\overline{\Gamma}$ is the intensity-weighted mean relaxation rate (first moment), μ_2 is the second moment, and τ is the delay time. $\overline{\Gamma}$ determined at various scattering angles is related to the effective translational diffusion coefficient D_T:

$$\overline{\Gamma} = D_T q^2 \quad \textbf{(2.3)}$$

where the scattering vector, q, depends on the refractive index of the scattering liquid, n, the wavelength of incident light, λ, and the scattering angle, θ, as follows:

$$q = \frac{4\pi n}{\lambda}\sin\left(\frac{\theta}{2}\right) \quad \textbf{(2.4)}$$

Plots of $\overline{\Gamma}$ vs q^2 obtained for each solvent and for various concentrations were found to be linear and pass through the origin in accordance with Eq. 2.3, indicating diffusive relaxation and allowing D_T to be determined from the slope. Representative plots of $\overline{\Gamma}$ vs. q^2 for PS/MIC-CdS in the four solvents and at approximately the same concentration ($c \sim 0.2$ mg/mL) are shown in Figure 2.10a, with different slopes indicating different effective diffusion coefficients D_T in the various solvents.

To account for interparticle interactions in solution, D_T is expressed as a function of concentration:

$$D_T = D_0(1 + k_d c), \tag{2.5}$$

from which the single-particle diffusion coefficient, D_0, is obtained by extrapolation to zero concentration. Plots of D_T vs. c for each solvent system are shown in Figure 2.10b. All plots are shown to be linear with small negative slopes for the THF, chloroform, and toluene systems, and a larger positive slope for the acetone system; the resulting D_0 values are shown in Table 2.2.

The hydrodynamic radii, r_h, of PS/PMMA-CdS in the four solvents (Table 2.2) were calculated from D_0 values using the Stokes-Einstein equation:

$$r_h = \frac{kT}{6\pi\eta D_0} \tag{2.6}$$

where k is the Boltzmann constant, T is the temperature, and η is the solvent viscosity. Similar to r_g values from static light scattering, r_h values are different for each solvent, with a minimum value of r_h = 21 nm for acetone and a maximum value of r_h = 31 nm for toluene. The order of r_h values for PS/PMMA-CdS in the different solvents follows a similar trend to the r_g values, except the order of chloroform and THF are reversed: r_h (acetone) < r_h (THF) < r_h (chloroform) < r_h (toluene). The ratio $\mu_2 / \overline{\Gamma}^2$ from cumulant analysis gives a measure of particle size polydispersity in the various solvents. Similar polydispersities (0.18-0.23) were obtained in all four solvents, and were consistent with polydispersity values determined previously for PS-CdS particles in toluene solutions.[20] In addition, CONTIN analysis of selected autocorrelation functions obtained at relatively low solution concentrations in each solvent (scattering angle of 90°) showed size distributions consistent with a single population of particles (Figure 2.11).

Hydrodynamic radii provide a reasonable estimate for overall PS/PMMA-CdS particle sizes, including both the CdS/PACd core and the solvated PS/PMMA brush layer. The difference $t_b = r_h - r_c$ gives the estimated brush thickness in each solvent (Table 2), where the core radius, r_c = 6.3 nm, is assumed to be constant based on similar aggregation numbers in all solvents. To explain the determined r_h values in terms of PS/PMMA brush conformations, we consider literature values[56, 57] of Flory-Huggins interaction parameters for each of the two chains in the four different solvents: $\chi_{\text{PS-Ace}}$ = 1.1, $\chi_{\text{PS-THF}}$ = 0.474, $\chi_{\text{PS-Chl}}$ = 0.45, $\chi_{\text{PS-Tol}}$ = 0.34, $\chi_{\text{PMMA-Ace}}$ = 0.18, $\chi_{\text{PMMA-THF}}$ = 0.442, $\chi_{\text{PMMA-Chl}}$ = 0.39, $\chi_{\text{PMMA-Tol}}$ = 0.45.

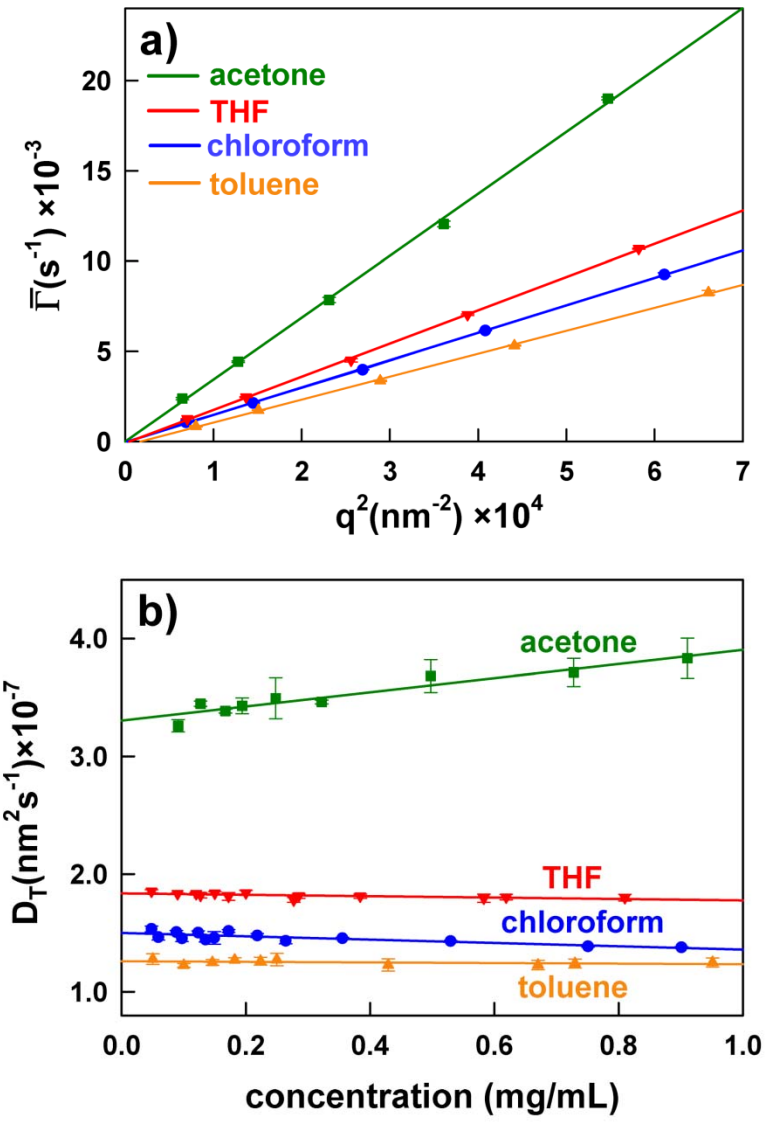

Figure 2.10. Dynamic light scattering (DLS) results for PS/PMMA-CdS. (a) Representative plots of $\bar{\Gamma}$ vs. q^2 for PS/PMMA-CdS dispersions in different solvents of approximately equal concentration (~0.2 mg/mL). (b) Plots of D_T vs. concentration for PS/PMMA-CdS in acetone, THF, chloroform, and toluene.

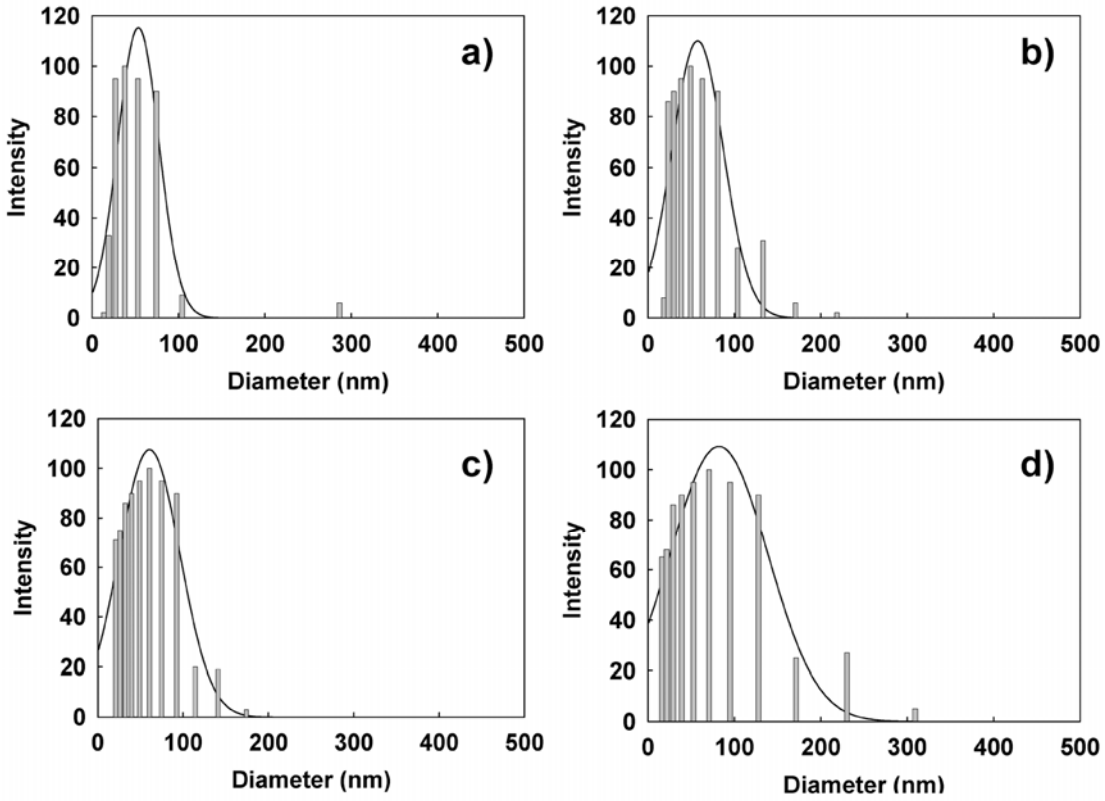

Figure 2.11. Hydrodynamic size distributions from CONTIN analysis of dynamic light scattering (DLS) data for PS/PMMA-CdS in various solvents: (a) acetone, (b) THF, (c) chloroform, and (d) toluene. Results are from representative autocorrelation functions obtained at a 90°-scattering angle and approximately equal concentrations (~0.1 mg/mL).

Of the four solvents, acetone is the only poor solvent for PS ($\chi_{PS\text{-}Ace}$ = 1.1), although it is an extremely good solvent for PMMA ($\chi_{PMMA\text{-}Ace}$ = 0.18). PS chains within the mixed brush are therefore expected to be in a collapsed state in acetone, with the PMMA chains extended into the solvent to maintain steric stabilization of PS/PMMA-CdS (Scheme2. 2). In this conformation of the mixed brush, it is the end-to-end distance of the PMMA chains that will determine the overall brush thickness in acetone (t_b = 15 nm). The percentage extension of the PMMA chains relative to their fully-stretched conformation can therefore be calculated using:

$$\textit{chain extension}\ (\%) = 100 \times (t_b/[aN]) \qquad \textbf{(2.7)}$$

where $N = N_{PMMA}$ = 236 and a is the length of one fully extended repeat unit (a = 0.25 nm). From this calculation, the chain extension of the PMMA chains in acetone is 25 %. ^{1}H NMR of PS/PMMA-CdS in acetone-D6 show distinct resonances from PS phenyl ring protons (not shown), indicating that the collapsed PS chains retain mobility due to some swelling by acetone.

The other three solvents (THF, chloroform, toluene) are good solvents for both PS and PMMA ($\chi < 0.5$), such that both types of chains will adopt extended conformations within the mixed brush layer (Scheme 2.2). Based on the interaction parameters listed above, THF and chloroform are slightly selective for PMMA while toluene is slightly selective for PS. However, despite differences in the relative stretching of PS and PMMA

in these solvents, the degree of polymerization of the PS chains is significantly longer than the PMMA chains (N_{PS} = 296 > N_{PMMA} = 236). We therefore assume that the PS chains will extend further from the core than the PMMA chains in all three solvents, and equate the brush thicknesses t_b in THF, chloroform and toluene to the end-to-end distance of the PS chains. % PS chain extension values were calculated from Eq.2.7 where N = N_{PS} = 296, giving 27 % (THF), 28 % (chloroform), and 34 % (toluene). This order of increase in PS chain stretching within the mixed brush follows the increase in PS solvent quality, as indicated by the interaction parameters: $\chi_{PS\text{-}THF}$ = 0.474, $\chi_{PS\text{-}Chl}$ = 0.45, $\chi_{PS\text{-}Tol}$ = 0.34.

Based on the discussion above, the order of measured hydrodynamic radii (Table 2.2) correlates well with a simple model for solvent-responsive conformational changes within the mixed brush layer of "smart" PS/PMMA-CdS particles (Scheme 2.2). In acetone, the mixed brush adjusts so that the insoluble PS chains are collapsed and the soluble PMMA chains dominate the brush. Based on this conformation, a combination of the relatively short PMMA block length compared to PS and the decrease in steric crowding due to collapse of the PS chains (resulting in the smallest chain stretching % in acetone) explains why r_h of PS/PMMA-CdS is smallest in acetone. In the other three solvents, both blocks are solubilized within the brush and steric crowding increases relative to acetone. With PS in an expanded state, the extension of the longer PS chains determine the brush thickness, and r_h is observed to increase in the order of increasing solvent quality for the PS block (i.e. THF < chloroform < toluene).

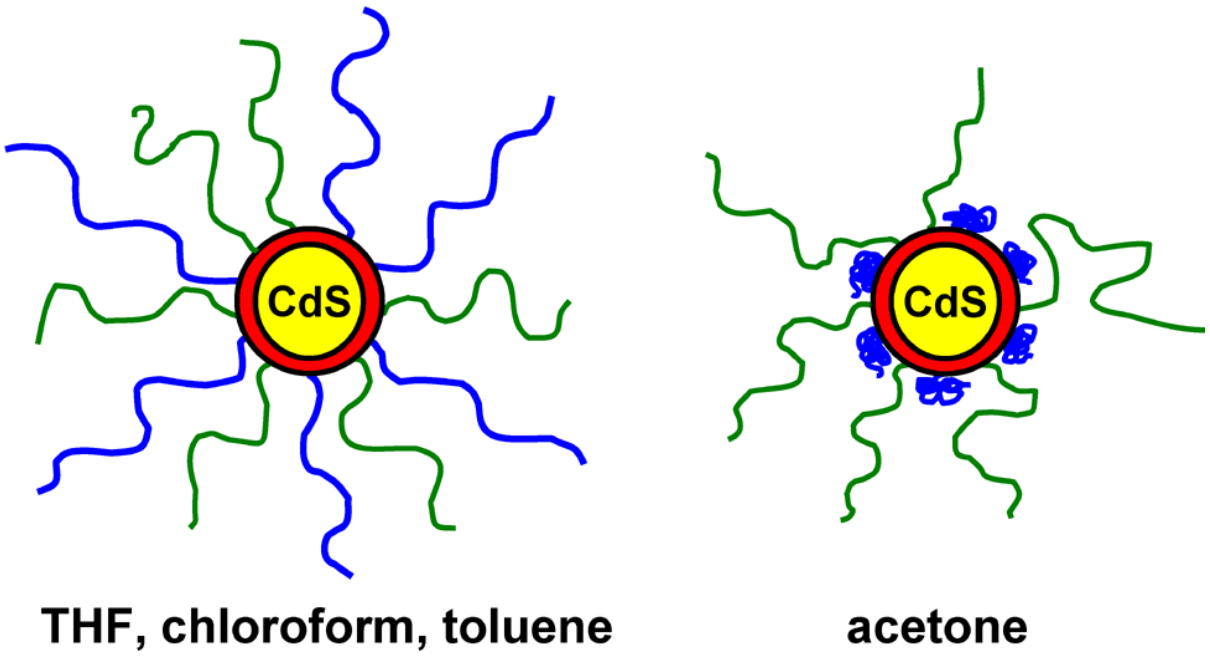

Scheme 2.2. Mixed-brush conformations of environmentally-responsive PS/PMMA-CdS nanoparticles in different solvents based on DLS data.

Further structural information is available from the ratio r_g/r_h obtained from a combination of SLS and DLS. For all solvents, ratio values are similar, in the range of 1.1-1.3, with the most expanded conformation of PS/PMMA-CdS in toluene showing the largest value of r_g/r_h (Table 2.2). The ratios are larger than that predicted for hard spheres, $r_g/r_h = 0.775$, but consistent with ratios reported previously for spherical star-like micelles.[58, 59]

2.3.6. Dispersion of PS/PMMA-CdS in PS and PMMA Homopolymers. The environmentally-responsive mixed brush layer also allowed PS/PMMA-CdS nanoparticles to be dispersed in both PS and PMMA homopolymers. We previously showed that PS-CdS nanoparticles can be easily dispersed in PS homopolymers due to enthalpically-neutral interactions between the QD stabilizing chains and the surrounding polymer;[20, 29] it has also been demonstrated that PS-CdS and PMMA homopolymer undergo fast micron-scale phase separation during spin-coating from toluene solutions, due to the large positive enthalpy of mixing for PS and PMMA.[34] Here, we prepared solutions of both PS/PMMA-CdS / PS and PS/PMMA-CdS / PMMA blends in toluene, and investigated the dispersion of QDs in blend films formed by spin-coating each of these solutions onto glass.

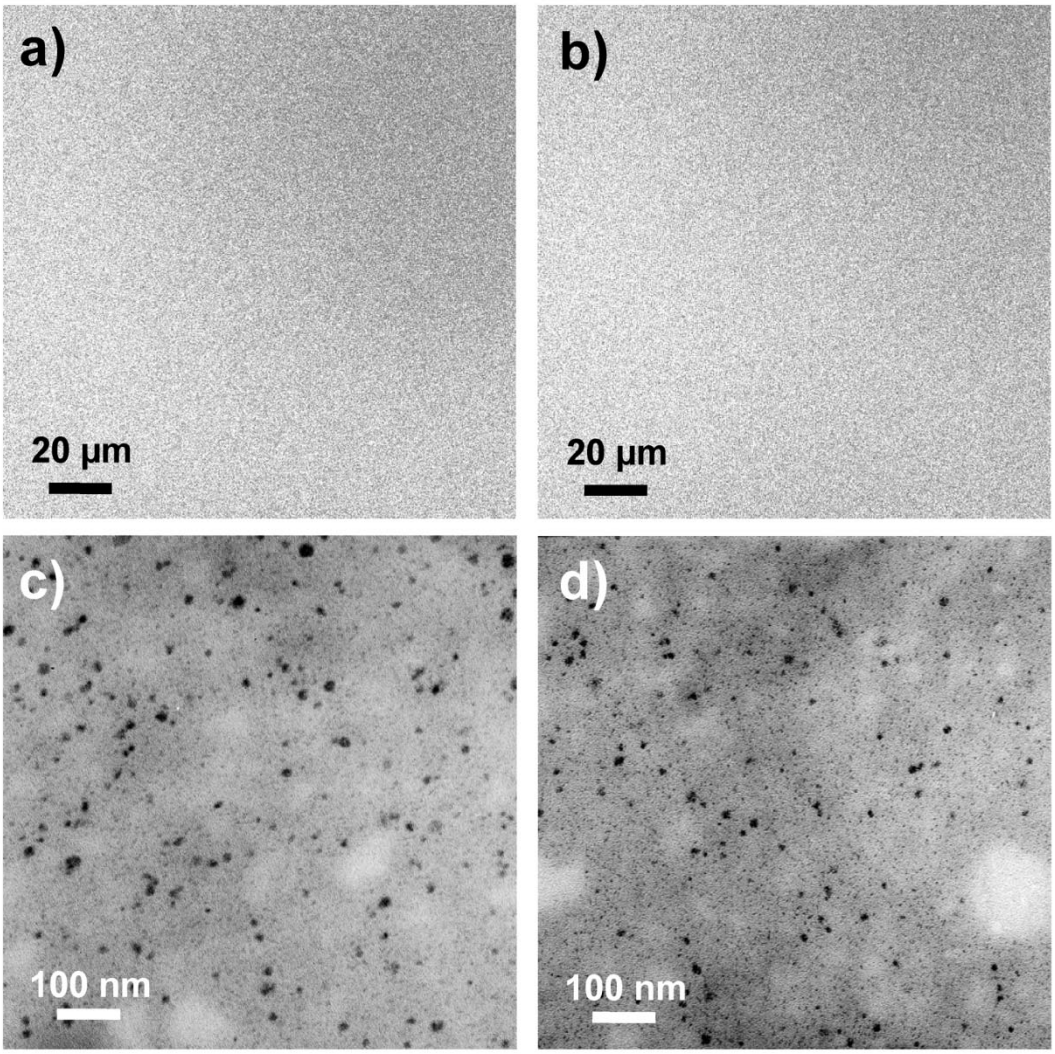

Figure 2.12. PS/PMMA-CdS dispersed in blend films with (a, c) PS and (b, d) PMMA homopolymer by spin-coating from toluene solutions. (a, b) Laser scanning confocal fluorescence microscopy (LSCFM) images of blend films, showing spatially-uniform PL from QDs dispersed in both homopolymers. (c, d) TEM images of microtomed sections of blend films.

Figure 2.12a and 2.12b show laser scanning confocal fluorescence microscopy (LSCFM) images of blend films of PS/PMMA-CdS nanoparticles with PS and PMMA homopolymers, respectively. The spatially homogeneous light colour is due to QD PL, indicating uniform dispersion of PS/PMMA-CdS in both homopolymers on the optical length scale. PL spectra obtained for both films (Figuure 2.13) confirmed that the PL properties of PS/PMMA-CdS colloids were retained upon dispersion in both polymer matrices. TEM of microtomed sections indicate that the QDs were also well dispersed at the nanoscale in both PS (Figure 2.12c) and PMMA (Figure 2.12d) homopolymers. Small, light regions in the TEM images of both films (~100 nm) are attributed to some nanoscale phase separation of the homopolymers (relatively low electron density) from the nanoparticle / homopolymer mixtures.

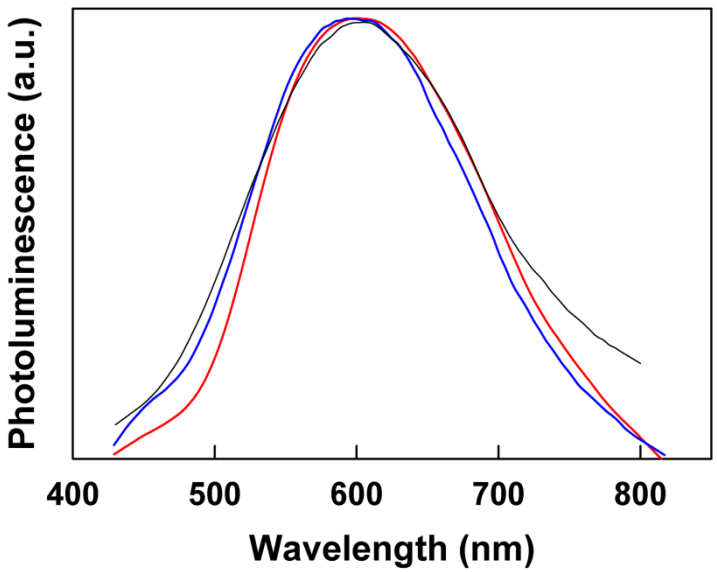

Figure 2.13. Photoluminescence emission spectra (λ_{ex} = 400 nm) of PS/PMMA-CdS dispersed in toluene (black line), a blend film of 30/70 (w/w) PS/PMMA-CdS / PS (blue line) and a blend film of 30/70 (w/w) PS/PMMA-CdS / PMMA (red line).

The observed dispersion of PS/PMMA-CdS in both PS and PMMA homopolymers by spin-coating suggests a low driving force for phase separation of the nanoparticles from either of these mutually incompatible polymers. This is attributed to the conformational response of the mixed brush during spin-coating. When the nanoparticles are blended with PS, the brush conformation will adjust to maximize surface exposure of PS segments; when the nanoparticles are blended with PMMA, the brush will maximize surface exposure of PMMA segments. In both environments, therefore, the PS/PMMA-CdS surface can adopt a conformation to minimize the positive enthalpy of mixing. However, drop-casting the same blend compositions with slow toluene evaporation over 7 days reveals significant micron-scale phase separation between PS/PMMA-CdS and both homopolymers (Figuure 2.14), indicating an overall unfavourable free energy of mixing between PS/PMMA-CdS and both PS and PMMA; this is attributed to a combination of entropic autophobic effects and residual surface exposure of incompatible chain segments. This shows that the demonstrated uniform dispersion of mixed-brush quantum dots in either PS or PMMA homopolymers by spin-coating is due to a combination of relatively small enthalpies of mixing and fast solvent evaporation.

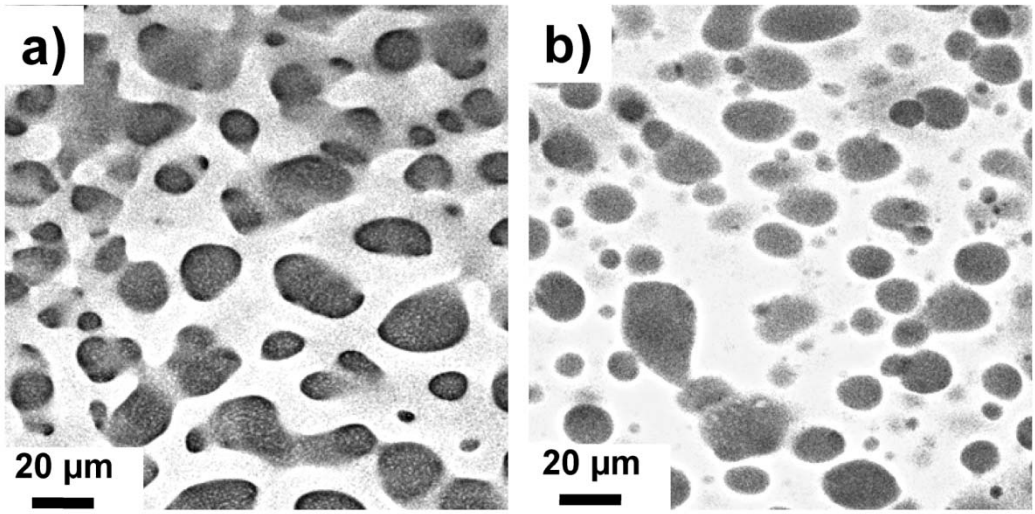

Figure 2.14. Laser scanning confocal fluorescence microscopy (LSCFM) images of blend films of PS/PMMA-CdS with (a) PS and (b) PMMA homopolymers, prepared by drop-casting and slow solvent evaporation over 7 days. Unlike spin-coated films of the same composition (Figure 2.12), micron-scale phase separation is observed between the photoluminescent PS/PMMA-CdS nanoparticle phase and the non-photoluminescent homopolymer phases, suggesting kinetic trapping of uniform PS/PMMA-CdS dispersion in the spin-coated blend films.

2.4. Conclusions

We have prepared the first example of semiconductor quantum dots (QDs) with a mixed PS/PMMA stabilizing brush layer (PS/PMMA-CdS) via the self-assembly of a PS-*b*-PAA-*b*-PMMA triblock copolymer followed by templated growth of cadmium sulfide QDs in the ionic micelle cores. These QDs can be dispersed in solvents with wide-ranging polarities, including acetone, which is a non-solvent for the PS chains. UV-vis and photoluminescence data demonstrate that QD sizes and optical properties are independent of the solvent medium, with demonstrated long-term stability in most solvents. 2D 1H NOESY experiments on PS/PMMA-CdS in THF indicate intimate mixing of PS and PMMA segments, confirming that PS and PMMA chains are statistically distributed within the mixed brush layer. Static light scattering (SLS) of PS/PMMA-CdS indicate that particle molecular weights are nearly identical in the various solvents, showing that the copolymer chains are locked into the mixed brush via kinetic freezing of the poly(cadmium acrylate) layer. A combination of SLS and dynamic light scattering (DLS) show significant changes in r_g and r_h for PS/PMMA-CdS in the various solvents, with r_h values increasing in the order acetone < THF < chloroform < toluene. Changes in hydrodynamic particle size are explained by solvent-responsive conformational changes in the mixed brush layer in order to maintain colloidal stability in different solvent media. In addition, conformational changes in the mixed brush allow PS/PMMA-CdS QDs to be well dispersed in both PS and PMMA homopolymers. Studies on the application of these QDs with mixed polymer brush layers for three-dimensional self-assembly in colloids and polymer blends are discussed in the following chapter.

2.5. References

(1) von Werne, T.; Patten, T. E. *J. Am. Chem. Soc.* **1999,** *121*, 7409.

(2) Farmer, S. C.; Patten, T. E. *Chem. Mater.* **2001,** *13*, 3920.

(3) Carrot, G.; D., R.-H.; Pottier, A.; Degee, P.; Hilborn, J.; Dubois, P. *Macromolecules* **2002,** *35*, 8400.

(4) Ohno, K.; Koh, K.; Tsujii, Y.; Fukuda, T. *Macromolecules* **2002,** *35*, 8989.

(5) Skaff, H.; Ilker, M. F.; Coughlin, E. B.; Emrick, T. *J. Am. Chem. Soc.* **2002,** *124*, 5729.

(6) Sill, K.; Emrick, T. *Chem. Mater.* **2004,** *16*, 1240.

(7) Carrot, G.; Scholz, S. M.; Plummer, C. J. G.; Hilborn, J. G. *Chem. Mater.* **1999,** *11*, 3571.

(8) Corbierre, M. K.; Cameron, N. S.; Sutton, M.; Mochrie, S. G. J.; Lurio, L. B.; Ruhm, A.; Lennox, R. B. *J. Am. Chem. Soc.* **2001,** *123*, 10411.

(9) Potapova, I.; Mruk, R.; Prehl, S.; Zentel, R.; Basche, T.; Mews, A. *J. Am. Chem. Soc.* **2003,** *125*, 320.

(10) Skaff, H.; Emrick, T. *Chem. Commun.* **2003**, 52.

(11) Tadd, E.; Zeno, A.; Zubris, M.; Dan, N.; Tannenbaum, R. *Macromolecules* **2003,** *36*, 6497.

(12) Wang, X.-S.; Dykstra, T. E.; Salvador, M. R.; Manners, I.; Scholes, G.; Winnik, M. A. *J. Am. Chem. Soc.* **2004,** *126*, 7784.

(13) Corbierre, M. K.; Cameron, N. S.; Sutton, M.; Laaziri, K.; Lennox, R. B. *Langmuir* **2005,** *21*, 6063.

(14) Wang, M.; Oh, J. K.; Dykstra, T. E.; Lou, X.; Scholes, G. D.; Winnik, M. A. *Macromolecules* **2006,** *39*, 3664.

(15) Moller, M.; Kunstle, H.; Kunz, M. *Synth. Met.* **1991,** *41-43*, 1159.

(16) Cummins, C. C.; Schrock, R. R.; Cohen, R. E. *Chem. Mater.* **1992,** *4*, 27.

(17) Moffitt, M.; McMahon, L.; Pessel, V.; Eisenberg, A. *Chem. Mater.* **1995,** *7*, 1185.

(18) Forster, S.; Antonietti, M. *Adv. Mater.* **1998,** *10*, 195.

(19) Spatz, J. P.; Herzog, T.; Mossmer, S.; Ziemann, P.; Moller, M. *Adv. Mater.* **1999,** *11*, 149.

(20) Wang, C.-W.; Moffitt, M. G. *Langmuir* **2004,** *20*, 11784.

(21) Zhang, M.; Drechsler, M.; Muller, A. H. E. *Cherm. Mater.* **2004,** *16*, 537.

(22) Bennett, R. D.; Miller, A. C.; Kohen, N. T.; Hammond, P. T.; Irvine, D. J.; Cohen, R. E. *Macromolecules* **2005,** *38*, 10728.

(23) Kang, Y.; Taton, T. A. *J. Am. Chem. Soc.* **2003,** *125*, 5650.

(24) Kang, Y.; Taton, T. A. *Angew. Chem. Int. Ed.* **2005,** *44*, 409.

(25) Kang, Y.; Taton, T. A. *Macromolecules* **2005,** *38*, 6115.

(26) Filali, M.; Meier, M. A. R.; Schubert, U. S.; Gohy, J.-F. *Langmuir* **2005,** *21*, 7995.

(27) Duxin, N.; Liu, F.; Vali, H.; Eisenberg, A. *J. Am. Chem. Soc.* **2005,** *127*, 10063.

(28) Niu, H.; Zhang, L.; Gao, M.; Chen, Y. *Langmuir* **2005,** *21*, 4205.

(29) Wang, C.-W.; Moffitt, M. G. *Langmuir* **2005,** *21*, 2465.

(30) Yusuf, H.; Kim, W.-G.; Lee, D.-H.; Guo, Y.; Moffitt, M. G. *Langmuir* **2007,** *23*, 868.

(31) Yusuf, H.; Kim, W.-G.; Lee, D.-H.; Aloshyna, M.; Brolo, A. G.; Moffitt, M. G. *Langmuir* **2007**, *in press*

(32) Cheyne, R. B.; Moffitt, M. G. *Langmuir* **2005,** *21*, 10297.

(33) Cheyne, R. B.; Moffitt, M. G. *Macromolecules* **2007,** *40*, 2046.

(34) Wang, C.-W.; Moffitt, M. *Chem. Mater.* **2005,** *17*, 3871.

(35) Zhang, Z.; Horsch, M. A.; Lamm, M. H.; Glotzer, S. C. *Nano Lett.* **2003,** *3*, 1341.

(36) Zhang, Z.; Glotzer, S. C. *Nano Lett.* **2004,** *4*, 1407.

(37) Zhang, Z.; Keys, A. S.; Chen, T.; Glotzer, S. C. *Langmuir* **2005,** *21*, 11547.

(38) Vanakaras, A. G. *Langmuir* **2006,** *22*, 88.

(39) Li, D.; Sheng, X.; Zhao, B. *J. Am. Chem. Soc.* **2005,** *127*, 6248.

(40) Shan, J.; Nuopponen, M.; Jiang, H.; Viitala, T.; Kauppinen, E.; Kontturi, K.; Tenhu, H. *Macromolecules* **2005,** *38*, 2918.

(41) Shan, J.; Chen, J.; Nuopponen, M.; Viitala, T.; Jiang, H.; Peltonen, J.; Kauppinen, E.; Tenhu, H. *Langmuir* **2006,** *22*, 794.

(42) Chiu, J. J.; Kim, B. J.; Kramer, E. J.; Pine, D. J. *J. Am. Chem. Soc.* **2005,** *127*, 5036.

(43) Zubarev, E. R.; Xu, J.; Sayyad, A.; Gibson, J. D. *J. Am. Chem. Soc.* **2006,** *128*, 4958.

(44) Zubarev, E. R.; Xu, J.; Sayyad, A.; Gibson, J. D. *J. Am. Chem. Soc.* **2006,** *128*, 15098.

(45) Erhardt, R.; Boker, A.; H., Z.; H., K.; W., P.-H.; Krausch, G.; Abetz, V.; Muller, A. H. E. *Macromolecules* **2001,** *34*, 1069.

(46) Xu, H.; Erhardt, R.; Abetz, V.; Muller, A. H. E.; Goedel, W. A. *Langmuir* **2001,** *17*, 6787.

(47) Erhardt, R.; Zhang, M.; Boker, A.; Zettl, H.; Abetz, C.; Frederik, P.; Krausch, G.; Abetz, V.; Muller, A. H. E. *J. Am. Chem. Soc.* **2003,** *125*, 3260.

(48) Hoppenbrouwers, E.; Li, Z.; Liu, G. *Macromolecules* **2003,** *36*, 876.

(49) Hautekeer, J.-P.; Varshney, S. K.; Fayt, R.; Jacobs, C.; Jerome, R.; Teyssie, P. *Macromolecules* **1990,** *23*, 3893.

(50) Zhong, X. F.; Varshney, S. K.; Eisenberg, A. *Macromolecules* **1992,** *25*, 7160.

(51) Guegan, P.; Cernohous, J. J.; Khandpur, A. K.; Hoye, T. R.; Macosko, C. W. *Macromolecules* **1996,** *29*, 4605.

(52) Henglein, A. *Chem. Rev.* **1989,** *89*, 1861.

(53) Cammas, S.; Harada, A.; Nagasaki, Y.; Kataoka, K. *Macromolecules* **1996,** *29*, 3227.

(54) Vangeyte, P.; Leyh, B.; Auvray, L.; Grandjean, J.; Misselyn-Baudin, A.-M.; Jerome, R. *Langmuir* **2004,** *20*, 9019.

(55) Voets, I. K.; de Keizer, A.; Cohen Stuart, M. A.; de Waard, P. *Macromolecules* **2006,** *39*, 5952.

(56) Xuan, Y.; Peng, J.; Cui, L.; Wang, H.; Li, B.; Han, Y. *Macromolecules* **2004,** *37*, 7301.

(57) Shiomi, T.; Kuroki, K.; Kobayashi, A.; Nikaido, H.; Yokoyama, M.; Tezuka, Y.; Imai, K. *Polymer* **1995,** *36*, 2443.

(58) Forster, S.; Zisenis, M.; Wenz, E.; Antonietti, M. *J. Chem. Phys.* **1996,** *24*, 9956.

(59) Moffitt, M.; Eisenberg, A. *Macromolecules* **1997,** *30*, 4363.

CHAPTER 3

"Smart" Self-Assembled Quantum Dots Regulate and Stabilize Structure in Phase-Separated Polymer Blends

---

3.1. Introduction

Colloidal semiconductor quantum dots (QDs) and metal nanoparticles are widely recognized as potential functional elements in polymer-based devices, due to their range of interesting optical and electronic properties. For many applications, engineering specific collective properties in polymer/nanoparticle composites will require controlled spatial organization of both organic and inorganic components on multiple length scales.[1-9] Several strategies for the dispersion and ordering of QDs and metal nanoparticles within polymers have been demonstrated, starting with hybrid building blocks consisting of an inorganic nanoparticle core and an external polymer brush stabilizing layer. Polymer-stabilized nanoparticles have been shown to undergo self-assembly in block copolymer films,[2-4] at the air-water interface,[5, 6] in aqueous media,[1, 7, 8] and in phase-separating polymer blends,[9,10] leading to a wide range of hierarchical assemblies.

More recently, inorganic nanoparticles coated with mixed brushes of two different types of homopolymer chains have received considerable attention.[11-16] In response to various external stimuli, these "smart" particles undergo changes in surface properties via conformational rearrangements of the mixed polymer brush, introducing new possibilities for three-dimensional (3D) self-assembly into complex and controllable superstructures.[16] In Chapter one, we have described the synthesis of cadmium sulfide (CdS) QDs with mixed polystyrene/poly(methyl methacrylate) (PS/PMMA) brush layers (designated PS/PMMA-CdS, via micellization of a polystyrene-*b*-poly(acrylic acid)-*b*-poly(methyl methacrylate) (PS-*b*-PAA-*b*-PMMA) triblock copolymer, followed by growth of QDs in the PAA cores.[17] Based on static and dynamic light scattering results, the stable mixed

brush layers of the "smart" QDs were found to undergo changes in conformation in response to different solvent and polymer environments, allowing them to be dispersed in solvents of wide-ranging polarities, and in films of either PS or PMMA homopolymers.

The mesoscale or microscale phase morphology of immiscible homopolymer blends plays a critical role in the performance of polymer-based photovoltaic and light-emitting devices,[18] as well as being of general interest for surface patterning applications.[9, 19] Both types of applications can be severely limited by the thermodynamic tendency of blend films to undergo uncontrolled phase coarsening upon heating, driven by a combination of interfacial tension between polymer components and preferential interactions at the surface and substrate. Various studies demonstrate that phase morphologies can be regulated and stabilized by additives such as random copolymers,[20-24] block copolymers[23,25] and inorganic nanoparticles,[26-29] generally known as compatibilizers, which tend to mitigate unfavorable interactions between immiscible blend components, usually by segregating at the polymer/polymer interface. To date, the role of added compatibilizers has been limited to lowering the interfacial tension or enhancing interfacial adhesion. However, as pointed out by Chung *et al*.,[28] the possibility of using absorbing and photoluminescent QDs as compatibilizers in polymer blend-based devices could lead to dual-functional nanoparticles which both stabilize the blend structure and impart specific optical properties to the final device.

In this chapter, we show that CdS QDs coated with mixed polymer brushes (PS/PMMA-CdS) (described in Chapter 2) are driven to the polymer/polymer interface of phase-separating blends of PS and PMMA homopolymers during spin-coating, resulting in self-assembled photoluminescent rings of PS/PMMA-CdS encapsulating the dispersed

PMMA phase. The directed organization of QDs arises from an overall lowering of interfacial tension between blend components due to the mixed polymer surface layer of PS/PMMA-CdS. Most importantly, we show that the interfacial segregation of mixed brush-stabilized QDs regulates the phase separation process during spin-coating, and dramatically stabilizes the domain structure during subsequent annealing. This provides the first example of QDs acting as both compatibilizers and photoluminescent elements in a polymer blend, demonstrating the potential for expanding the role of QDs in polymer-based devices via appropriate design of the external polymer layer. This work also highlights unique opportunities for self-assembly of QDs into complex architectures within phase-separating polymer blend films via spontaneous interfacial segregation.

3.2. Experimental

3.2.1. Preparation of Spin-Coated Blend Films. Stock solutions of PS/PMMA-CdS, PS homopolymer, and PMMA homopolymer were prepared by co-dissolving appropriate quantities of each component in spectroscopic grade toluene to polymer concentrations of 6 wt%. The stock solutions were stirred for 4 h and left to stand overnight in the dark to equilibrate. Blend solutions of the desired composition were then prepared by filtering measured amounts of each stock solution through two membrane filters (0.45 μm nominal pore size) connected in series into glass sample vials. For all blends, the ratio of PS homopolymer to PMMA homopolymer was 30:70 (w:w), while the weight percentage of PS/PMMA-CdS QDs relative to the total polymer weight varied (0, 3, 10, 20, or 30%).

Before spin-coating, 18×18 mm glass microscope coverslips were cleaned by 30 min sonication in spectroscopic grade methanol, chloroform and toluene, successively, then dried overnight under vacuum at 70 ºC. Various blend films were obtained by depositing one drop of blend solution on the glass substrate and spin-coating at 3000 rpm for one minute. The blend films were then dried overnight under active vacuum at 25 ± 1 ºC to remove any residual solvent. For annealing experiments, blend films were annealed in a vacuum oven at 150 ± 1 ºC. After a designated time, annealed films were quenched in cold de-ionized water immediately after removal from the vacuum oven. To test reproducibility, several films were prepared for each blend composition and annealing period.

Some of the blend films were washed in selective solvents prior to atomic force microscopy (AFM) imaging, in order to determine the lateral distribution of the various phases. To selectively remove the PS phase, films were placed in a Petri dish containing ~20 mL cyclohexane and stirred for ~20 min, followed by washing several times with clean solvent. Using an identical procedure, acetic acid (99.7%) washing was used to selectively remove the PMMA phase. After allowing the washed films to air-dry under ambient conditions for 4 h, the films were dried overnight under active vacuum at 25 ± 1 ºC overnight before AFM imaging.

3.2.2. Atomic Force Microscopy (AFM). A Veeco AFM Instrument equipped with a Veeco tip (Nanoprobe-MLCT-EXMT-A) running in contact mode was used to obtain AFM images. The effect of vibration was minimized by a vibration-resistant

housing on a vibration isolation platform maintained at 80 psi. Each film was imaged several times at different locations on the substrate.

3.2.3. Laser Scanning Confocal Fluorescence Microscopy (LSCFM). Laser scanning confocal fluorescence microscopy measurements were carried out on a Zeiss LSM 410 equipped with an Ar/Kr laser. All films were excited at 488 nm, using a band-pass 485 ± 20 nm line selection filter and a FT 510 dichroic beam splitter. A long-pass 515 nm emission filter was employed such that only light above 515 nm reached the PMT. A Zeiss Plane-Aprochromat 63 x oil-immersion objective was employed. A pinhole diameter of 1.31 Airy Units was used for all measurements, resulting in an optical section thickness of 0.75 μm FWHM. Control films containing no PS/PMMA-CdS showed no significant detector signal under these conditions, confirming that light intensity in images of films containing PS/PMMA-CdS was due to QD emission.

3.2.4. Transmission Electron Microscopy (TEM). TEM was performed on a Hitachi H-700 electron microscope, operating on an accelerating voltage of 75 keV. Blend films were embedded in an Epon resin, and then ~50 nm-thick sections were obtained with a diamond knife on Reichert UltraCut E ultra-micotome. The thin sections were then placed on carbon/Formvar-coated 300 mesh copper grids for imaging.

3.2.5. Photoluminescence Measurements. Static photoluminescence (PL) measurements were recorded on an Edinburgh Instruments FLS 920 instrument equipped with a Xe 450W arc lamp and a red-sensitive PMT (R928-P). All spectra were obtained

using an excitation wavelength of 400 nm and a 420 nm bandpass filter, and recorded at 1 nm spectral resolution. For the PL measurements of blend films, back-face excitation with an incidence angle of 30º to the substrate normal was employed.

3.2.6. Analysis of AFM Surface Features. To determine the heights and diameters of surface features after various selective solvent treatments, at least four different regions of each film were imaged. Feature topologies were measured using the AFM software (SPM lab), with more than 100 individual domains were measured for each sample.

To determine surface correlation lengths, Λ_m, radial average plots of fast Fourier transform (FFT) power spectra from AFM images were obtained; for each FFT spectrum, 25 different line profiles were averaged to produce plots of intensity $I(q)$ vs. scattering vector q. The dominant wave vector q_m was determined from a Gaussian fit to the main scattering peak, from which the correlation length was calculated using $\Lambda_m = 2\pi / q_m$.

3.3. Results and Discussion

The synthesis and characterization of cadmium sulfide (CdS) QDs with mixed polystyrene/poly(methyl methacrylate) (PS/PMMA) stabilizing layers, designated PS/PMMA-CdS (Scheme 3.1), have been described in the chapter 2.[17] From the UV-vis absorption threshold, λ_{thresh} = 512 nm, a QD diameter of ~7 nm is determined, corresponding to the high end of the QD size distribution. From static light scattering analysis, an average CdS QD is surrounded by a collapsed layer of ~200 poly(cadmium

acrylate) (PACd) chains, which is covalently attached to an external brush layer consisting of an equal number of randomly-distributed PS and PMMA chains (~200 chains of each type), with molecular weights M_n = 30800 g/mol and M_n = 23600, respectively; from the measured aggregation number and estimated core size (QD +

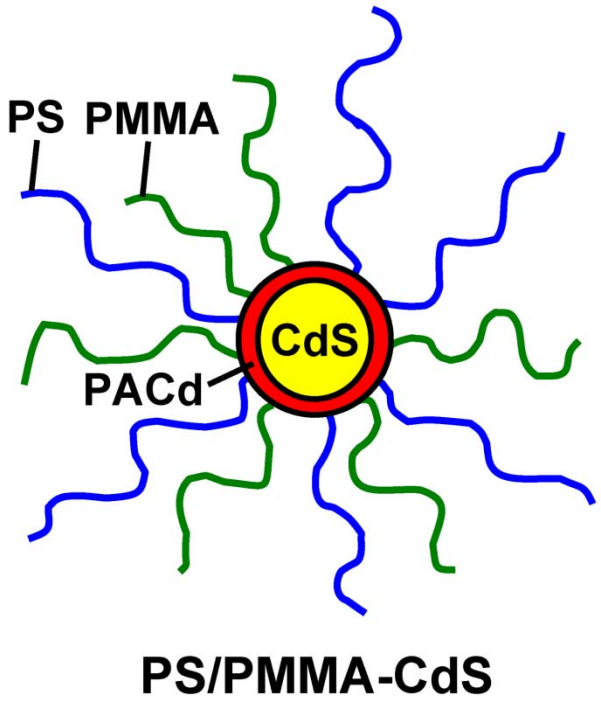

Scheme 3.1. Structure of PS/PMMA-CdS Mixed Brush-Stabilized QDs

PACd), the surface density of the mixed brush is ~0.8 chains/nm^2.[17] The overall hydrodynamic diameter of PS/PMMA-CdS QDs in toluene was determined by dynamic light scattering (DLS) to be 62 nm.

Blend solutions of PS and PMMA homopolymers of composition PS:PMMA = 30:70 (w/w) were obtained by mixing stock solutions of each component in toluene. PS homopolymer (M_n = 130000 g/mol, M_w/M_n = 1.01) was prepared in our lab by anionic polymerization, and PMMA homopolymer (M_w = 120000 g/mol) was purchased from Aldrich. Various quantities of PS/PMMA-CdS QDs dispersed in toluene were added to obtain a series of blend solutions with a constant PS:PMMA ratio (30:70) and various PS/PMMA-CdS contents: 0, 10, 20, 30% (w/w), relative to the total polymer mass. Blend films were then obtained by spin-coating each solution onto clean glass substrates at 3000 rpm. Blend film thicknesses determined from AFM scratch tests were between 120 nm and 200 nm.

The morphologies of thin PS:PMMA blend films after spin-coating and with subsequent annealing have been widely investigated;[30-35] results for our control films without added PS/PMMA-CdS are consistent with previous studies. Figure 3.1 shows atomic force microscopy images (AFM, Veeco Instruments) of PS:PMMA films immediately after spin-coating (a,e), and following 4 h (b,f), 8 h (c,g) and 24 h (d,h) annealing at 150 °C. In Figure 3.1e-h, the films were washed with cyclohexane prior to AFM imaging, selectively dissolving the PS phase and allowing PS and PMMA domains to be identified. Comparing Figure 3.1a and 3.1e, it is apparent that the spin-coated blend morphology (no annealing) consists of small PMMA islands protruding above a continuous layer of PS. Selectively dissolving the PMMA phase with acetic acid was found to remove the entire film, including the PS phase, from the glass (not shown); this indicates that the PMMA islands are attached to a continuous PMMA wetting layer at the substrate (Figure 3.1i, *i*), as previously reported.[31, 33, 35]

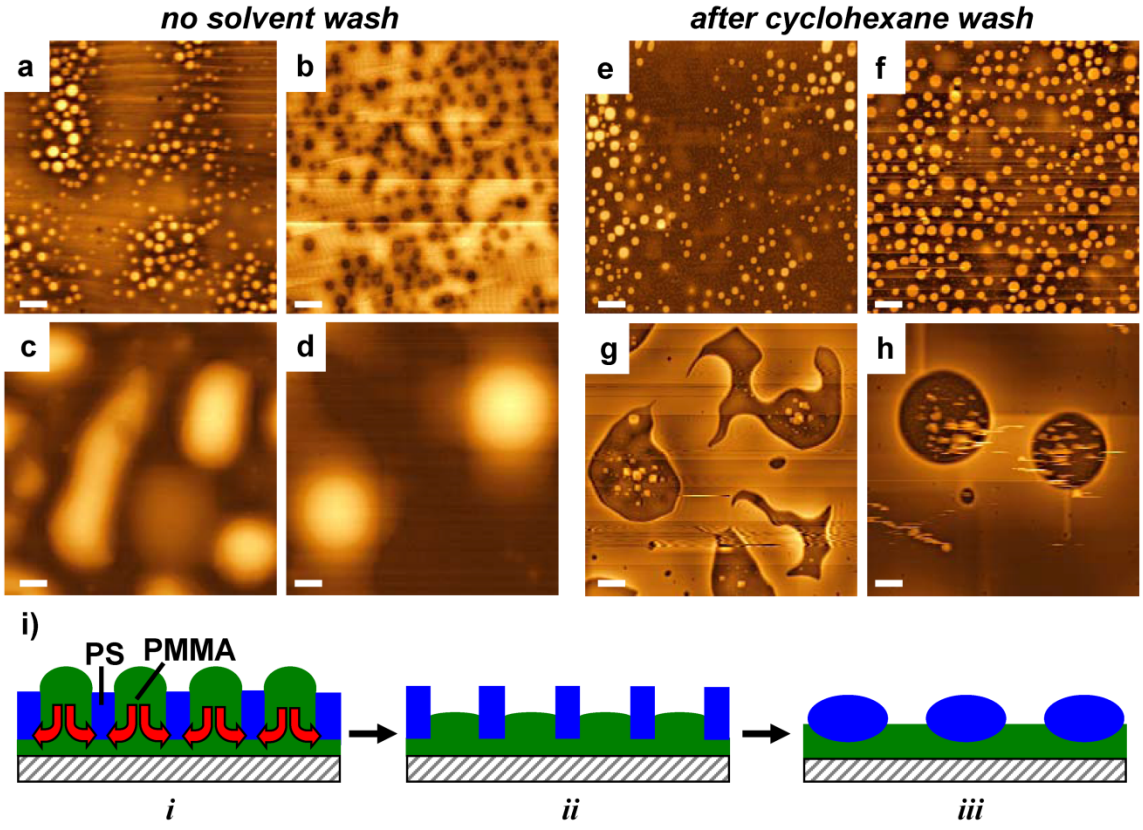

Figure 3.1. Atomic force microscopy (AFM) images of neat PS:PMMA (30:70) blend films for various periods of annealing at 150 ºC following spin-coating. In a-d), films were imaged with no selective solvent washing; in e-h), films were washed with cyclohexane to remove the PS phase. a,e) 0 h annealing; b,f) 4 h annealing; c,g) 8 h annealing; d,h) 24 h annealing. All scale bars represent 2 μm. Part i) shows a schematic (not to scale) of the PS and PMMA phase distributions following spin-coating (*i*) and for different stages of phase coarsening (*ii*, *iii*), as described in text.

The morphology of spin-coated PS:PMMA blends is the result of a surface-oriented phase separation process, which becomes trapped in a non-equilibrium state by fast solvent evaporation. Annealing the neat PS:PMMA films thus resulted in dramatic changes in the film structure, as the system evolved in the direction of a more favorable free energy state. First, the island morphology rapidly transformed into a pitted structure (Figure 3.1b and 3.1f) as the protruding PMMA domains drained into the continuous PMMA bottom layer (Figure 3.1i, *ii*). Next, rupture of the PS top layer occurred due to unfavorable interactions between PS and PMMA (Figure 3.1c and 3.1g). Subsequent phase coarsening resulted in tall (~500 nm) circular PS droplets (Figure 3.1d and 3.1h) resting on top of a bottom layer of PMMA (Figure 3.1i, *iii*).

Figure 3.2a-d shows AFM data of spin-coated PS:PMMA (30:70) blends containing 10% PS/PMMA-CdS QDs.[36] The series of images represents different selective solvent treatments following spin-coating, from which the lateral distribution of the various phases were determined. Comparison of Figure 3.2a (no solvent wash), Figure 3.2b (cyclohexane wash, PS removal), and Figure 3.2c (acetic acid wash, PMMA removal) indicates a morphology consisting of PMMA islands within a PS matrix, similar to the neat PS:PMMA blend. Removal of both PS and PMMA phases (cyclohexane then acetic acid wash) shows the location of the PS/PMMA-CdS QDs within the ternary blend (Figure 3.2d): a clear distribution of free-standing rings reveals that the PS/PMMA-CdS

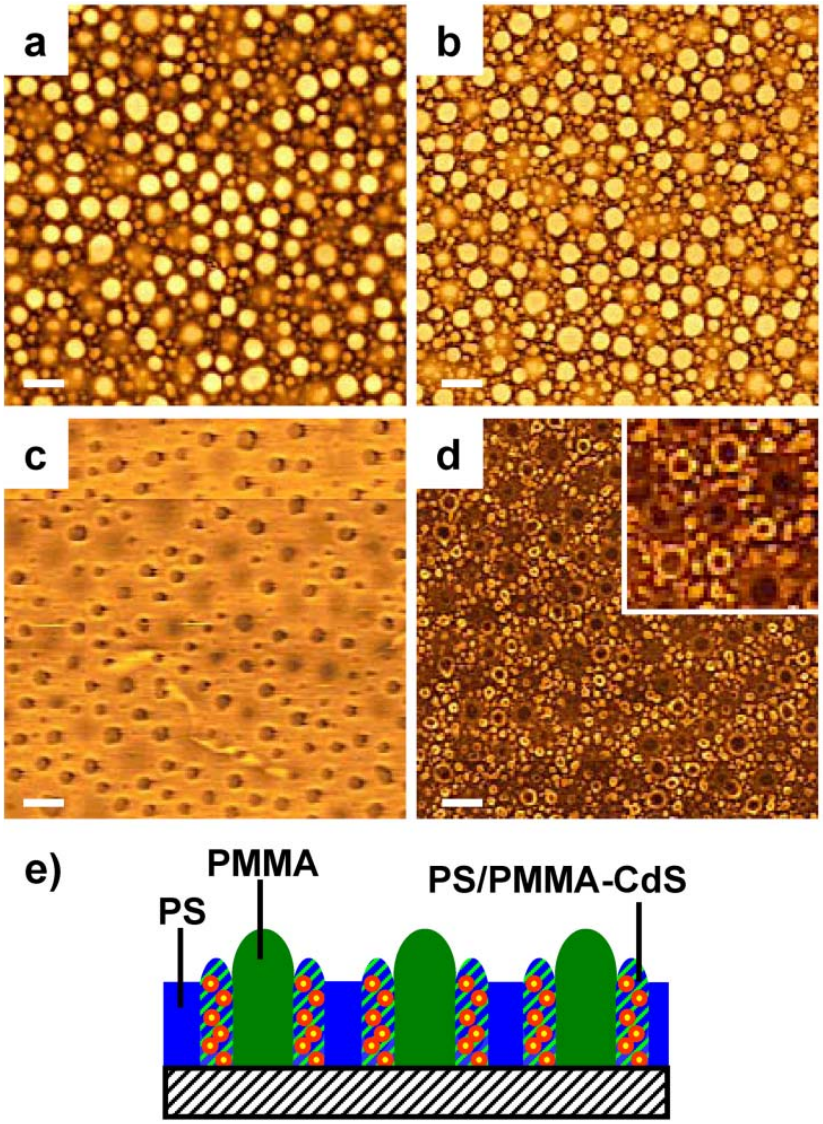

Figure 3.2. Atomic force microscopy (AFM) images of PS:PMMA (30:70) blend films with 10% PS/PMMA-CdS QDs following spin-coating: a) film without solvent washing; b) film washed with cyclohexane to remove the PS phase only; c) film washed with acetic acid to remove the PMMA phase only; d) film washed with cyclohexane then acetic acid to remove both the PS and PMMA phases; remaining rings of PS/PMMA-CdS indicate interfacial self-assembly of QDs during spin-coating. All scale bars represent 2 μm; the dimensions of inset to d) are 5 μm x 5 μm. Part e) shows a schematic (not to scale) of phase distributions in the spin-coated film with relative heights of the PS, PMMA and PS/PMMA-CdS phases.

QDs self-assembled at the PS/PMMA interface during spin-coating, forming an encapsulating phase surrounding the PMMA islands.

From topographic analysis of the AFM images in Figure 3.2 (not shown), the heights of the three phases relative to glass were determined. AFM film topologies before and after washing with cyclohexane show the average height of the PS matrix to be ~70 nm, compared to ~130 nm for the PMMA islands. After removal of both PS and PMMA homopolymers, the remaining PS/PMMA-CdS rings have an intermediate height of ~85 nm. These relative heights are explained by the effect of different affinities of the three components for the solvent during spin-coating, with PS having the highest affinity for toluene and PMMA having the lowest.[31] Following phase separation, the PS-rich phase will contain the most solvent, and will therefore collapse to a level below that of the other two phases when the last of the toluene evaporates; this leaves a topology of relatively tall PMMA islands surrounded by PS/PMMA-CdS rings of intermediate height. We note that solvent swelling of the PS phase, and the relative increase in its volume fraction during spin-coating, also explains why PS constitutes the matrix phase in the spin-coated films, despite PMMA being the major polymer component.

Another marked effect of adding 10% PS/PMMA-CdS QDs to the spin-coated blends is the absence of a PMMA wetting layer at the glass substrate, in contrast to the phase distribution in the neat blend. This is most evident from AFM data after selective solvent treatment: washing the blend film with acetic acid (Figure 3.2c) was found to remove the PMMA domains while leaving the PS matrix intact, indicating that PS does not rest on top of a bottom layer of PMMA. A possible explanation is that, in the early stages of spin-coating when sufficient toluene is still present, PS/PMMA-CdS QDs may

partition between the PS-rich and PMMA-rich phases. As a result, the non-polar styrene segments from PS/PMMA-CdS would lower the affinity of the PMMA phase for the polar glass substrate. Figure 3.2e summarizes the blend morphology determined from AFM data in Figure 3.2a-d, with PS, PMMA, and PS/PMMA-CdS regions each spanning the entire film.

The localization of PS/PMMA-CdS QDs at the PS/PMMA interface during spin-coating is a function of their mixed polymer brush surface layer, which governs nanoparticle interactions with the surrounding environment. QD segregation is observed to be complete on the time scale of spin-coating, in contrast to the study of Chung *et al*. in which interfacial self-assembly of surface-modified silica nanoparticles occurred during subsequent annealing.[28] To a simple approximation, the exterior of PS/PMMA-CdS QDs resembles a poly(styrene-*co*-methyl methacrylate) random copolymer, consisting of an isotropic distribution of styrene and methyl methacrylate segments. The location of a polymer 3 in a phase-separated mixture of polymer 1 (dispersed phase) and polymer 2 (matrix phase) has been described by Hobbs *et al*.[37] using spreading coefficients λ_{31}, and λ_{13}, defined as

$$\lambda_{31} = \gamma_{12} - [\gamma_{31} + \gamma_{23}]; \; \lambda_{13} = \gamma_{23} - [\gamma_{31} + \gamma_{12}] \qquad (\mathbf{3.1})$$

where γ_{ij} are interfacial tensions between components i and j. If $\lambda_{31} > 0$ and $\lambda_{13} < 0$, then polymer 3 will form a shell encapsulating polymer 1, whereas polymer 3 will tend to form a separate dispersed phase if λ_{31} and λ_{13} are both negative. When polymer 3 is a random copolymer made up of repeat units of polymers 1 and 2, Lee *et al*. have used a binary interaction model to show that encapsulation of the dispersed phase is strongly

favoured,[21] in agreement with experimental evidence.[21, 24] The mixed polymer surface layer of PS/PMMA-CdS QDs thus directs their self-assembly at the PS/PMMA interface, driven by an overall decrease in the interfacial tension of blend components.

We note that this simplified picture, based on binary enthalpic interactions between pairs of PS and PMMA segments, does not include possible entropic "dry brush" effects, which can also play an important role in determining the segregation of polymer brush-coated nanoparticles in block copolymers and homopolymer matrices.[38] In our previous work on QDs coated with *homogeneous* PS brush layers with molecular weight and surface density similar to the mixed brush particles considered here,[39] we found that the QDs localized within the PS phase of PS/PMMA polymer blends during solvent evaporation, rather than segregating to the polymer/polymer interface; as well, in PS homopolymers of various molecular weights, the PS-coated QDs remained well dispersed even after 8 days of annealing, with no evidence of autophobic phase separation, except at extremely high nanoparticle loadings (50 wt%).[39] This suggests that the interfacial segregation observed in the present system is primarily due to the mixture of segments in the brush layer, rather than to "dry brush" effects. However, entropic effects should be further considered in future work, by investigating the influence of the mixed brush density and the molecular weights of brush and homopolymer chains on interfacial segregation.

Annealing the spin-coated blend films for various times at 150°C reveals a dramatic stabilizing effect of 10% PS/PMMA-CdS QDs on the polymer blend

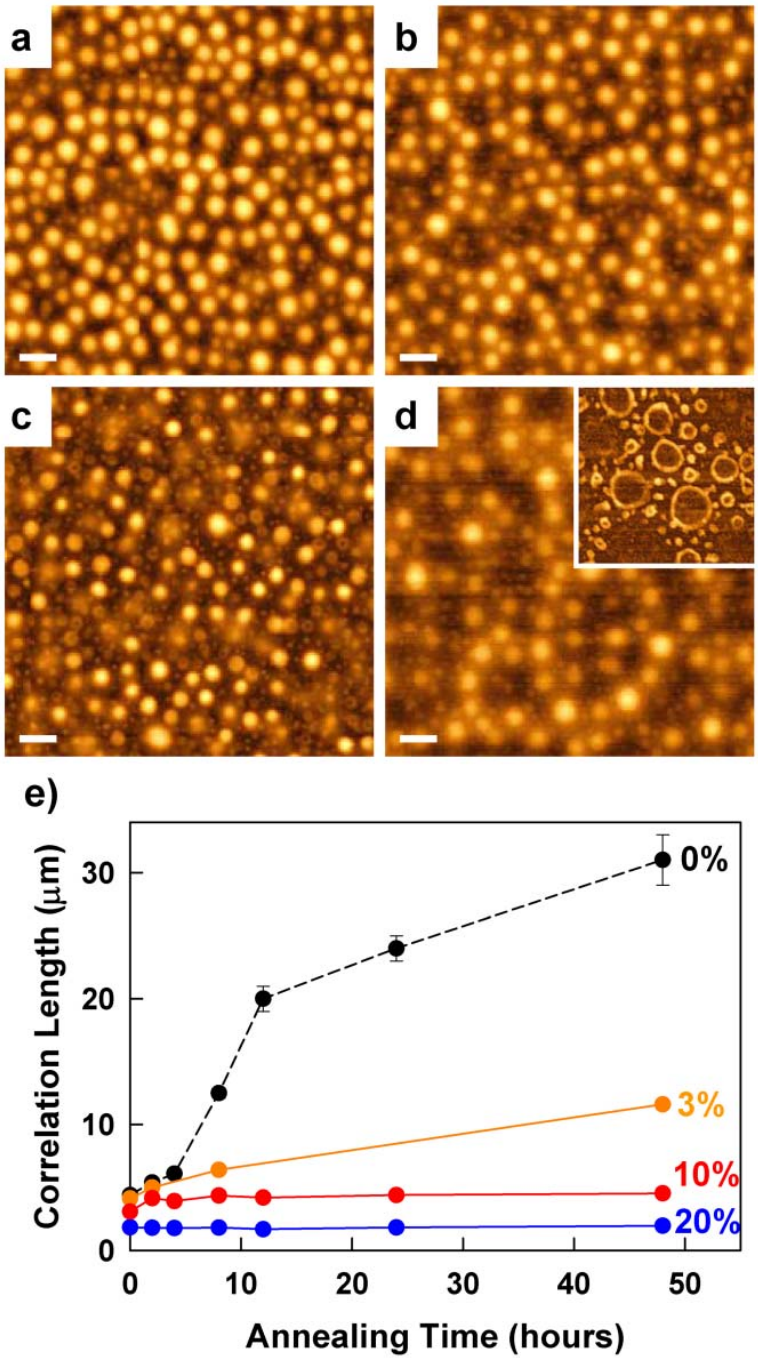

Figure 3.3. Atomic force microscopy (AFM) images of PS:PMMA (30:70) blend films with 10% added PS/PMMA-CdS QDs for various periods of annealing at 150 ºC following spin-coating: a) 4 h annealing; b) 8 h annealing; c) 12 h annealing; d) 24 h annealing. Inset to d) shows film washed with cyclohexane then acetic acid to reveal the distribution of PS/PMMA-CdS QDs. All scale bars represent 2 μm; the dimensions of inset to d) are 5 μm x 5 μm. e) Plots of the surface correlation length, Λ_m, vs. annealing time for different PS/PMMA-CdS QD contents. Λ_m determined from fast Fourier transforms (FFT) of AFM images, as described in the text.

morphology (Figure 3.3a-d). Compared to the surface topology immediately after spin-coating (Figure 3.2a), the distribution and size of the PMMA islands remain constant during annealing. This is in marked contrast to the rapid phase inversion and domain coarsening observed for the neat PS:PMMA blend films (Figure 3.1). Washing the annealed films with cyclohexane and acetic acid shows that the PS/PMMA-CdS QDs remain localized at the PS/PMMA interface throughout the annealing process (Figure 3.3d, inset).

The phase coarsening of blend films with different PS/PMMA-CdS QD contents was quantified via fast Fourier transforms (FFT) of AFM surface morphologies. From the dominant wave vectors, q_m, of FFT-AFM power spectra, the correlation lengths of the surface morphologies, defined as $\Lambda_m = 2\pi / q_m$, were determined for various annealing times (Figure 3e). For the control PS:PMMA blend (0% PS/PMMA-CdS), the plot of Λ_m vs. t shows a large increase in Λ_m over the 48 h annealing period, with three distinct growth regions associated with the various stages of surface morphology evolution observed in Figure 3.1. By comparison, when 3% PS/PMMA-CdS is added to the blend, the coarsening process is slowed significantly, with a relatively small increase in Λ_m over 48 h. Moreover, for the 10% and 20% PS/PMMA-CdS blends, the spin-coated morphologies are found to be pinned by the added QDs, with Λ_m values for these films remaining constant throughout the annealing process (with the exception of a very small initial increase in the 10% PS/PMMA-CdS film). This stabilizing effect is consistent with a decrease in interfacial tension caused by the localization of PS/PMMA-CdS QDs during

spin-coating, which lowers the driving force for phase coarsening during annealing. In addition, the absence of a PMMA wetting layer in the QD-containing blends should provide kinetic stabilization relative to the neat blends, in which the first stage of phase coarsening is the fast hydrodynamic flow of PMMA islands into the connected PMMA bottom layer (Figure 3.1).

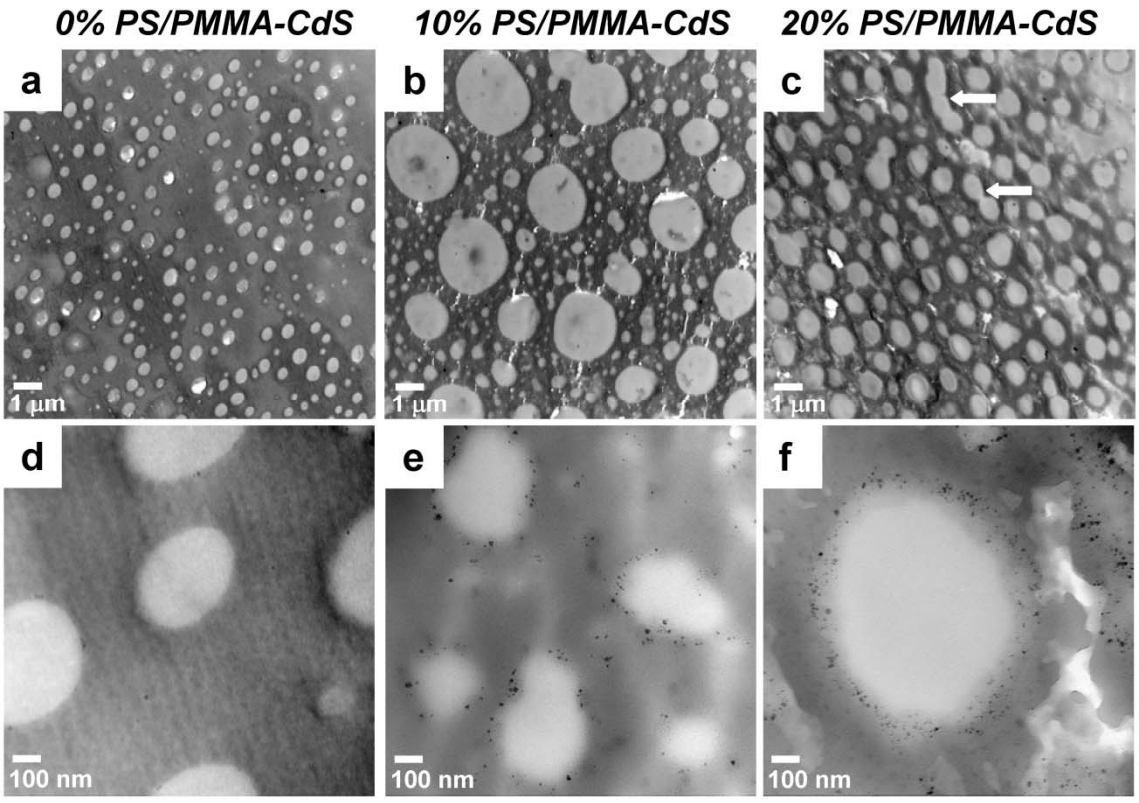

Figure 3.4. Transmission electron microscopy (TEM) images of parallel sections of PS:PMMA (30:70) blend films with a,d) 0%, b,e) 10% and c,f) 20% added PS/PMMA-CdS QDs.

Along with imparting thermal stability during annealing, the interfacial segregation of PS/PMMA-CdS QDs also regulates the domain morphology during spin-coating. The effect of different PS/PMMA-CdS QD contents on blend morphologies immediately following spin-coating is illustrated by transmission electron microscopy (TEM, Hitachi H-700) of microtomed sections cut parallel to the plane of the films (Figure 3.4). For the neat blend (0% PS/PMMA-CdS, Figure 3.4a), the internal film morphology consists of small PMMA domains (white), with mean diameter ~400 nm, in a matrix of PS (dark grey). With the addition of 10% PS/PMMA-CdS QDs (Figure 3.4b), the PMMA domain size actually increases relative to the control blend, despite a lowering of interfacial tension. This can be understood in terms of PS/PMMA-CdS QDs preventing accumulation of PMMA at the substrate, as discussed above, which will increase the amount of PMMA in the PS matrix, and thus the domain size, relative to the neat blend. Size distribution analysis reveals a clearly bimodal distribution of PMMA domains in the 10% PS/PMMA-CdS blend (Figure 3.5), with mean sizes of ~400 nm and ~1600 nm for the two separate domain populations.[40] The regulating effect of PS/PMMA-CdS QDs on phase separation is evident by comparison of the 10% and 20% PS/PMMA-CdS blends (Figure 4b and 4c). With increased PS/PMMA-CdS QD content, the PMMA domains show a mean diameter of ~700 nm and are significantly less polydispersed than the 10% PS/PMMA-CdS blend; notably, the population of large domains (>1000 nm) is no longer present, indicating that domain coalescence is suppressed. We also observe several linear PMMA regions in the 20% PS/PMMA-CdS blend (Figure 3.4c, white arrows) which appear to be trapped in the process of pinching into circular domains, suggesting the remnants of a percolation-to-cluster transition from

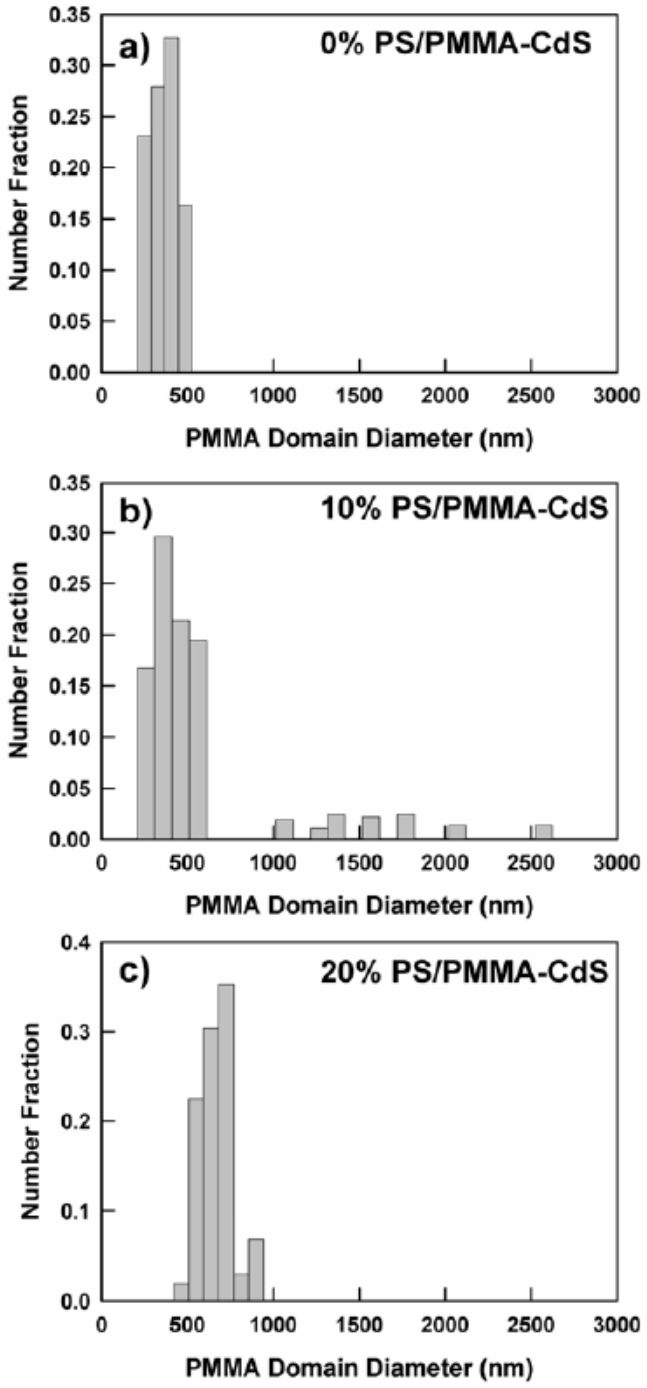

Figure 3.5. PMMA domain size distributions from transmission electron microscopy (TEM) images of parallel sections of PS:PMMA (30:70) blend films with different amounts of PS/PMMA-CdS: a) 0% b) 10% and c) 20%.

a bicontinuous phase structure. The difference between the film morphologies in the 10% and 20% PS/PMMA-CdS blends can be explained by either a decrease in the rate of domain coarsening or a shift in the thermodynamic boundary for phase-separation, such that earlier domain structures are trapped by solvent evaporation as the PS/PMMA-CdS content is increased. From these results, therefore, it appears that the addition of mixed brush-coated QDs to polymer blend films should provide routes to a range of thermally-stable domain structures of technological interest, including mesoscale bicontinuous morphologies for polymeric OLED and photovoltaic devices.

Higher-magnification TEM of the PS/PMMA interface in the control blend (0% PS/PMMA-CdS) is shown in Figure 3.4d. TEM images of the 10% and 20% PS/PMMA-CdS blends at the same magnification (Figure 3.4e and 3.4f, respectively) confirm that the QDs (black dots) are localized at the interface between the PMMA domains (white) and the PS matrix (dark grey). The QDs are seen to be dispersed within an encapsulating shell of mixed PS and PMMA chains (light grey) surrounding the PMMA islands, supporting the AFM data discussed previously. From comparison of Figure 3.4e and 3.4f, it is noted that the thickness of the encapsulating phase increases when the PS/PMMA-CdS content increases from 10% to 20%.

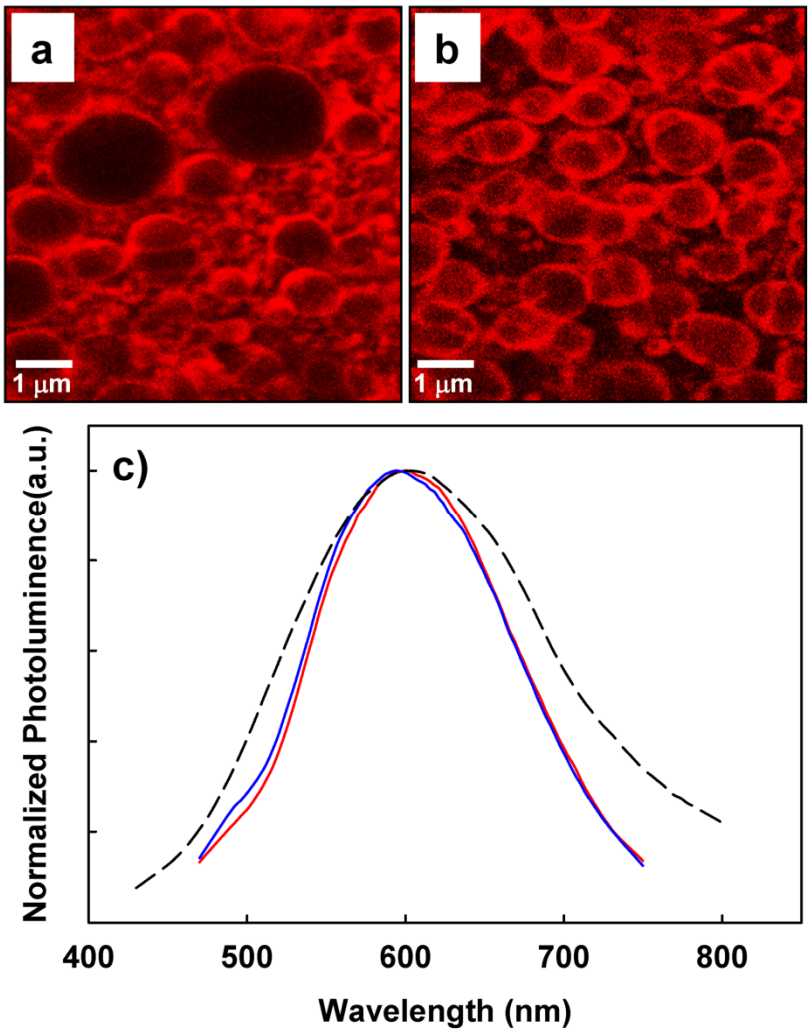

Figure 3.6. Laser scanning confocal fluorescence microscopy (LSCFM) images of PS:PMMA (30:70) blend films with a) 10% and b) 20% added PS/PMMA-CdS QDs. c) Normalized photoluminescence (PL) spectra of blend films in a) (red line) and b) (blue line); PL spectrum of PS/PMMA-CdS QDs dispersed in toluene (dashed line) is shown for comparison.

In addition to the compatibilizing effect afforded by their mixed polymer brush layers, PS/PMMA-CdS nanoparticles exhibit the interesting photoluminescence (PL) associated with their QD cores. Laser scanning confocal fluorescence microscopy (LSCFM, Zeiss LSM-410) of the 10% and 20% PS/PMMA-CdS blend films shows PL rings from localized QDs surrounding PMMA domains within the phase-separated films (Figure 3.6a and 3.6b); the PL from assembled QDs following spin-coating was found to persist with long periods of annealing. PL spectra of the blend films are very similar to that of the individual PS/PMMA-CdS particles dispersed in dilute toluene solution (Figure 3.6c), indicating that the QD optical properties are retained during phase separation and interfacial self-assembly. The slight narrowing of the ~600 nm trap state emission peak relative to QD PL in toluene is attributed to scattering effects within the blend film.

The interfacial organization of stable QDs with interesting optical function opens up intriguing possibilities for tuning and enhancing the collective properties of polymer blend-based device structures.[28] In addition, we note that this system provides a general route to novel patterned surfaces, including mesoscale arrays of QD/polymer rings. These hierarchical structures form as a result of interfacial self-assembly in the fast spin-coating process, and can be subsequently "developed" by removal of the two homopolymer phases using selective solvents (Figure 3.7).

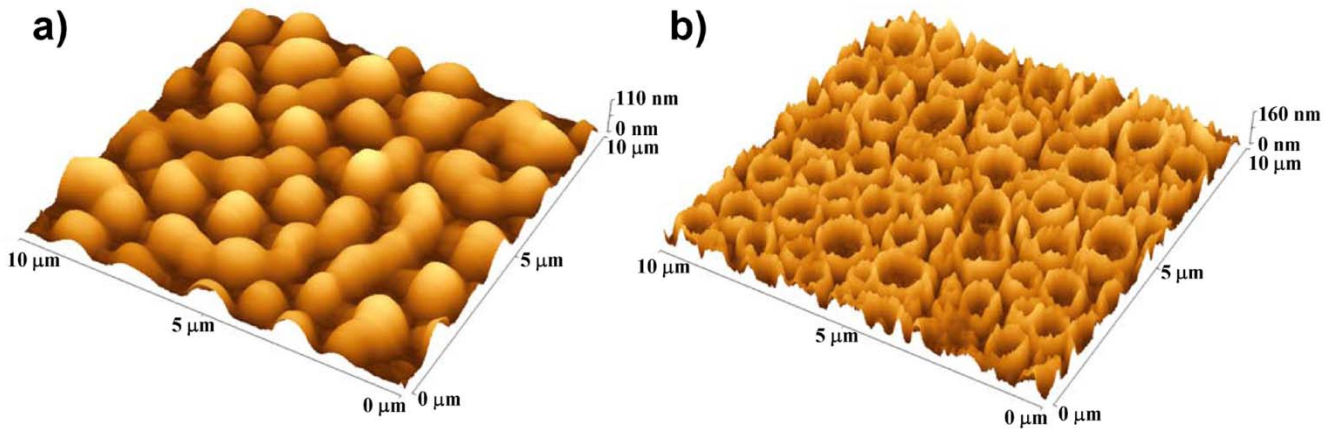

Figure 3.7. Three-dimensional (3D) atomic force microscopy (AFM) images of PS:PMMA (30:70) blend films with 20% added PS/PMMA-CdS QDs: a) film obtained by spin-coating and 8 h annealing at 150 ºC, with no solvent washing; b) film obtained by spin-coating and 8 h annealing at 150 ºC, followed by solvent washing with cyclohexane then acetic acid to remove the PS and PMMA phases, respectively. Nearly identical blend morphologies were obtained by spin-coating and solvent development without annealing.

3.4. Conclusions

We have shown that CdS QDs with external mixed polymer brush layers of PS and PMMA chains are driven to the interface of PS:PMMA blends during spin-coating, regulating the domain size and stabilizing the phase-separated blend morphologies during subsequent annealing. This work underlines the principle that colloidal inorganic elements such as QDs, which are widely recognized for their interesting optical properties, can also play an important role in the self-organization and stability of polymer blend-based devices. As the present example shows, such systems can take advantage of appropriate polymer surface layers to control the interactions between nanoparticle and homopolymer components, providing new opportunities for tunable collective function via synergistic self-assembly.

3.5. References

(1) Shenhar, R.; Norsten, T. B.; Rotello, V. M. *Adv. Mater.* **2005,** *17*, 657.

(2) Bockstaller, M. R.; Mickiewicz, R. A.; Thomas, E. L. *Adv. Mater.* **2005,** *17*, 1331.

(3) Haryono, A.; Binder, W. H. *Small* **2006,** *2*, 600.

(4) Lin, Y.; Böker, A.; He, J.; Sill, K.; Xiang, H.; Abetz, C.; Li, X.; Wang, J.; Emrick, T.; Long, S.; Wang, Q.; Balazs, A.; Russell, T. P. *Nature* **2005,** *434*, 55.

(5) Fahmi, A. W.; Oertel, U.; Steinert, V.; Froeck, C.; Stamm, M. *Macromol. Rapid Comm.* **2003,** *24*, 625.

(6) Cheyne, R. B.; Moffitt, M. G. *Macromolecules* **2007,** *40*, 2046.

(7) Kim, B.-S.; Qiu, J.-M.; Wang, J.-P.; Taton, T. A. *Nano Lett.* **2005,** *5*, 1987.

(8) Yusuf, H.; Kim, W.-G.; Lee, D.-H.; Aloshyna, M.; Brolo, A. G.; Moffitt, M. G. *Langmuir* **2007,** *23*, 5251.

(9) Wang, C.-W.; Moffitt, M. *Chem. Mater.* **2005,** *17*, 3871.

(10) Minelli, C.; Geissbuehler, I.; Eckert, R.; Vogel, H.; Heinzelmann, H.; Liley, M. *Colloid Polym. Sci.* **2004,** *282*, 1274.

(11) Li, D.; Sheng, X.; Zhao, B. *J. Amer. Chem. Soc.* **2005,** *127*, 6248.

(12) Shan, J.; Nuopponen, M.; Jiang, H.; Viitala, T.; Kauppinen, E.; Kontturi, K.; Tenhu, H. *Macromolecules* **2005,** *38*, 2918.

(13) Shan, J.; Chen, J.; Nuopponen, M.; Viitala, T.; Jiang, H.; Peltonen, J.; Kauppinen, E.; Tenhu, H. *Langmuir* **2006,** *22*, 794.

(14) Chiu, J. J.; Kim, B. J.; Kramer, E. J.; Pine, D. J. *J. Amer. Chem. Soc.* **2005,** *127*, 5036.

(15) Zubarev, E. R.; Xu, J.; Sayyad, A.; Gibson, J. D. *J. Amer. Chem. Soc.* **2006,** *128*, 4958.

(16) Zubarev, E. R.; Xu, J.; Sayyad, A.; Gibson, J. D. *J. Amer. Chem. Soc.* **2006,** *128*, 15098.

(17) Guo, Y.; Moffitt, M. G. *Macromolecules* **2007,** *40*, 5868.

(18) Moons, E. *J. Phys.: Condens. Matter* **2002,** *14*, 12235.

(19) Boltau, M.; Walheim, S.; Mlynek, J.; Krausch, G.; Steiner, U. *Nature* **1998,** *391*, 877.

(20) Takenaka, M.; Hashimoto, T.; Dobashi, T. *Phys. Rev. E* **1995,** *52*, 5142.

(21) Lee, M. S.; Lodge, T. P.; Macosko, C. W. *J. Polym. Sci. Part B: Poly. Phys.* **1997,** *35*, 2835.

(22) Russo, A. P.; Nauman, E. B. *J. Polym. Sci. Part B: Poly. Phys.* **2000,** *38*, 1301.

(23) Barham, B.; Fosser, K.; Voge, G.; Waldow, D.; Halasa, A. *Macromolecules* **2001,** *34*, 514.

(24) Winey, K. I.; Berba, M. L.; Galvin, M. E. *Macromolecules* **1996,** *29*, 2868.

(25) Adedeji, A.; Lyu, S.; Macosko, C. W. *Macromolecules* **2001,** *34*, 8663.

(26) Tanaka, H.; Lovinger, A. J.; Davis, D. D. *Phys. Rev. Lett.* **1994,** *72*, 2581.

(27) Ginzburg, V. V.; Qiu, F.; Paniconi, M.; Peng, G.; Jasnow, D.; Balazs, A. C. *Phys. Rev. Lett.* **1999,** *82*, 4026.

(28) Chung, H.-J.; Ohno, K.; Fukuda, T.; Composto, R. J. *Nano Lett.* **2005,** *5*, 1878.

(29) Minelli, C.; Frommen, C.; Hinderling, C.; Pugin, R.; Heinzelmann, H.; Liley, M. *Colloid Polym. Sci.* **2006,** *284*, 482.

(30) Tanaka, K.; Takahara, A.; Kajiyama, T. *Macromolecules* **1996,** *29*, 3232.

(31) Walheim, S.; Boltau, M.; Mlynek, J.; Krausch, G.; Steiner, U. *Macromolecules* **1997,** *30*, 4995.

(32) Harris, M.; Appel, G.; Ade, H. *Macromolecules* **2003,** *36*, 3307.

(33) Zong, Q.; Li, Z.; Xie, X. *Macromol. Chem. Phys.* **2004,** *205*, 1116.

(34) Heriot, S. Y.; Jones, R. A. L. *Nature Mater.* **2005,** *4*, 782.

(35) Li, Y.; Yang, Y.; Yu, F.; Dong, L. *J. Polym. Sci. Part B: Poly. Phys.* **2006,** *44*, 9.

(36) The CdS content of PS/PMMA-CdS is ~5 wt%, so that the inorganic content of these blends is in fact extremely low.

(37) Hobbs, S. Y.; Dekkers, M. E. J.; Watkins, V. H. *Polymer* **1988,** *29*, 1598.

(38) a.) Bansal, A.; Yang, H.; Li, C.; Cho, K.; Benicewicz, B. C.; Kumar, S. T.; Schadler, L. S. *Nature Materials* **2005**, *4*, 693.; b.) Corbierre, M. K.; Cameron, N. S.; Sutton, M.; Laaziri, K.; Lennox, R. B. *Langmuir* **2005**, *21*, 6063; c.) Chiu, J. J.; Kim, B. J.; Yi, G.-R.; Bang, J.; Kramer, E. J.; Pine, D. J. *Macromolecules* **2007**, *40*, 3361.

(39) Wang, C.-W.; Moffitt, M. G. *Langmuir* **2005,** *21*, 2465.

(40) We note that the larger PMMA domains in the 10% PS/PMMA-CdS blend do not protrude significantly above the PS phase, and so are not detected in the AFM images in Figures 3 and 4. TEM of film sections of the 10% and 20% PS/PMMA-CdS blends after 24 h annealing (Supporting Information) confirms that the internal film morphologies, along with the surface features tracked by AFM, are stable to annealing.

CHAPTER 4

Amphiphilicity-Driven Self-Assembly of Polymer-Coated Quantum Dots into Morphologically-Tunable Aggregates

4.1. Introduction

En route to future applications in photonics, biolabelling, drug delivery and sensing, increasing research interest has focus on various strategies for the self-assembly of quantum dots (QDs) and metal nanoparticles into complex colloidal superstructures with tunable morphologies and internal organization.[1-24] In many of these approaches, the incorporation of QDs and metal nanoparticles into polymer environments plays an important role in directing self-assembly, with the polymer component acting as a scaffold, glue or matrix within the final assemblies. For example, recent research has demonstrated supramolecular assembly of nanoparticle "bricks" and polymer "mortar",[5-11] layer-by-layer assembly of nanoparticles on preformed polymer spheres through electrostatic interactions,[12-14] and organization of nanoparticles within self-assembled block copoloymer colloids.[18-24] In spite of these successes, the range of tunable morphologies for composite nanoparticle/polymer colloids is still quite limited, and fine control over the internal organization of QDs or metal nanoparticles within these colloids is generally not achieved.

Scientists seeking improved strategies for the self-assembly of nanoparticles in colloidal media can find inspiration in the vast structural complexity and diversity shown by the self-assembly of amphiphilic block copolymers in mixtures of water and polar organic solvents. For example, a broad range of aggregate morphologies (shown in Figure 4.1) have been demonstrated via the self-assembly of a amphiphilic PS-*b*-PAA diblock copolymer in DMF/water mixtures, simply by varing the amount of added

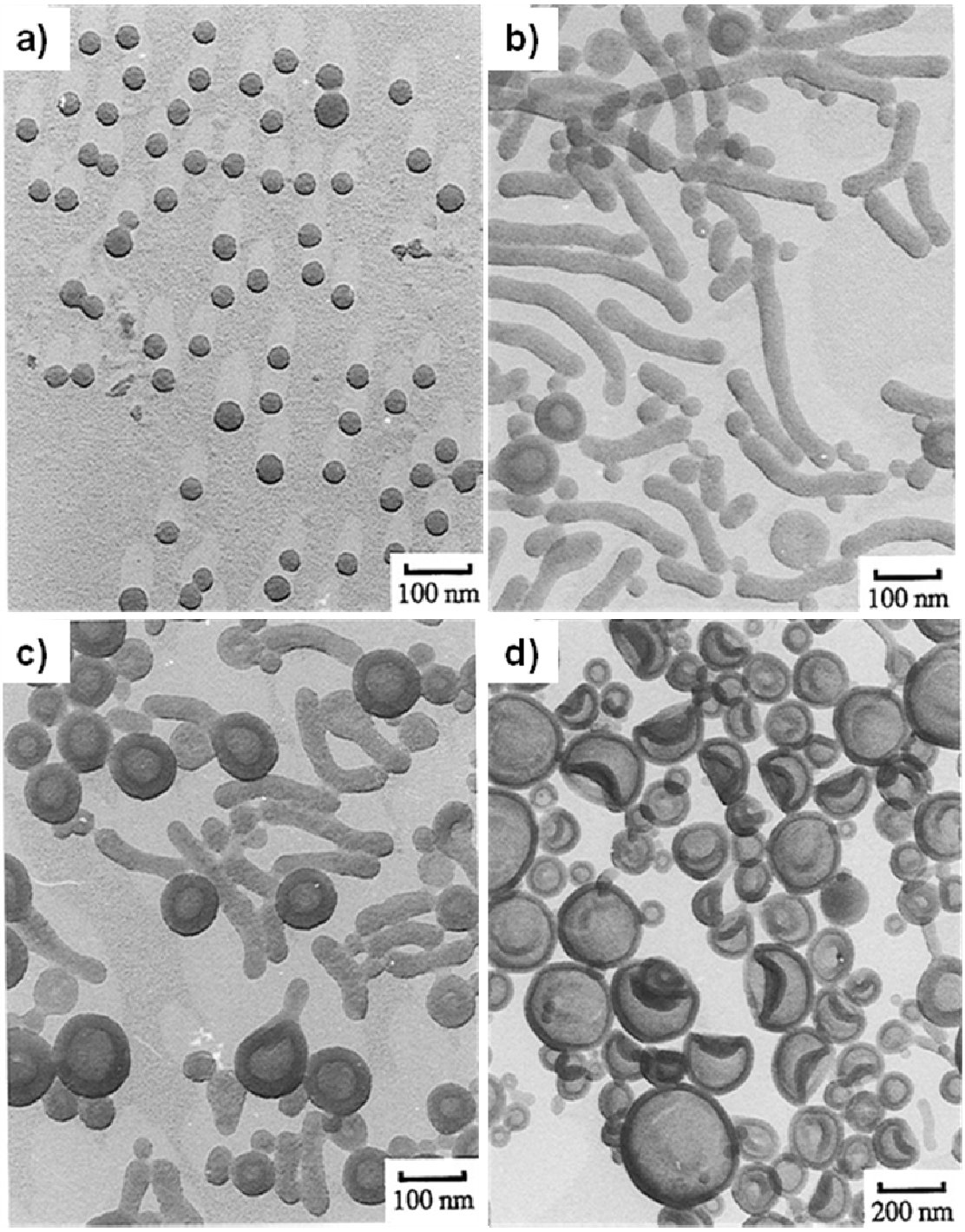

Figure 4.1. Morphologies of PS-*b*-PAA aggregates in aqueous solution with different amounts of added NaCl to DMF solutions prior to water addition. From a to d, the concentration of NaCl increased from 2.1 to 16.0 mM.[25] (Adapted with permission from Lifeng Zhang and Adi Eisenberg, *Macromolecules,* **1996,** *29*, 8805-8815. Copyright 2009 American Chemical Society.)

NaCl prior to water addition.[25] The interesting self-assembly behavior of PS-*b*-PAA and other amphiphilic block copolymer arises from the amphiphilic nature of the copolymer chains, which interact anisotropically via the hydrophilic and hydrophobic segments on neighboring molecules. Therefore, a promising strategy toward increased complexity and control of self-assembled morphologies of nanoparticle/polymer colloids is to produce nanoparticle building blocks which are amphiphilic and exhibit anisotropic interparticle interactions such that their self-assembly behavior can mimic that of block copolymers. Some successes in this area have already been demonstrated by functionalizing nanoparticles with mixtures of hydrophobic and hydrophilic polymer chains,[26,27] or by decorating specific regions of nanoparticle surfaces with polymer brushes.[24,28] However, in these various systems, the range of complex and tunable morphologies exhibited by block copolymers has not yet been achieved by varying experimental parameters for a single type of amphiphilic nanoparticle.

As described in previous chapters of this thesis, our work employs a triblock copolymer, PS-*b*-PAA-*b*-PMMA, in order to form functional nanoparticles of CdS QDs coated with a polymer surface layer, consisting of a mixture of PS and PMMA chains from the end blocks of the constituent copolymer. In Chapter 2, we described the synthesis and characterization of CdS QDs with mixed PS/PMMA polymer brush layers, (termed PS/PMMA-CdS) in organic solvents of varying polarity, demonstrating the environmentally-responsive nature of the PS/PMMA-CdS surfaces. In Chapter 3, we then showed that PS/PMMA-CdS nanoparticles self-assemble at the polymer/polymer interface in phase-separating blend films of the corresponding PS and PMMA

homopolymers, resulting in regulation and stabilization of the domain morphologies. Self-assembly in polymer blend films is the result of the mixed layer of polar PMMA and non-polar PS on the surface of PS/PMMA-CdS, which drives the nanoparticles to the interface of polar and non-polar blend components. In this chapter, we describe the conversion of PS/PMMA-CdS to amphiphilic nanoparticles, via the hydrolysis of the polar poly (methyl methacrylate) (PMMA) surface chains to water-soluble poly (methacrylic acid) (PMAA) chains. Subsequent self-assembly experiments for PS/PMAA-CdS nanoparticles in various mixtures of water and polar organic solvents display a spectrum of unprecedented and tunable QD/polymer aggregate morphologies, including spherical, worm-like, continent-like and vesicular supermicelles, each containing a unique and well-defined internal organization of QDs.

4.2. Experimental

4.2.1. Synthesis of Polystyrene-*b*-Poly (Acrylic Acid)-*b*-Poly(Methyl Methacrylate) (PS-*b*-PAA-*b*-PMMA) Triblock Copolymer. The triblock copolymer used as a starting material in this chapter was introduced in Chapter 2, and was synthesized via sequential anionic polymerization to produce PS-*b*-PtBA-*b*-PMMA followed by selective hydrolysis of PtBA to PAA. The composition of the resulting PS-*b*-PAA-*b*-PMMA copolymer is shown in Table 4.1.

Table 4.1. Characteristics of PS-*b*-PAA-*b*-PMMA Triblock Copolymer Synthesized by Sequential Anionic Polymerization

M_n, g/mol	M_w/M_n	N_{PS}	N_{PAA}	N_{PMMA}
59700	1.05	296	41	236

4.2.2. Preparation of Polystyrene-*b*-Poly(Cadmium Acrylate)-*b*-Poly(Methyl Methacrylate) (PS-*b*-PACd-*b*-PMMA) Micelles. The methodology used for preparing triblock copolymer-stabilized QDs was similar to that described previously in Chapter 2. First, the PS-*b*-PAA-*b*-PMMA copolymer was dissolved in benzene/methanol (90:10 v/v) at a concentration of ca. 2 wt%. The formation of reverse micelles via self-assembly of insoluble poly (cadmium acrylate) (PACd) blocks was induced by the addition of an excess of 0.25 M cadmium acetate dihydrate (Aldrich) in methanol (1.5 mol cadmium acetate dihydrate:1 mol acrylic acid repeat units) followed by stirring of the solution for 4 h. The micellized PS-*b*-PACd-*b*-PMMA was recovered by freeze-drying and then dried in a vacuum oven at 70°C for 24 h. Excess cadmium acetate was removed by washing the freeze-dried powder repeatedly with methanol followed by drying under vacuum at 70°C for 24 h.

4.2.3. Preparation of Cd^{2+}-Crosslinked and Diamide-Crosslinked PS/PMMA-CdS. Similar to the procedure described in Chapter 2, in order to grow CdS QDs in the Cd^{2+}-containing cores of PS-*b*-PACd-*b*-PMMA micelles, the micelles were exposed to an

atmosphere of 100% humidity for 1 week, followed by exposure to wet H_2S for a total of 24 hours. Two different methods were attempted to stabilize the resulting PS-*b*-PAA(CdS)-*b*-PMMA micelles. The first method was identical with that described in Chaper 2: the yellow powder PS-*b*-PAA(CdS)-*b*-PMMA was dispersed in THF (2 wt %), then excess cadmium acetate dihydrate in methanol (2 mol cadmium acetate dihydrate : 1 mol acrylic acid repeat units) was added to re-neutralize the acrylic acid blocks, providing bridging Cd^{2+} crosslinks within the PAA layer in the micelle cores. After overnight stirring, the sample was recovered by precipitation into methanol, then washed repeatedly with methanol and dried for 24 h under vacuum oven at 70 ^{o}C. This product is designated as PS/PMMA-CdS (Cd^{2+}-crosslinked), and is similar to PS/PMMA-CdS described in Chapter 2 and 3. However, our work showed that this crosslinking strategy was unable to prevent dissociation of the micelles under later hydrolysis conditions. Therefore, we employed a diamine crosslinker to stabilize the PAA layer in the cores of micelles. This second method is described as follow: The yellow powder PS-*b*-PAA(CdS)-*b*-PMMA was dispersed in THF (2 wt%), followed by the fast immediate addition of 0.5 equivalents of cadmium acetate dihydrate in methanol (0.5 mol cadmium acetate dehydrate : 1 mol acrylic acid repeat units) and the solution was stirred overnight. Then, a 1.0 wt% solution of *N*-ethyl-*N*'-(3-dimethylaminopropyl)carbodiimide methiodide (EDC) activator in deionized water was added (0.5 mol EDC : 1 mol acrylic acid repeat units) all at once, and the solution was left to react for 30 min with stirring. Finally, a 1.0 wt% solution of 2,2'-(ethylenedioxy)bis(ethylamine) crosslinker in water was added in one portion (0.25 mol crosslinker : 1 mol acrylic acid repeat units) and the reaction solution was stirred overnight. The sample was recovered by precipitating into

methanol, washed repeatedly with methanol, then dried for 24 h under vacuum at 70 ^{0}C. This product was designated PS/PMMA-CdS (diamide-crosslinked).

4.2.4. Hydrolysis of PMMA blocks for PS/PMMA-CdS (Cd^{2+}-Crosslinked) and PS/PMMA-CdS (Diamide-Crosslinked). Either PS/PMMA-CdS (Cd^{2+}-crosslinked) or PS/PMMA-CdS (diamide-crosslinked) was dissolved in 1,4-dioxane (ca. 10 wt%) under argon in a sealed high-pressure Schlenk tube. To hydrolyze the PMMA ester groups, the reaction solution also contained 2 mol KOH : 1 mol methyl methacrylate repeat units, and 18-crown-6 as a phase transfer catalyst (0.2 mol [18-crown-6] : 1 mol methyl methacrylate repeat units). The reaction was carried out at 110 ^{0}C for 4 days. To recover the hydrolyzed product, the solution was further diluted with 1,4-dioxane, precipitated into 0.2 M acetic acid (2 mol acetic acid : 1 mol methyl methacrylate repeat units) then dried under vacuum at 60 ^{0}C for 24 h. We designated the resulting products as PS/PMAA-CdS (Cd^{2+}-crosslinked) and PS/PMAA-CdS (diamide- crosslinked), respectively. As described later in the Results and Discussion section, PS/PMAA-CdS (diamide-crosslinked) was the only sample carried forward to self-assembly experiments and is therefore also given the simpler designation PS/PMAA-CdS in some sections of the text.

4.2.5. Self-assembly of PS/PMAA-CdS in Mixtures of Polar Organic Solvents and Water (Immediate Quenching Method). Various QD/polymer aggregates described in this chapter were produced using the following general procedure: PS/PMAA-CdS (diamide-crosslinked) micelles were dissolved in polar organic solvents

(DMF or THF) to form ~2 g polymer solution with various initial polymer concentrations, c_0 = 0.5 wt%, 1.0 wt%, and 2.0 wt%. The DMF used was 99.9+% HPLC grade ([H_2O] < 0.03 wt%), and THF used was 99.9+% HPLC grade ([H_2O] < 0.02 wt%). To each solution, deionized water was added dropwise at a rate of 10 μL/10 s with rapid stirring. During water addition, the point was observed which an increase in turbidity suggested the onset of self-assembly at the critical water concentration (cwc). After the cwc, water addition was continued at the same rate up to 25 wt% water for DMF solutions and 75 wt% water for THF solutions, at which points aggregate morphologies could be considered to be kinetically frozen. However, DMF solutions were also subsequently dumped into 5× excess deionized water to quench the solutions and ensure kinetic freezing of the aggregates. The self-assembled samples were then dialyzed against deionized water for 5 days to remove residual organic solvent. For all experiments, the stirring rate during water addition was held approximately constant by using the same setting on the stir plate with same stir bars. The room temperature was measured to be 23 ± 1 ^{0}C for all self-assembly experiments. Aqueous QD/polymer colloids were sealed with Teflon in vials and stored in a dark drawer when not in use.

4.2.6. Self-assembly of PS/PMAA-CdS in Mixtures of THF and Water (Annealing Method). The annealing experiments for PS/PMAA-CdS self-assembly in various mixtures of water and THF were prepared using the following procedure: PS/PMAA-CdS (diamide-crosslinked) micelles were dissolved in THF solutions to form four ~2 g polymer solutions with an initial polymer concentration of c_0 = 1.0 wt%. To each solution, water was added dropwise at a rate of 10 μL/10 s up to four different water

contents above cwc (c_{water} = 11, 15, 25, 50 wt%) with rapid stirring. The four solutions were then stirred for 2 weeks with medium stirring speed in order to anneal at various water contents, then dumped into 10 g water to quench. Finally, the quenched solutions were dialyzed against deionized water for 5 days to remove any residual THF.

4.2.7. Gel Permeation Chromatography (GPC). GPC measurements were performed using a Viscotek Model 302 liquid chromatography system equipped with refractive index (RI), low-angle light scattering (LALS, θ = 7°), right-angle light scattering (RALS, θ = 90°), and UV detectors. THF was used as the eluent at a flow rate of 1 mL/min, and the column temperature was set at 35 °C. All polymer solutions were filtered through membrane filters with a nominal pore size of 0.45 μm before injection into the GPC column. The data were collected and analyzed on a Dell Dimension 2300 computer with appropriate GPC software from Viscotek. Two ViscoGEL HR High-Resolution Columns (styrene-divinyl benzene columns) in series were used: G3000 HR 60 k and GMHHR-M Mixed Bed 4 M columns.

4.2.8. ^{1}H NMR. ^{1}H NMR spectra of PS/PMMA-CdS (Cd^{2+}-crosslinked) or (diamide-crosslinked) and PS/PMAA-CdS (Cd^{2+}-crosslinked) or (diamide-crosslinked) were recorded using a Bruker AC 300 MHz spectrometer.

4.2.9. UV-vis Absorption and Photoluminescence Measurements. Absorption spectra were recorded on a Cary 50-scanning UV-vis spectrophotometer. Static photoluminescence (PL) measurements were recorded on an Edinburgh Instruments FLS

920 instrument equipped with a Xe 450W arc lamp and a red-sensitive PMT (R928-P). Typical PL measurements involved λ_{ex} = 400 nm excitation and collection of emitted light with a long-pass 420 nm emission filter in place. For PL measurements of QDs in solution, the PS/PMMA-CdS and PS/PMAA-CdS samples were dispersed in various solvents (spectroscopic grade toluene and DMF, respectively) at a concentration such that the measured absorbance at 400 nm was less than 0.1. All spectra were collected at 1 nm spectral resolution and the appropriate solvent background was subtracted.

4.2.10. Transmission Electron Microscopy (TEM). Routine TEM imaging at UVic (Department of Biology) was performed on a Hitachi H-700 electron microscope, operating at an electron accelerating voltage of 75 kV. Solution-cast samples of PS/PMAA-CdS were prepared by depositing a drop of 2 mg/mL solution in THF on a copper grid (300 mesh) coated with an amorphous carbon film with immediate blotting of the excess solution; the grids were then dried at room temperature for 2 hours before imaging. For TEM of various aggregates in aqueous solutions, the original solutions were diluted to a concentration of 0.5 mg/mL, and then a 10 μL drop was deposited on a carbon/Formvar-coated 300-mesh copper grid with immediate blotting of the excess solution; the grids were then dried at room temperature for 2 h before imaging. Particle size analysis and statistics of various feature dimensions were carried out on the images, with regions of the TEM grids randomly sampled and a minimum of 100 particles measured and included in each analysis.

In order to better observe the internal structure of various aggregates, powdered samples obtained by drying the aqueous solutions were embedded in epoxy resin (Epon),

and then ~50 nm-thick sections were obtained with a diamond knife on a Reichert UltraCut E ultra-micotome. The thin sections were then placed on carbon/Formvar-coated 300 mesh copper grids for imaging.

High-resolution TEM imaging was carried out at Simon Fraser University on an FEI Tecnai scanning transmission electron microscope (STEM), operating at an accelerating voltage of 200 kV. This instrument allowed high-angle annular dark-field (HAADF) STEM images to be obtained for improved contrast within QD/polymer aggregates. Energy-dispersive X-ray spectroscopy (EDX) was performed using an energy-dispersive X-ray detector installed on the FEI Tecnai STEM with an energy resolution of 1.36 eV for Mn Kα radiation; the scan time was 90 seconds.

4.2.11. Powder X-ray Diffraction (XRD). About 15 mg of powdered PS/PMAA -CdS was dissolved in ethanol and smeared onto a zero-background holder. Step-scan X-ray powder diffraction data were obtained over the 2θ range 20-100^{o} with Cr (30 kv, 15 mA) (wavelength is 0.228 nm) radiation on a Rigaku Miniflex diffractometer with variable divergence slit, 4.2^{o} scattering slit, and 0.3 mm receiving slit. The scanning step size was 0.02^{o} with a counting time of 6 s per step.

4.2.12. Dynamic Light Scatteing (DLS). DLS experiments on PS/PMAA-CdS in DMF before self-assembly were carried out on a Brookhaven Instruments photo correlation spectrometer equipped with a BI-200SM goniometer, a BI-900AT digital

autocorrelator, and a Melles Griot He-Ne laser (632.8 nm) with maximum power output of 75 mW. All DLS measurements were conducted at 23 ^{0}C.

4.2.13. Atomic Force Microscopy (AFM). A Veeco AFM Instrument equipped with a Veeco tip (Nanoprobe-MLCT-EXMT-A) running in contact mode was used to obtain AFM images. The effect of vibration was minimized by a vibration-resistant housing on a vibration isolation platform maintained at 80 psi. Each sample was imaged several times at different locations on the substrate. The statistical analysis of heights and full width half maximum (FWHM) widths of QD/polymer aggregates was carried out by measuring surface height profiles for at least 100 features in different regions of suitable AFM images.

4.2.14. Laser Scanning Confocal Fluorescence Microscopy (LSCFM). Laser scanning confocal fluorescence microscopy measurements were carried out on a Zeiss LSM 410 equipped with an Ar/Kr laser. All films were excited at 488 nm, using a band-pass 485 ± 20 nm line selection filter and a FT 510 dichroic beam splitter. A long-pass 515 nm emission filter was employed such that only light above 515 nm reached the PMT. A Zeiss Plane-Aprochromat 63 x oil-immersion objective was employed. A pinhole diameter of 1.31 Airy Units was used for all measurements, resulting in an optical section thickness of 0.75 μm FWHM.

4.2.15. Zeta Potential Measurement. Zeta potentials and hydrodynamic particle sizes of various QD/polymer aggregates in water were measured at different pH values using a Zeta PALS Analyzer (Brookhaven Instuments Corporation, USA). Zeta potential values were calculated from electrophoretic mobility values using the Smoluchowski equation. The hydrodynamic size analysis of the samples was conducted by photon correlation spectroscopy (PCS) measurements through a BI-9000 Brookhaven light scattering apparatus (Brookhaven Instrument Cooperation), fitted with a 20 mW He-Ne, with the detector angle set at 90^0. The various aqueous colloids were diluted with a 0.01 M NaCl aqueous solution to a concentration of about 0.05 mg/mL NaCl as a salt background. The pH values of the aqueous solutions were adjusted by titrating 0.1 M HCl and NaOH solutions. The zeta potential and size analysis was carried out at 25 ^{0}C.

4.3. Results and Discussion

4.3.1. Hydrolysis of PS/PMMA-CdS (Cd^{2+}-Crosslinked) to PS/PMAA-CdS (Cd^{2+}-Crosslinked). The schematic of the synthesis of PS/PMMA-CdS (Cd^{2+}-crosslinked) is shown in Figure 4.2 (as described in section 4.2.4). Subsequently, the PMMA chains of PS/PMMA-CdS (Cd^{2+}-crosslinked) were hydrolyzed to form PS/PMAA-CdS (Cd^{2+}-crosslinked), as represented in Figure 4.3. The ^{1}H NMR spectra of the two samples before and after hydrolysis and key proton peak assignments are shown in Figure 4.4. Most importantly, the resonance at δ = 3.59 ppm (3 methyl ester protons from each methyl methacrylate repeat unit) in (b) has disappeared in (c), which proved that the PMMA ester groups were converted to PMAA acid groups. However, the GPC

spectra of PS/PMMA-CdS (Cd^{2+}-crosslinked) and PS/PMAA-CdS (Cd^{2+}-crosslinked) (Figure 4.5) indicates significant dissociation of micelles to single chains under the hydrolysis conditions. Figure 4.5a shows the single chains of the triblock copolymer starting natural (used for a reference) at an elution volume ~14 mL; the lower molecular weight peak at ~15 mL is attributed to PS or PS-*b*-P*t*BA due to "killing" during anionic polymerization step. Figure 4.5b shows the main peak shifted to lower elution volumes (centered at ~13 mL), confirming that PS/PMMA-CdS (Cd^{2+}-crosslinked) are particles formed via the micellization of copolymer single chains. The slight high elution-volume shoulder indicates a small fraction of unmicellized single chains in the sample. Following hydrolysis, (Figure 4.5c) the GPC of the particles changed significantly, with the main peak separating into two distinct peaks: a low elution-volume peak attributed to micelles and a significantly stronger peak attributed to copolymer single chains. A number of factors may contribute to the dissociation of copolymer chains from the surface of QDs during hydrolysis, including softening of the PACd layer at the QD surface via heating and plasticization with the polar dioxane solvent, and also the exchange of divalent "bridging" Cd^{2+} with univalent K^{+} ions. This significant loss of functional and stabilizing copolymer chains from the amphiphilic nanoparticles would be extremely detrimental to subsequent self-assembly experiments. Therefore, we pursued a strategy to covalently crosslink the cores of PS/PMMA-CdS, in order to provide structural stability prior to hydrolysis.

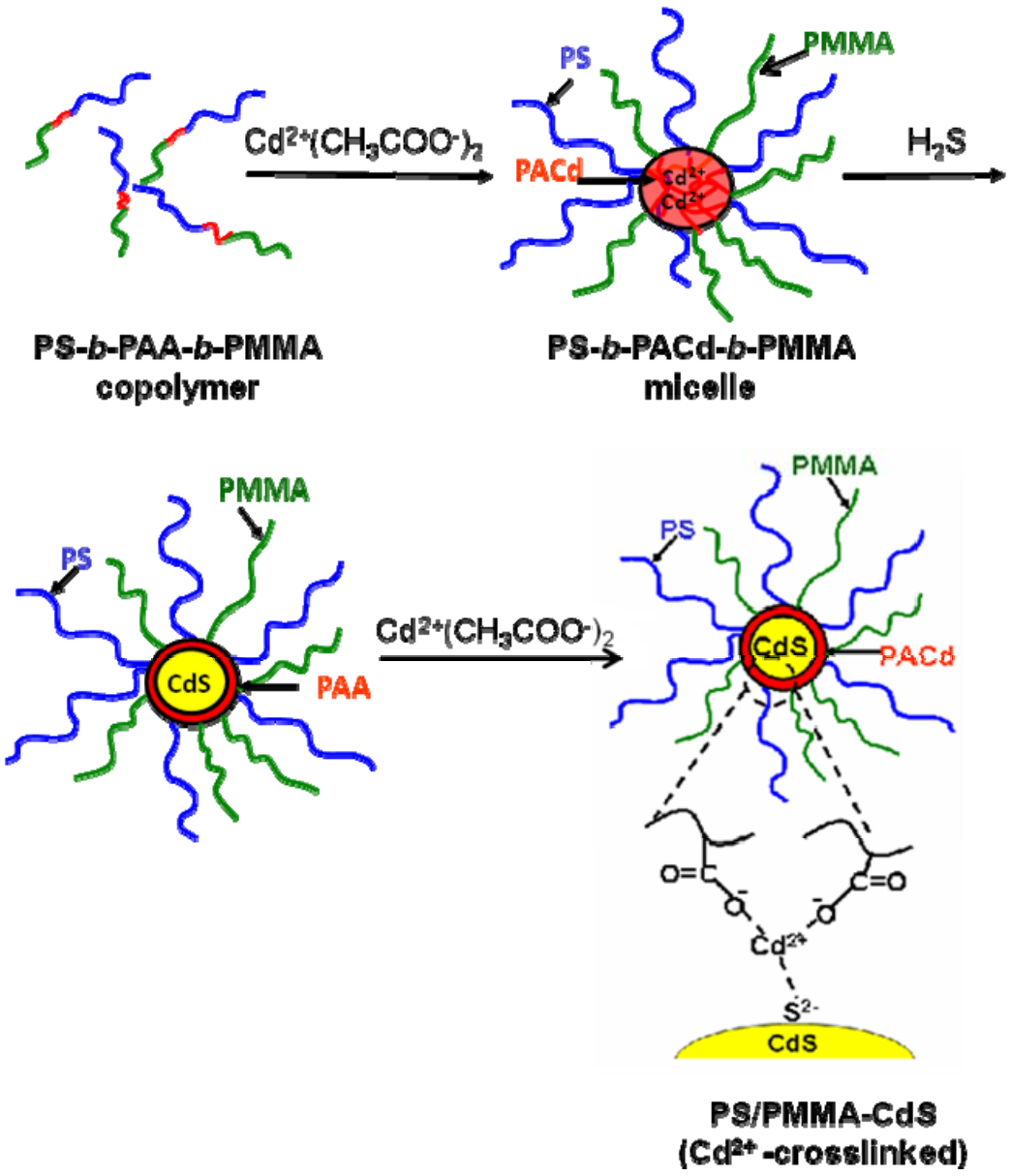

Figure 4.2. Schematic showing various synthetic steps for the formation of PS/PMMA-CdS (Cd^{2+}-crosslinked).

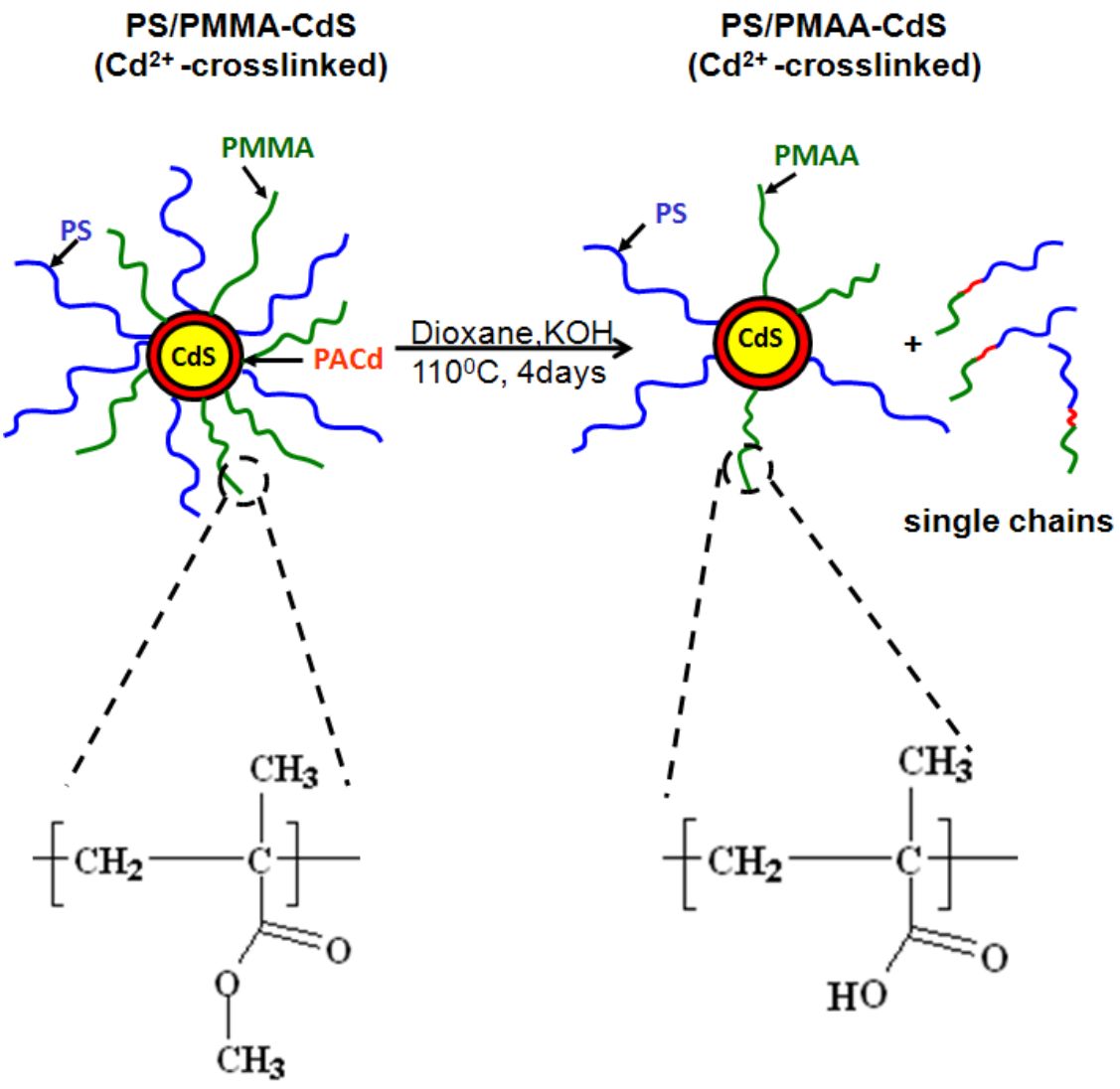

Figure 4.3. Schematic of hydrolysis of PS/PMMA-CdS (Cd^{2+}-crosslinked) to PS/PMAA-CdS (Cd^{2+}-crosslinked) nanoparticle.

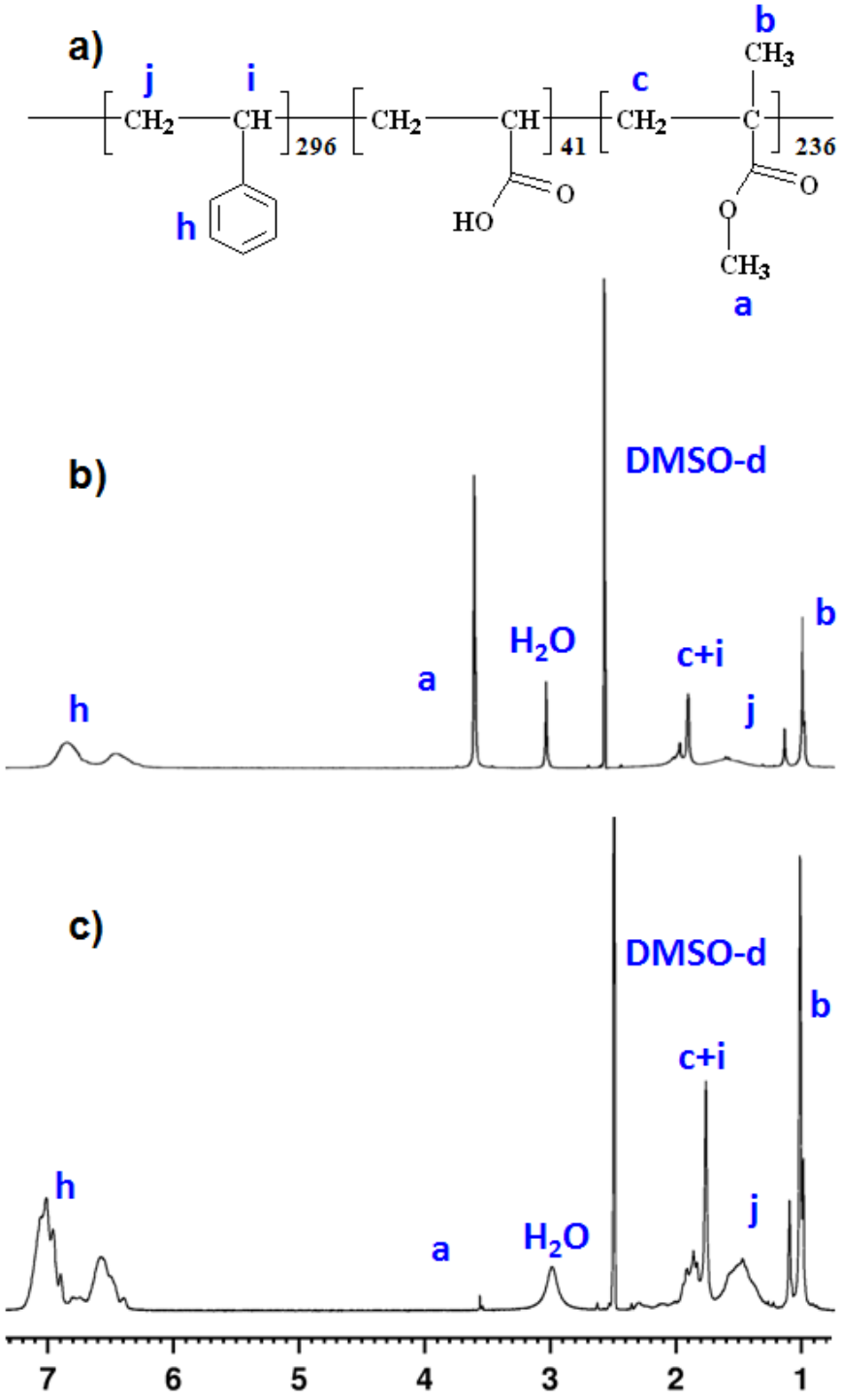

Figure 4.4. (a) ^{1}H NMR peak assignments of PS-*b*-PAA-*b*-PMMA triblock copolymer, and ^{1}H NMR spectra of (b) PS/PMMA-CdS (Cd^{2+} -crosslinked), (c) PS/PMAA-CdS (Cd^{2+}-crosslinked) in DMSO-d.

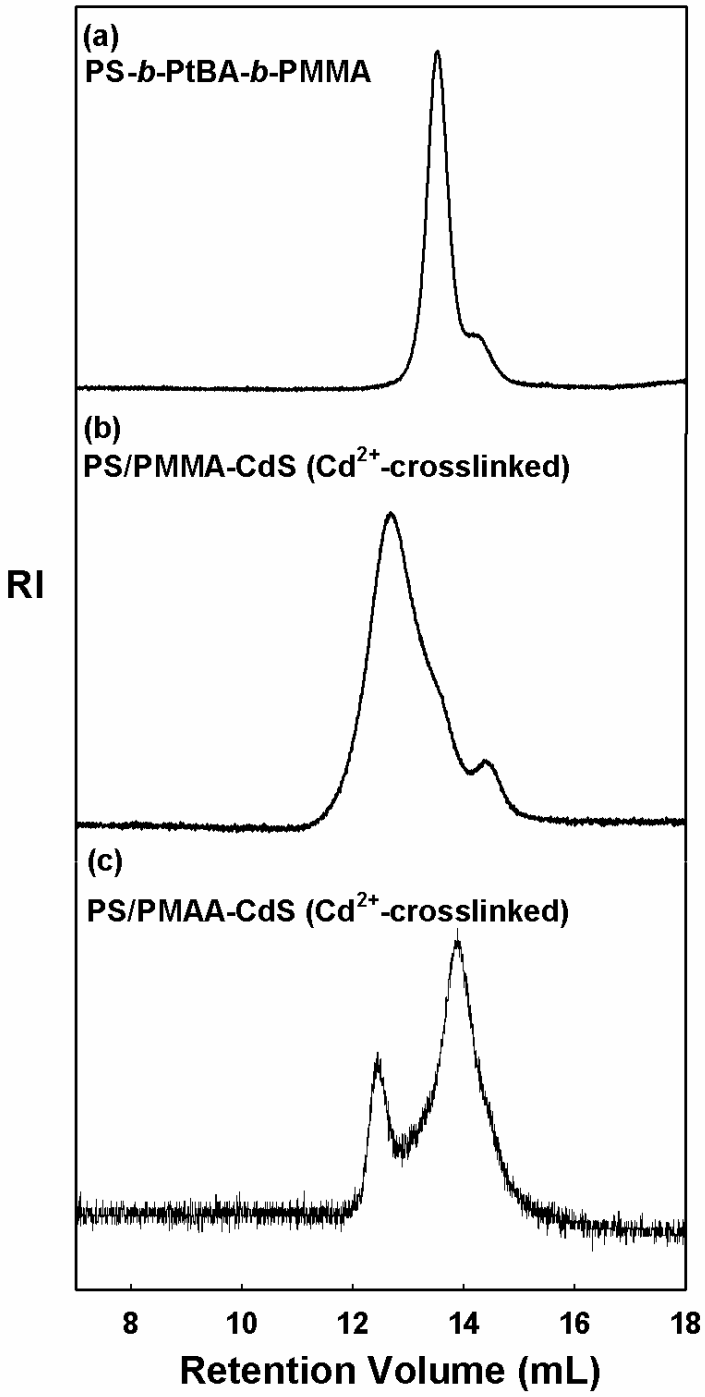

Figure 4.5. GPC (refractive index detector response) of (a) PS-*b*-PtBA-*b*-PAA starting copolymer (single chains), (b) PS/PMMA-CdS (Cd^{2+}-crosslinked) (before hydrolysis reaction), and (c) PS/PMAA-CdS (Cd^{2+}-crosslinked) (after hydrolysis reaction). All GPC chromatograms were run with THF as the eluting solvent.

4.3.2. Hydrolysis of PS/PMMA-CdS (Diamide-Crosslinked) to PS/PMAA-CdS (Diamide-Crosslinked). The schematic of the synthesis of PS/PMMA-CdS (diamide-crosslinked) is shown in Figure 4.6 (as described in section 4.2.4). Figure 4.7 describes the subsequent hydrolysis reaction to convert PS/PMMA-CdS with covalently-crosslinked cores to amphiphilic nanoparticles with external PS and PMAA chains. A similar chemical crosslinking strategy has been used previously to crosslink the coronae of block copolymer micelles.[21-23] The ^{1}H NMR spectra and peak assignments in Figure 4.8 confirm essentially complete hydrolysis of PMMA to PMAA in the mixed brush layer, similar to the results for the Cd^{2+}-crosslinked nanoparticles. However, comparison of GPC results in Figure 4.9b and 4.9c indicate that diamide- crosslinked cores prevent dissociation of the micelles during the hydrolysis reaction, in contrast to the results for the Cd^{2+}-crosslinked nanoparticles. Prior to hydrolysis, the GPC chromatogram of PS/PMMA-CdS (diamide-crosslinked) (Figure 4.9b) looks very similar to that of PS/PMMA-CdS (Cd^{2+}-crosslinked) with a single dominant micelle peak eluting at ~13 mL. But unlike the previous case, the hydrolysis reaction does not change the GPC chromatogram significantly (Figure 4.9b and c), indicating that the amphiphilic nanoparticles PS/PMAA-CdS (diamide-crosslinked) have remained intact, with no significant single chain population developing. Since it is this sample of core-crosslinked amphiphilic nanoparticles that is carried forward to subsequent self-assembly experiments, we subsequently refer to PS/PMAA-CdS (diamide-crosslinked) simply as PS/PMAA-CdS.

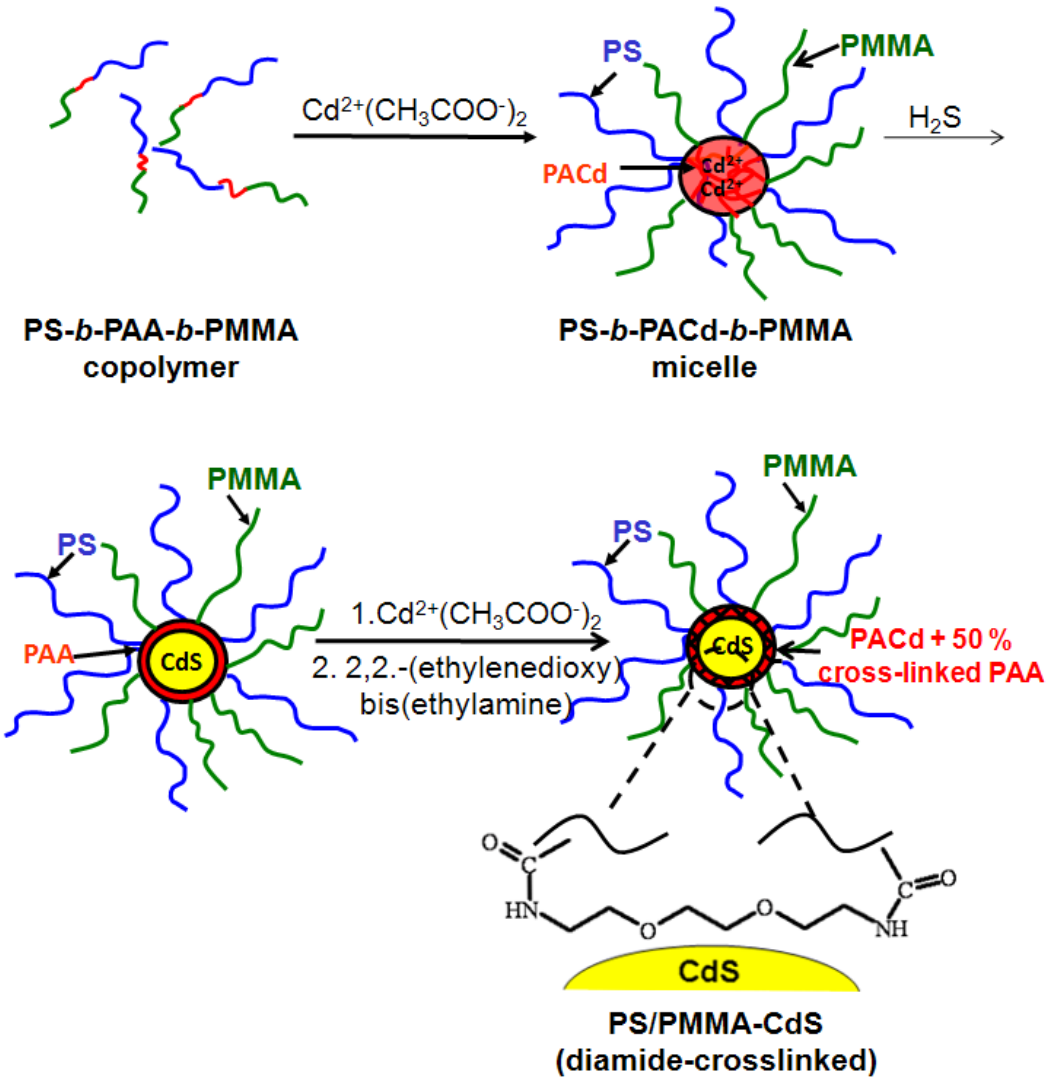

Figure 4.6. Schematic showing various synthetic steps for the formation of PS/PMMA-CdS (diamide-crosslinked).

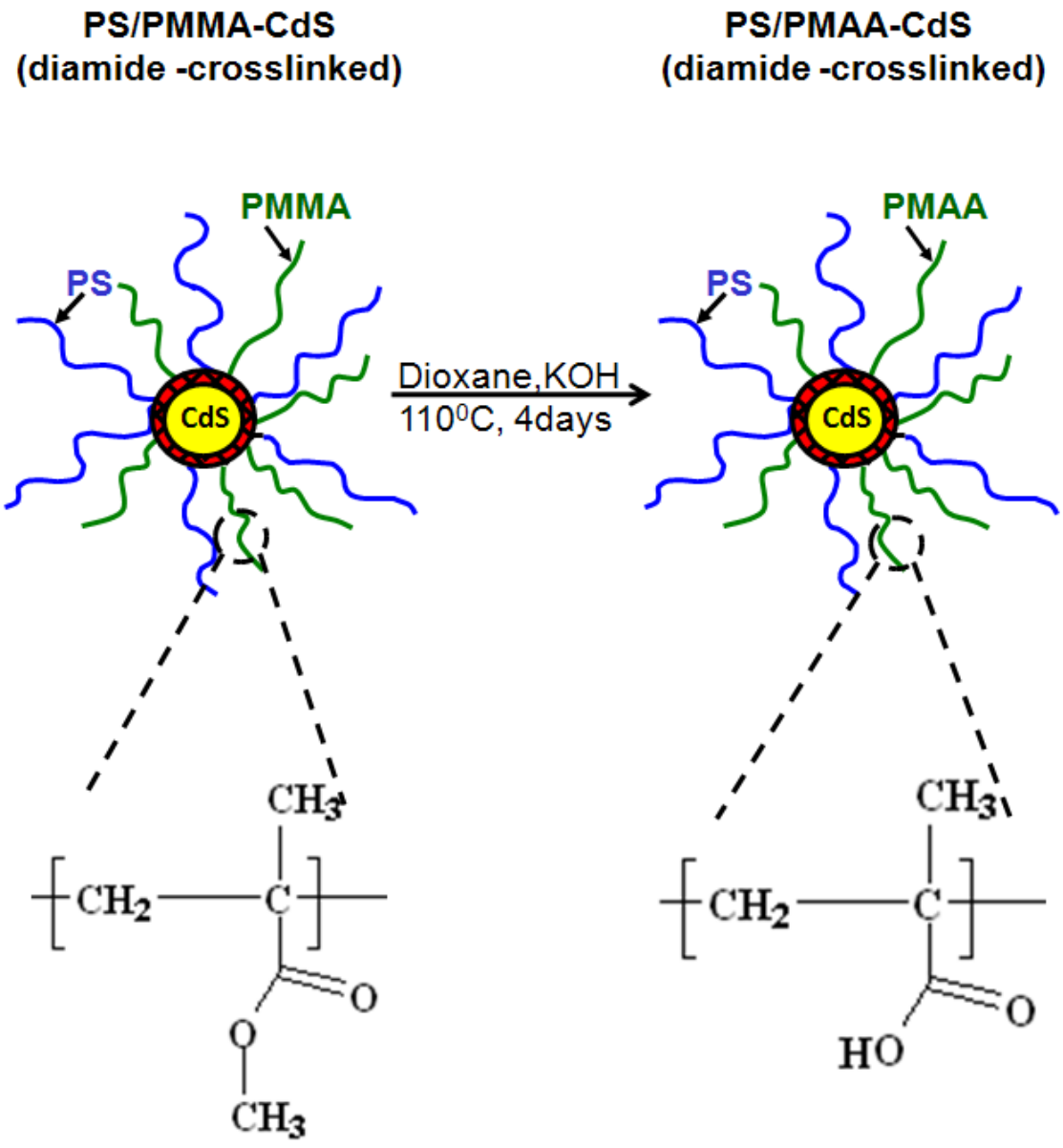

Figure 4.7. Schematic of hydrolysis of PS/PMMA-CdS (diamide-crosslinked) to PS/PMAA-CdS (diamide-crosslinked) nanoparticle.

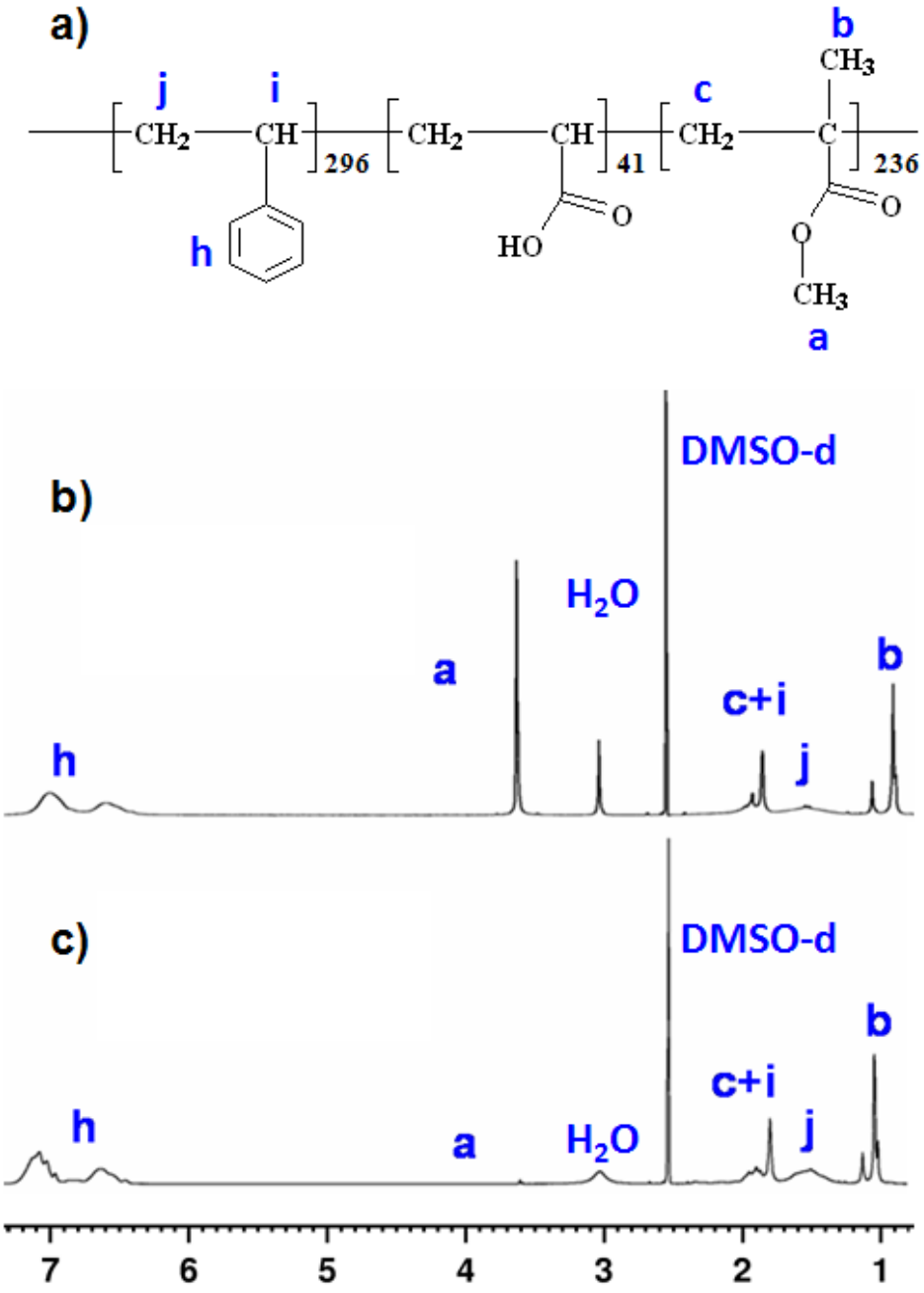

Figure 4.8. (a) ^{1}H NMR peak assignments of PS-*b*-PAA-*b*-PMMA triblock copolymer, and ^{1}H NMR spectra of (b) PS/PMMA-CdS (diamide-crosslinked), (c) PS/PMAA-CdS (diamide-crosslinked) in DMSO-d.

.

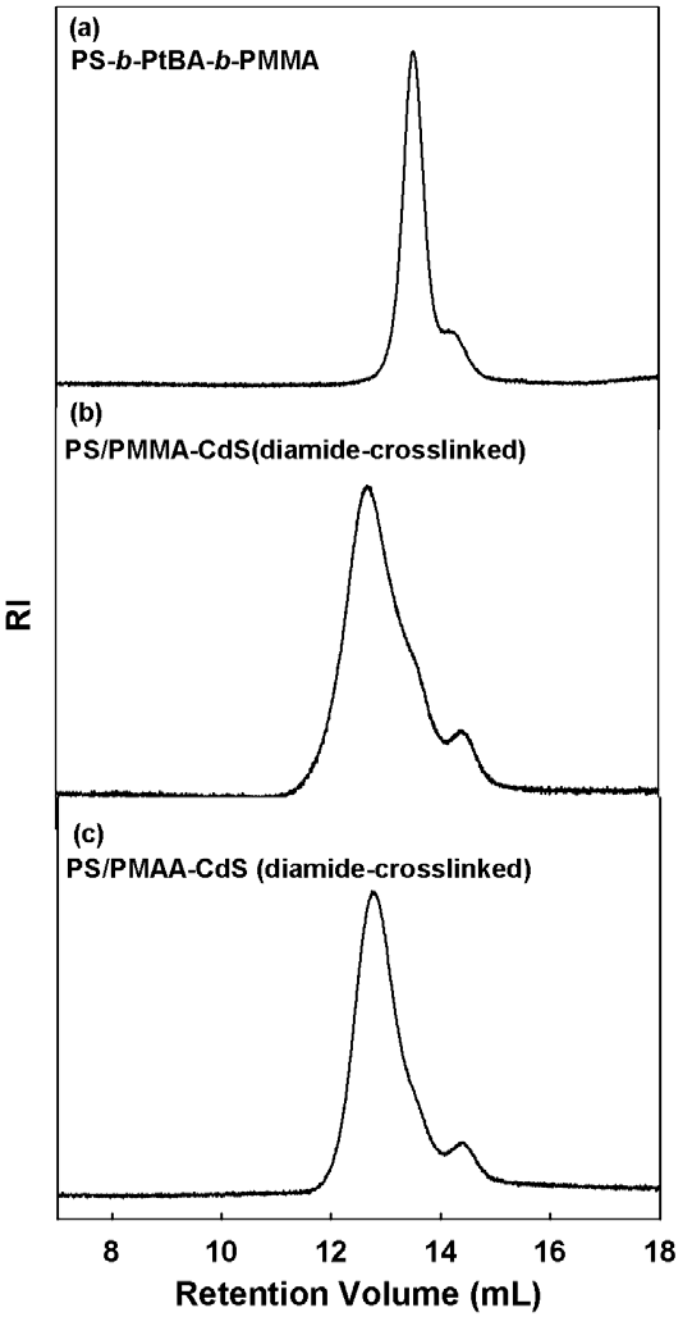

Figure 4.9. GPC (refractive index detector response) of (a) PS-*b*-PtBA-*b*-PAA starting copolymer (single chains), (b) PS/PMMA-CdS (diamide-crosslinked) (before hydrolysis reaction), and (c) PS/PMAA-CdS (diamide-crosslinked)(after hydrolysis reaction).All GPC chromatograms were run with THF as the eluting solvent.

4.3.3. Characterization of PS/PMAA-CdS Amphiphilic Nanoparticles

4.3.3.1. UV-vis Absorption Spectroscopy. UV-vis spectra of PS/PMMA-CdS and PS/PMAA-CdS nanoparticles, each dispersed in DMF, provide information on the size and size distribution of CdS QDs in the micelle cores before and after the hydrolysis.The UV-vis spectrum of PS/PMMA-CdS (Figure 4.10 blue line) indicates that the QD size distribution before the hydrolysis reaction is similar to the previous PS/PMMA-CdS sample described in the Chapter 2 and 3, specifically, a bimodal QD size distribution was determined by two exciton shoulders observed at ~340 nm and ~450 nm, corresponding to populations of smaller and larger CdS QDs, respectively. From the absorption threshold, λ_{thresh} = 502 nm, a QD diameter of $2r_{CdS}$ = 6.2 nm is determined from an empirical equation based on the data of Henglein as described in Chapter 2. Following hydrolysis, the UV-vis spectrum of PS/PMAA-CdS (Figure 4.10, red line) is significantly different from that of PS/PMMA-CdS: the lower-wavelength shoulder corresponding to a population of QDs has disappeared. However, the absorption threshold, λ_{thresh} = 503 nm, representing the larger QDs in the distribution, did not change significantly. From λ_{thresh} = 503 nm, the corresponding diameter of CdS QDs following the hydrolysis reaction is $2r_{CdS}$ = 6.3 nm. This result suggests that QDs in the cores of PS/PMAA-CdS nanoparticles were annealed during the course of hydrolysis (i.e. 4 days at 110^{o}C), such that a population of smaller QDs in the cores underwent coalescence and merged with the larger population of QDs, whose size is restricted by the size of the micelle cores; Therefore, the hydrolysis reaction provided the additional benefit of narrowing the CdS QD size distribution, while converting a sample containing multiple-

QD cores to one in which most of the amphiphilic PS/PMAA-CdS nanoparticles contained a single QD per core (confirmed by TEM, as discussed in the next section).

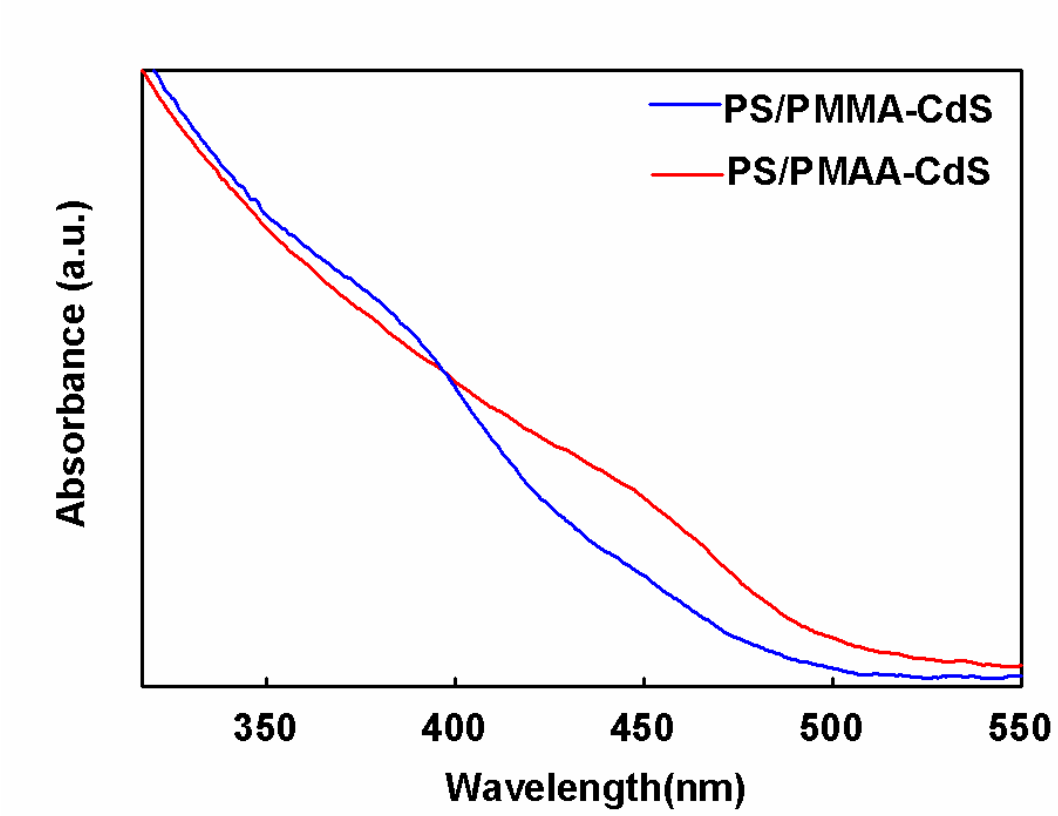

Figure 4.10. UV-vis absorption spectra of PS/PMMA-CdS (blue line) and PS/PMAA-CdS (red line) in DMF.

4.3.3.2. Transmission Electron Microscopy (TEM). The high electron density of CdS QDs relative to the polymer component of PS/PMAA-CdS provides good contrast for QD size distribution analysis by TEM. Figure 4.11a shows a typical region on a TEM grid on which PS/PMAA-CdS nanoparticles dispersed in THF have been cast, showing a population of distinct and well-separated QDs (dark dots). Unlike PS/PMMA-CdS

observed by TEM (described in Chapter 2), we find mainly single dark dots for each core rather than clusters of smaller dots, suggesting single-QD cores. The TEM results are also consistent with the unimodal QD size distribution suggested by the UV-vis result. Size distribution analysis (Figure 4.11b) was carried out based on measurement of 100 CdS QDs in several regions of the TEM grids, giving an average QD size of $2r_{CdS}$ = 5.8 nm, consistent with the result from UV-vis ($2r_{CdS}$ = 6.3 nm). The resulting QD diameter distribution is clearly unimodal, with a relative standard deviation of 6.9 %.

4.3.3.3. High Resolution TEM (HRTEM) and Powder X-ray Diffraction (XRD). An HRTEM image of a single isolated CdS QD in the core of PS/PMAA-CdS is shown in Figure 4.12a. The clear lattice planes reveal the crystallinity of the CdS QDs, although different lattice planes with different spacing are observed on the right and left side of the QD, indicating a polycrystalline QD. On the left-hand side of the image, a *d* spacing of 0.34 nm is measured, consistent with the (111) plane of a cubic (zinc blend) lattice. Furthermore, powder X-ray diffraction analysis of PS/PMAA-CdS was employed to examine the crystal structure of the CdS QDs. The XRD diffractogram (Figure 4.12b) also matched the cubic CdS X-ray diffraction pattern in the JCPDS database, with the exception of the peak observed at $2\theta = 30^{o}$. The *d*

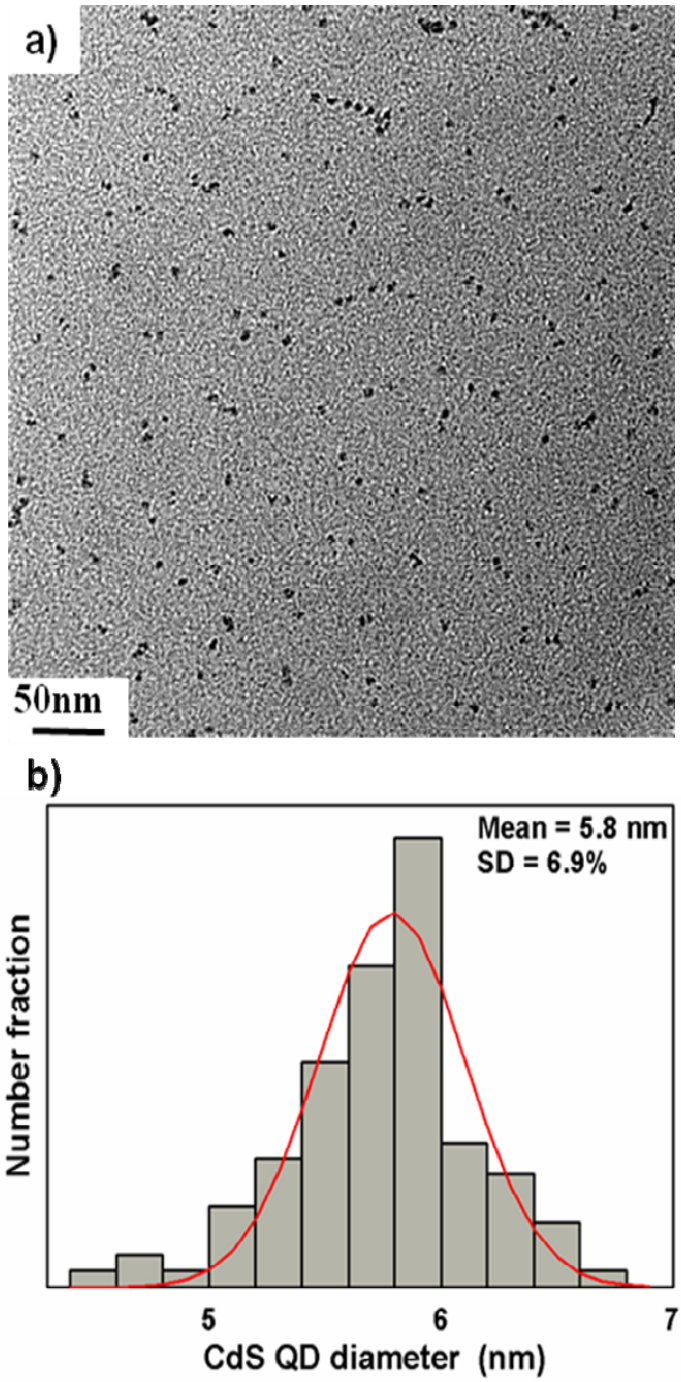

Figure 4.11. (a)Transmission electron micrograph (TEM) of PS/PMAA-CdS cast from a dilute (2 mg/mL) THF solution. (b) CdS QD size distribution determined from several TEM images such as that shown in (a).

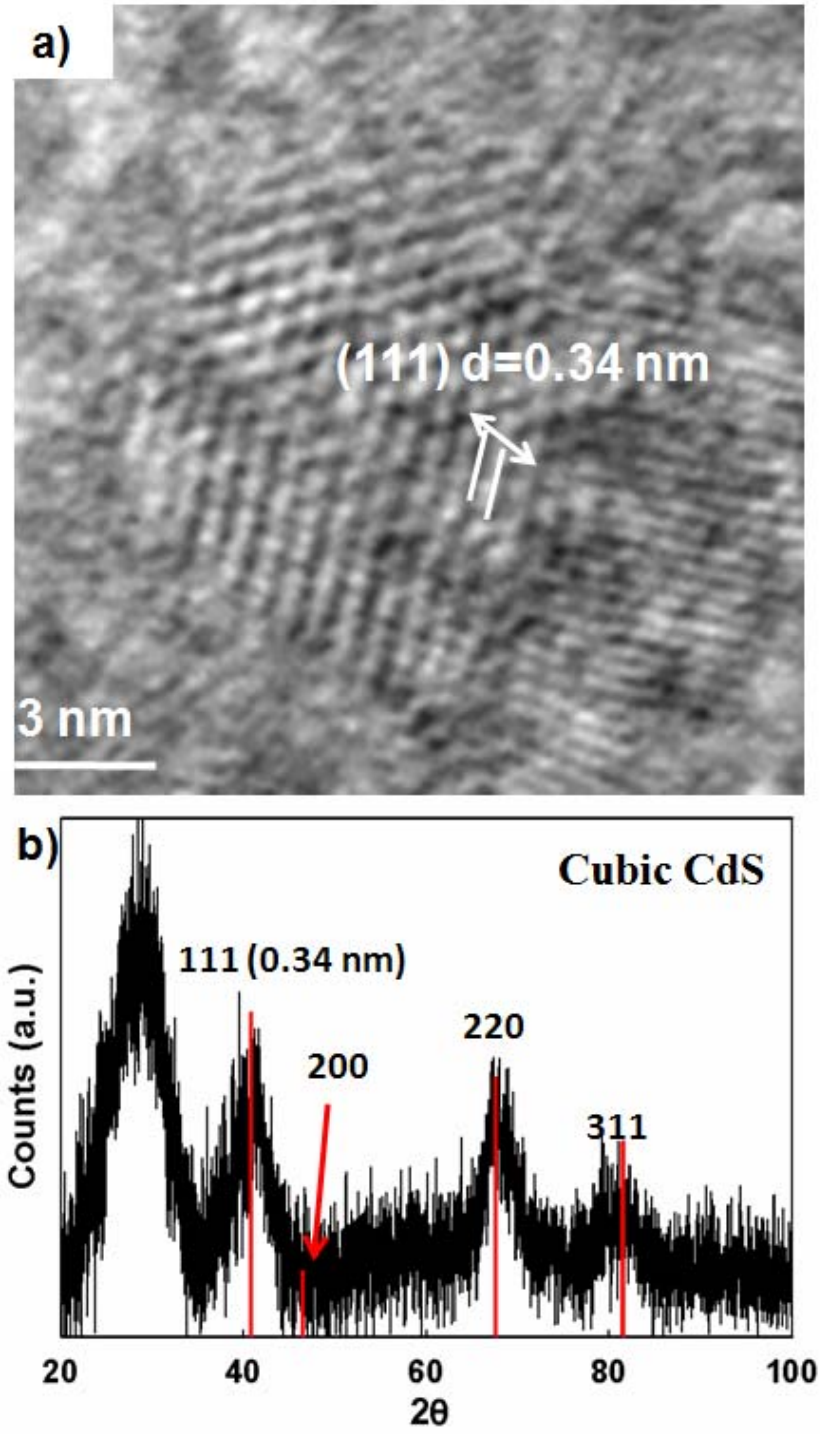

Figure 4.12. (a) High resolution transmission electron micrograph (HRTEM) of a single CdS QD for PS/PMAA-CdS cast from a dilute (2 mg/mL) THF solution. (b) X-ray powder diffraction pattern from PS/PMAA-CdS. The red lines correspond to peak positions for cubic CdS.

spacing corresponding to that peak is 0.56 nm, which may be associated with the mean distance between polymer chains (PS or PMAA) on the QD surface. The surface area per coronal chains for PS/PMMA-CdS nanoparticles was calculated to be 1.3 nm^2/chain in Chapter 2, which gives a mean distance of ~1 nm between chains, assuming a square lattice arrangement of chains. Considering the approximate nature of that calculation, and also the fact that PS/PMMA-CdS and PS/PMAA-CdS described in this chapter (unlike PS/PMMA-CdS in Chapter 2 and 3) are covalently crosslinked within the cores, which may decrease the distances between chains, the assignment of the $2\theta = 30^o$ diffraction peak to an interchains distance at the QD surface does not seem unreasonable.

4.3.3.4. Photoluminescence (PL). Figure 4.13 shows the normalized PL spectrum of PS/PMMA-CdS (blue line) and PS/PMAA-CdS (red line) dispersed in DMF, excited at λ_{ex} = 400 nm and with emission collected using a 420 nm long pass filter. Both spectra show a broad peak attributed to emission from CdS QD trap states, centered at ~620 nm and ~640 nm for PS/PMMA-CdS and PS/PMAA-CdS, respectively. The red-shift in trap state emission during the hydrolysis reaction is reasonable, considering the change in the QD size distribution determined by UV-vis. The coalescence of small QDs within the cores appears to result in a decrease in the mean energy of surface trap states.

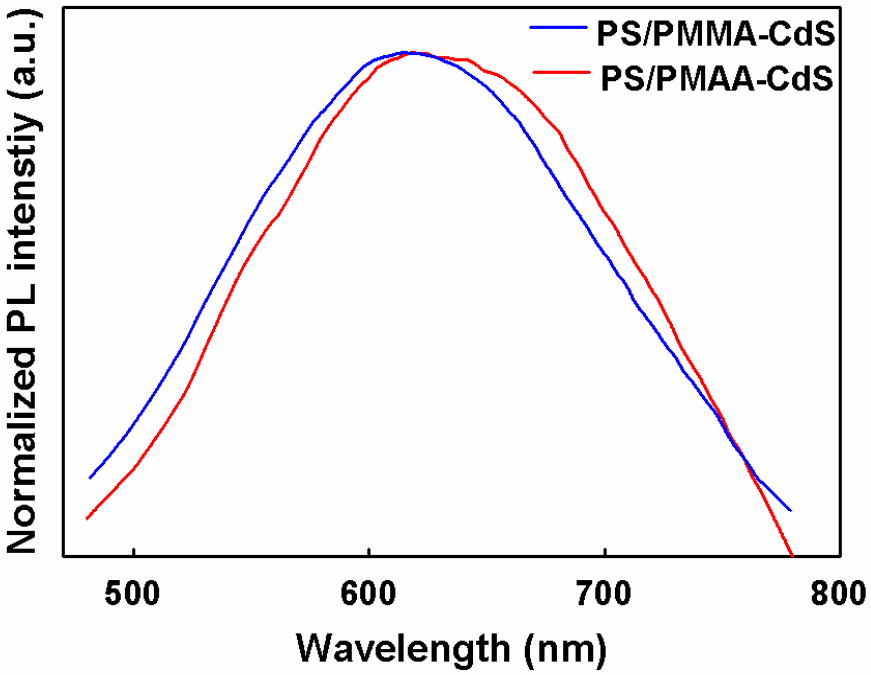

Figure 4.13. Photoluminescence spectra of PS/PMMA-CdS (blue line) and PS/PMAA-CdS (red line) in DMF, $\lambda_{ex} = 400$ nm.

4.3.3.5. Dynamic Light Scattering (DLS). The hydrodynamic diameter ($2r_h$) of PS/PMAA-CdS dispersed in DMF was determined from dynamic light scattering (DLS) measurements at multiple concentrations and at a scattering angle of 90°. The hydrodynamic diameter is an overall solution particle size, including both the QD-containing core and the solvent-swollen PS/PMAA coronal layer (as represented in Figure 4.14a). Figure 4.14b shows effective hydrodynamic diameters determined from a single-angle (90°) measurement of the diffusion coefficient at various concentrations; the mean $2r_h$ value for individual particles in DMF (i.e. without interparticle effects) is determined to be 51 nm via extrapolation to zero concentration. The polar organic solvent DMF was selected as a good solvent for both hydrophobic PS and hydrophilic PMAA

coronal chains, so that the PS/PMAA-CdS could be dispersed as individual particles. The determined hydrodynamic diameter of PS/PMAA-CdS in DMF is very consistent with sizes of PS/PMMA-CdS in solvents in which both blocks are soluble, as described in Chapter 2. This indicates that amphiphilic PS/PMAA-CdS exists as individual dispersed particles, and not aggregates, in pure DMF. We note that the GPC data for PS/PMMA-CdS and PS/PMAA-CdS (Figure 4.9) also indicates similar hydrodynamic sizes in THF before and after hydrolysis of the PMMA chains, based on almost identical elution volumes for the main peaks in Figure 4.9b and 4.9c. Therefore, conversion of the PMMA chains to PMAA does not lead to PS/PMAA-CdS self-assembly in either pure DMF or THF. Both of these polar organic solvents are therefore appropriate starting media for PS/PMAA-CdS self-assembly via drop-wise water addition.

4.3.4. Self-assembly of PS/PMAA-CdS Nanoparticles into QD/Polymer Aggregates of Various Morphologies.

4.3.4.1. Spherical Supermicelles (c_o = 0.5 wt% DMF/Water and THF/Water, Immediate Quenching Method). The self-assembly of PS/PMAA-CdS nanoparticles was first investigated in DMF/water and THF/water mixtures, starting with an initial polymer concentration of c_o = 0.5 wt% and using the immediate quenching method described in section 4.2.5 (and represented in Figure 4.15). In those experiments, PS/PMAA-CdS nanoparticles was dispersed in either in DMF or THF, to a concentration of c_o = 0.5 wt%, yielding clear yellow solutions. The solution clarity suggests an absence

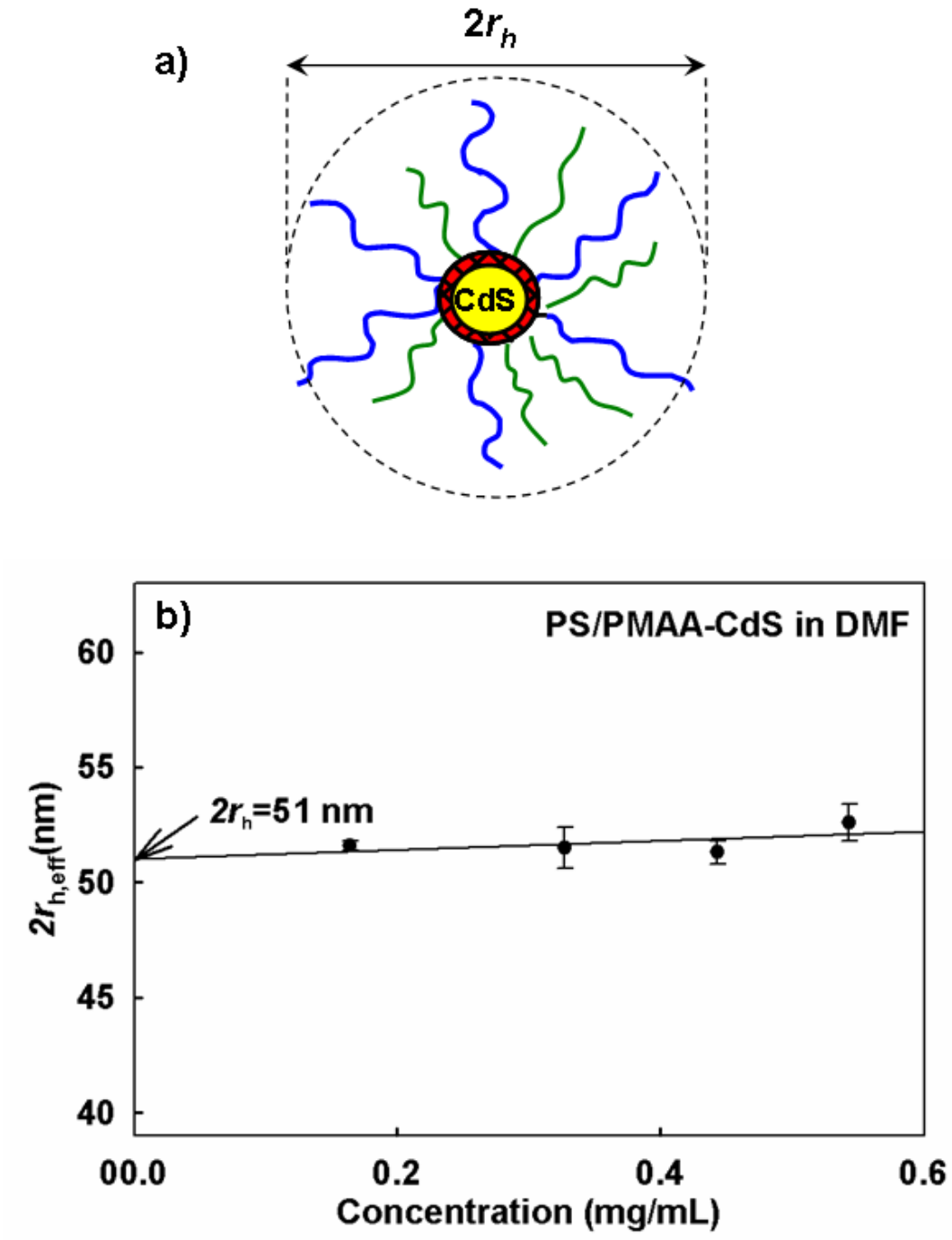

Figure 4.14. The plot of effective $2r_h$ vs concentration for PS/PMAA-CdS in DMF.

of particle aggregation as confirmed by GPC and DLS for the THF and DMF solutions, respectively. In both of cases, steady drop-wise water addition effected a sudden and obvious increase in turbidity at the critical water content (cwc), indicating PS/PMAA-CdS self-assembly into aggregates. In DMF/water, the observed cwc was 6.0 wt% water, while in THF/water the cwc was 12 wt% water. Since aggregate formation arises due to phase separation of hydrophobic PS blocks as the solvent quality more added water is required decrease, to induce aggregation when the initial medium is a better solvent for PS.[29] Of DMF and THF, THF is less polar and therefore a better solvent for PS, such that the cwc is higher in THF than DMF for the same initial polymer concentration.

As shown in Figure 4.15, water is continuously added at a steady rate above the cwc, up to a water concentration where the chain dynamics are sufficiently slow such that the aggregate morphologies cannot change in response to environmental changes on experimental time scales. At this stage, the aggregate morphologies are kinetically frozen, and the self-assembly process is essentially quenched. The slowing of chain mobility with increasing water content above the cwc is due to the progressive leaching of plasticizing organic solvent from the PS cores of the aggregates, in response to changing chemical potential outside the aggregates. Since THF is a better solvent for PS than DMF, and therefore partitions more strongly into the aggregates, higher water contents are required to quench self-assembly in THF than in DMF. Based on the work of Eisenberg and coworkers,[30-36] water was added at a steady rate to 25 wt% in DMF/water and 75 wt% in THF/water, at which stage the aggregates were considered to be essentially frozen. To further ensure queching in THF/water, the colloids were further dumped into 5× excess water after 75 wt% water had been reached by steady drop-wise addition.

Finally, the kinetically stable aggregates were transferred into purely aqueous media by dialysis against deionized water for 5 days, which removed residual organic solvent.

Figure 4.16 shows TEM images of the aggregates formed from water addition to DMF and THF with the same initial PS/PMAA-CdS concentration c_o = 0.5 wt%. The aggregates formed in DMF/water (Figure 4.16a) are spherical particles with mean diameter 34 nm and a relative standard deviation of 15 %, as determined by size distribution analysis of 100 particles from several TEM images (Figure 4.16c). These colloidal aggregates appear to be supermicelles produced from self-assembly of PS/PMAA-CdS via aggregation of PS chains above the cwc. The core of the supermicelles should therefore consist of PS chains, with PMAA chains in the corona oriented towards the aqueous medium. High-magnification TEM images (inset of Figure 4.16a) of these supermicelles show typically 1 to 2 CdS QDs (dark dots) localized at the interface between the PS cores (grey spheres) and the PMAA corona (invisible in TEM images), suggesting supermicelles with very low aggregation numbers of ~ 2 PS/PMAA-CdS nanoparticles.

In contrast, much larger spherical supermicelles were formed in THF/water (Figure 4.16b), with a mean diameter of 140 nm and a relative standard deviation of 36 % (Figure 4.16d) , the much higher PS/PMAA-CdS aggregation numbers are evinced by the large number of QDs clearly surrounding each PS core. In systems of PS-*b*-PAA self-assembly in mixture of water and polar organic solvents, it has been shown previously that larger aggregates tend to form when the initial dielectric constant of the solvent is lower (i.e. less polar solvents); this is explained by a combination of increased stretching of PS blocks due to increased solvent swelling in the core, and decreased electrostatic

repulsion between PAA blocks in the corona.[30-37] Here, we have shown for the first time that similar size control based on initial solvent selection can be exercised for QD/polymer aggregates via amphiphilic self-assembly of PS/PMAA-CdS.

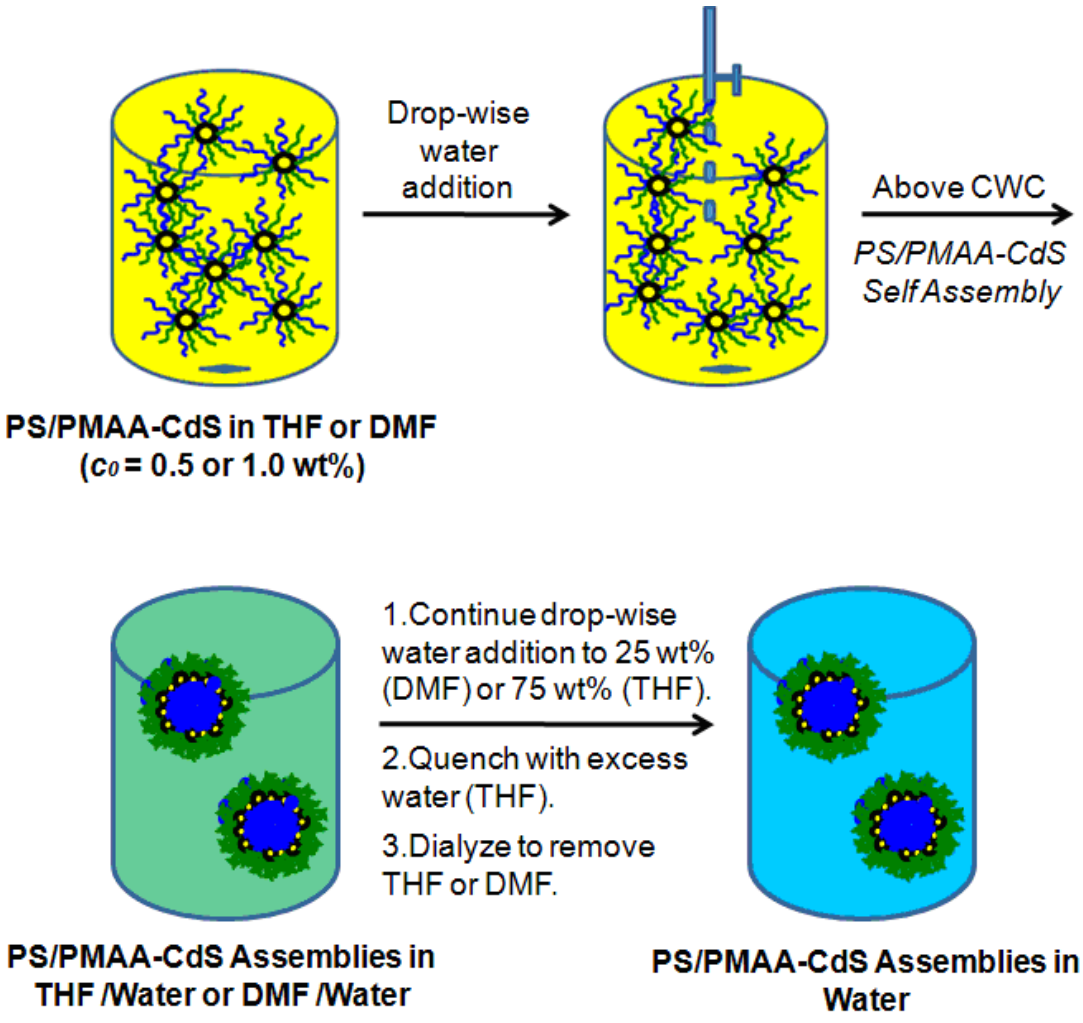

Figure 4.15. Schematic showing steps for self-assembly of PS/PMAA-CdS in DMF/water and THF/water (immediate quenching method).

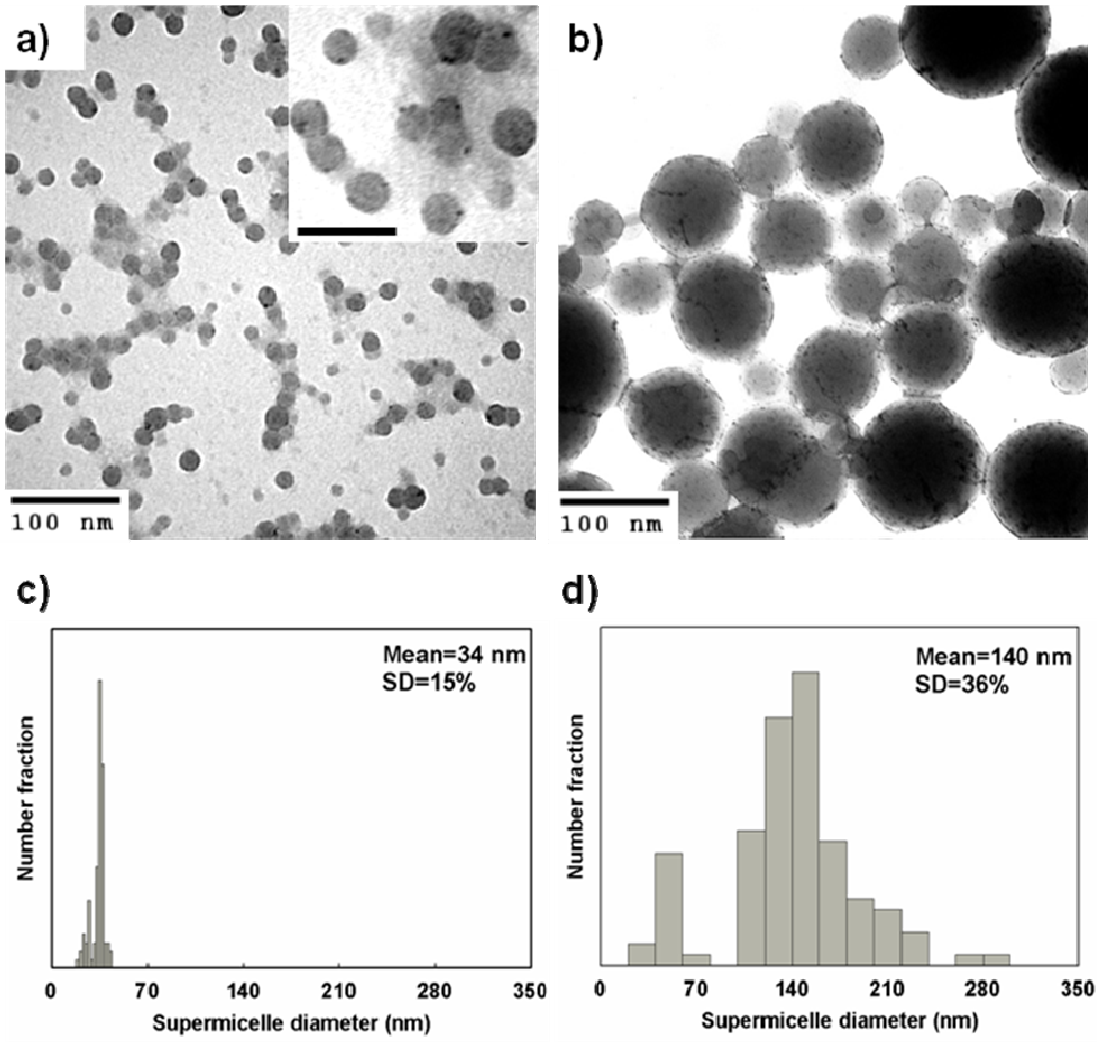

Figure 4.16. TEM images of QD/polymer aggregates (spherical supermicelles) of PS/PMAA-CdS obtained from initial polymer concentration c_o = 0.5 wt% in DMF (a) and THF (b). The scale bar in the inset of (a) is 100 nm. Aggregate size distributions based on measurement of 100 particles for (a) and (b) are shown in (c) and (d), respectively.

It is important to note that TEM images of colloids deposited on TEM grids, such as those shown in Figure 4.16, represent 2D projections of 3D objects, such that the 3D spatial distribution of QDs cannot be easily determined. To confirm that the QDs are localized at the surface of the PS cores within spherical supermicelles, we obtained microtomed cross-sections of spheres formed in THF/water. The TEM image of the cross-sections (Figure 4.17a) confirms the proposed organization of QDs within the spherical supermicelles. In addition, dark-field TEM images of large spherical supermicelles from THF/water (Figure 4.17b), in which high-electron density QDs are visible as bright spots and less-electron dense PS domains appear grey, more clearly show a regular distribution of discrete QDs on the supermicelle core surfaces. From cross-section TEM images, the surface density of QDs is ~1000/μm^2. As well, based on measurement of 100 CdS QDs from cross-setion TEM images, we determined the QD size distribution within spherical supermicelles formed in THF/water (Figure 4.17d), with a mean size of 5.1 nm in reasonable agreement with that determined for QDs in PS/PMAA-CdS prior to self-assembly (5.8 nm).

The formation of spherical supermicelles suggests that the self-assembly behavior of PS/PMAA-CdS is similar to amphiphilic block copolymers, which have an anisotropic distribution of hydrophilic and hydrophobic segments. In Chapter 2, we showed that the PS and PMMA chains are statistically distributed in the corona of PS/PMMA-CdS dispersed in polar organic solvents using NOESY proton NMR experiments. Since GPC results discussed previously indicate the core-crosslinked particles retain their general structure during hydrolysis, PS and PMAA chains should also be statistically distributed in the corona of PS/PMAA-CdS dispersed in pure THF or DMF, with an isotropic

distribution of hydrophobic and hydrophilic segments. Figure 4.17c presents the proposed mechanism of spherical supermicelle formation. The left-hand side of the schematic shows individual PS/PMAA-CdS with an isotropic distribution of PS and PMAA coronal chains in pure DMF or THF. Upon addition of water, the solvent environment becomes increasingly unfavorable to PS chains; eventually PS chains collapse into a globular conformation, and local phase separation of PS chains and PMAA chains within the corona of each particle gives rise to an anisotropic Janus nanoparticle. This local phase separation is possible due to the conformational flexibility of PS and PMAA chains within PS/PMAA-CdS, despite the fact that junctions between coronal chains and the core surface cannot rearrange due to crosslinking. Once the PS/PMAA-CdS nanoparticles are in the Janus conformation, anisotropic interparticle interactions above the cwc give rise to spherical supermicelles with PS cores, PMAA coronae, and CdS QDs localized at the interface.

Following formation of the spherical supermicelles, the collapsed PS chains will adopt a stretched conformation in order to extend to the centers of the supermicelle cores. The extent of PS stretching can therefore be determined by comparing the average PS

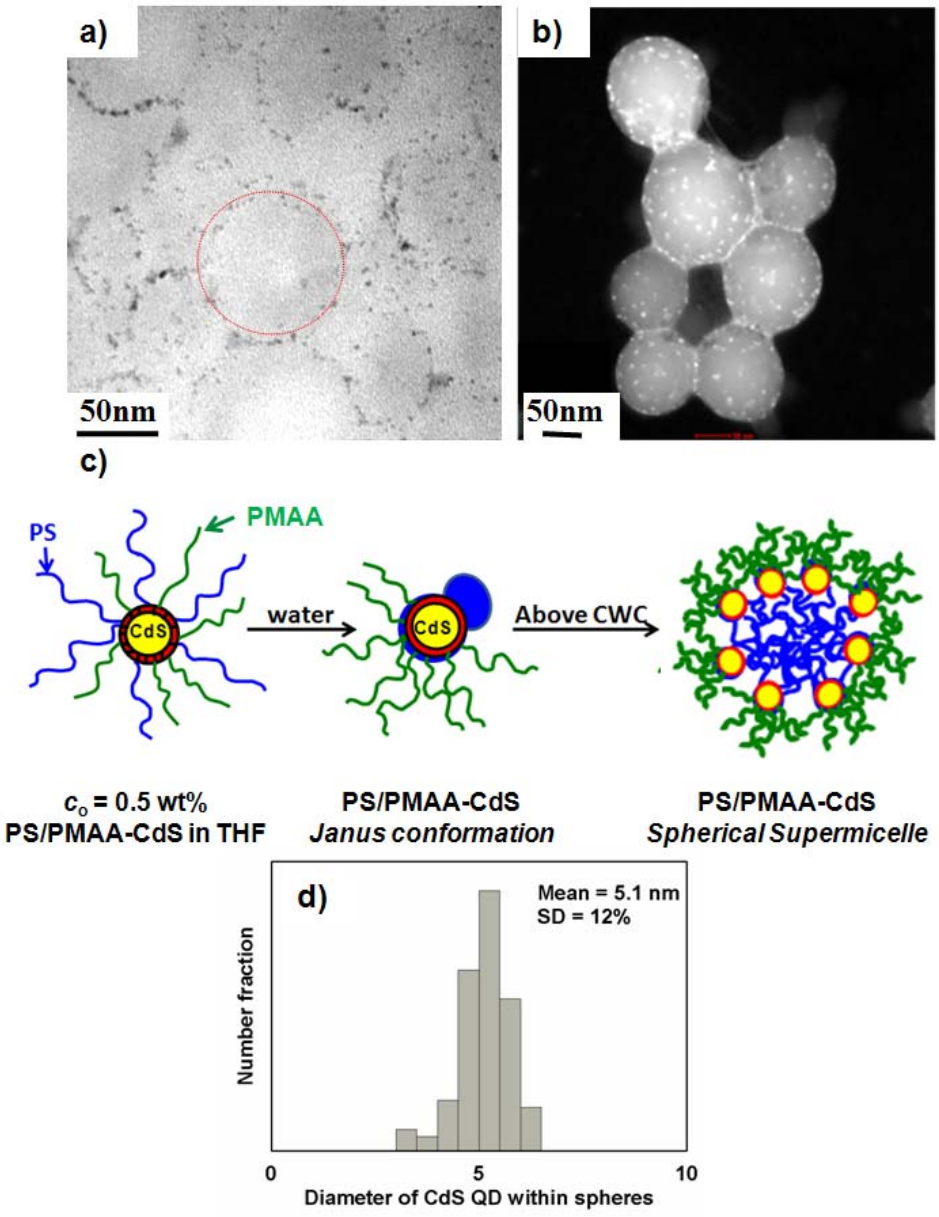

Figure 4.17. TEM images of QD/polymer aggregates (spherical supermicelles) obtained from initial polymer concentration c_o = 0.5 wt% in THF: (a) TEM image of PS/PMAA-CdS cross-section film; (b) dark-field TEM image. (c) Proposed self-assembly process for QD/polymer spherical supermicelles in mixtures of water and polar organic solvents. (d) QDs size distributions based on measurement of 100 particles for (a) and other TEM images.

chain dimension in the supermicelles (equal to the mean supermicelle core radius) with the fully-stretched dimension of a PS chain of 296 repeat units (74 nm, as calculated in Chapter 2)

$$\text{PS chain extension (\%)} = r_{\text{PS core}}/74\text{ nm} \times 100\% \quad (\mathbf{4.1})$$

Based on TEM results described in Figure 4.16, this gives PS chain extensions of 23% and 95% in spherical supermicelles formed in DMF/water and THF/water, respectively. We point out that this analysis neglects the small number of PS segments that must wrap around the core surface during local intraparticle phase separation of PS and PMAA chains due to covalent connectivity between PS chains and the core.

4.3.4.2. Worm-like Supermicelles (c_o = 1.0 wt%, THF/water, Immediate Quenching Method). For block copolymer systems, such as PS-*b*-PAA in polar organic solvent/water mixtures, it has been shown that the observed morphology is dependent on the initial polymer concentration; for example, for solutions of a given PS-*b*-PAA copolymer in DMF with different initial concentrations, the observed morphology upon water addition will be spheres, rods or vesicles in order of increasing initial concentration.[37-40] This trend is explained on the basis of increasing micelle aggregation number as the initial polymer concentration increases as described by Equation 2:[39,40]

$$N_{agg} = 2\ (c_o/cmc)^{1/2} \qquad \textbf{(4.2)}$$

As aggregation numbers increase with increasing c_o (Equation 2), chain stretching of PS in the cores also increases, which progressively lowers the entropy. Therefore, with increasing N_{agg}, changes in morphology will occur in order to lower the curvature at the core/solvent interface, which relaxes the stretching of PS chains.[30-37] Considering these well-established concepts for block copolymer self-assembly, it was of interest to determine the change in morphology for QD/polymer aggregates in a given solvent system by changing the initial concentration of PS/PMAA-CdS. Therefore, we increased the initial concentration from c_0 = 0.5 wt% to c_0 = 1.0 wt% in both DMF and THF, and determined the aggregate morphologies obtained via water-induced self-assembly, using the method of immediate quenching and dialysis. Compared to the lower initial polymer concentration (c_0 = 0.5 wt%),cwc values were slightly lower for c_0 = 1.0 wt% in both DMF (5 wt%, compared to 6 wt%) and THF (10 wt%, compared to 12 wt%). This consistent with results on the effect of initial polymer concentration on cwc values previously determined for systems of PS-*b*-PAA. [30-37]

For DMF/water, c_o = 1.0 wt%, we observe spherical supermicelles that are larger (61 nm) than those observed for c_o = 0.5 wt% in the same solvent system (34 nm) (not shown). However, for THF/water, c_o = 1.0 wt%, a dramatically different supermicelle morphology is observed compared to c_o = 0.5 wt%. TEM images of the resulting worm-like supermicelles (or "worms") are shown in Figure 4.18b. As shown in Figure 4.18a, the worms are mainly linear aggregates with high aspect ratios, although some branching is observed at the ends of worms, resulting in Y-shape aggregates. The lengths of worms are very polydispersive, ranging from ~200 nm to ~10 μm; the widths of the worms are

less polydisperse than the lengths, but show some variability between the worms and also along the length of a given worm, with an average width of 339 nm and a relative standard deviation of 38% (Figure 4.19c). Figure 4.18a also shows that the worm-like supermicelles consist of discrete segments along their length, and closely resembling earth worms in their appearance. Individual segments consist of grey regions separated by darker lines of higher electron density. The high-magnification image of a worm in Figure 4.18b indicates that the darker lines between the segments are regions of discrete close-packed QDs; with a mean spacing of 106 nm (sd = 6%) between QD regions (Figure 4.19d). As will be discussed later, each worm segment consists of a bilayer of PS chains oriented along the long axis of the worm; therefore, from the mean length of a single segment (spacing between QD regions), the percentage of PS extension was calculated to be 72%, less than that found in spheres for c_0 = 0.5 wt% in the same solvent system.

A TEM image of a cross-section of an individual worm is shown in Figure 4.18c, indicating a periodic internal structure with regularly spaced QD regions. Moreover, the electron density contrast reveals the relative spatial distribution of PS and PMAA within the worm-like supermicelles. The dark grey regions between the close-packed QDs are attributed to PS. The lighter-coloured matrix surrounding the close-packed QDs is attributed to the less electron dense PMAA. The internal structure of worms is therefore very reminiscent of the lamellar morphology from microphase separation of symmetric block copolymers, with alternating PS and PMAA regions and QD localized within the PMAA phase. Figure 4.18d shows a dark field TEM image, clearly showing segmented

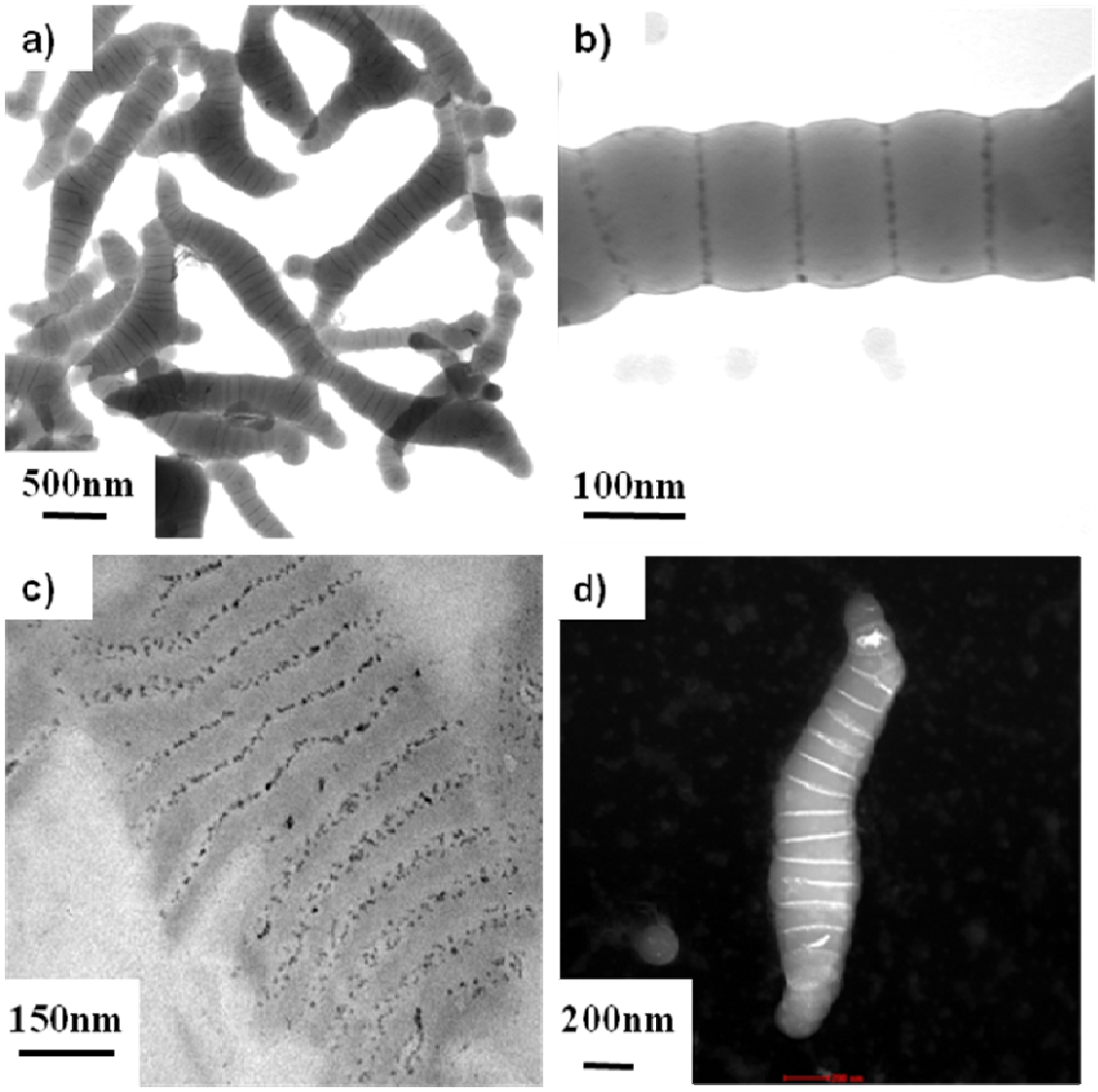

Figure 4.18. TEM images of QD/polymer aggregates (worm-like supermicelles) of PS/PMAA-CdS obtained from initial polymer concentration c_o = 1.0 wt% in THF: (a) low and (b) high-magnification TEM images; (c) TEM image of cross-section film; (d) dark-field TEM image.

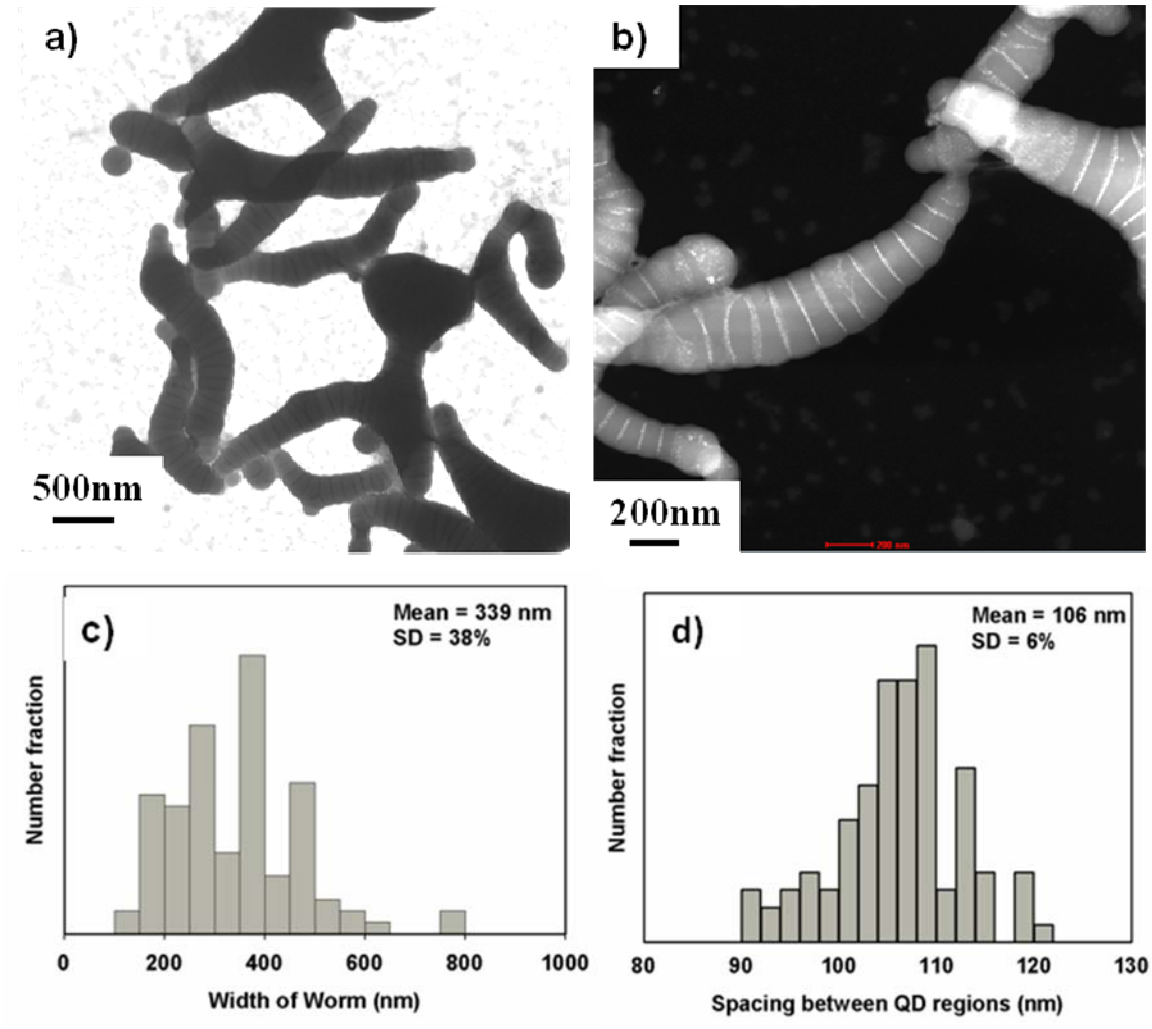

Figure 4.19. TEM images of QD/polymer aggregates (worm-like supermicelles) of PS/PMAA-CdS obtained from initial polymer concentration c_o = 1.0 wt% in THF: (a) low -magnification TEM images and (b) dark field TEM image; (c) TEM image of cross-section film; (d) dark-field TEM image. (c) and (d) are size distributions of width of worm and spacing between QD regions measured from 100 particles or regions in several TEM images.

structures of worm-like supermicelles with bright QD regions regularly spaced along the worm. Based on cross-section TEM images such as that shown in Figure 4.18c, the mean QD diameter within the worms was determined to be 5.1 nm, consistent with QD sizes in individual PS/PMAA-CdS.

In order to further probe the 3D structure of the worm-like supermicelles by TEM, several aggregates were imaged in dark-field mode at various rotation angles of the sample holder (Figure 4.20). The dashed line in each image indicates the axis of rotation, with rotation angles of 0^o (Figure 4.20a), 30^o (Figure 4.20b), and 50^o (Figure 4.20c). Figure 4.20a at 0^o shows the side view of the worm in the centre of image, in which QD regions resemble dense lines. As the aggregate is rotated (as indicated in the schematic), the QD regions resemble ellipsoid shapes (Figure 4.22b), and then QD regions become less distinct (Figure 4.20c) as the worm long axis is rotated at an increasing angle out of the plane of the image. This suggests that the regions of close-packed QDs are two-dimensional disks, regularly spaced along the length of worms.

To confirm the presence and specific location of CdS QDs within the worms, we applied TEM with energy dispersive X-ray (EDX) spectroscopy which allowed local elemental analysis in different regions of the worm-like supermicelles (Figure 4.21). The energy resolution of EDX used in the instrument is 1.36 eV. A dark-field TEM image of a typical worm is shown in Figure 4.21a with three red spots indicating three different regions of elemental analysis: (1) within an electron-dense disk, (2) within a segment

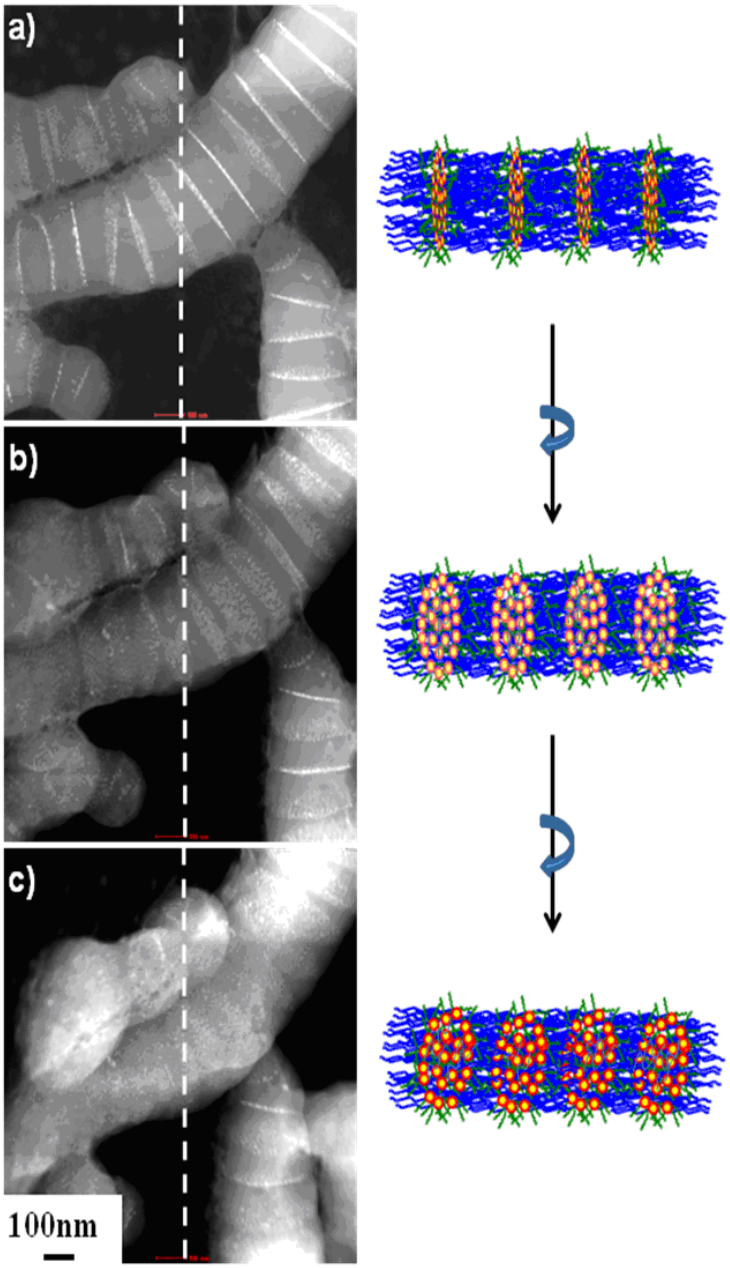

Figure 4.20. Dark-field TEM images of QD/polymer aggregates (worms) for different angles of rotation of the TEM sample holder (dashed lines indicate axis of rotation) : (a) 0^{o}; (b) 30^{o}; (c) 50^{o}. The right-hand side shows a schematic of the 2D projections of the proposed supermicelle structures at corresponding angles of rotation.

between two disks, and (3) outside of the worm-like supermicelle. The accompanying EDX spectra (Figure 4.21b) clearly show strong elemental contribution of Cd and S in region 1 (within a disk) and only extremely weak Cd and S signal in region 2 (between two disks), with no detectable Cd and S signal in the background region (outside of the supermicelle). We further confirm the localization of CdS QDs within the reguarly spaced disks by obtaining an EDX intensity profile of the Cd L-peak and the S K-peak along a line following the long axis of a worm (Figure 4. 22a). The Cd and S signals show clearly overlapping oscillations in intensity along the worm long-axis, with maxima corresponding to the disks of high electron density, confirming the localization of CdS QDs within these regions. The mean periodicity in the oscillation of Cd and S signal in Figure 4.22b is ~110 nm, which is in good agreement with the mean distance between disk regions determined from TEM images of multiple worm-like supermicelles (106 nm).

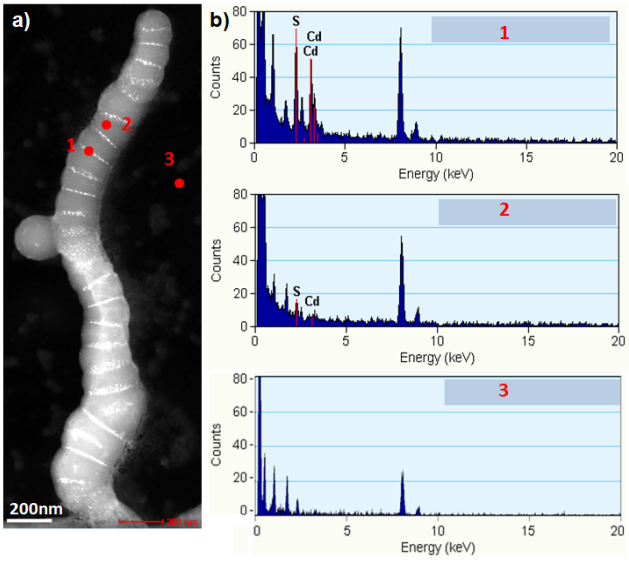

Figure 4.21. (a) Dark-field TEM image of QD/polymer aggregate (worm) (b) Energy-dispersive X-ray spectra corresponding to regions 1,2 and 3 indicated by red spots in (a).

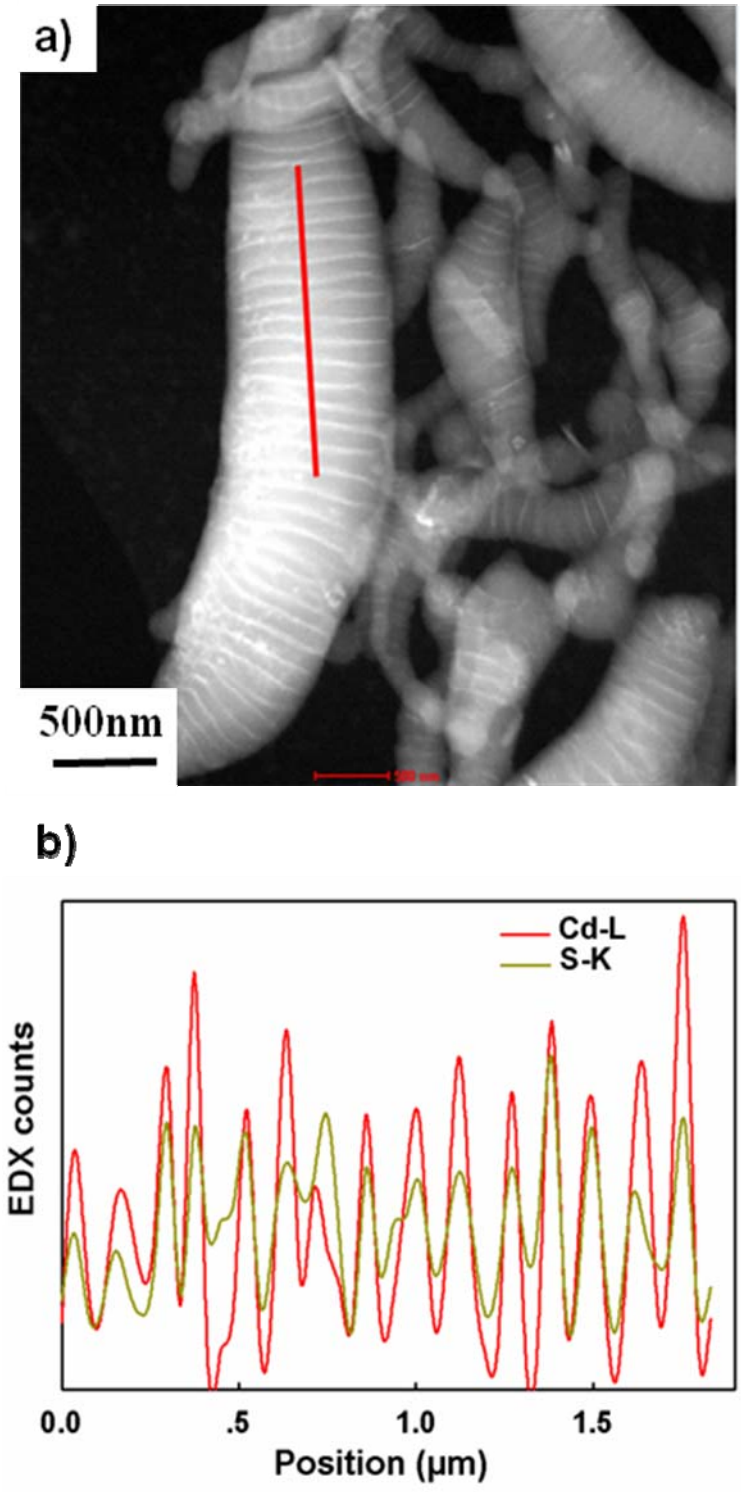

Figure 4.22. (a) Dark-field TEM image of QD/polymer aggregates (worms). (b) EDX profiles corresponding to red line indicated in (a).

Using AFM in contact mode, the 3D topology of worm-like supermicelles after disposition onto glass substrates was determined. Since the PS regions of the supermicelles are below their glass transition temperature ($T_g \approx 100^oC$) at room temperature, it is reasonable to assume that the micelle shape will not be significantly affected by solvent evaporation or interaction with the substrate. An AFM image of a typical worm is shown in Figure 4.23a, with accompanying height profile and corresponding 3D image shown in Figure 4.23b. Both 2D and 3D AFM images clearly show the segmental structure of worms with periodic lower regions separating higher segments. We believe that the thinner low regions correspond to the QD disks. The disk regions may have a lower relative height due to the localization of solubilized PMAA coronal chains in these regions (as discussed in the subsequent section), which will collapse to the surface of the worm upon water evaporation. Measurement of worm height (h) and full-width-at-half-maximum (FWHM) width (w) was carried out for 100 aggregates from AFM images. The resulting distributions of h and w are shown in Figure 4.23c and 4.23d, respectively. The mean values of h = 500 nm and w = 500 nm were determined from the distributions, confirming that the worms have approximately cylindrical shape. Although the 3D structure of the worm in Figure 4.23b appears somewhat distorted relative to a cylinder, we believe that this is in part due to an artifact associated with the shape of the AFM tip. We also note that the worm width determined by AFM (500 nm) is ~30% greater than the width determined by TEM (339 nm); this may be due to the collapsed PMAA chains on the surface of worms following water evaporation, which will contribute to the topographic width of worms by AFM, but will be invisible by TEM due to their low electron density.

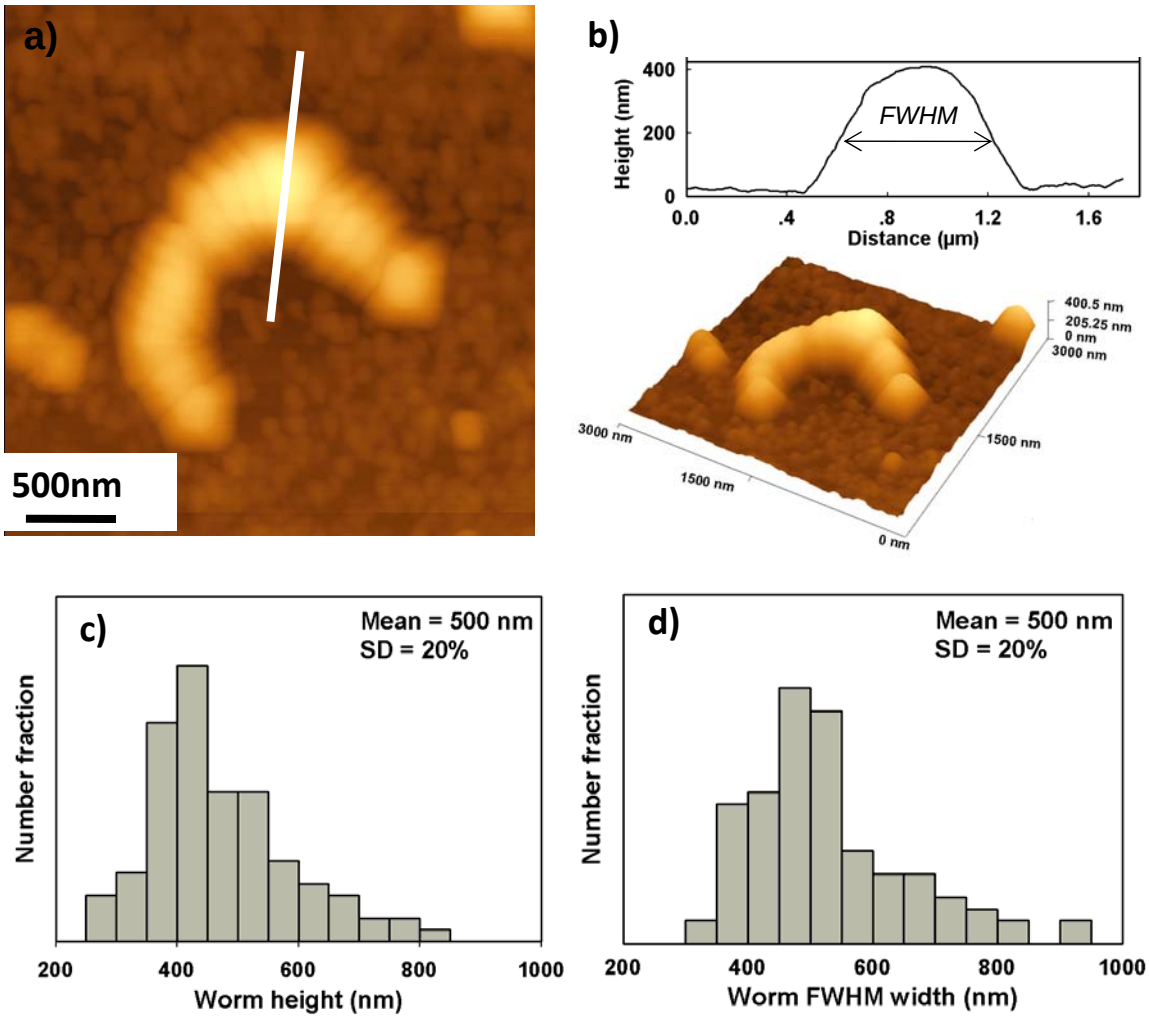

Figure 4.23. (a) AFM images of QD/polymer aggregate (worm) cast on glass from aqueous solution. (b) Surface feature topology profile for white line in (a). and 3D obtained from (a); (c) Height and (d) FWHM width distributions determined from 100 measured aggregates in several AFM images.

The worm-like supermicelles are photoluminescent, due to emission of localized QDs. Laser scanning confocal fluorescence microscopy (LSCFM) images of worms deposited on glass are shown in Figure 4.24, obtained using λ_{ex} = 488 nm and λ_{em} > 515 nm corresponding to trap state absorption and emission of CdS QDs, respectively. Individual worms clearly show photoluminescence under these conditions (Figure 4. 24a). A higher magnification image of a worm (Figure 4.24b) shows that the photoluminescence intensity along the length of the aggregate is not uniform, but patchy. The optimal spatial resolution of the LSCFM instrument is ~200 nm in the xy plane, such that localized photoluminescence from discrete CdS QD disks with ~100 nm spacing cannot be resolved. However, the patchy nature of QD photoluminescence along the worm in Figure 4.24b is likely the result of the internal organization of QDs determined by TEM and EDX.

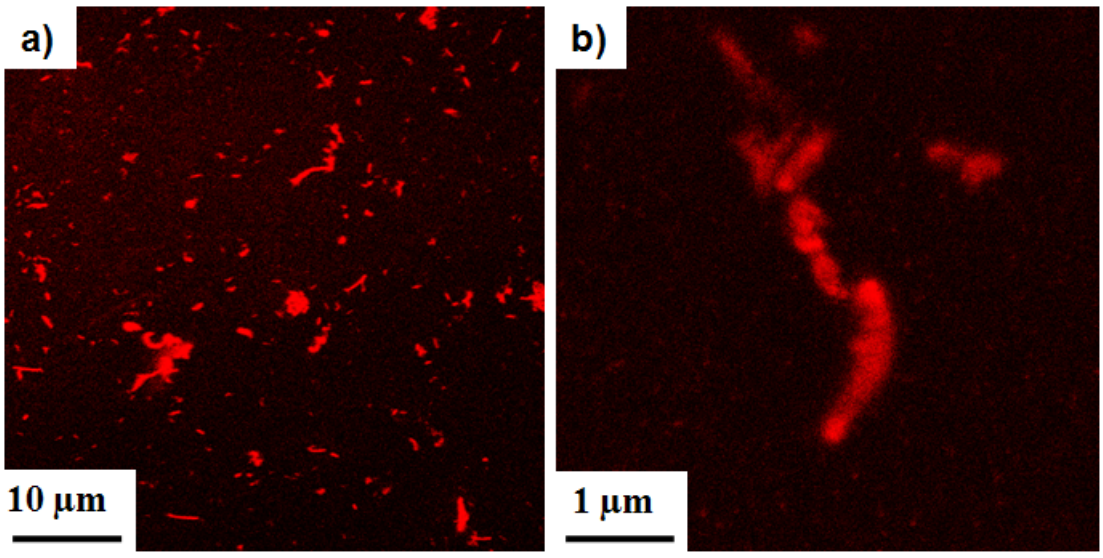

Figure 4.24. Laser scanning confocal fluorescence microscopy (LSCFM) images of QD/polymer aggregates (worms). λ_{ex} = 488 nm, $\lambda_{em} \geq$ 515 nm.

4.3.4.3. Self-assembly of PS/PMAA-CdS into Large Internally-Structured Aggregates (Continents) via Annealing Method. The worms described in the previous section, produced via steady dropwise addition of water to c_0 = 1.0 wt% PS/PMAA-CdS in THF, begin to form at water contents above the cwc (~10 wt% water). However, as water was continuously added above the cwc, the thermodynamic state of the system changed and the dynamics of aggregate growth progressively slowed, until the supermicelles became kinetically frozen at some water content below the target concentration of 75 wt%. Therefore, the observed worms could either represent structures which formed under equilibrium conditions at a particular water content above cwc, and then became kinetically frozen, or else structures that formed far from equilibrium before being trapped at high water contents. To provide some insight into the thermodynamic and kinetic contributions of worm-like supermicelle formation, and also to determine their mechanism of formation, we carried out PS/PMAA-CdS self-assembly experiments in different THF/water mixtures via the annealing method. In these annealing experiments, four separate solutions of PS/PMAA-CdS at c_o = 1.0 wt% in THF were prepared. To each of the four polymer solutions, water was added dropwise at a rate of 10 μL/10 s up to a different water concentration above the cwc: 11 wt%, 15 wt%, 25 wt% and 50 wt% water. In contrast to previously described experiments in which water was continuously added to 75 wt%, water addition was stopped at the indicated water content and then all four solutions were left to anneal with moderate stirring for 2 weeks, before finally quenching in excess water then dialyzing to remove residual THF.. The resulting colloids therefore provide “snapshots” of supermicelle states at different water contents above the cwc. For lower water contents, the expected growth dynamics should be fast

relative to the annealing time, allowing the supermicelles to reach equilibrium, however, we cannot rule out the possibility of kinetic contributions to the structure of aggregates annealed at higher water contents.

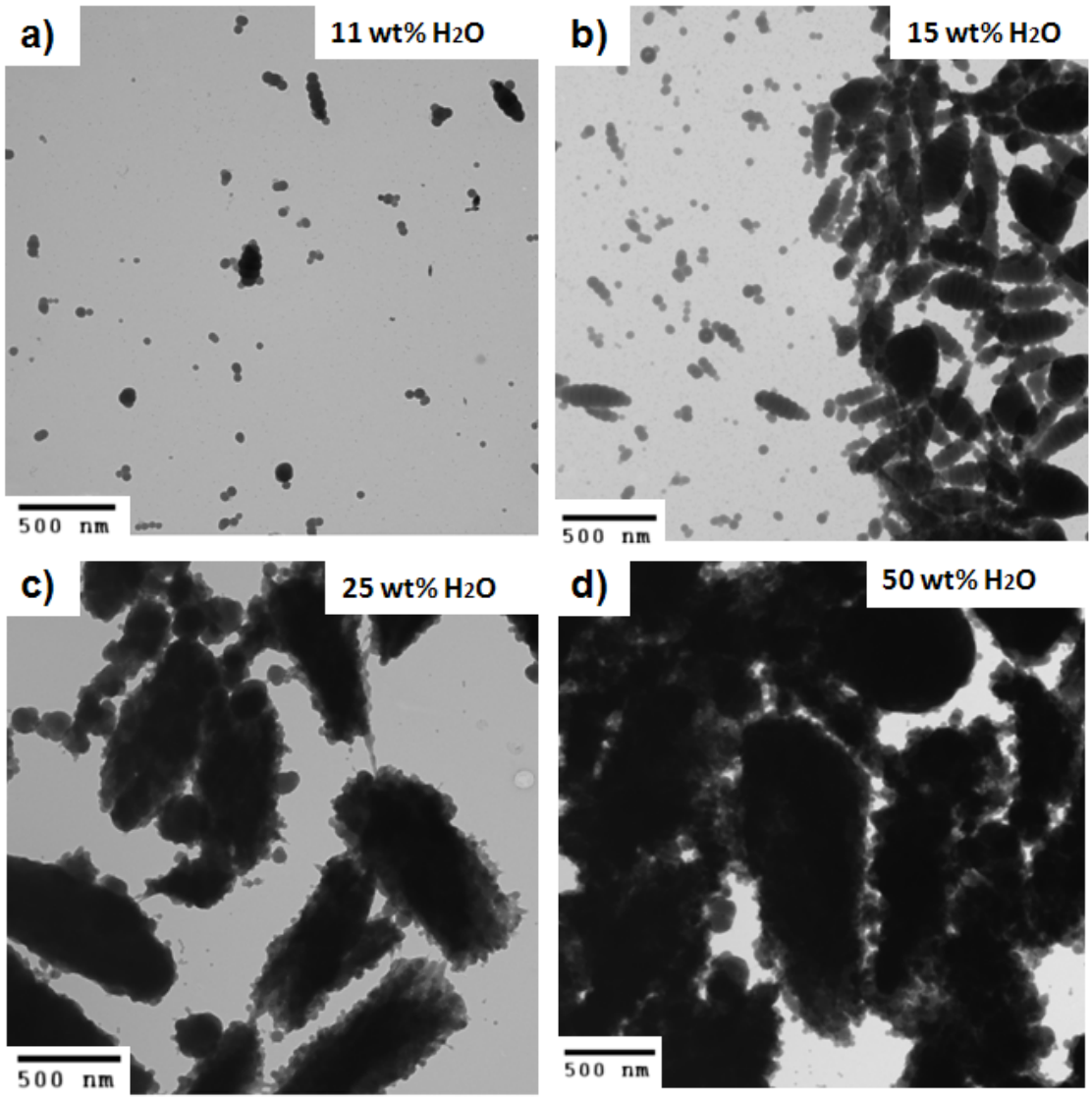

Figure 4.25. TEM images of QD/polymer aggregates from self-assembly of PS/PMAA-CdS in THF/water mixtures (c_o = 1.0 wt%) at different water contents. Colloids were annealed at the indicated water contents for two weeks (annealing method) before final quenching and dialysis.

Figure 4.25 shows PS/PMAA-CdS aggregates obtained from the annealing experiments in THF/water at various water contents. At 11 wt% water (Figure 4.25a), a mixture of small spheres, chains of spheres, and short worms were observed. At 15 wt% water (Figure 4.25b), spheres, chains of spheres, and largers and thicker worms formed; we observe that many worm-like aggregates at this water content are thicker in the middle and thinner at the ends. At 25 wt% water (Figure 4.25c), very few individual spheres or worms were observed, and the predominant aggregate morphology was a relatively large continent-like structure. The height of these aggregates obtained from AFM analysis (not shown) is ~200 nm. From several TEM images, the widths and lengths are extremely polydisperse, although aggregate dimensions up to ~5 μm were observed. At 50 wt% water (Figure 4.25d), similar, though somewhat larger, continents were found. Many continents formed at 25 wt% and 50 wt% water had an approximately rectangular shape.

We did not observe these large continent-like aggregates for the same initial polymer concentration (c_0 = 1 wt%) when water was added at a steady rate to 75 wt% water, indicating that continents formed on a slower time scale than was provided by the immediate quenching method. We further note the general trend with increasing water content under annealing conditions for worms to grow thicker as well as longer, leading to continent-like aggregates at ~25 wt% water. However, for water added continuously to 75 wt%, we observed long and relatively thin worms, indicating worm-like supermicelles were kinetically trapped before evolution to continents had time to occur.

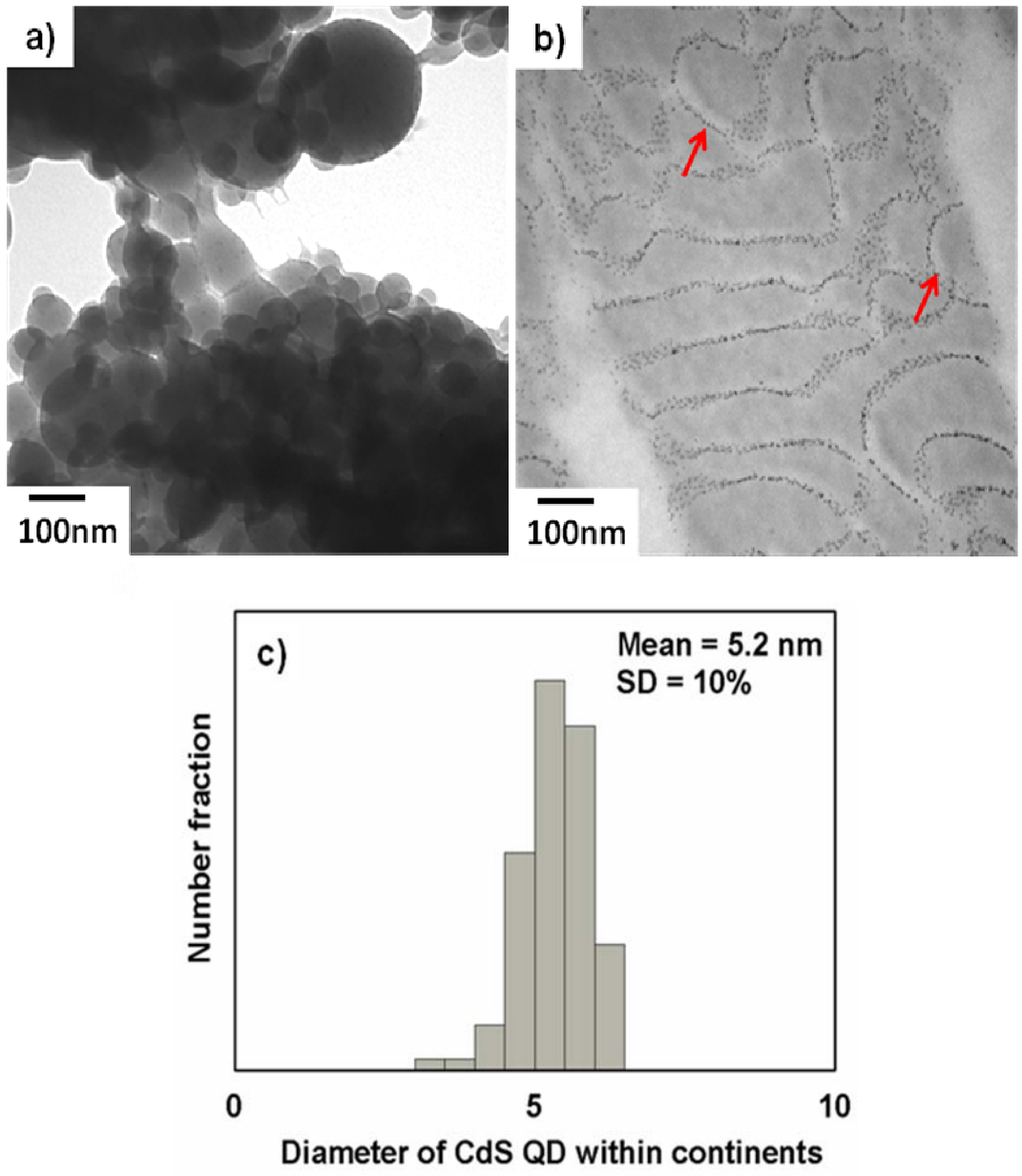

Figure 4.26. (a) High-magnification TEM image of QD/polymer aggregates (continents) from self-assembly of PS/PMAA-CdS in THF/water (c_o = 1.0 wt%, 50 wt% water, annealing method) (b) cross section TEM image of continent. (c) Statistical analysis of diameter of CdS QDs within continent aggregates obtained from measuring 100 particles.

A high magnification-TEM image (Figure 4.26a) of a continent-like aggregate formed at 50 wt% water reveals an agglomeration of spherical aggregates at the edge of the continent, suggesting that these larger aggregates grow via the coalescence of spherical supermicelles. We further obtained cross-sections of continent-like aggregates formed under the same conditions (Figure 4.26b) and discovered an internal lamellal structure consisting of regions of QDs (dark dots) dispersed in PMAA regions (light) alternating with PS regions (grey). The internal structure of these continents is therefore analogous to that of worms described in the previous section, except with more extended lamella compared to the discrete segments of worms. Close to the edge of the aggregate within the cross-section image (red arrows Figure 4.26b), the QD/PMAA regions appear curved or circular, suggesting that the more extended lamellae observed within the aggregates evolve via the coalescence of spherical supermicelles from the edges. The mean diameter of CdS QDs within the continents could also be obtained from the cross-section images, giving a value of 5.2 nm, consistent with the sizes of CdS QDs obtained from individual PS/PMAA-CdS nanoparticles.

4.3.4.4. Proposed Formation Mechnism for Worms and Continents. The annealing experiment in THF/water at 11 wt% water shows aggregates presenting just above the cwc (~10 wt% water) where the PS/solvent interfacial tension and driving force for self-assembly are relatively low. Several aggregates observed at this water concentration appear to be early transition structures for worms and continents at higher water contents, and therefore shed some light on their formation mechanism.

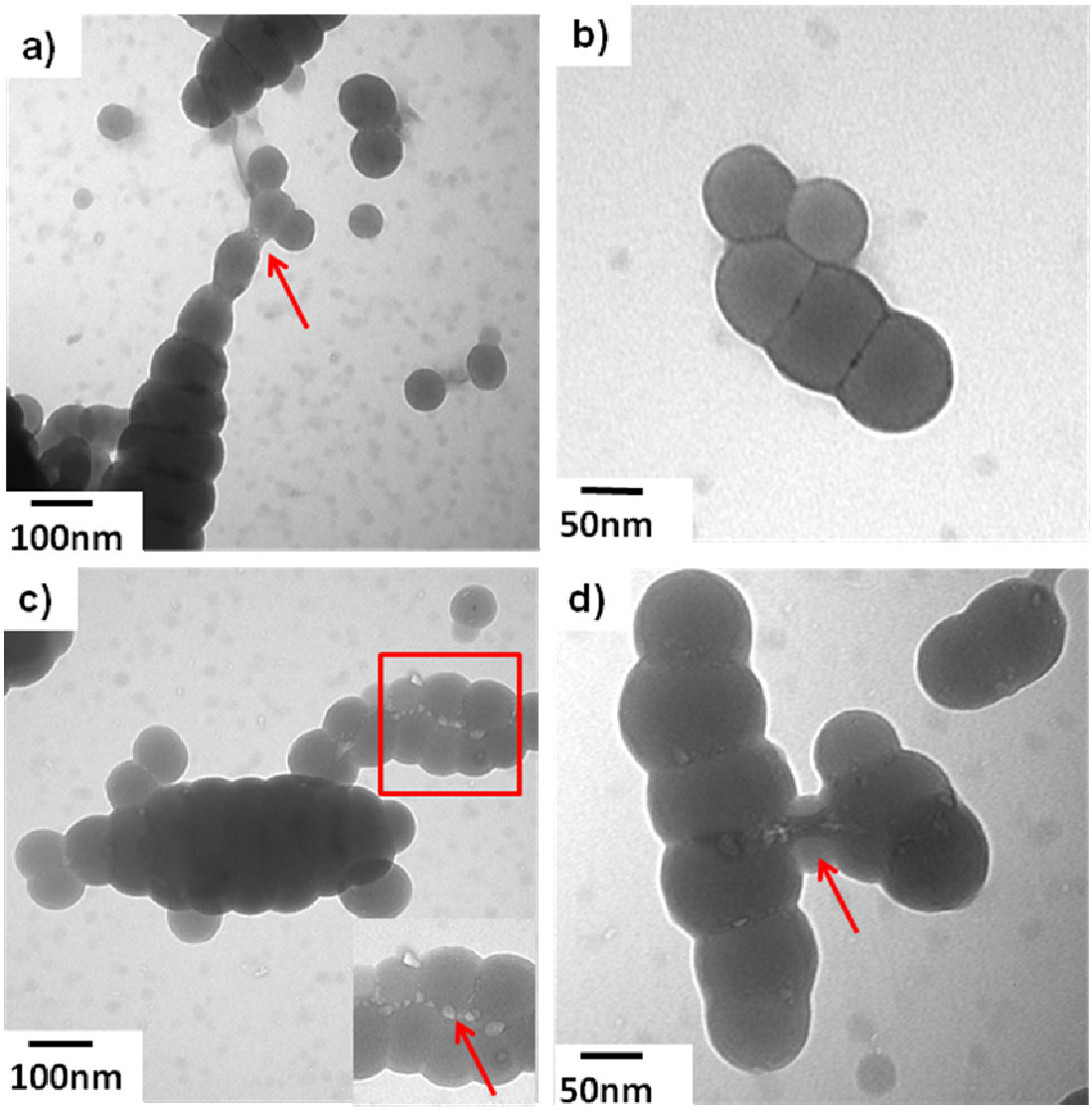

Figure 4.27. High magnification TEM images of various QD/polymer aggregates from self-assembly of PS/PMAA-CdS in THF/water (c_o = 1.0 wt%, 11wt % water, annealing method)

Figure 4.27 shows various types of PS/PMAA-CdS aggregates observed at 11 wt% water after 2 weeks annealing and subsequent quenching and dialysis. Coexisting with different morphologies is a population of small spherical supermicelles with mean diameter ~40 nm. Figure 4.27a shows a worm-like aggregate which appears to be growing via addition of spherical supermicelles to the end of the worm (indicated by an arrow), suggesting that worms form and grow via the "chaining" of spheres. This is further supported by the presence of short worms such as that shown in Figure 4.27b, which clearly formed by end-on coalescence of spheres with an additional sphere adding from the side. The side addition of spheres as observed in Figure 4.27a and Figure 4.27b appears to be one pathway by which worms become thicker, following the initial chaining of relatively small spherical supermicelles. The worm-like supermicelle in Figure 4.27a is clearly thicker than at the worm end, where spheres have more recently added by end-on addition. Another apparent pathway for worm thickening is the "zipping together" of thinner worms; aggregates in Figure 4.27c and Figure 4.27d provide evidence for this process. In Figure 4.27c, we see a relatively thick worm at the centre of the image with spheres adding at the ends and at the sides. In addition, to the upper right of that worm, we see an aggregate which clearly formed from the side-on combination of two worms (inset of Figure 4.27c). We note that each thin worm in the pair has a thickness of approximately ~40 nm, close to the diameter of the coexisting spherical supermicelles, further suggesting that the each of the combining thin worms formed via chaining of spheres. In the inset of Figure 4.29c, we note that several channels of relatively electron dense material have opened up between the combining worms, which may facilitate mass transfer of polymer and QDs as the worms zip together. Another

example of two combining worms is shown in Figure 4.27d, this aggregate appears to have formed via two worms connecting in one region along their lengths, where a channel of electron-dense material has opened up (arrow).

Considering the similar internal structure of worm-like and continent-like aggregates, it appears that continents evolve via the formation and thickening of worms. We note that continent-like aggregates are generally rectangular in shape, with a distinct long axis and with internal lamella running perpendicular to the long axis, as they do in the higher-aspect ratio worms. Based on the TEM evidence described above, we propose a mechanism for the formation of worms and continents via self-assembly of PS/PMAA-CdS at c_o = 1.0 wt% in THF/water mixtures. As described in Figure 4.28, self-assembly above the cwc begins with the formation of spherical supermicelles. The spheres then undergo one-dimension assembly ("chaining") followed by internal rearrangement involving localized diffusion of chains between neighboring spheres. In this way, worm-like supermicelles with an internal lamellar structure form, such that each worm segment constitutes a bilayer comprised of PS chains oriented along the long axis; PS chains issue from both sides of the regularly-spaced disks consisting of close-packed QDs and bulk-phase PMAA. As well, some PMAA chains will extend from the worm into solution from the edges of each disk, maintaining colloidal stability when worm-like supermicelles are transferred into pure water. Next, the growth of worms (lengthening and thickening) appears to involve either addition of spheres to worms or the combination of worms, leading to continents with more extensive internal lamellae. The addition of spheres to the sides of worms or the combination of worms will lead to an increase in the short

lateral dimension (thickening), whereas the addition of spheres to the ends of worms will increase the long lateral dimension (lengthening).

The proposed mechanism may explain why worm-like supermicelles, and not continents, were observed for c_0 = 1.0 wt% in THF with water addition by the immediate quenching method, when kinetic factors are taken into account. In that experiment, water was added between the cwc and 75 wt% water at a steady rate over a time period of ~21 min, and then immediately quenched to kinetically freeze the aggregates. During this period of steady water addition, the driving force for self-assembly increased, but the chain dynamics became progressively slower, until eventual freezing by the time water addition was complete. Due to the combination of slow dynamics and the limited time for self-assembly, the kinetic contributions are much more important in the immediate quenching than in the annealing experiments. We therefore propose that the formation of worms, instead of continents, via the former method, was due to the insufficient time provided for the worms to thicken into continents, although the worms did grow in length to an upper limit 6 μm, comparable to that of the continents. This implies that worm lengthening is relatively fast, on the order of minutes, whereas thickening into continents occurs on much longer time scales, on the order of days to weeks. This is probably due to the much larger amount of material that must coalescence with growing supermicelles to thicken a long, thin worm, compared to the amount material that must coalescence to form a long, thin worm.

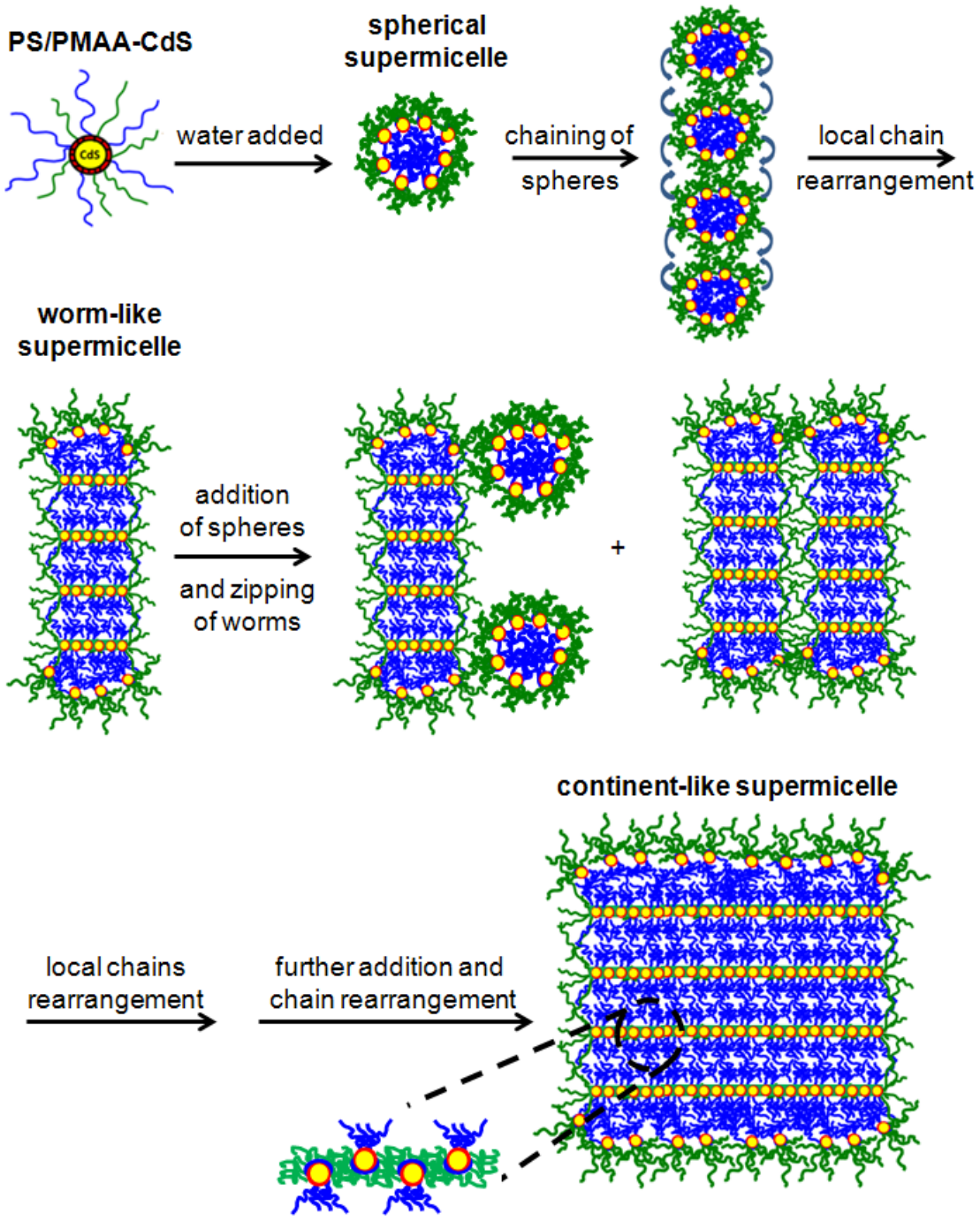

Figure 4.28. Proposed mechanism for the formation and growth of QD/polymer worms and continent aggregates.

Considering the proposed models of worm-like and continent aggregates described in Figure 4.28, we note that their internal structures are very similar in all but one respect-the percentage of PMAA chains in the bulk phase (i.e. within the internal lamellae) compared to PMAA chains in solution (i.e. within the supermicelle corona), which is greater in continents compared to worms. Furthermore, in the spherical supermicelles, all of the PMAA chains are present in solution. This suggests that at sufficiently high water contents above the cwc, the transition from spheres, to worms, to continents is partially driven by the progressive removal of PMAA chains from solution, and their transfer into the bulk phase within internal lamellae. A possible thermodynamic explanation for this is an increase in the conformational entropy of PMAA chains in the bulk lamellar phase compared to solubilized PMAA chains within the supermicelle coronae. We point out that the coronal PMAA chains of the various morphologies are close-packed within a brush-like structure issuing from junction points at the supermicelle surface. As water at pH = 7 is progressively added above cwc , these close-packed PMAA chains in solution will become negatively charged, due to the increasing dielectric constant of the mixed solvent, leading to deprotonation and charging of coronal chains, as observed by Eisenberg and coworkers[25] for water addition to PS-*b*-PAA copolymers in DMF. We note that the pKa of PMAA homopolymer has been reported to be 4.71.[41] The combination of the charging and closed-packing of PMAA upon water addition results in strong electrostatic repulsion between chains, which gives rise to a strong negative conformational entropy contribution due to high degree of stretching of solubilized coronal chains. A relaxation of this negative entropy contribution occurs as PMAA chains are transferred from the corona into the internal

bulk phase of a supermicelle, resulting in the morphological evolution from spheres to worms to continents. In the following section, we provide experimental evidence for the importance of PMAA interchain repulsive interactions on the supermicelle morphologies, by demonstrating that completely different aggregate structures can be obtained simply by adding a small amount of salt or acid to PS/PMAA-CdS solutions in THF prior to water addition.

4.3.4.5. QD/polymer Vesicles via Salt or Acid Addition (c_o = 1.0 wt% THF/Water, Immediate Quenching Method). We next carried out PS/PMAA-CdS self-assembly starting with c_o = 1.0 wt% in THF with the addition of a small quantity of NaCl (R_{NaCl} = 3 NaCl : methacrylic acid repeat units). NaCl was added to THF in a 4.5 M aqueous solutions, resulting in an initial water content of 2.5 wt% water, well below the cwc. Water was then added dropwise at a steady rate to induce self-assembly via the immediate quenching method. We note that the conditions for this experiment are identical to those used previously to produce worm-like supermicelles (e.g. Figure 4.18), except for the presence of a small quantity of salt, which will screen the electrostatic repulsive interactions between PMAA chains during the self-assembly process. If such repulsive interactions play an important role in the formation of worms and continents, as proposed in the previous section, we expected the screening of these interactions to have a dramatic effect on the aggregate morphology. The observed cwc for this experiment was ~13 wt%, slightly higher than that observed for same polymer concentration without added NaCl (~10 wt% water).

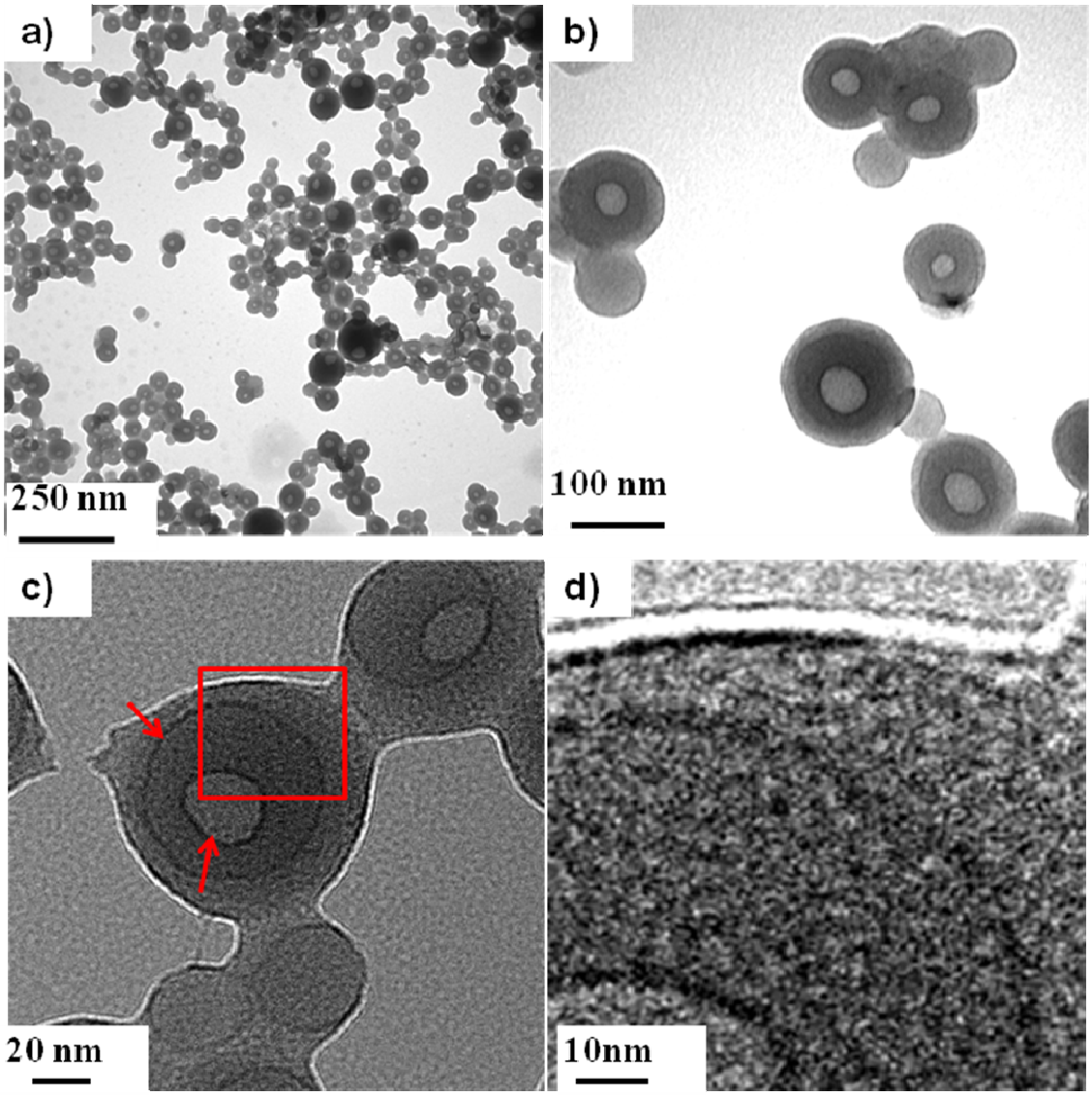

Figure 4.29. TEM images of QD/polymer vesicles formed via self-assembly of PS/PMAA-CdS in THF/water with small quantity of added NaCl (c_o = 1.0 wt%, R_{NaCl} = 3.0 immediate quenching method).

Following quenching and dialysis, TEM reveals an aggregate morphology that is dramatically different from the worm-like supermicelles formed in the absence of NaCl, confirming the important role of electrostatic interchain repulsion on the self-assembly of PS/PMAA-CdS in THF/water. In Figure 4.29a, the resulting aggregates are clearly spherical particles; higher magnification images (Figure 4.29b,c) show that they are vesicles rather than simple spherical supermicelles. The light circle near the centre of each particle in the TEM images suggests the aggregates have a spherical shape with a "hollow" region (a water pool) in the centre, consistent with the structure of vesicle. Figure 4.31c also shows two concentric circles of high-electron density within the vesicles (indicated by arrows), suggesting an internal organization of concentric shells of QDs. At even higher magnification (Figure 4.29d), it appears that vesicles are made up of very densely-packed nanoparticles, although it is impossible to resolve individual QDs and to carry out their size analysis from these images. We attempted to obtain cross-sections of these vesicles, in order to better resolve the internal organization of QDs; however, the vesicle structure was clearly destroyed either by the embedding or the microtoming process (Figure 4.30). But within the resulting vesicle debris, dark dots of ~5 nm are clearly dispersed, along with grey PS regions of irregular shape, confirming that the vesicles do consist of self-assembled QDs.

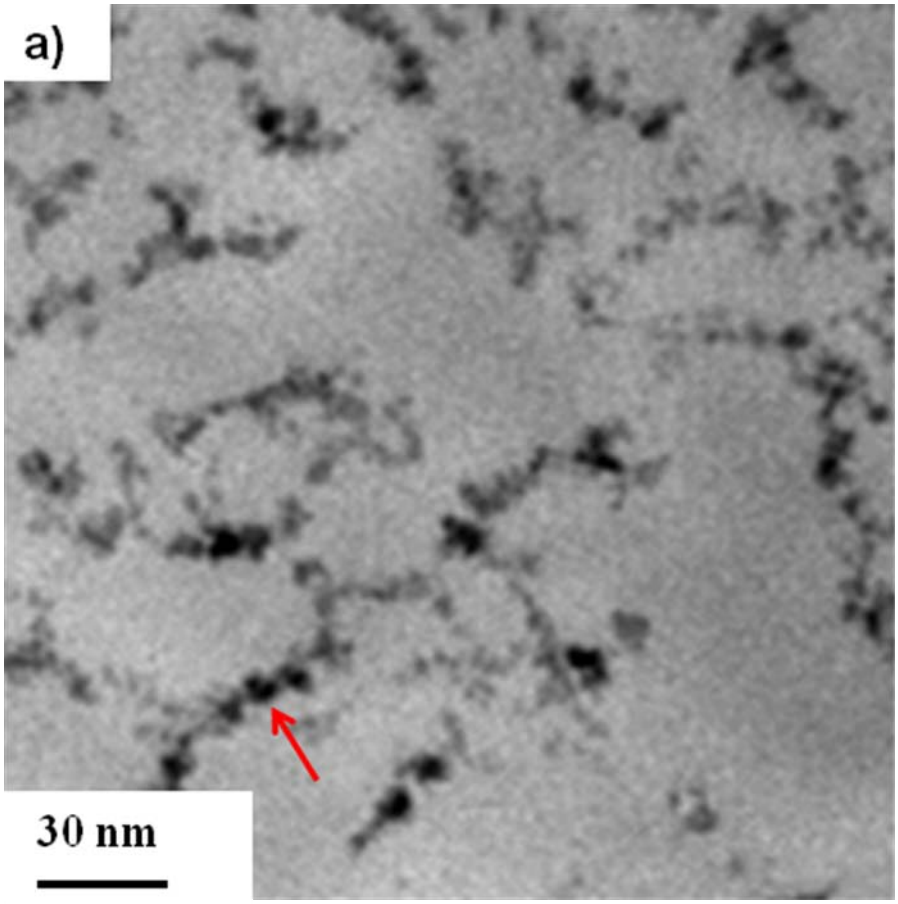

Figure 4.30. Cross-section TEM images of QD/polymer vesicles formed via self-assembly of PS/PMAA-CdS in THF/water with small quantity of added NaCl (c_o = 1.0 wt%, R_{NaCl} = 3.0 immediate quenching method).

The structure and formation mechanism for vesicles of PS/PMAA-CdS with NaCl added prior to self-assembly is shown in Figure 4.31. Similar to the formation of other aggregates via PS/PMAA-CdS self-assembly,we propose that water addition initially induces local reorganization of coronal chains to form surfactant-like Janus particles. However, rather than forming spherical supermicelles, or spheres followed by worms and continents, the resulting Janus particle self-assembles into a bilayer vesicle structure, with PS chains forming the vesicle wall, PMAA chains dissolved in water (both

surrounding the vesicle and within an internal water pool), and QDs localized at the two PS/PMAA interfaces, forming two concentric shells of close-packed QDs within the assembly. As discussed extensively by Eisenberg and coworkers, for PS-*b*-PAA diblock copolymer self-assembly, [25,29-36,38-40,42] the formation of vesicles is the result of the competition between stretching of soluble and insoluble blocks, such that a decrease in interfacial curvature is thermodynamic favorable. In the present case, the vesicle morphology allows the QD junctions to densely pack at the PS/PMAA interfaces while lowering the degree of PS stretching relative to spherical and worm-like supermicelle (as will be shown later). This is balanced by the unfavorable contribution of stretching of PMAA chains, which will be much more crowded in vesicles (both in the internal pool and the external corona) than at the higher-curvature interface found in spheres. The high local density of PMAA in the vesicle morphology would be extremely unfavorable if electrostatic repulsion between negatively charged segments was significant. However, by adding NaCl and screening these repulsive interactions during self-assembly, the thermodynamic balance favors the formation of vesicles rather than spheres. As well, NaCl screening of repulsive electrostatic interactions prevents the formation of worms and continents, which, as discussed previously, is the direct result of repulsion between solubilized PMAA chains.

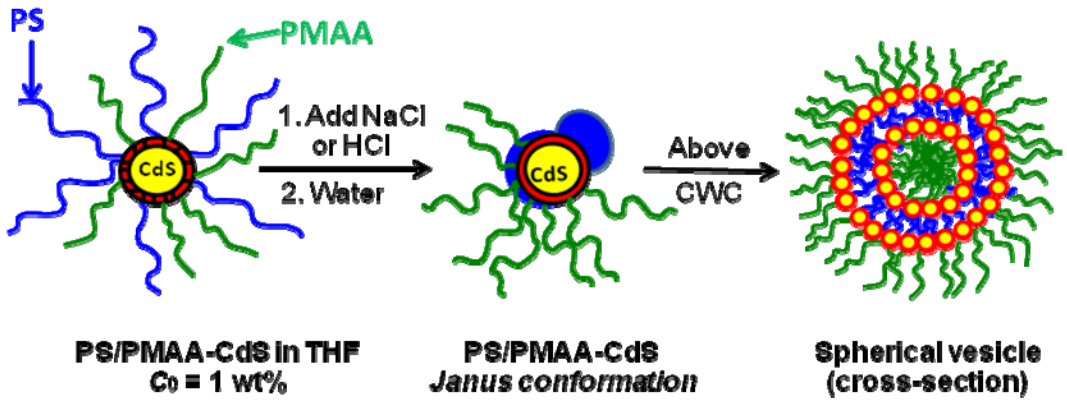

Figure 4.31. Proposed self-assembly process for QD/polymer vesicles in THF/water.

Figure 4.32 shows TEM size distribution analysis of vesicle dimensions. As shown in Figure 4.32b, the mean vesicle diameter is 93 nm, with a relative standard deviation of 13 %. Figure 4.32c shows a dark-field TEM image of a single vesicle, indicating the PS wall thickness. The wall thickness distribution is shown in Figure 4.34d, indicating a mean thickness of 24 nm, with relative standard deviation of 17%. Considering that each wall represents a bilayer of PS chains, we calculated the percentage of PS chain extension in the vesicle to be ~16%, significantly less than the calculated PS extension in spheres (95%) and worms (72%) formed under different conditions in THF/water.

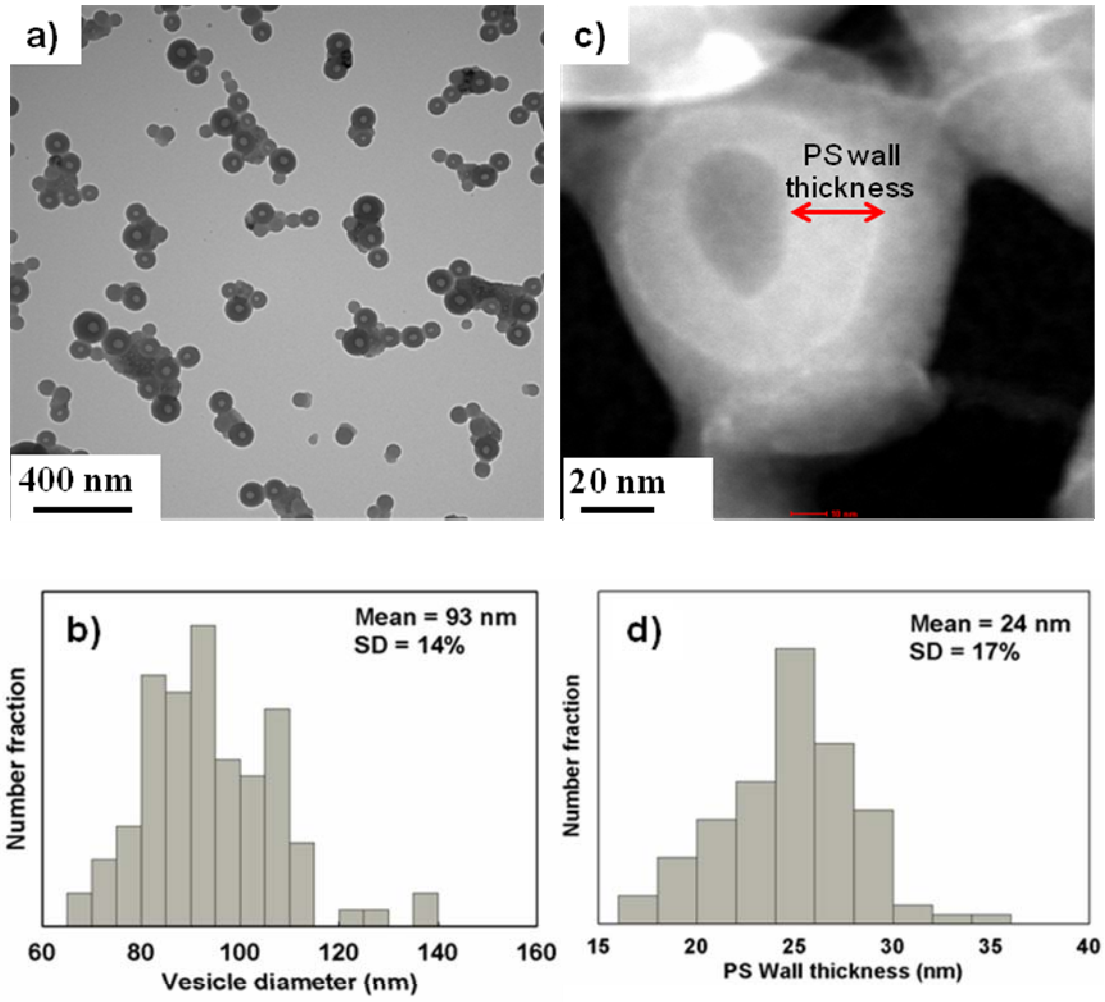

Figure 4.32. (a),(b) TEM images of QD/polymer vesicles formed via self-assembly of PS/PMAA-CdS in THF/water with small quantity of added NaCl (c_0 =1.0 wt%, R_{NaCl} = 3.0, immediate quenching method) (c) and (d) Vesicle diameter and PS wall thickness size distribution determined from measurement of 100 particles in several TEM images.

AFM was employed to determine the 3D topology of the vesicles after their disposition from aqueous solutions onto a glass substrate. After dialysis, the PS is glassy, so the vesicle shape should not be distorted by solvent evaporation or interaction with the glass substrate. The topology of the vesicles is shown in Figure 4.33a, and a height profile along the indicated white line is shown in Figure 4.33b. The 3D AFM image shows the shape of the vesicle to be square, which is likely an artifact arising from the tip shape. AFM does not reveal any central holes or pits in the particle topologies, indicating that the hole region observed by TEM is encapsulated inside of the vesicles. The distribution analysis from AFM images of heights and FWHM diameters was obtained (Figure 4.33c,d). The mean height and diameter values of 110 nm and 130 nm suggest that the vesicles are approximately spherical in shape, rather than disk-like structures. The diameter of vesicles determined by AFM (130 nm) is about 30 % greater than the diameter determined by TEM (93 nm), most likely due to the contribution of the PMAA chains on the surface of vesicles, similar to the difference between TEM and AFM dimensions of worm-like aggregates discussed previously.

Using TEM with EDX, we applied elemental analysis to confirm the presence of CdS QDs inside the vesicles. A dark-field TEM image of a typical vesicle is shown in Figure 4.34a with 6 spots indicating six different regions of elemental analysis, including a reference region outside of the vesicle. Clearly, the resulting EDX spectra support localization of CdS QDs inside the vesicle.

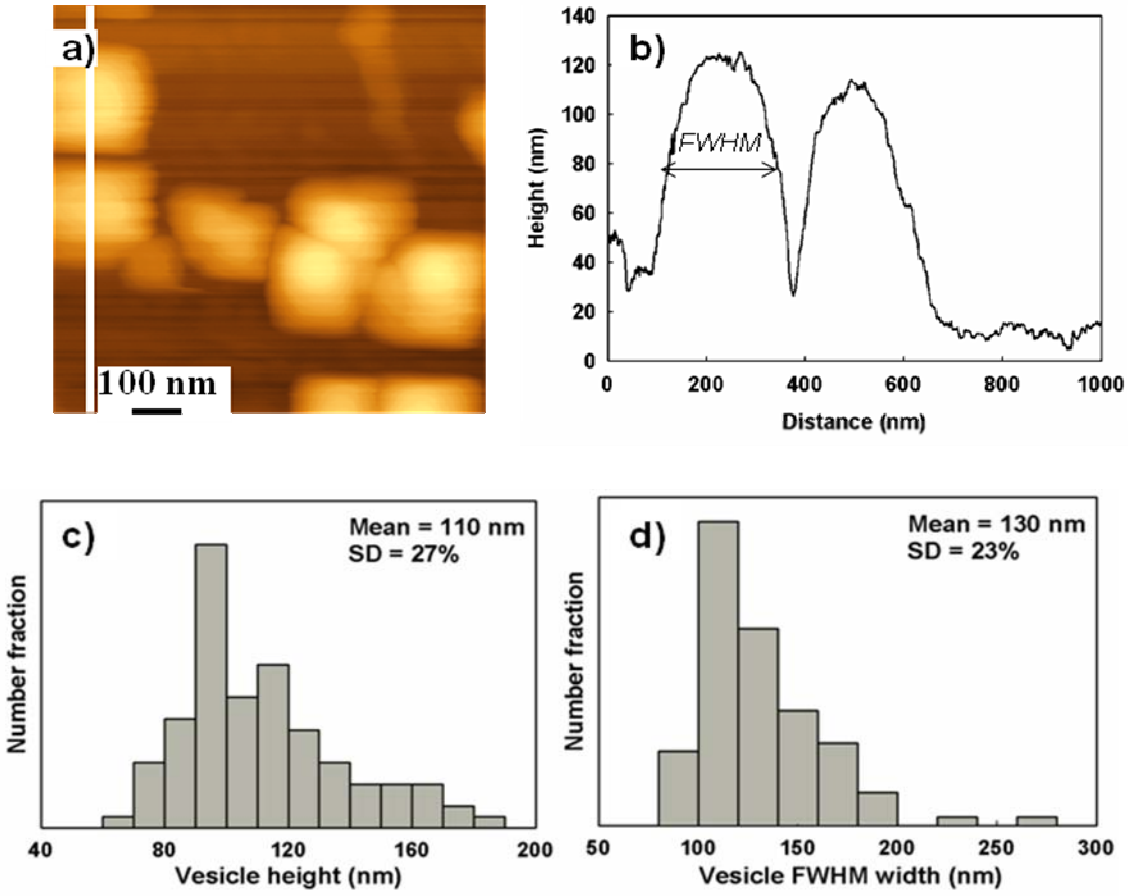

Figure 4.33. (a) AFM images of QD/polymer vesicles cast on glass from aqueous solution. (b) Surface feature topology profile for white line in (a); (c) Height and (d) FWHM width distributions determined from 100 measured aggregates in several AFM images.

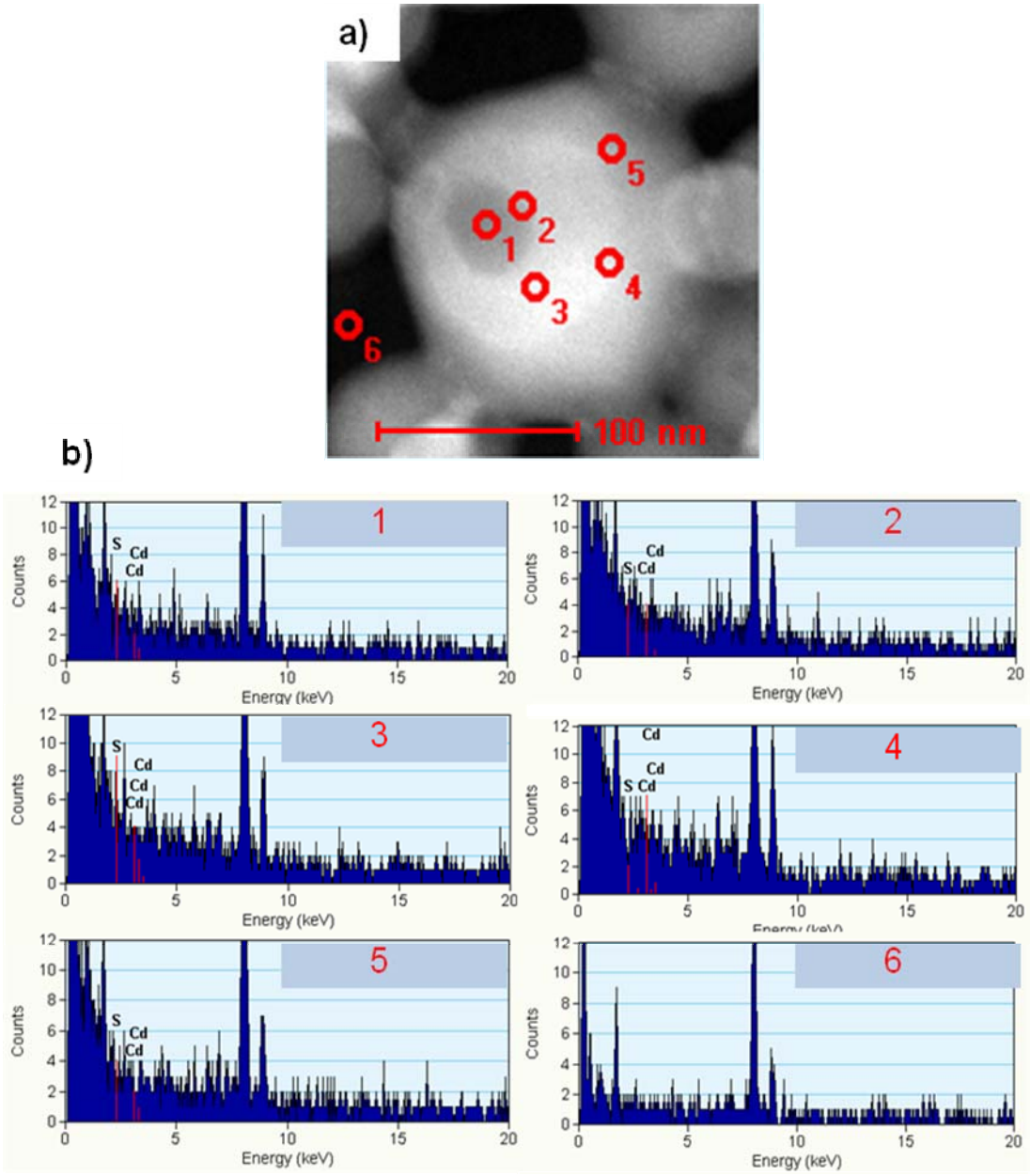

Figure 4.34. (a) Dark field TEM image of QD/polymer vesicles formed by adding NaCl (b) Energy-dispersive X-ray spectra corresponding to regions 1, 2, 3, 4, 5 and 6 indicated by red spots in (a).

In order to further prove that the role of salt addition is to screen the electrostatic repulsion between PMAA chains, we choose an independent method to lower the interchain repulsion- i.e. decreasing the negative charge on PMAA chains by adding acid (HCl), R_{HCl} = 0.08 (0.08 mol HCl: 1 mol methacrylic acid repeat units) rather than NaCl to c_o = 1.0 wt% PS/PMAA-CdS in THF and adding water via the immediate quench method. We found an almost identical vesicle morphology as when NaCl was added prior to self-assembly (Figure 4.35a and b). Figure 4.35c and d show TEM size distribution analysis of vesicle dimensions with a mean vesicle diameter of 83 nm, and a mean PS wall thickness is 23 nm, both in reasonable agreement with that of vesicles formed by adding NaCl. The similar colloidal structures in these two cases suggests the important and consistent morphological effect of lowering electrostatic repulsion between PMAA chains during self-assembly, either by lowering pH or adding salt.

4.3.4.6. pH-Dependent Surface Charge and Hydrodynamic Diameter of PS/PMAA-CdS Vesicles. Due to their external PMAA layer, it is of practical interest to control the surface charge of these QD/polymer vesicles in order to apply them to a broad range of biological applications, such as drug delivery, and photoluminescentbiological labeling. Particle surface charges will influence both their transport and electrostatic binding properties in biological systems, such that it is of interest to both measure and tune this parameter in aqueous colloids. The surface charge of colloidal particles in water is generally characterized using the zeta potential. In this study, zeta potential and hydrodynamic size of vesicles formed with R_{NaCl} = 3.0 were investigated by changing the pH via adding acid or base. It is important to note that, due to the glassy nature of the PS walls following dialysis, the basic morphology of the vesicles will remain constant during

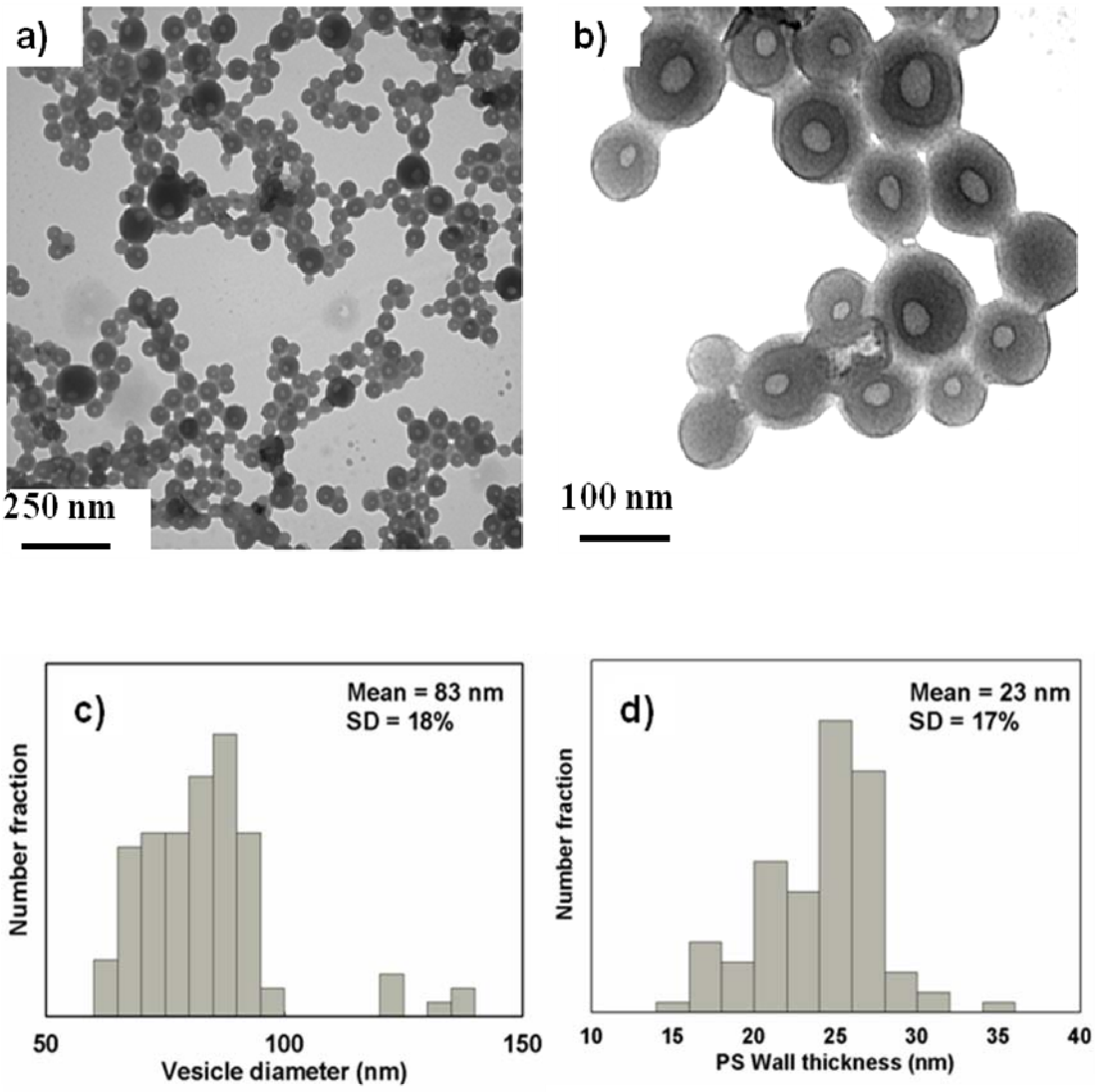

Figure 4.35. (a) and (b)TEM images of QD/polymer vesicles formed via self-assembly of PS/PMAA-CdS in THF/water with small quantity of added HCl (c_o = 1.0 wt%, R_{HCl} = 0.8 immediate quenching method). (c) and (d) Vesicle diameter and PS wall thickness size distribution determined from measurement of 100 particles in several TEM images.

the acid/base titrations, although the solubilized PMAA corona can expand or contract in response to changes in pH. Figure 4.36a shows that the zeta potential of the vesicles is negative over the investigated pH range, indicating negative surface charge, and increases in magnitude with increasing pH, consistent with an increase in the degree of ionization of the polyacid external chains. Meanwhile, the hydrodynamic diameter of the vesicles increases with increasing pH (Figure 4.36b), because the increasing electrostatic repulsive interactions between PMAA chains leads to higher degrees of stretching within the coronal layer, as shown in Figure 4. 36c.

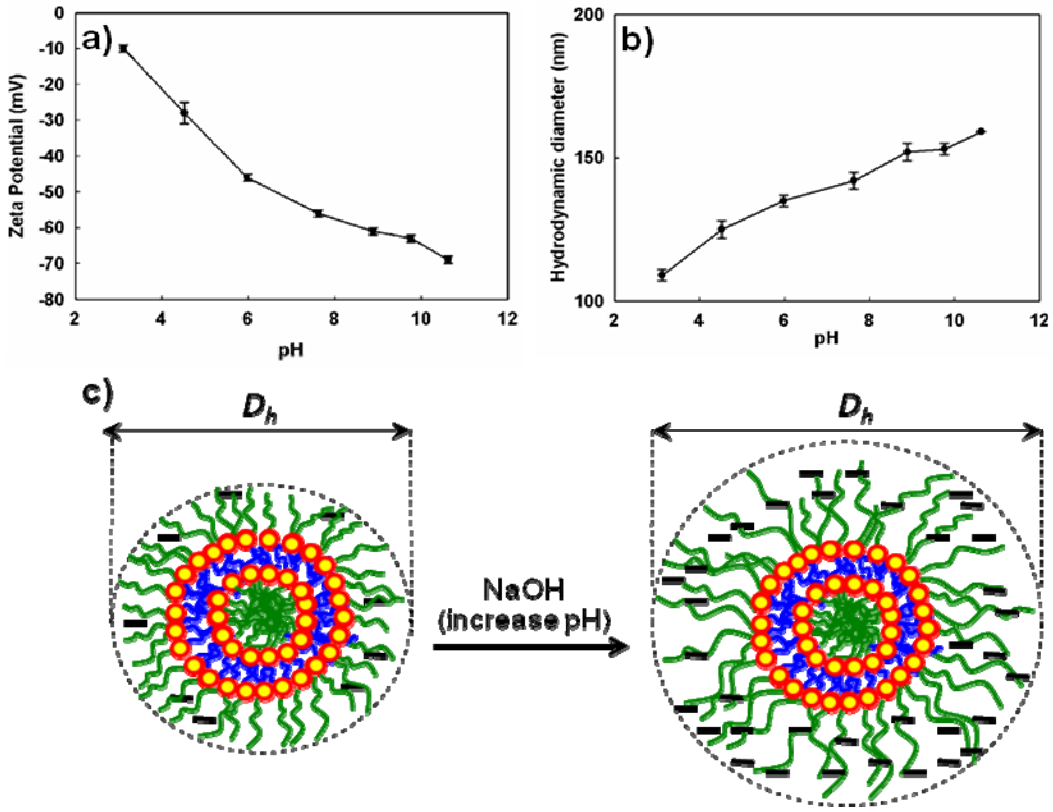

Figure 4.36. (a) Plot of zeta potential vs pH value of QD/polymer vesicle (formed with R_{HCl} = 0.08). (b) Plot of hydrodynamic diameter of QD/polymer vesicle (formed with R_{HCl} = 0.08). (c) Schematic diagram of vesicle with increasing pH value.

4.3.4.7. Photoluminescence of QD/Polymer Spherical Supermicelles and Vesicles. Figure 4.37 shows normalized and smoothed PL spectra of the spherical supermicelles and the vesicles, compared to the PL spectra of individual PS/PMAA-CdS dispersed in THF. The PL spectra of aggregate morphologies are blue-shifted relative to the emission spectrum of the individual PS/PMAA-CdS, with vesicles showing a larger blue shift than spheres. The following possible factors may lead to the observed blue-shifts in QD PL: 1) selective incorporation of smaller QDs from the original PS/PMAA-CdS population into the aggregates; 2) changes in QD surface trap state energies due to conformational rearrangements resulting in changes in polymer-QD surface interactions near the QD surface during self-assembly of PS/PMAA-CdS; and 3) increases in the relative intensity of light scattering at lower wavelengths due to increased particle size.

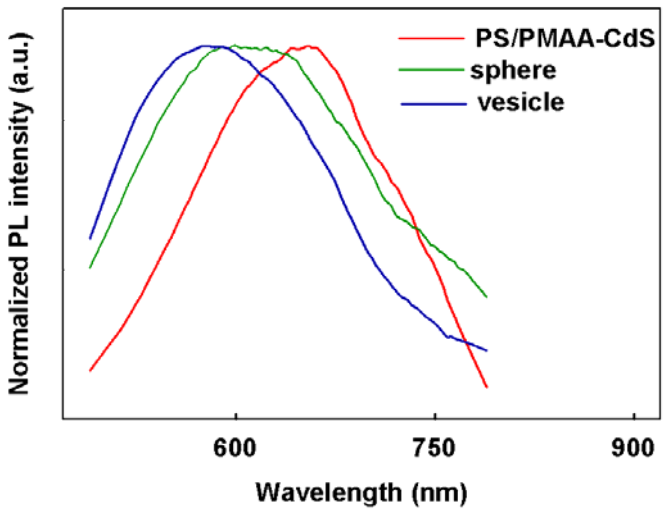

Figure 4.37. Photoluminescence spectra of PS/PMAA-CdS dispersed in THF (red line), QD/polymer spherical supermicelle (dark green line), and QD/polymer vesicle (formed with R_{HCl} = 0.8) (dark blue line), all spectra run at excition wavelength λ_{ex} = 400 nm using a 420 nm long-pass filter.

4.4 Conclusions

This chapter demonstrates the synthesis and characterization of semiconductor quantum dots (QDs) with mixed PS (hydrophobic) / PMAA (hydrophilic) polymer brush stabilizing layers. The block copolymer-like self-assembly behavior of these amphiphilic PS/PMAA-CdS nanoparticles suggest local phase separation of randomly-distributed PS and PMAA coronal chains within the mixed brush structure, resulting in anisotropic interactions between nanoparticles mediated by energetic contributions from interfacial tension and chain stretching. As a result, we show that a broad spectrum of rich and tunable self-assembled QD/polymer morphologies (e.g. spheres, worms, continents and vesicles) can be formed in aqueous colloids by varing several experimental variables, including the initial solvent, the initial polymer concentration, the addition of salt or acid and the conditions of water addition (i.e., immediate quenching vs annealing methods). All of the self-assembled aggregates have a unique and well-defined internal organization of QDs. Considering thermodynamic and kinetic aspects, a mechanism for the formation of worms and continents from spherical supermicelles was proposed. In addition, zeta potential measurements show that the surface charge of PS/PMAA-CdS vesicles can be controlled via changes in pH. These QD/polymer colloids demonstrate an important advance in the development of complex QD materials with structural hierarchy via self-assembly.

4.5. Refernce:

(1) Chen, Y.; Ji, T.; Rosenzweig, Z. *Nano Lett* **2003**, *3*, 581-584.

(2) Chen, Y.; Rosenzweig, Z. *Nano Lett* **2002**, *2*, 1299-1302.

(3) Yonezawa, T.; Matsune, H.; Kimizuka, N. *Adv. Mater.* **2003**, *15*, 499-503.

(4) Cha, J.; Birkedal, H.; Euliss, L.; Bartl, M.; Wong, M.; Deming, T.; Stucky, G. *J. Am. Chem. Soc.* **2003**, *125*, 8285-8289.

(5) Shenhar, R.; Jeoung, E.; Srivastava, S.; Norsten, T.; Rotello, V. *Adv. Mater.* **2005**, *17*, 2206-2210.

(6) Boal, A.; Ilhan, F.; DeRouchey, J.; Thurn-Albrecht, T.; Russell, T.; Rotello, V. *Nature* **2000**, *404*, 746-748.

(7) Frankamp, B.; Boal, A.; Rotello, V. *J. Am. Chem. Soc.* **2002**, *124*, 15146-15147.

(8) Srivastava, S.; Frankamp, B.; Rotello, V. *Chem. Mater.* **2005**, *17*, 487-490.

(9) Maya, L.; Muralidharan, G.; Thundat, T.; Kenik, E. *Langmuir* **2000**, *16*, 9151-9154.

(10) Naka, K.; Itoh, H.; Tampo, Y.; Chujo, Y. *Langmuir* **2003**, *19*, 5546-5549.

(11) Fullam, S.; Rao, S.; Fitzmaurice, D. *J Phys ChemB* **2000**, *104*, 6164-6173.

(12) Caruso, F. *Adv. Mater.* **2001**, *13*, 11.

(13) Radtchenko, I.; Sukhorukov, G.; Gaponik, N.; Kornowski, A.; Rogach, A.; Mohwald, H. *Adv. Mater.* **2001**, *13*, 1684-1687.

(14) Wang, D.; Rogach, A.; Caruso, F. *Nano Lett* **2002**, *2*, 857-861.

(15) Sheng, W.; Kim, S.; Lee, J.; Kim, S.; Jensen, K.; Bawendi, M. *Langmuir* **2006**, *22*, 3782-3790.

(16) Joumaa, N.; Lansalot, M.; Theretz, A.; Elaissari, A. *Langmuir* **2006**, *22*, 1810-1816.

(17) Sherman, R.; Ford, W. *Langmuir* **2005**, *21*, 5218-5222.

(18) Moffitt, M.; Vali, H.; Eisenberg, A. *Chem. Mater.* **1998**, *10*, 1021-1028.

(19) Duxin, N.; Liu, F.; Vali, H.; Eisenberg, A. *J. Am. Chem. Soc.* **2005**, *127*, 10063-10069.

(20) Kang, Y.; Erickson, K.; Taton, T. *J. Am. Chem. Soc.* **2005**, *127*, 13800-13801.

(21) Kang, Y.; Taton, T. *J. Am. Chem. Soc.* **2003**, *125*, 5650-5651.

(22) Kang, Y.; Taton, T. *Angew. Chem. Int. Ed.* **2005**, *44*, 409-412.

(23) Kang, Y.; Taton, T. *Macromolecules* **2005**, *38*, 6115-6121.

(24) Zhang, M.; Drechsler, M.; Muller, A. *Chem. Mater.* **2004**, *16*, 537-543.

(25) Zhang, L.; Eisenberg, A. *Macromolecules* **1996**, *29*, 8805-8815.

(26) Zubarev, E.; Xu, J.; Sayyad, A.; Gibson, J. *J. Am. Chem. Soc.* **2006**, *128*, 15098-15099.

(27) Zubarev, E.; Xu, J.; Sayyad, A.; Gibson, J. *J. Am. Chem. Soc.* **2006**, *128*, 4958-4959.

(28) Li, D.; Sheng, X.; Zhao, B. *J. Am. Chem. Soc.* **2005**, *127*, 6248-6256.

(29) Yu, Y.; Eisenberg, A. *J. Am. Chem. Soc.* **1997**, *119*, 8383-8384.

(30) Yu, G.; Eisenberg, A. *Macromolecules* **1998**, *31*, 5546-5549.

(31) Yu, K.; Bartels, C.; Eisenberg, A. *Macromolecules* **1998**, *31*, 9399-9402.

(32) Yu, K.; Bartels, C.; Eisenberg, A. *Abst Pap Am Chem* **1998**, *216*, U53-U53.

(33) Yu, K.; Eisenberg, A. *Macromolecules* **1998**, *31*, 3509-3518.

(34) Yu, K.; Zhang, L.; Eisenberg, A. *Langmuir* **1996**, *12*, 5980-5984.

(35) Yu, Y.; Zhang, L.; Eisenberg, A. *Langmuir* **1997**, *13*, 2578-2581.

(36) Yu, Y.; Zhang, L.; Eisenberg, A. *Macromolecules* **1998**, *31*, 1144-1154.

(37) Zhang, L.; Eisenberg, A. *Science* **1995**, *268*, 1728-1731.

(38) Zhang, L.; Eisenberg, A. *Macromolecules* **1999**, *32*, 2239-2249.

(39) Zhang, L.; Eisenberg, A. *Macromol Symp***1997**, *113*, 221-232.

(40) Zhang, L.; Eisenberg, A. *Polym Advan Techol* **1998**, *9*, 677-699.

(41) Serizawa, T.; Taniguchi, K.; Akashi, M. *Colliod Surface A* **2000**, *169*, 95-105.

(42) Zhang, L.; Yu, K.; Eisenberg, A. *Science* **1996**, *272*, 1777-1779.

CHAPTER 5

Contributions to Original Knowledge

and Suggestions for Future Work

5.1. Contributions to Original Knowledge

The aim of this section is to provide a summary of the results and the main contributions to original knowledge in this thesis.

Chapter 2 described the synthesis of semiconductor quantum dots (QDs) with a mixed layer of PS/PMMA stabilizing coronal chains (PS/PMMA-CdS). The synthesis was achieved through the self-assembly of a PS-*b*-PAA-*b*-PMMA triblock copolymer followed by growth of cadmium sulfide QDs in the resulting micelle cores of Cd^{2+}-coordinated PAA blocks. UV-vis and photoluminescence results showed that these hybrid nanoparticles could be dispersed in different organic solvents with a range of polarities, while showing long-term stability of QD size in the various solvents. The distribution of PS and PMMA chain junctions on the core surface was determined to be statistical by 2D ^{1}H NOESY experiments, on the basis of significant through-space correlations between PS and PMMA segments within the corona in THF. Furthermore, SLS and DLS data revealed that both the hydrodynamic radius and radius of gyration underwent significant changes in solvents with different polarities, due to solvent-responsive conformational changes within the mixed brush layer. To our knowledge, this work provided the first example of semiconductor QDs coated with mixed polymer brush layers. It represents a key step toward a new type of self-assembling building block for QD/polymer films and colloids with structural hierarchy.

Chapter 3 demonstrated the self-assembly of PS/PMMA-CdS nanoparticles in films of PS/PMMA polymer blends. Due to their mixed polymer coronal layer, consisting of PS and PMMA chains, PS/PMMA-CdS was driven to the PS/PMMA interface during

phase separation via spin-coating. In this way, the nanoparticles regulated the domain size and stabilized the phase-separated blend morphologies during subsequent annealing experiments. In addition, CdS QDs provide additional photoluminescence to the spin-coated blend films. After selective removal of PS and PMMA homopolymers by washing the blend films with selective solvents, we showed that tunable QD surface patterns were obtained as result of interfacial self-assembly within the blends. This work reveals that nanoparticles coated with mixed polymer brush layers could play an important role in the polymer blend films, which are critical in the performance of polymer-based photovoltaic and light-emitting devices, since they are able to control the domain size of blend films, as well as increase the lifetime of devices by stabilizing domain sizes at high temperatures.

Finally, Chapter 4 described the first synthesis and characterization of amphiphilic CdS QDs with mixed hydrophobic PS/hydrophilic PMAA polymer brush layers (PS/PMAA-CdS). The synthesis of amphiphilic PS/PMAA-CdS began with the formation of PS/PMMA-CdS as described in Chapter 2, except that the PAA layer in the core was covalently crosslinked for increased micelle stability; the PMAA chains in the mixed corona were then hydrolyzed to PMAA without any significant micelle dissociation, forming PS/PMAA-CdS. The amphiphilic PS/PMAA-CdS nanoparticles were found to show interesting and tunable self-assembly behavior in DMF/water and THF/water mixtures, suggesting phase separation of PS and PMAA chains within the mixed brush structure to form Janus particles with anisotropic interactions. As a result of their block copolymer-like self-assembly behavior in selective solvent mixtures, PS/PMAA-CdS form a wide range of interesting colloidal superstructures, including

spherical supermicelles, worms, continents and vesicles, each with well-defined internal organizations of QDs. Based on annealing experiments at relatively low water contents, a mechanism of the formation of worm-like and continent-like aggregates was proposed. This work demonstrated that the self-assembly of amphiphilic nanoparticles can form a wide range of interesting QD/polymer colloids with structural hierarchy in aqueous solution, which is very promising to produce nanostructured devices with the complex QD organization.

5.2. Future Work

Inspired by the wide range of amphiphilic block copolymer morphologies in aqueous media, further work in this area should continue to explore the possible structures that are obtainable via this amphiphilic nanoparticle approach, by further investigation of the experimental parameter space. Along with continuing to vary the important self-assembly parameters described in Chapter 4, including the nature of the initial solvent, the initial polymer concentration, and the amount of additives such as acid and salt, the effects of other important variables should also be explored, based on knowledge obtained from self-assembled block copolymer aggregates in solution.[1--8] For example, new triblock copolymers with different relative block lengths could be synthesized using the methods described in Chapter 2, in order to vary the surface composition of the amphiphilic nanoparticles. Shorter PMAA blocks relative to PS block lengths will favour high-curvature morphologies over a wider range of experimental conditions, due to a lowering of the relative importance of PMAA chain repulsions. This should allow access to the

broader range of bilayer-based colloidal morphologies found in crew-cut block copolymer systems, including tubules, Plumber's nightmare, onions, and concentric vesicles.[9] As well, mixed solvent systems, such as the mixtures of THF and DMF, could be applied, in order to provide finer control over the polarity of the initial solvent medium and thus the degree of PS stretching; for example, gradually decreasing the solvent polarity should favour a gradual increase in the PS chain stretching, and a concomitant increase in the tendency to form morphologies with high curvature. This should provide a handle to explore interesting morphological transitions, such as that between spheres and cylinders, which is observed in several block copolymer systems. These and other studies would not only extend the range of control over three-dimensional nanoparticle self-assembly into unprecedented hierarchical structures, but also open up routes to numerous device structures for photonics, electronics and biology.

Another direction of future research should produce analogous amphiphilic nanoparticles, but with different inorganic cores for different optical, electronic and magnetic functionality. For example, noble metal nanoparticles (Au, Ag) exhibit interesting surface plasmon effects which can be modulated via controlled self-assembly.[10-13] Magnetic nanoparticles (Fe_2O_3) with amphiphilic character also open up intriguing possibilities for producing new spintronic and magnetic storage devices via fine hierarchical structural control. As well, external magnetic fields could be applied to amphiphilic magnetic nanoparticles during self-assembly, allowing fundamental investigations to be carried out on the relative of importance of external (top-down) vs. internal (bottom-up) forces for structural control at various length scales.[14-16]

Reference:

(1) Yu, G.; Eisenberg, A. *Macromolecules* **1998**, *31*, 5546-5549.

(2) Yu, K.; Zhang, L.; Eisenberg, A. *Langmuir* **1996**, *12*, 5980-5984.

(3) Yu, Y.; Eisenberg, A. *J. Am. Chem. Soc.* **1997**, *119*, 8383-8384.

(4) Yu, Y.; Zhang, L.; Eisenberg, A. *Macromolecules* **1998**, *31*, 1144-1154.

(5) Zhang, L.; Eisenberg, A. *Macromolecules* **1999**, *32*, 2239-2249.

(6) Zhang, L.; Eisenberg, A. *Science* **1995**, *268*, 1728-1731.

(7) Zhang, L.; Eisenberg, A. *Macromolecules* **1996**, *29*, 8805-8815.

(8) Zhang, L.; Yu, K.; Eisenberg, A. *Science* **1996**, *272*, 1777-1779.

(9) Soo, P.; Eisenberg, A. *J Polym Sci Pol Phys* **2004**, *42*, 923-938.

(10) Shenhar, R.; Jeoung, E.; Srivastava, S.; Norsten, T.; Rotello, V. *Adv. Mater.* **2005**, *17*, 2206-2210.

(11) Boal, A.; Ilhan, F.; DeRouchey, J.; Thurn-Albrecht, T.; Russell, T.; Rotello, V. *Nature* **2000**, *404*, 746-748.

(12) Srivastava, S.; Frankamp, B.; Rotello, V. *Chem. Mater.* **2005**, *17*, 487-490.

(13) Cao, Y.; Din, R.; Mirkin, C. *Abstr Pap Am Chem* **2001**, *222*, U312-U313.

(14) Kim, B.; Qiu, J.; Wang, J.; Taton, T. *Abstr Pap Am Chem* **2006**, *231*, -.

(15) Kim, B.; Taton, T. *Langmuir* **2007**, *23*, 2198-2202.

(16) Keng, P.; Shim, I; Pyun, J.; *ACS Nano* **2007**,1, 279-292.